Neuroscience Bulletin

The Official Journal of The Chinese Neuroscience Society

神经科学通报

Volume 37
Number 1
January 2021

Astrocytic Lactate Modulates Passive Coping Response

Springer

www.neurosci.cn

CONTENTS

Neuroscience Bulletin

About the Cover

In humans, a symptom of the passive coping response can be described as hopelessness, which is a core feature of major depressive disorder (MDD). Exploring the regulatory mechanism of the passive coping response to behavioral challenge could provide new strategies to conquer MDD. Yin *et al*. found that astrocyte-derived lactate modulates the passive coping response to behavioral challenge. The cover image shows the mouse stealing lamp-oil is trapped in the jar, and a passive state emerges when the mouse finds it is impossible to get out. The smoke arising from the lamp billows into the sky and forms the encephaloid cloud, which mimics what is happening in the brain of this frustrated mouse. The lactate derived from astrocytes spreads to the neuron just like sunlight scattering onto a tree. See pages 1-14. (Cover image provided by Dr. Ya-Nan Yin)

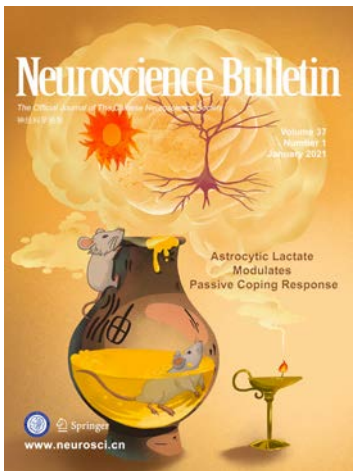

Volume 37 Number 1
January 2021

Original Articles

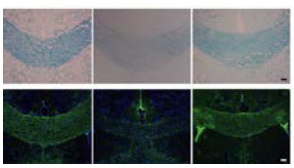

p24

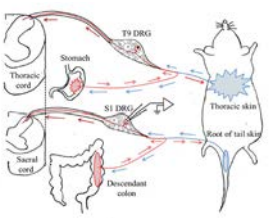

p52

CONTENTS

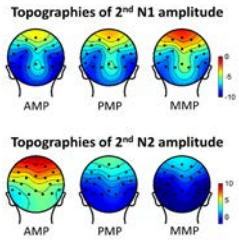

p75

Letters to the Editor

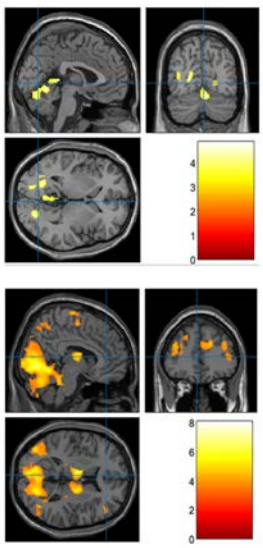

p88

Reviews

www.neurosci.cn

CONTENTS

Research Hightlights

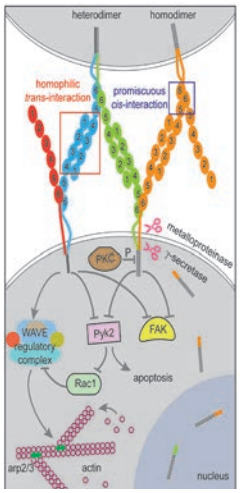

p127

Neurosci. Bull. January, 2021, 37(1):1–14
https://doi.org/10.1007/s12264-020-00553-z

www.neurosci.cn
www.springer.com/12264

ORIGINAL ARTICLE

Astrocyte-Derived Lactate Modulates the Passive Coping Response to Behavioral Challenge in Male Mice

Ya-Nan Yin[1] · Jian Hu[1] · Yi-Li Wei[1] · Ze-Lin Li[1] · Zhou-Cai Luo[1] · Rui-Qi Wang[1] · Ke-Xin Yang[1] · Shu-Ji Li[1] · Xiao-Wen Li[1] · Jian-Ming Yang[1] · Tian-Ming Gao[1]

Received: 9 March 2020 / Accepted: 6 May 2020 / Published online: 12 August 2020

Abstract Every organism inevitably experiences stress. In the face of acute, intense stress, for example, periods of passivity occur when an organism's actions fail to overcome the challenge. The occurrence of inactive behavior may indicate that struggling would most likely be fruitless. Repeated serious stress has been associated with mood disorders such as depression. The modulation of passive coping response patterns has been explored with a focus on the circuit level. However, the cellular and molecular mechanisms are largely uncharacterized. Here, we report that lactate is a key factor in the astrocytic modulation of the passive coping response to behavioral challenge in adult mice. We found increased extracellular lactate in the medial prefrontal cortex (mPFC) when mice experienced the forced swimming test (FST). Furthermore, we discovered that disturbing astrocytic glycogenolysis, which is a key step for lactate production in the mPFC, decreased the duration of immobility in the FST. Knocking down monocarboxylate transporter 4 (MCT4), which is expressed exclusively in astrocytes and transports lactate from astrocytes to the extracellular space, caused similar results in the FST. The behavioral effect of both the pharmacological disturbance of astrocytic glycogenolysis and viral disruption of MCT4 expression was rescued *via* the administration of *L*-lactate. Moreover, we found that both pharmacological and viral modulation of astrocyte-derived lactate in mPFC slices increased the excitability of layer V pyramidal neurons, and this enhancement was reversed by exogenous *L*-lactate administration. These results highlight astrocyte-derived lactate as a biological mechanism underlying the passive coping response to behavioral challenge and may provide new strategies to prevent mood disorders.

Keywords Astrocyte · Lactate · Forced swimming test · Passive coping · Neuronal excitability

Introduction

Various stresses are ineluctable for an organism. Slight stress can heighten the vigilance of an organism encountering danger or a person confronting a work emergency; in these situations, stress is beneficial for survival and development. Nevertheless, in challenging situations, organisms confront acute, intense stress and exhibit periods of passivity when they fail to overcome challenges. In humans, a symptom of the passive coping response can be described as hopelessness, which is a core feature of major depressive disorder (MDD). MDD is a fear-based crippling and very common illness that affects an enormous proportion of the global population with a lifetime prevalence of nearly 20% [1] and is the leading cause of disability [2]. Exploring the regulatory mechanism of the passive coping

Electronic supplementary material The online version of this article (https://doi.org/10.1007/s12264-020-00553-z) contains supplementary material, which is available to authorized users.

✉ Jian-Ming Yang
jimmyyoung@smu.edu.cn

✉ Tian-Ming Gao
tgao@smu.edu.cn

[1] State Key Laboratory of Organ Failure Research, Key Laboratory of Mental Health of the Ministry of Education, Guangdong-Hong Kong-Macao Greater Bay Area Center for Brain Science and Brain-Inspired Intelligence, Guangdong Province Key Laboratory of Psychiatric Disorders, Collaborative Innovation Center for Brain Science, Department of Neurobiology, School of Basic Medical Sciences, Southern Medical University, Guangzhou 510515, China

response to behavioral challenge could untangle the etiopathogenesis of MDD. Furthermore, it can provide new strategies to overcome MDD.

Existing research on the regulatory mechanism of the passive coping response to behavioral challenge mainly focuses on the circuit level [3–6]. However, in addition to neurons, glial cells, especially astrocytes, play important roles in maintaining the proper functioning of the brain. Astrocytes regulate synaptic transmission, neuronal activity, and neural circuit function [7]. Furthermore, the density, morphology, and gene expression of astrocytes are associated with stress [8]. Nevertheless, there is limited knowledge on the roles astrocytes play in the response to stress, especially intense stress, which may lead to passive coping patterns in challenging situations.

In the brain, astrocytes, rather than neurons, store glycogen [9, 10]. After glycogenolysis and glycolysis [11], astrocytes produce and transfer lactate to neurons through monocarboxylate transporters (MCTs) [12–14]. Lactate can be converted into pyruvate to prepare for the tricarboxylic acid cycle and oxidative phosphorylation and is an important signaling molecule [11]. *L*-lactate promotes the expression of synaptic plasticity-related genes such as Zif268, c-Fos, and Arc [15]. In day-old chicks, glycogen stores decrease after taste-aversion training [16, 17], and injection of the glycogen phosphorylation inhibitor 1,4-dideoxy-1,4-imino-D-arabinitol (DAB) impairs taste aversion memory [18]. *L*-lactate is sufficient to rescue impaired taste-aversion memory [19]. Disrupting the production and transport of lactate damages long-term memory formation in rats and can be rescued by *L*-lactate [20]. In addition, stress controls lactate formation [21–23], and lactate seems to be substantially involved in regulating responses to stress [24]; however, there is minimal direct evidence. Therefore, we explored the role of astrocyte-derived lactate in the passive coping response in a challenging situation.

The forced-swimming test (FST) is widely used to evaluate the despair aspect of depression-like behavior and to screen antidepressants in rodents [25–27]. At the outset of a rodent swimming in a cylinder, a brief period of vigorous activity occurs; subsequently, a passive state emerges when the rodent finds it is impossible to escape from the cylinder [4]. Furthermore, transitions between active and passive coping responses in the FST are clearly demarcated; therefore, the FST is an appropriate model to imitate challenging conditions involving acute and intense stress.

Previous studies have shown that stress induces lactate metabolism in the mPFC [28–30]. The PFC is answerable to coordinated thought and action and is crucial for planning as well as executive and cognitive control [31–33]. Activating the mPFC reduces the immobility time in the FST [34–36] and has an antidepressant-like effect [37]; furthermore, astrocytes in the mPFC mediate depression-like behavior [38–41], and the mPFC has been shown to play a role in managing the passive coping response [4, 42–44]. Therefore, we focused on the mPFC to determine whether astrocyte-derived lactate modulates the passive coping response to behavioral challenge and to explore the possible mechanisms.

Materials and Methods

Animals

Male C57BL/6J mice (aged 8 weeks) were obtained from the Guangdong Medical Laboratory Animal Center (Guangzhou, China). Four mice were housed in a cage under standard laboratory conditions: 12 h light–dark cycle, lights on at 08:00, temperature 24 ± 1 °C. Sufficient food and water were provided, and mice could freely move and eat. Two mice with guide cannulae in place shared one cage but were kept apart with a separator. The behavioral tests were executed between 10:00 and 16:00. All procedures were approved by the Southern Medical University Animal Ethics Committee and were performed according to the Regulations for the Administration of Affairs Concerning Experimental Animals (China). Before the behavioral test, each mouse was handled twice a day for 3 days. Efforts were made to minimize animal suffering and to reduce the number of animals used.

Microdialysis

The microdialysis cannulae (CMA 7 guide cannulae), probes (CMA 7), and fluorinated ethylene propylene tubing were all from CMA Microdialysis, Inc., Stockholm, Sweden. Mice were anesthetized with 0.75% pentobarbital sodium and placed in a stereotaxic instrument (Stoelting, Wood Dale, IL, USA). Following skin preparation, the scalp was opened, and a small hole was drilled into the skull (1 mm diameter). Microdialysis probe guide cannulae were implanted unilaterally in the mPFC at the following coordinates: + 1.8 mm anteroposterior (AP), ± 0.3 mm mediolateral (ML), and − 1.5 mm dorsoventral (DV) relative to bregma according to The Mouse Brain in Stereotaxic Coordinates [45]. The guide cannulae were fixed with dental cement. After surgery, each mouse was kept warm with an electric blanket and rehoused after recovery. All unilateral manipulations were counterbalanced across hemispheres. The active dialysis surface length of the membrane was 1 mm.

Microdialysis experiments were conducted 24 h after surgery. The probe was inserted into the guide cannula and perfused with artificial cerebrospinal fluid (aCSF, in mmol/

L: 126 NaCl, 26 $NaHCO_3$, 3 KCl, 1.25 NaH_2PO_4, 10 glucose, 2 $CaCl_2$, and 1 $MgSO_4$) at 2 μL/min using a high-precision pump (CMA 402 syringe pump, CMA Microdialysis, Inc.). After at least 2 h for equilibration, five dialysate samples (20 μL each) were automatically collected from each mouse using an MAB85 microfraction collector every 10 min over a 50-min period. During collection of the fifth sample, mice experienced a 6-min FST. At the end of the experiment, each mouse was perfused, and dissected for further histological verification. Only mice with cannulae positioned properly in the mPFC were used.

Lactate Measurement

To quantify lactate in microdialysis dialysate samples, Lactate Assay Kit-WST was used (L256, Dojindo Molecular Technologies, Inc.). Before measurements were made, the dye mixture stock solution, working solution, and lactate standard solution were prepared. Twenty microliters of lactate standard solution and sample solution were mixed with 80 μL of working solution. The microplate was incubated at 37 °C for 30 min. The absorbance was measured at 450 nm using a microplate reader. The concentration of lactate in the sample was determined using a calibration curve [46].

Drug Stereotaxic Microinjection

Mice were anesthetized with 0.75% pentobarbital sodium and mounted on a stereotaxic frame (Stoelting). Stainless-steel guide cannulae were placed unilaterally or bilaterally into the mPFC (AP, + 1.8; ML, ± 0.3; DV, − 2.5 mm). The unilateral guide cannulae (length, 3 mm; C315G/SPC; Plastics One) were fixed with dental cement, and dummy stylets (the same length as the guide cannulae; C315DC/SPC, Plastics One) were inserted into the guide cannulae to prevent blockage. The bilateral guide cannulae (62022; RWD) were implanted as described above. Seven days after implantation, behavioral tests were performed.

mPFC injections of DAB (300 or 1000 μmol/L; D1542; Sigma-Aldrich) and sodium *L*-lactate (10 or 100 mmol/L; 71718; Sigma-Aldrich) were made 15 min before the behavioral tests [20]. For unilateral drug infusion, the dummy stylets were extracted, and infusion cannulae (the same length as the guide cannulae; C315I/SPC, Plastics One) connected to 5 μL microsyringes (Hamilton, Reno, NV, USA) installed on a microinfusion pump (RWD200, Shenzhen, China) *via* polyethylene tubing (C313C, Plastics One Inc.) were inserted into the guide cannulae. Each mouse was injected with 1 μL of the drug at 0.1 μL/min [38]. For bilateral drug infusion, the operation was similar to that described above, with the addition of an injection needle (62250, RWD) and polyethylene tubing (62320, RWD). Each mouse was injected with 0.5 μL of the drug on each side at 0.1 μL/min. To ensure that the drug diffused completely, the infusion cannulae were left in place for an additional 5 min after the microinfusion pump stopped. After performing the behavioral tests, the mice were perfused, and dissected for further histological verification. Only mice with cannulae properly positioned in the mPFC were used.

Virus Generation and Stereotaxic Injections

The adeno-associated virus (AAV) shRNA knockdown vector system is an efficient method of modulating expression. For MCT4 knockdown, the following short-hairpin sequences were used: pAAVE1821: 5′-TGTTATGAAACCAGCCGTGGG-3′; pAAVE1822: 5′-AAACTTTGGTTGCATCCAGCA-3′; and pAAVE1823: 5′-TAGATCTGGATAATGCTTCTG-3′. High titers of engineered AAV vectors ($9.7 \times 10^{12} - 2.79 \times 10^{13}$ particles/ml) were serotyped with AAV8 coat proteins and produced by Shanghai Sunbio Medical Biotechnology.

Mice were anesthetized with 0.75% pentobarbital sodium and placed into a stereotaxic instrument (Stoelting). Engineered AAVs were stereotaxically injected bilaterally into the mPFC (AP, + 1.8; ML, ± 0.3; DV, − 2.8 mm). Using a microinjector pump (KDS, Stoelting) and a Hamilton syringe, 0.25 μL of virus solution was injected at 0.1 μL/min. After a 5-min delay, the needle was retracted 0.4 mm, and an additional 0.25 μL of virus was delivered. The needle was withdrawn 5 min after the second infusion. The above steps were repeated on the other side of the brain. Four injection sites were used for each mouse. After the behavioral tests were complete, the mice were anesthetized, perfused, and dissected for further histological verification. Only mice with proper eGFP expression in the mPFC were used.

Western Blot Analysis

Three weeks after virus injection, mice were rapidly decapitated and fluorescent mPFC tissue was detached with the aid of fluorescence microscopy. The subsequent manipulations were performed as previously described [47, 48]. Tissue homogenates were prepared in a detergent-based lysis buffer containing (in mmol/L) 50 Tris-HCl, pH 7.4, 150 NaCl, 2 EDTA, 1 phenylmethylsulfonyl fluoride, 50 sodium fluoride, 1 sodium vanadate, 1 dithiothreitol, 1% sodium deoxycholate, 1% SDS, and protease inhibitors. Protein samples were separated by 10% SDS-PAGE and transferred to PVDF membranes (Millipore), which were blocked with 5% skim milk at room temperature for 1 h followed by incubation with primary antibodies

(polyclonal anti-MCT4 antibody, 1:250; #SC-50329, Santa Cruz Biotechnology) at 4 °C overnight. HRP-conjugated secondary antibodies (1:10,000; ZB-2305, ZSGB-Biotech) were incubated in TBS for 1 h at room temperature. A monoclonal mouse anti-GAPDH antibody (1: 1,000; 3683S, Cell Signaling) was used for loading normalization. The protein expression levels were assessed by quantifying the gray density of the bands with FluorChem SP software.

Forced Swimming Test

Two clear glass cylinders (height 45 cm, diameter 19 cm) were filled to 23 cm with water (23.5 ± 1 °C). An opaque baffle plate was placed between the two glass cylinders to exclude interference with each other. The camera was placed as close as possible to obtain the highest resolution and sharp images of the mice. Before the mice were placed into the cylinders, the experimenter started the video recording, held the mouse by the tail, and gently placed it in the water. The tail was slowly released once the mouse reached the water. The duration of the test was 6 min, and the immobility time during the last 4 min was recorded by experimenters who were blinded to the experimental group [38, 40].

Open Field Test

The mice were tested using open transparent plastic chambers (40 × 40 × 30 cm^3). A video camera and a 25-W red light bulb (illumination density at the center of the maze, 0.3 lx) were placed 180 cm above the center of the apparatus. In the 5-min test, a mouse was gently placed in the center and allowed to explore freely without external disturbance. The digitized image of the path taken by each mouse was stored, and the total distance moved through a trial was analyzed using EthoVision 7.0 software [38]. Sometimes, mice were tested in an open chamber (Accuscan Instruments Inc., Columbus, OH, USA) with a similar setup, and the total distance was analyzed using VersaMax analyzer software [40].

Slice Preparation

Slices were prepared as described previously [49, 50]. Each mouse (8 or 11 weeks old, male) was anaesthetized with ether, the skull was quickly opened, and the brain was removed into ice-cold modified artificial cerebrospinal fluid (aCSF) containing (in mmol/L) 220 sucrose, 2 KCl, 12 $MgSO_4$, 0.2 $CaCl_2$, 1.3 NaH_2PO_4, 26 $NaHCO_3$, and 10 *D*-glucose. Coronal mPFC slices (300 μm) were cut in ice-cold modified aCSF using a VT-1000S vibratome (Leica). The slices were rinsed and transferred to nylon mesh inside a storage chamber containing regular aCSF (in mmol/L: 126 NaCl, 3 KCl, 1 $MgSO_4$, 2 $CaCl_2$, 1.25 NaH_2PO_4, 26 $NaHCO_3$, and 10 *D*-glucose) at 34 °C for 30 min. The slices were incubated for an additional 1 h at 25 ± 1 °C before recording. All solutions were saturated with 95% O_2/5% CO_2 (*v*/*v*). For histological verification of the drug and virus injections, the slices were imaged under a fluorescence microscope (Olympus, Tokyo, Japan).

Electrophysiological Recording

mPFC slices were placed in the recording chamber, which was superfused (2 mL/min) with oxygen-saturated aCSF at 32–34 °C. Whole-cell patch-clamp recording was performed as previously described [49, 50]. Layer V pyramidal neurons of the mPFC were visualized with infrared optics using an upright microscope equipped with a 40× water-immersion lens (BX51WI; Olympus) and an infrared-sensitive CCD camera. Borosilicate glass pipettes were pulled on a micropipette puller (P-97, Sutter Instruments) with resistances of 4–6 MΩ. A MultiClamp 700B amplifier and 1440A digitizer (Molecular Devices) were used for recording.

For spontaneous excitatory postsynaptic current (sEPSC) recording, pyramidal neurons were held at − 70 mV in the presence of 20 μmol/L bicuculline methiodide to block the GABAergic input, with the pipette solution containing (in mmol/L): 130 K-gluconate, 20 KCl, 10 HEPES, 0.2 EGTA, 4 MgATP, 0.3 NaGTP, and 10 NaCreatine (pH 7.40, 285 mOsm).

For spontaneous inhibitory postsynaptic current (sIPSC) recording, pyramidal neurons were held at 0 mV in the presence of 50 μmol/L AP5 and 20 μmol/L CNQX to block the glutamatergic input, with the pipette solution containing (in mmol/L): 110 Cs_2SO_4, 0.5 $CaCl_2$, 2 $MgCl_2$, 5 EGTA, 5 HEPES, 5 TEA and 5 ATP-Mg (pH 7.40, 285 mOsm).

For action potential (AP) recording, pyramidal neurons were held at − 70 mV with the same pipette solution used for sEPSC recording. To evaluate neuronal excitability in the current-clamp experiments, APs were recorded by injecting a series of depolarizing pulses (from 40 to 160 pA in 20-pA increments), and a depolarizing ramp of current (from 0 to 160 pA, 5 s in duration) were applied [51]. For the modulation or rescue of electrophysiological phenotypes, the slices were perfused with ACSF containing DAB (50 μmol/L) or DAB (50 μmol/L) + *L*-lactate (5 mmol/L) for about 15 min prior to the experiment and throughout the recording period. During electrophysiological recording, series resistance was controlled at < 20 MΩ and not compensated. Cells were abandoned if membrane potentials were more positive than 0 mV or if series resistance fluctuated by > 20% of the initial value. Data were filtered at 1 kHz and sampled at 10 kHz.

Real-Time Quantitative PCR (qPCR)

Three weeks after virus infection, fluorescent brain tissue of the mPFC was removed with the aid of fluorescence microscopy. Total RNA was extracted with RNAiso Plus (Takara) according to the manufacturer's instructions, and a PrimeScript RT Reagent Kit (Takara) was used to synthesize cDNA. The Stratagene Mx3005P System (Agilent Technologies) was used for real-time PCR with SYBR Premix Ex Taq (Takara). The reactions were run in triplicate, and β-actin levels were used as an endogenous control for normalization for the ΔΔCt method. *Mct4*, forward primer, 5′-GACACGGCTTGGATCTCCTC-3′, reverse primer, 5′-CATTCCCAGGGACGCAAAGAG-3′; *β-actin*, forward primer, 5′-GAGATTACTGCCCTGGC TCCTA-3′, reverse primer, 5′-TCATCGTACTCCTGCTT GCTGAT-3′.

Statistical Analysis

Animals were randomly allocated to treatment groups. Analyses were conducted by blinded experimenters in all behavioral and electrophysiological tests. The number of samples was based on our experience. Statistical analysis was performed using GraphPad software (GraphPad Prism v6.0; GraphPad Software). The normality and equal variance of samples between different groups were assessed using the D'Agostino & Pearson omnibus normality test and F test, respectively. When these tests were passed, *t*-tests and one-way ANOVAs (followed by the least significant difference (LSD) test for *post hoc* comparisons) were performed; if the tests were not passed, a Mann–Whitney *U* test and Kruskal–Wallis one-way ANOVA (followed by Dunn's correction) were used. Two-way ANOVA (followed by Bonferroni's multiple comparisons test) was used in appropriate situations. All statistical tests were two-tailed, and significance was assigned at $P < 0.05$. The results are presented as the mean ± SEM.

Results

Increased Lactate Level in the mPFC During the FST

To explore whether lactate is involved in the regulation of the passive coping response, we first measured the lactate concentration in the mPFC during the FST.

Microdialysis was conducted to obtain dialysates from the mPFC during the FST. Mice with microdialysis cannulae were randomly divided into two groups: one group (the FST group) encountered stress, and the other was the control group. Dialysates from both groups were collected every 10 min. During the fifth dialysate sampling, the FST group experienced 6 min of FST (Fig. 1A, B). The positions of cannulae and tracks of probes were validated by histological methods (Fig. 1C). The FST group had significantly higher lactate levels than the control group and baseline concentrations (Fig. 1D, E, F). These results suggested that lactate in the mPFC plays a role in passive coping.

Astrocytic Glycogen Metabolism is Required in the mPFC for the Passive Coping Response to Behavioral Challenge

The expression of glucose metabolic pathways differs between astrocytes and neurons. Astrocytes, but not neurons, contain mostly glycogen, which is stored in the form of glucose [52]. Lactate is mainly produced by astrocytes *via* glycogenolysis and glycolysis [11] (Fig. 2A). To test whether astrocytic glycogenolysis in the mPFC affects the passive coping response to behavioral challenge, we randomly injected mice unilaterally with 300 μmol/L or 1000 μmol/L of the glycogen phosphorylation inhibitor DAB to block glycogenesis [20, 53] before they experienced the FST and open field test (OFT) (Fig. 2B). Trypan blue injection showed the infusion site (Fig. 2C).

Treatment with 1000 μmol/L but not 300 μmol/L DAB decreased the passive coping response in the FST (Fig. 2D). Then, the OFT was used to confirm that the decreased passive coping response was not caused by impairment of locomotor activity. We found that neither 300 μmol/L nor 1000 μmol/L DAB injections affected the OFT behavior (Figs. 2E and S1). These results showed that mice treated with 1000 μmol/L DAB exhibited a decreased passive coping response without impairment of locomotor activity.

Decreased Passive Coping Induced by Glycogen Metabolism Inhibition with DAB is Rescued by *L*-lactate

Lactate is the end-product of glycolysis in astrocytes, and during the FST, lactate levels were increased in the mPFC (Fig. 1F). We then asked whether the DAB-induced decrease in passive coping could be rescued by the administration of exogenous lactate.

The mPFC was unilaterally injected with a combination of 1000 μmol/L DAB or vehicle and either 10 mmol/L *L*-lactate, 100 mmol/L *L*-lactate, or vehicle and then the mice were subjected to the FST and OFT. DAB injection with vehicle decreased the passive coping response, verifying our results above (Fig. 2D). Conversely, 100 but not 10 mmol/L *L*-lactate co-administered with DAB rescued the decreased passive coping response (Fig. 2F). Furthermore, each group of mice showed a similar total distance

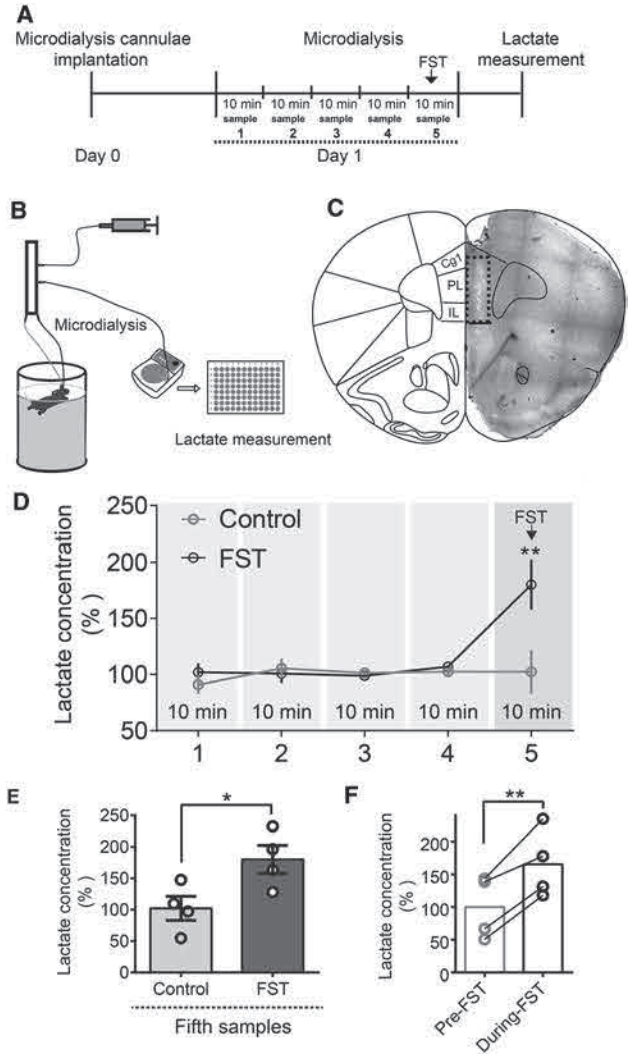

Fig. 1 The FST increases lactate production in the mPFC of mice. **A** Experimental procedures. **B** Schematic of microdialysis during the FST. **C** The position of cannulae and probe tracks (dashed rectangle). **D** Lactate levels in the control and FST groups during the entire microdialysis process (n = 4 mice/group; two-way ANOVA, $F(1, 6) = 9.731$, $P = 0.0206$, Bonferroni *post hoc* test, fifth samples: $t = 3.846$, df = 36, $P = 0.0028$). **E** Lactate levels in the control and FST groups during the FST (n = 4 mice/group; unpaired t-test, $t = 2.648$, df = 6, $P = 0.0381$). **F** Lactate levels before and during the FST (n = 4 mice/group; paired t-test, $t = 6.156$, df = 3, $P = 0.0086$). Error bars indicate the SEM, $^{*}P < 0.05$, $^{**}P < 0.01$.

travelled and other parameters in the OFT (Figs 2G and S2). These results suggested that astrocytic glycogen metabolism and lactate production participate in the modulation of passive coping.

Lactate Transport through MCT4 Plays an Essential Role in Passive Coping

To further explore whether the DAB-induced effect we found in the FST is indeed due to the modulation of lactate

Fig. 2 DAB decreases the passive coping response in the FST, and this is rescued by *L*-lactate. **A** The different glucose metabolic pathways in astrocytes and neurons. Glycogen is predominant in astrocytes [red arrows, upregulated pathways; black dashed arrows, downregulated pathways; dashed rectangle, very low abundance; red cross, target for DAB (inhibitor of glycogen phosphorylation)]. **B** Behavioral test procedures. **C** The dashed rectangle containing trypan blue represents the infusion site. (Cg1, anterior cingulate cortex; PL, prelimbic; IL, infralimbic; DP, dorsal peduncular cortex; scale bar, 500 μm). **D** Immobility duration in the FST after 300 μmol/L or 1000 μmol/L DAB (vehicle n = 13 mice; 300 μmol/L DAB n = 12; 1000 μmol/L DAB n = 14; one-way ANOVA, $F(2, 36) = 8.421$, $P = 0.001$, uncorrected Fisher's LSD test, $t = 3.723$, df = 36, $P = 0.0007$). **E** Total distance travelled in the OFT after 300 μmol/L or 1000 μmol/L DAB (vehicle: n = 13; 300 μmol/L DAB n = 12; 1000 μmol/L DAB n = 14; one-way ANOVA, $F(2, 36) = 0.1744$, $P = 0.3959$, uncorrected Fisher's LSD test). **F** Immobility time in the FST for drug-injected mice (vehicle + vehicle: n = 14; 1000 μmol/L DAB + vehicle: n = 14; 1000 μmol/L DAB + 10 mmol/L *L*-lactate: n = 13; 1000 μmol/L DAB + 100 mmol/L *L*-lactate: n = 11; one-way ANOVA, $F(3, 48) = 11.68$, $P < 0.0001$, uncorrected Fisher's LSD test, $t = 4.693$, df = 48, $P < 0.0001$; $t = 3.005$, df = 48, $P = 0.0042$). **G** Locomotor activity of drug-injected mice in the OFT (vehicle + vehicle: n = 14; 1000 μmol/L DAB + vehicle: n = 14; 1000 μmol/L DAB + 10 mmol/L *L*-lactate: n = 13; 1000 μmol/L DAB + 100 mmol/L *L*-lactate: n = 11; Kruskal-Wallis one-way ANOVA, Kruskal-Wallis statistic = 1.039, $P = 0.7918$). Error bars indicate the SEM, $^{**}P < 0.01$, $^{***}P < 0.001$, NS, not significant.

in astrocytes, we examined the effects of knocking down the expression of lactate transporters in the mPFC.

In mammals, MCTs belong to a large family of transporters composed of 14 members, which participate in the transport of monocarboxylates such as lactate. Three MCT isoforms, MCT1, MCT2, and MCT4, are found in the rodent brain. MCT1 is expressed by ependymocytes, the endothelial cells of microvessels, and astrocytes but not neurons. MCT2 is predominantly expressed in neurons. MCT4 expression is specific to astrocytes, and is strongly expressed in the cortex [13]. Consequently, we selected MCT4 as an intervention target to modulate the release of lactate by astrocytes.

We produced *Mct4*-shRNA AAV (Fig. 3A), one control shRNA virus, and three *Mct4*-shRNA viruses with enhanced green fluorescent protein (EGFP) after expression (Fig. 3B), screened the efficacy of the interference sequences at the mRNA level (Fig. 3C), and confirmed the knockdown efficiency at the protein level (Fig. 3D). Knocking down MCT4 in the mPFC reduced the passive coping response (Fig. 3F) and had no effect on locomotor activity (Fig. 3G).

We then tested whether the decreased passive coping response caused by MCT4 knockdown could be rescued by the administration of exogenous lactate. *Mct4*-shRNA virus

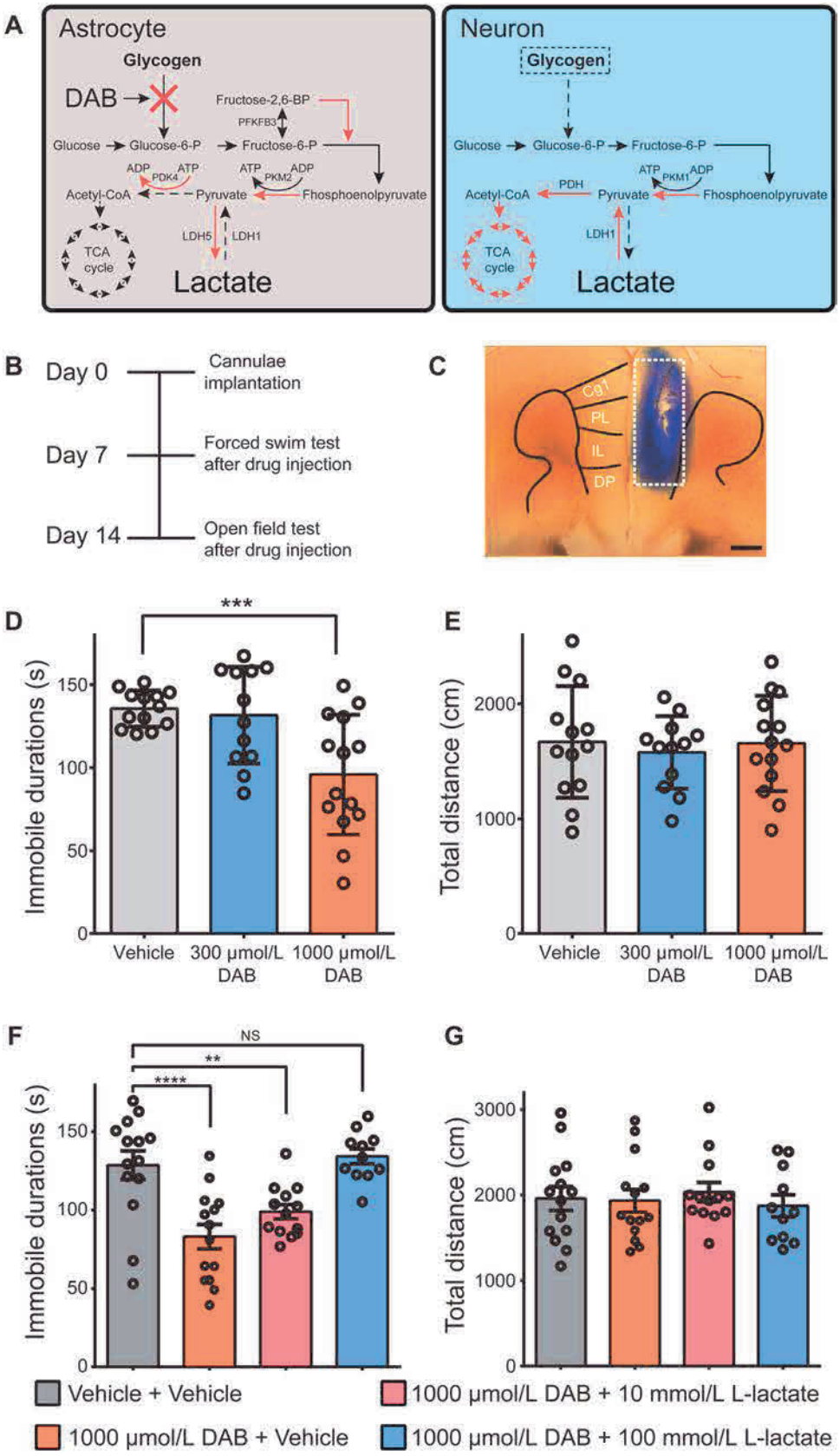
A
Astrocyte
Glycogen
DAB
Fructose-2,6-BP
PFKFB3
Glucose
Glucose-6-P
Fructose-6-P
ADP
PDK4
ATP
ATP
PKM2
ADP
Acetyl-CoA
Pyruvate
Fhosphoenolpyruvate
TCA cycle
LDH5
LDH1
Lactate
Neuron
Glycogen
Glucose
Glucose-6-P
Fructose-6-P
ATP
PKM1
ADP
PDH
Acetyl-CoA
Pyruvate
Fhosphoenolpyruvate
LDH1
TCA cycle
Lactate
B
Day 0
Cannulae implantation
Day 7
Forced swim test after drug injection
Day 14
Open field test after drug injection
C
Cg1
PL
IL
DP
D
***
Immobile durations (s)
150
100
50
0
Vehicle
300 μmol/L DAB
1000 μmol/L DAB
E
Total distance (cm)
2000
1000
0
Vehicle
300 μmol/L DAB
1000 μmol/L DAB
F
NS
**
****
Immobile durations (s)
150
100
50
0
G
Total distance (cm)
3000
2000
1000
0
Vehicle + Vehicle
1000 μmol/L DAB + Vehicle
1000 μmol/L DAB + 10 mmol/L L-lactate
1000 μmol/L DAB + 100 mmol/L L-lactate

was injected bilaterally into the mPFC. Two weeks later, cannulae were implanted bilaterally into the mPFC. One week later, the FST and OFT were conducted sequentially (Fig. 4A). The bilateral administration of *L*-lactate rescued the decreased passive coping response caused by *Mct4*-shRNA (Fig. 4C), while each group of mice showed normal locomotor activity in the OFT (Fig. 4D). These results suggested that astrocyte-derived lactate plays a critical role in the passive coping response.

Astrocyte-Derived Lactate Modulates Neuronal Excitability in the mPFC

Next, we explored the possible cellular mechanism underlying the lactate-mediated passive coping response. Synaptic transmission is critical for responses to environmental changes [5]. In addition, layer V pyramidal neurons in the mPFC primarily project to other regions [54], and direct stimulation of these neurons through optogenetic manipulation decreases the immobility time in the FST [34].

Therefore, we first used whole-cell patch-clamp recording to detect synaptic transmission, including sEPSCs and sIPSCs, in layer V pyramidal neurons in the mPFC. Surprisingly, decreasing the expression of MCT4 had no effect on either the frequency or amplitude of the sEPSCs (Fig. 5A–C) or sIPSCs (Fig. 5D–F).

Next, we evaluated the intrinsic excitability of layer V pyramidal neurons with decreased MCT4 expression in the mPFC. In current-clamp mode, the firing responses of neurons to depolarizing current injections were analyzed. Compared to that in the control group, the number of spikes was increased in the *Mct4*-shRNA2 group (Fig. 6A, B), indicating enhanced neuronal excitability after MCT4 knockdown. Then, we questioned whether *L*-lactate administration could rescue the changed excitability.

Hydrosoluble drugs diffuse easily and spread over a wide area *in vivo*. According to previous research, the final average concentration within the diffusion area is approximately one-twentieth the initial concentration [20]. Therefore, we selected 5 mmol/L *L*-lactate for electrophysiological recording *in vitro*. The results showed that 5 mmol/L *L*-lactate restored the enhanced excitability of the MCT4-knockdown group to a level similar to that of the control group (Fig. 6A, B).

We also examined the intrinsic excitability of layer V pyramidal neurons after blocking astrocytic glycogen metabolism with DAB in mPFC slices. Fifty micromolar DAB increased the number of spikes, and this effect was reversed by 5 mmol/L *L*-lactate (Fig. 6C, D). These results showed that astrocyte-derived lactate participates in the modulation of neuronal excitability in the mPFC.

Discussion

The passive coping response is a naturally-occurring behavioral state that possesses both adaptability research value and major clinical significance. Little is known about the cellular and molecular mechanisms of the passive coping response to behavioral challenge. By disturbing lactate production and transport in astrocytes, we found that astrocyte-derived lactate modulates the passive coping response.

In our study, mice struggled severely at the beginning of the FST but subsequently transitioned into another behavioral pattern that had a combination of features, including trying to escape from the tank, repeated failure despite trying harder, giving up momentarily, and then trying again. During the behavioral state transitions, the real-time lactate levels were unclear. Updated fluorescent protein-based sensors can produce real-time readouts of lactate levels with high sensitivity and cell-type specificity [55]. Therefore, in future, using these new techniques, a wealth of interesting research on lactate can be conducted.

In the *in vivo* experiments, both DAB and *Mct4*-shRNA reduced the passive activity; in the slice electrophysiological recording, both DAB and *Mct4*-shRNA increased the excitability of layer V pyramidal neurons. Moreover, both *in vivo* and *in vitro* changes were rescued by exogenous *L*-lactate administration. Previous studies have shown that stimulating mPFC neurons decreases the total duration of immobility in the FST [34–36]. Therefore, the increased neuronal excitability may be the cellular mechanism underlying the reduced passive coping response. However, the validity of this hypothesis is uncertain due to a lack of direct evidence. It should be noted that the relationship between lactate and neuronal excitability is problematic. Similar to our results, it has been shown that lactate decreases the activity of cortical neurons, and provides negative feedback for neuronal activity *via* a receptor-mediated mechanism [56].

Exogenous *L*-lactate has been shown to excite locus coeruleus neurons [24]. In CA1, the intra-astrocyte application of a lactate dehydroxylase inhibitor, which blocks the conversion from pyruvate to lactate, results in the hyperpolarization of neighboring pyramidal neurons, and the change can be rescued by extracellular application of lactate [57]. Meanwhile, lactate enhances the excitability of orexin neurons [58]. The different responses to lactate probably result from the diverse brain areas and unequal intrinsic properties of the treated neurons.

Acute peripheral administration of lactate decreases the duration of immobility in the FST and increases the hippocampal lactate concentration [59]. Peripheral lactate treatment rescues the increased immobility of transgenic

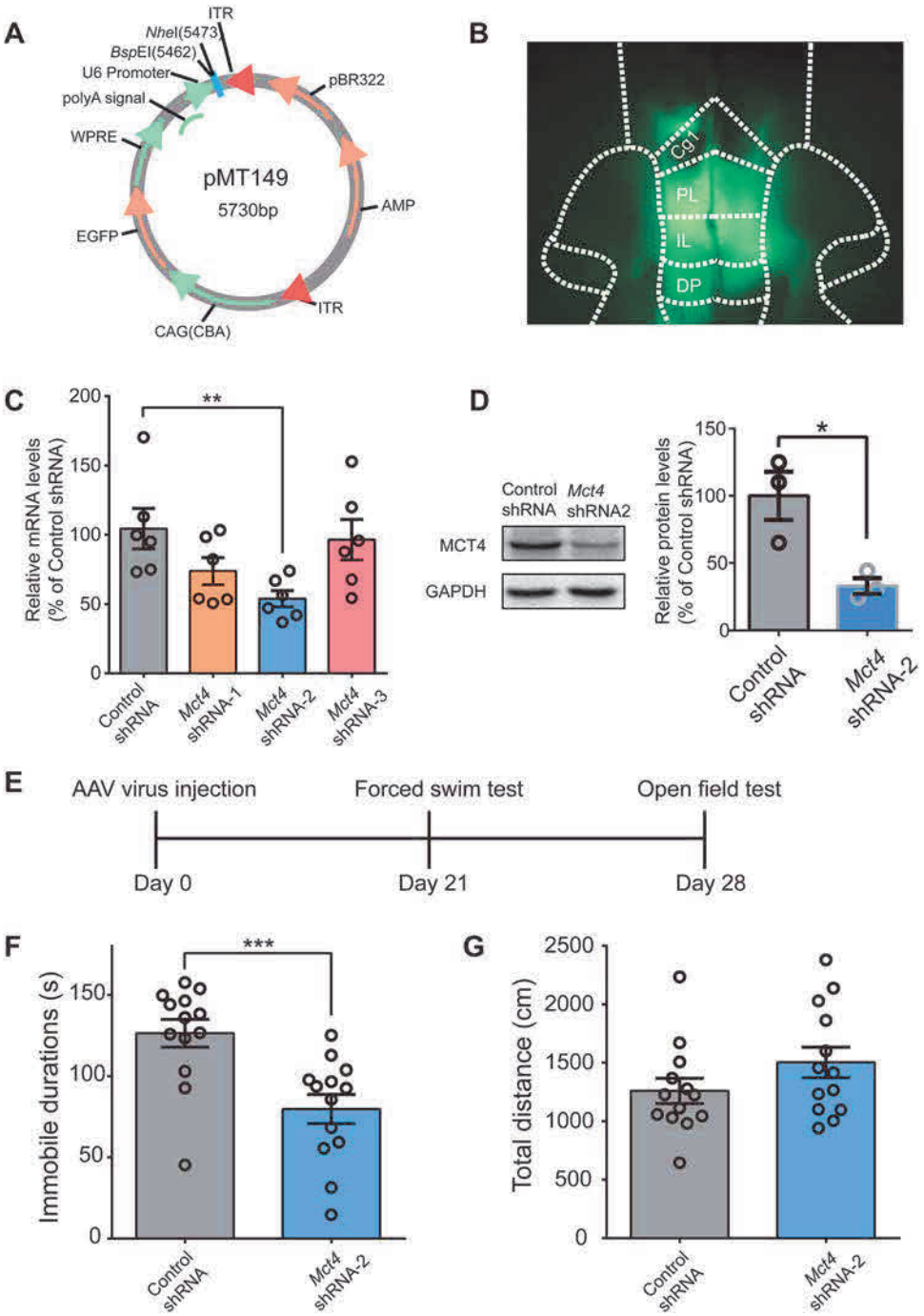

Fig. 3 Disruption of MCT4 expression decreases the passive coping response. **A** Vector design for generation of the AAV shRNA. **B** Image of eGFP expression in the mPFC 3 weeks after virus injection. **C** Relative *Mct4* expression at the mRNA level after control and interfering virus injection (n = 6 mice/group; one-way ANOVA, $F(3, 20) = 3.739$, $P = 0.0278$, uncorrected Fisher's LSD test, $t = 3.020$, df = 20, $P = 0.0068$). **D** Western blots showing the expression of MCT4 after virus injection. Left, Western blot bands of MCT4 and GAPDH in the control and interfering groups; right, quantification of the relative protein expression (n = 3 mice/group; unpaired t-test, $t = 3.541$, df = 4, $P = 0.024$). **E** Schematic of the behavioral tests after virus injection. **F** Immobility time of virus-injected mice in the FST (control shRNA virus-injected mice: n = 13; *Mct4* shRNA-2 virus-injected mice: n = 13; Mann-Whitney test, U = 21.00, $P = 0.0006$). **G** Locomotor activity of virus-injected mice in the OFT (n = 13 mice/group; Mann-Whitney test, U = 60.00, $P = 0.2201$). Error bars indicate the SEM; $^{*}P < 0.05$, $^{**}P < 0.01$, $^{***}P < 0.001$.

mice in the FST [60]. Peripheral treatment may influence the whole brain, therefore the different responses to lactate in the behavioral tests may be due to differences in brain regions. In various regions, the diversity of cellular characteristics and projections may also contribute to this difference.

In astrocytes, pyruvate is converted to lactate by lactate dehydrogenase 5, and astrocytes release lactate through three processes: transmembrane monocarboxylate transporters (MCT1 and MCT4), pannexins, and a high-capacity cation channel [13, 61, 62]. In this study, we found that lactate released through MCT4 is critical for passive coping behavior, but we cannot preclude the possibility that other processes are also involved in astrocyte-derived lactate release. Further exploration is required to reach a systematic conclusion about the relationship between astrocyte-derived lactate and passive coping behavior. MCT4 has also been found in other cells such as tanycytes in the hypothalamus [63]. Whether MCT4 in cells other than astrocytes in the mPFC plays a role requires further research.

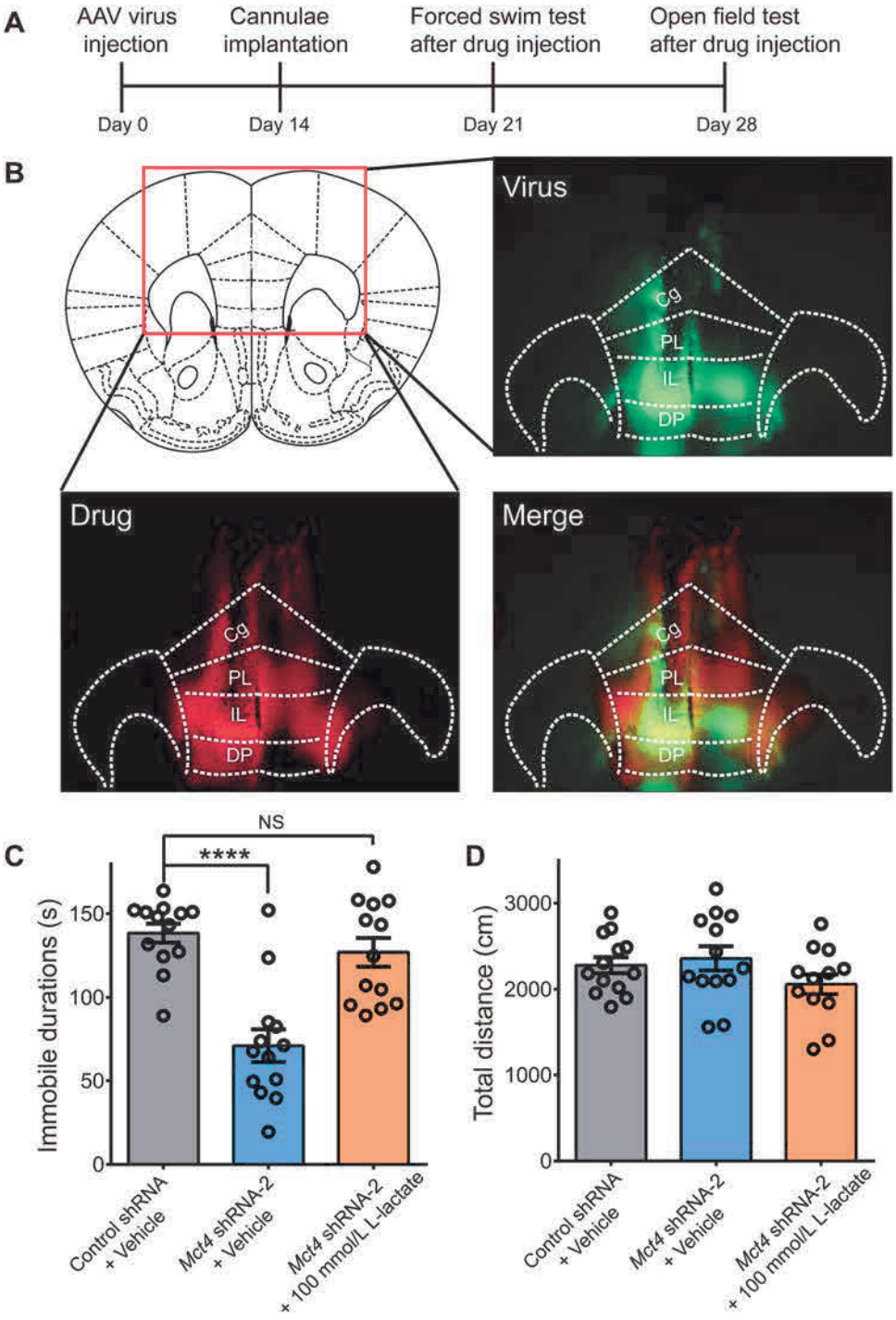

Fig. 4 *L*-lactate rescues the decreased passive coping response induced by disruption of MCT4 expression. **A** Schematic of the experimental design. **B** Location of expressed eGFP and diffused drug in the mPFC. **C** Quantification of the immobility of the mice injected with AAVs and drugs (n = 13 mice/group, one-way ANOVA, $F(2, 36) = 19.30$, $P < 0.0001$, uncorrected Fisher's LSD test, $t = 5.804$, df = 36, $P < 0.0001$). **D** Locomotor activity of mice in the OFT (n = 13 mice/group, one-way ANOVA, $F(2, 36) = 1.781$, $P = 0.183$, uncorrected Fisher's LSD test). Error bars indicate the SEM; ****$P < 0.0001$, NS, not significant.

The different metabolic profiles in astrocytes and neurons suggest that there may be metabolic exchange between lactate-producing and lactate-consuming cells. The astrocyte–neuron lactate shuttle model was first proposed 20 years ago [64], and since then, a wide range of studies have produced evidence supporting this model [20, 65, 66], However, there are some controversies about this hypothesis [67]. Other studies have claimed that glucose is taken up preferentially by neurons [68, 69], and active neurons do not require imported lactate [70], thus challenging the hypothesis. Lactate performs metabolic functions and acts as a signaling molecule in neurons through two main mechanisms: *via* the transmembrane transporter MCT2 and by acting on specific receptors [71]. Future studies are required to investigate how astrocyte-derived lactate influences neurons.

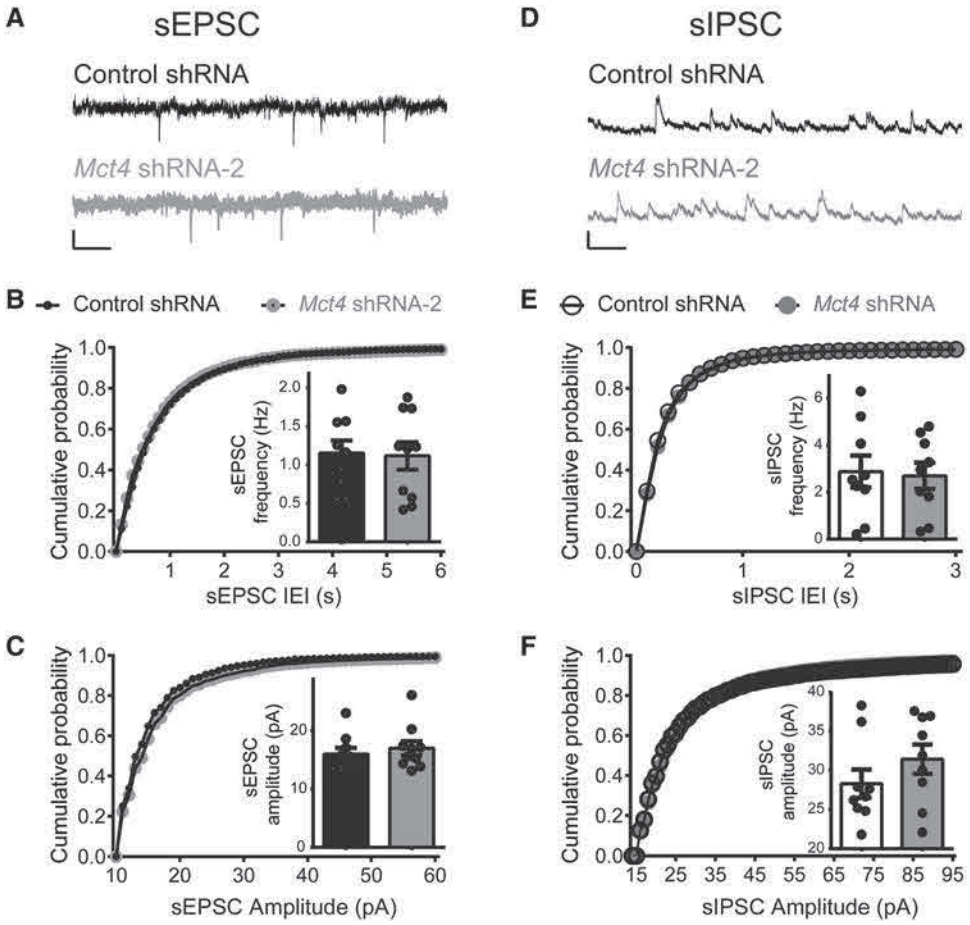

Fig. 5 Synaptic transmission of mPFC pyramidal neurons is unaffected by MCT4 disruption. **A** Representative traces of sEPSCs in the mPFC layer V pyramidal neurons from control and *Mct4* shRNA virus-injected mice (scale bars, 0.2 s and 10 pA). **B** Cumulative probability plots of sEPSC inter-event intervals (IEIs) and histograms of sEPSC frequency (n = 9 neurons, 3 control mice; n = 10 neurons, 3 *Mct4* shRNA mice; unpaired t-test, t = 0.1493, df = 17, P = 0.883). **C** Cumulative probability plots and histograms of sEPSC amplitudes (n = 9 neurons, 3 control mice; n = 10 neurons, 3 *Mct4* shRNA mice; Mann-Whitney test, U = 36.00, P = 0.4856). **D** Representative traces of sIPSCs in mPFC layer V pyramidal neurons from control and *Mct4* shRNA virus-injected mice (scale bars, 0.2 s and 20 pA). **E** Cumulative probability plots of sIPSC IEIs and histograms of sIPSC frequency (n = 9 neurons from 3 mice for both groups; unpaired t-test, t = 0.2094, df = 16, P = 0.8368). **F** Cumulative probability plots and histograms of sIPSC amplitudes (n = 9 neurons of 3 mice for both groups; unpaired t-test, t = 1.206, df = 16, P = 0.2454). Error bars indicate the SEM.

In addition to the FST [72], animal models that mimic challenging situations in the presence of acute and intense stress include the tail suspension test [73], the shock probe defensive burying test [74], and learned helplessness [75]. Although the FST is widely used, additional models would make our hypothesis more conclusive. Furthermore, chronic stress is associated with depression [76–78], and depression models such as the chronic social defeat stress model, and the learned helplessness and chronic mild stress paradigms are characterized by prolonged stress exposure. This prompted us to investigate whether lactate can affect the susceptibility of mice to depression-inducing stress. There are sexual dimorphisms in behavior. Women have more conspicuous passive coping responses and are more likely to develop mood disorders than men [79–81]. Therefore, future work should pay more attention to females.

In addition to the mPFC [3, 4], the entopeduncular nucleus [5], dorsal raphe [4–6], ventral tegmental area [5], lateral habenula [4–6], and anteroventral bed nuclei of the stria terminalis [3] have been reported to participate in regulating passive coping behavior. Whether lactate exerts the same effect in different areas is unknown. Astrocytes have been shown to regulate the behavioral state switch from active to passive. During behavioral state transitions, astrocytes act like a commander that receives the failed swim attempts detected by noradrenergic neurons, integrates the noradrenergic failure signal, and uses GABAergic neurons to trigger a passive behavioral state [82]. This finding emphasizes the importance of the role astrocytes play in the behavioral state transition in challenging situations. It will be valuable to

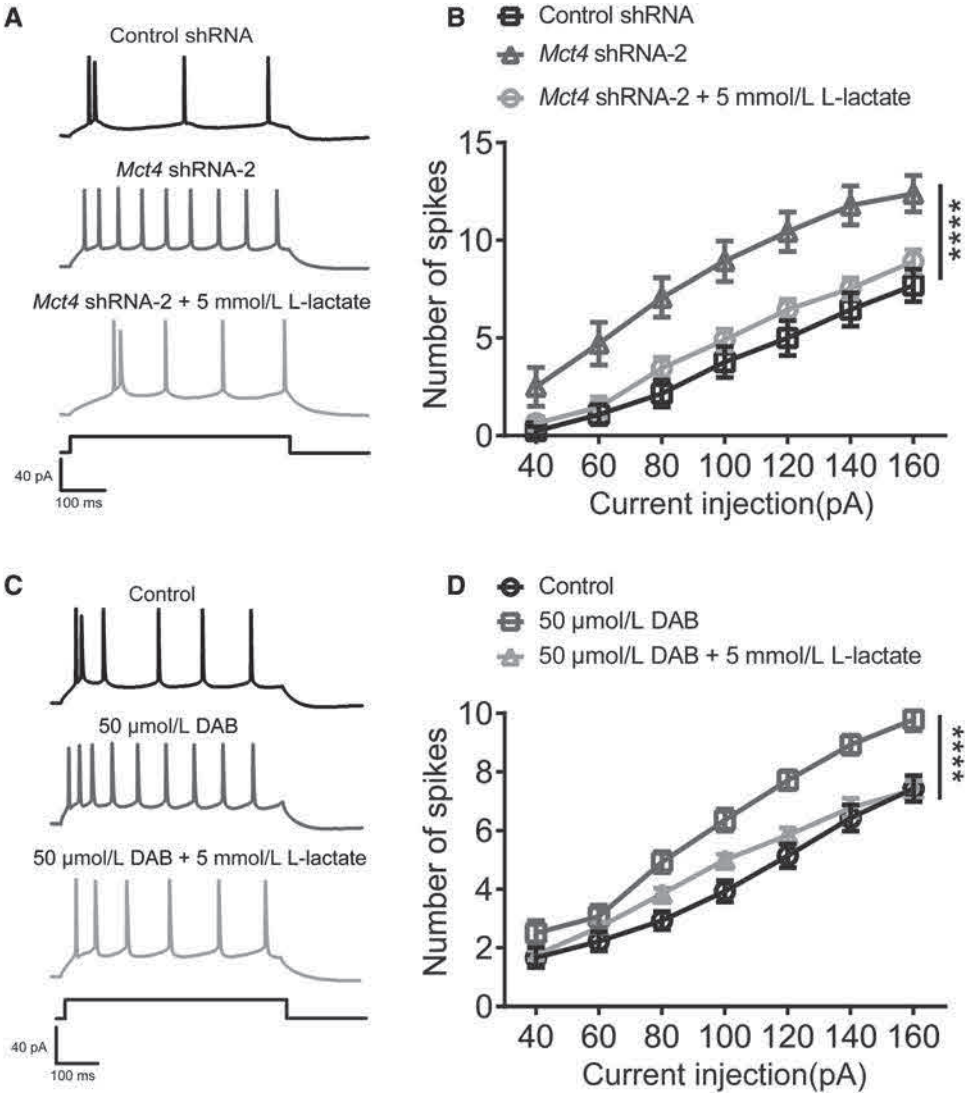

Fig. 6 Reduction of lactate activity by DAB or *Mct4*-shRNA in the mPFC increases neuronal excitability. **A** Depolarizing current injections produce trains of action potentials (APs) in mPFC layer V pyramidal neurons from different groups through viral modulation of MCT4 expression (scale bars, 100 ms and 40 pA). **B** Numbers of APs produced by depolarizing current injection (n = 13 neurons of 4 control shRNA group mice; n = 14 neurons of 4 *Mct4* shRNA group mice; n = 11 neurons of 4 *Mct4* shRNA + 5 mmol/L *L*-lactate group mice; two-way ANOVA test, $F(2, 244) = 61.79$, $P < 0.0001$). **C** Depolarizing current injection produces trains of APs in mPFC layer V pyramidal neurons in three groups through pharmacological disturbance of astrocytic glycogenolysis (scale bars, 100 ms and 40 pA). **D** Numbers of APs induced by depolarizing current injection (n = 14 neurons of 4 control group mice; n = 14 neurons of 4 50 μmol/L DAB group mice; n = 13 neurons of 4 50 μmol/L DAB + 5 mmol/L *L*-lactate group mice; two-way ANOVA test, $F(2, 237) = 50.32$, $P < 0.0001$). Error bars indicate the SEM; $^{****}P < 0.0001$.

explore whether lactate acts as a messenger in the behavioral state-switching process.

In summary, our findings highlight the significant role astrocyte-derived lactate plays in passive behavior adjustment and may provide novel insights into the mechanism of mood disorders such as MDD.

Acknowledgements We thank members of the Prof. Tian-Ming Gao's laboratory (Drs. Zheng-Yi Luo, Ji-Hong Liu, Song Lin, Lang Huang, Qiang-Long You, and Neng-Yuan Hu, Southern Medical University) for comments on the experimental design and manuscript. This work was supported by grants from the National Natural Science Foundation of China (31830033, 81671356, 81971080), the Program for Changjiang Scholars and Innovative Research Team in University (IRT_16R37), Key-Area Research and Development Program of Guangdong Province (2018B030334001).

Conflict of interest The authors declare no competing financial interests.

References

1. Kessler RC, Angermeyer M, Anthony JC, R DEG, Demyttenaere K, Gasquet I, *et al.* Lifetime prevalence and age-of-onset distributions of mental disorders in the World Health Organization's World Mental Health Survey Initiative. World Psychiatry 2007, 6: 168–176.
2. Hasin DS, Sarvet AL, Meyers JL, Saha TD, Ruan WJ, Stohl M, *et al.* Epidemiology of adult DSM-5 major depressive disorder and its specifiers in the United States. JAMA Psychiatry 2018, 75: 336–346.
3. Johnson SB, Emmons EB, Lingg RT, Anderson RM, Romig-Martin SA, LaLumiere RT, *et al.* Prefrontal-bed nucleus circuit modulation of a passive coping response set. J Neurosci 2019, 39: 1405–1419.
4. Warden MR, Selimbeyoglu A, Mirzabekov JJ, Lo M, Thompson KR, Kim SY, *et al.* A prefrontal cortex-brainstem neuronal projection that controls response to behavioural challenge. Nature 2012, 492: 428–432.
5. Cerniauskas I, Winterer J, de Jong JW, Lukacsovich D, Yang H, Khan F, *et al.* Chronic stress induces activity, synaptic, and

transcriptional remodeling of the lateral habenula associated with deficits in motivated behaviors. Neuron 2019, 104: 899–915.
6. Andalman AS, Burns VM, Lovett-Barron M, Broxton M, Poole B, Yang SJ, *et al.* Neuronal dynamics regulating brain and behavioral state transitions. Cell 2019, 177: 970–985
7. Bazargani N, Attwell D. Astrocyte calcium signaling: the third wave. Nat Neurosci 2016, 19: 182–189.
8. Murphy-Royal C, Gordon GR, Bains JS. Stress-induced structural and functional modifications of astrocytes-Further implicating glia in the central response to stress. Glia 2019, 67: 1806–1820.
9. Vilchez D, Ros S, Cifuentes D, Pujadas L, Valles J, Garcia-Fojeda B, *et al.* Mechanism suppressing glycogen synthesis in neurons and its demise in progressive myoclonus epilepsy. Nat Neurosci 2007, 10: 1407–1413.
10. Brown AM, Tekkok SB, Ransom BR. Energy transfer from astrocytes to axons: the role of CNS glycogen. Neurochem Int 2004, 45: 529–536.
11. Magistretti PJ, Allaman I. Lactate in the brain: from metabolic end-product to signalling molecule. Nat Rev Neurosci 2018, 19: 235–249.
12. Magistretti PJ, Pellerin L, Rothman DL, Shulman RG. Energy on demand. Science 1999, 283: 496–497.
13. Pierre K, Pellerin L. Monocarboxylate transporters in the central nervous system: distribution, regulation and function. J Neurochem 2005, 94: 1–14.
14. Halestrap AP, Price NT. The proton-linked monocarboxylate transporter (MCT) family: structure, function and regulation. Biochem J 1999, 343 Pt 2: 281–299.
15. Yang J, Ruchti E, Petit JM, Jourdain P, Grenningloh G, Allaman I, *et al.* Lactate promotes plasticity gene expression by potentiating NMDA signaling in neurons. Proc Natl Acad Sci U S A 2014, 111: 12228–12233.
16. O'Dowd BS, Gibbs ME, Ng KT, Hertz E, Hertz L. Astrocytic glycogenolysis energizes memory processes in neonate chicks. Brain Res Dev Brain Res 1994, 78: 137–141.
17. Hertz L, O'Dowd BS, Ng KT, Gibbs ME. Reciprocal changes in forebrain contents of glycogen and of glutamate/glutamine during early memory consolidation in the day-old chick. Brain Res 2003, 994: 226–233.
18. Gibbs ME, Anderson DG, Hertz L. Inhibition of glycogenolysis in astrocytes interrupts memory consolidation in young chickens. Glia 2006, 54: 214–222.
19. Gibbs ME, Lloyd HGE, Santa T, Hertz L. Glycogen is a preferred glutamate precursor during learning in 1-day-old chick: Biochemical and behavioral evidence. J Neurosci Res 2007, 85: 3326–3333.
20. Suzuki A, Stern SA, Bozdagi O, Huntley GW, Walker RH, Magistretti PJ, *et al.* Astrocyte-neuron lactate transport is required for long-term memory formation. Cell 2011, 144: 810–823.
21. De Bruin LA, Schasfoort EM, Steffens AB, Korf J. Effects of stress and exercise on rat hippocampus and striatum extracellular lactate. Am J Physiol 1990, 259: R773–779.
22. Elekes O, Venema K, Postema F, Dringen R, Hamprecht B, Korf J. Possible glial contribution of rat hippocampus lactate as assessed with microdialysis and stress. Acta Neurochir Suppl 1996, 67: 1–5.
23. Krugers HJ, Jaarsma D, Korf J. Rat hippocampal lactate efflux during electroconvulsive shock or stress is differently dependent on entorhinal cortex and adrenal integrity. J Neurochem 1992, 58: 826–830.
24. Tang F, Lane S, Korsak A, Paton JF, Gourine AV, Kasparov S, *et al.* Lactate-mediated glia-neuronal signalling in the mammalian brain. Nat Commun 2014, 5: 3284.
25. Gururajan A, Reif A, Cryan JF, Slattery DA. The future of rodent models in depression research. Nat Rev Neurosci 2019, 20: 686–701.
26. Porsolt RD, Bertin A, Jalfre M. Behavioral despair in mice: a primary screening test for antidepressants. Arch Int Pharmacodyn Ther 1977, 229: 327–336 .
27. Porsolt RD, Anton G, Blavet N, Jalfre M. Behavioural despair in rats: a new model sensitive to antidepressant treatments. Eur J Pharmacol 1978, 47: 379–391.
28. Uehara T, Itoh H, Matsuoka T, Rujescu D, Genius J, Seo T, *et al.* Effect of transient blockade of N-methyl-D-aspartate receptors at neonatal stage on stress-induced lactate metabolism in the medial prefrontal cortex of adult rats: Role of 5-HT1A receptor agonism. Synapse 2012, 66: 408–417.
29. Uehara T, Sumiyoshi T, Itoh H, Kurachi M. Role of glutamate transporters in the modulation of stress-induced lactate metabolism in the rat brain. Psychopharmacology (Berl) 2007, 195: 297–302.
30. Uehara T, Sumiyoshi T, Matsuoka T, Itoh H, Kurachi M. Role of 5-HT(1A) receptors in the modulation of stress-induced lactate metabolism in the medial prefrontal cortex and basolateral amygdala. Psychopharmacology (Berl) 2006, 186: 218–225.
31. Miller EK, Cohen JD. An integrative theory of prefrontal cortex function. Annu Rev Neurosci 2001, 24: 167–202 .
32. Kamigaki T. Prefrontal circuit organization for executive control. Neurosci Res 2019, 140: 23–36.
33. Fuster JX. The Prefrontal Cortex. Academic Press, 2015.
34. Kumar S, Black SJ, Hultman R, Szabo ST, DeMaio KD, Du J, *et al.* Cortical control of affective networks. J Neurosci 2013, 33: 1116–1129.
35. Hamani C, Diwan M, Macedo CE, Brandao ML, Shumake J, Gonzalez-Lima F, *et al.* Antidepressant-like effects of medial prefrontal cortex deep brain stimulation in rats. Biol Psychiatry 2010, 67: 117–124.
36. Fuchikami M, Thomas A, Liu R, Wohleb ES, Land BB, DiLeone RJ, *et al.* Optogenetic stimulation of infralimbic PFC reproduces ketamine's rapid and sustained antidepressant actions. Proc Natl Acad Sci U S A 2015, 112: 8106–8111.
37. Covington HE, 3rd, Lobo MK, Maze I, Vialou V, Hyman JM, Zaman S, *et al.* Antidepressant effect of optogenetic stimulation of the medial prefrontal cortex. J Neurosci 2010, 30: 16082–16090.
38. Cao X, Li LP, Wang Q, Wu Q, Hu HH, Zhang M, *et al.* Astrocyte-derived ATP modulates depressive-like behaviors. Nat Med 2013, 19: 773–777.
39. Etievant A, Oosterhof C, Betry C, Abrial E, Novo-Perez M, Rovera R, *et al.* Astroglial control of the antidepressant-like effects of prefrontal cortex deep brain stimulation. Ebiomedicine 2015, 2: 898–908.
40. Xiong W, Cao X, Zeng Y, Qin X, Zhu M, Ren J, *et al.* Astrocytic epoxyeicosatrienoic acid signaling in the medial prefrontal cortex modulates depressive-like behaviors. J Neurosci 2019, 39: 4606–4623.
41. Huang DM, Li CL, Zhang W, Qin JQ, Jiang WY, Hu CY. Dysfunction of astrocytic connexins 30 and 43 in the medial prefrontal cortex and hippocampus mediates depressive-like behaviours. Behav Brain Res 2019, 372: 111950.
42. Maier SF, Watkins LR. Role of the medial prefrontal cortex in coping and resilience. Brain Res 2010, 1355: 52–60.
43. Chen P, Lou S, Huang ZH, Wang Z, Shan QH, Wang Y, *et al.* Prefrontal cortex corticotropin-releasing factor neurons control behavioral style selection under challenging situations. Neuron 2020.
44. McKlveen JM, Myers B, Herman JP. The medial prefrontal cortex: coordinator of autonomic, neuroendocrine and behavioural responses to stress. J Neuroendocrinol 2015, 27: 446–456.
45. Franklin KBJ, Paxinos G. The Mouse Brain in Stereotaxic Coordinates. New York: Academic Press, 2008.
46. Hui S, Ghergurovich JM, Morscher RJ, Jang C, Teng X, Lu W, *et al.* Glucose feeds the TCA cycle via circulating lactate. Nature 2017, 551: 115–118.

47. Li B, Jie W, Huang L, Wei P, Li S, Luo Z, *et al.* Nuclear BK channels regulate gene expression via the control of nuclear calcium signaling. Nat Neurosci 2014, 17: 1055–1063.
48. Chen YH, Lan YJ, Zhang SR, Li WP, Luo ZY, Lin S, *et al.* ErbB4 signaling in the prelimbic cortex regulates fear expression. Transl Psychiatry 2017, 7: e1168.
49. Chen YJ, Zhang M, Yin DM, Wen L, Ting AN, Wang P, *et al.* ErbB4 in parvalbumin-positive interneurons is critical for neuregulin 1 regulation of long-term potentiation. Proc Natl Acad Sci U S A 2010, 107: 21818–21823.
50. Sun XD, Li L, Liu F, Huang ZH, Bean JC, Jiao HF, *et al.* Lrp4 in astrocytes modulates glutamatergic transmission. Nat Neurosci 2016, 19: 1010–1018.
51. Lin S, Li X, Chen YH, Gao F, Chen H, Hu NY, *et al.* Social isolation during adolescence induces anxiety behaviors and enhances firing activity in BLA pyramidal neurons via mGluR5 upregulation. Mol Neurobiol 2018, 55: 5310–5320.
52. Magistretti PJ, Allaman I. A cellular perspective on brain energy metabolism and functional imaging. Neuron 2015, 86: 883–901.
53. Walls AB, Sickmann HM, Brown A, Bouman SD, Ransom B, Schousboe A, *et al.* Characterization of 1, 4-dideoxy-1, 4-imino-d-arabinitol (DAB) as an inhibitor of brain glycogen shunt activity. J Neurochem 2008, 105: 1462–1470
54. Dembrow NC, Chitwood RA, Johnston D. Projection-specific neuromodulation of medial prefrontal cortex neurons. J Neurosci 2010, 30: 16922–16937.
55. Zhang Z, Chen W, Zhao Y, Yang Y. Spatiotemporal imaging of cellular energy metabolism with genetically-encoded fluorescent sensors in brain. Neurosci Bull 2018, 34: 875–886.
56. Bozzo L, Puyal J, Chatton JY. Lactate modulates the activity of primary cortical neurons through a receptor-mediated pathway. PLoS One 2013, 8: e71721.
57. Sada N, Lee S, Katsu T, Otsuki T, Inoue T. Epilepsy treatment. Targeting LDH enzymes with a stiripentol analog to treat epilepsy. Science 2015, 347: 1362–1367.
58. Parsons MP, Hirasawa M. ATP-sensitive potassium channel-mediated lactate effect on orexin neurons: implications for brain energetics during arousal. J Neurosci 2010, 30: 8061–8070.
59. Carrard A, Elsayed M, Margineanu M, Boury-Jamot B, Fragniere L, Meylan EM, *et al.* Peripheral administration of lactate produces antidepressant-like effects. Mol Psychiatry 2018, 23: 392–399.
60. Jouroukhin Y, Kageyama Y, Misheneva V, Shevelkin A, Andrabi S, Prandovszky E, *et al.* DISC1 regulates lactate metabolism in astrocytes: implications for psychiatric disorders. Transl Psychiatry 2018, 8: 76.
61. Sotelo-Hitschfeld T, Niemeyer MI, Machler P, Ruminot I, Lerchundi R, Wyss MT, *et al.* Channel-mediated lactate release by K(+)-stimulated astrocytes. J Neurosci 2015, 35: 4168–4178.
62. Karagiannis A, Sylantyev S, Hadjihambi A, Hosford PS, Kasparov S, Gourine AV. Hemichannel-mediated release of lactate. J Cereb Blood Flow Metab 2016, 36: 1202–1211.
63. Cortes-Campos C, Elizondo R, Llanos P, Uranga RM, Nualart F, Garcia MA. MCT expression and lactate influx/efflux in tanycytes involved in glia-neuron metabolic interaction. PLoS One 2011, 6: e16411.
64. Pellerin L, Magistretti PJ. Glutamate uptake into astrocytes stimulates aerobic glycolysis: a mechanism coupling neuronal activity to glucose utilization. Proc Natl Acad Sci U S A 1994, 91: 10625–10629.
65. Zhang Y, Chen K, Sloan SA, Bennett ML, Scholze AR, O'Keeffe S, *et al.* An RNA-sequencing transcriptome and splicing database of glia, neurons, and vascular cells of the cerebral cortex. J Neurosci 2014, 34: 11929–11947.
66. Machler P, Wyss MT, Elsayed M, Stobart J, Gutierrez R, von Faber-Castell A, *et al.* In vivo evidence for a lactate gradient from astrocytes to neurons. Cell Metab 2016, 23: 94–102.
67. Dienel GA. Brain lactate metabolism: the discoveries and the controversies. J Cereb Blood Flow Metab 2012, 32: 1107–1138.
68. Lundgaard I, Li B, Xie L, Kang H, Sanggaard S, Haswell JD, *et al.* Direct neuronal glucose uptake heralds activity-dependent increases in cerebral metabolism. Nat Commun 2015, 6: 6807.
69. Patel AB, Lai JC, Chowdhury GM, Hyder F, Rothman DL, Shulman RG, *et al.* Direct evidence for activity-dependent glucose phosphorylation in neurons with implications for the astrocyte-to-neuron lactate shuttle. Proc Natl Acad Sci U S A 2014, 111: 5385–5390.
70. Diaz-Garcia CM, Mongeon R, Lahmann C, Koveal D, Zucker H, Yellen G. Neuronal stimulation triggers neuronal glycolysis and not lactate uptake. Cell Metab 2017, 26: 361–374 e364.
71. Morland C, Lauritzen KH, Puchades M, Holm-Hansen S, Andersson K, Gjedde A, *et al.* The lactate receptor, G-protein-coupled receptor 81/hydroxycarboxylic acid receptor 1: Expression and action in brain. J Neurosci Res 2015, 93: 1045–1055.
72. Stone EA, Lin Y. An anti-immobility effect of exogenous corticosterone in mice. Eur J Pharmacol 2008, 580: 135–142.
73. Steru L, Chermat R, Thierry B, Simon P. The tail suspension test: a new method for screening antidepressants in mice. Psychopharmacology (Berl) 1985, 85: 367–370.
74. De Boer SF, Koolhaas JM. Defensive burying in rodents: ethology, neurobiology and psychopharmacology. Eur J Pharmacol 2003, 463: 145–161.
75. Maier SF. Learned helplessness and animal models of depression. Prog Neuropsychopharmacol Biol Psychiatry 1984, 8: 435–446.
76. Hammen C. Stress and depression. Annu Rev Clin Psychol 2005, 1: 293–319.
77. Muscatell KA, Slavich GM, Monroe SM, Gotlib IH. Stressful life events, chronic difficulties, and the symptoms of clinical depression. J Nerv Ment Dis 2009, 197: 154–160.
78. Monroe SM, Kupfer DJ, Frank E. Life stress and treatment course of recurrent depression: 1. Response during index episode. J Consult Clin Psychol 1992, 60: 718–724.
79. Mueller BR, Bale TL. Sex-specific programming of offspring emotionality after stress early in pregnancy. J Neurosci 2008, 28: 9055–9065.
80. Goel N, Bale TL. Examining the intersection of sex and stress in modelling neuropsychiatric disorders. J Neuroendocrinol 2009, 21: 415–420.
81. Shansky RM, Woolley CS. Considering Sex as a Biological variable will be valuable for neuroscience research. J Neurosci 2016, 36: 11817–11822.
82. Mu Y, Bennett DV, Rubinov M, Narayan S, Yang CT, Tanimoto M, *et al.* Glia accumulate evidence that actions are futile and suppress unsuccessful behavior. Cell 2019, 178: 27.

Neurosci. Bull. January, 2021, 37(1):15–30
https://doi.org/10.1007/s12264-020-00583-7

www.neurosci.cn
www.springer.com/12264

ORIGINAL ARTICLE

Conditional Deletion of *Foxg1* Alleviates Demyelination and Facilitates Remyelination *via* the Wnt Signaling Pathway in Cuprizone-Induced Demyelinated Mice

Fuxing Dong[1,2] · Dajin Liu[1] · Feiyu Jiang[1] · Yaping Liu[1] · Xiuxiang Wu[1] · Xuebin Qu[1] · Jing Liu[1] · Yan Chen[1] · Hongbin Fan[3] · Ruiqin Yao[1]

Received: 19 January 2020 / Accepted: 31 May 2020 / Published online: 5 October 2020

Abstract The massive loss of oligodendrocytes caused by various pathological factors is a basic feature of many demyelinating diseases of the central nervous system (CNS). Based on a variety of studies, it is now well established that impairment of oligodendrocyte precursor cells (OPCs) to differentiate and remyelinate axons is a vital event in the failed treatment of demyelinating diseases. Recent evidence suggests that *Foxg1* is essential for the proliferation of certain precursors and inhibits premature neurogenesis during brain development. To date, very little attention has been paid to the role of *Foxg1* in the proliferation and differentiation of OPCs in demyelinating diseases of the CNS. Here, for the first time, we examined the effects of *Foxg1* on demyelination and remyelination in the brain using a cuprizone (CPZ)-induced mouse model. In this work, 7-week-old *Foxg1* conditional knockout and wild-type (WT) mice were fed a diet containing 0.2% CPZ w/w for 5 weeks, after which CPZ was withdrawn to enable remyelination. Our results demonstrated that, compared with WT mice, *Foxg1*-knockout mice exhibited not only alleviated demyelination but also accelerated remyelination of the demyelinated corpus callosum. Furthermore, we found that *Foxg1* knockout decreased the proliferation of OPCs and accelerated their differentiation into mature oligodendrocytes both *in vivo* and *in vitro*. Wnt signaling plays a critical role in development and in a variety of diseases. GSK-3β, a key regulatory kinase in the Wnt pathway, regulates the ability of β-catenin to enter nuclei, where it activates the expression of Wnt target genes. We then used SB216763, a selective inhibitor of GSK-3β activity, to further demonstrate the regulatory mechanism by which *Foxg1* affects OPCs *in vitro*. The results showed that SB216763 clearly inhibited the expression of GSK-3β, which abolished the effect of the proliferation and differentiation of OPCs caused by the knockdown of *Foxg1*. These results suggest that *Foxg1* is involved in the proliferation and differentiation of OPCs through the Wnt signaling pathway. The present experimental results are some of the first to suggest that *Foxg1* is a new therapeutic target for the treatment of demyelinating diseases of the CNS.

Keywords *Foxg1* · Oligodendrocyte precursor cells · Demyelination · Remyelination · Wnt

Fuxing Dong and Dajin Liu have contributed equally to this work.

✉ Hongbin Fan
fandoc@163.com

✉ Ruiqin Yao
wenxi_yao@163.com

[1] Department of Cell Biology and Neurobiology, Xuzhou Key Laboratory of Neurobiology, Jiangsu Key Laboratory of New Drug Research and Clinical Pharmacy, Xuzhou Medical University, Xuzhou 221004, China

[2] Public Experimental Research Center, Xuzhou Medical University, Xuzhou 221004, China

[3] Department of Neurology, Affiliated Hospital of Xuzhou Medical University, Xuzhou 221006, China

Introduction

In the central nervous system (CNS), oligodendrocytes (OLs) are myelin-forming glial cells that play vital roles in rapid impulse conduction and normal axonal functions. Current studies have demonstrated that inflammatory stimuli or immune attacks can damage the myelin sheath, leading to OL death and myelin sheath loss, such as that observed in multiple sclerosis (MS), the most common

demyelinating disease [1]. It has been reported that in early MS lesions, neural stem cells (NSCs) rooted in the region of the lateral ventricle-subventricular zone migrate, proliferate, and differentiate into oligodendrocyte progenitor cells (OPCs) induced by the injury signal of the myelin sheath and later differentiate to myelinating OLs to repair the damaged myelin [2]. However, OPCs are slow-cycling cells, and only long-term nutritional factors can stimulate their rapid proliferation and differentiation [3]. Furthermore, the repair ability of endogenous remyelination is limited, resulting in difficulties in the regeneration/repair of the myelin sheath in demyelinating diseases. Therefore, elucidating the regulatory mechanism of the correct differentiation of OPCs is crucial for understanding the myelination and remyelination processes in the CNS and is also fundamental to the treatment of demyelinating diseases [4].

Foxg1, also referred to as brain factor-1, is an important member of the Forkhead box transcription factor family, which plays dual roles in transcriptional activation and transcriptional repression [5]. *Foxg1* is widely expressed in the cerebral cortex and is critical to the development of the CNS [6]. One or two homologous chromosome *Foxg1* gene translocations, deletions, or mutations are closely related to various diseases associated with the occurrence and development of the CNS [7, 8]. Previous studies have shown that loss of function or downregulation of *Foxg1* reduces the proliferation of neural precursor cells, accompanied by early differentiation into neurons [9, 10]. In addition, Tian *et al*. found that *Foxg1* deletion increases the numbers of neurons and astrocytes at an early stage after birth in conditional *Foxg1* gene-knockout mice, and they speculated that *Foxg1* might inhibit neurogenesis and glial cell formation in the early stage after birth [11]. However, the regulation of *Foxg1* in the development and differentiation of OPCs is still uncertain.

The Wnt signaling pathway plays an important role in the development and myelination of OPCs [12, 13]. GSK-3β, a key kinase in the Wnt signaling pathway, negatively regulates the entry of catenin and then affects the expression of Wnt target genes [14]. Recent studies have demonstrated that GSK-3β activation promotes OPC differentiation, which may be mediated by the accumulation of nuclear β-catenin [15]. Nevertheless, whether the effect of *Foxg1* on the development and maturation of OPCs is associated with the Wnt signaling pathway has not been reported.

To investigate the role of *Foxg1* in the proliferation and differentiation of oligodendrocyte lineage cells and myelin regeneration, we conditionally knocked out *Foxg1 in vivo* to assess the loss and repair of myelin during demyelinating injury in mice, and we further explored its regulatory mechanism *in vitro*. Our findings revealed a previously-unknown function of *Foxg1* in oligodendrocyte lineage cells, suggesting that downregulating the expression of *Foxg1* in the treatment of demyelinating CNS diseases may alleviate demyelination and promote remyelination, thus providing a new gene therapy target for demyelinating CNS diseases such as MS.

Materials and Methods

Animals

Foxg1 cKO mice (1 male Nestin-CreER^{TM}; *Foxg1*$^{fl/fl}$ mouse; 2 female *Foxg1*$^{fl/fl}$ mice) were donated by Professor Chunjie Zhao from the Medical School of Southeast University. Wild-type ICR mice were purchased from the Experimental Animal Center of Xuzhou Medical University. All mice were housed with free access to food and water under a 12/12-h dark/light cycle and specific pathogen-free conditions. For *Foxg1* conditional disruption in neural stem/progenitor cells (NSPCs), Nestin-CreER^{TM} mice were crossed with *Foxg1*$^{fl/fl}$ mice and induced with tamoxifen (TM; Sigma-Aldrich, St. Louis, MO, USA). The genotypes of all mice were determined by PCR analysis of tail genomic DNA with appropriate primers. Male and female mice were used for all experiments without bias. All experiments were performed according to the guidelines approved by Xuzhou Medical University Experimental Animal Ethics Committee.

The TM was dissolved in corn oil to a concentration of 10 mg/mL by shaking the solution for 3 h at 37°C. For CreER^{TM}-mediated recombination, TM was intraperitoneally injected into mice at 1 mg/20 g body weight [16, 17] 3 times on alternate days.

Experimental Model

Experimental demyelination was induced by feeding 7-week-old male mice 0.2% (w/w) cuprizone (CPZ, Sigma Aldrich, St. Louis, MO, USA) mixed into ground standard rodent chow [18, 19]. The main ingredients in the normal diet for mice in this experiment were crude protein (≥180 g/kg), crude fat (≥40 g/kg), and crude fiber (≤ 50 g/kg). These mice were fed CPZ for 5 weeks and then allowed to remyelinate for 2 weeks with normal food.

Experimental Groups

Depending on the experimental purpose, mice were sacrificed at different times as follows: (1) to assess the knockout efficiency of *Foxg1*, 8 wild-type mice (WT group) and 8 *Foxg1* cKO mice (cKO group) were sacrificed on day 7 after TM injection; (2) at the end of 5 weeks of

CPZ administration, 32 mice in 4 groups (WT, WT+CPZ, cKO, and cKO+CPZ; 8 mice per group) were sacrificed to explore the effects of *Foxg1* on CPZ-induced demyelination and OPC differentiation; (3) at the end of 4 weeks of CPZ administration, 24 mice in 3 groups (WT, WT+CPZ and cKO+CPZ; 8 mice per group) were sacrificed to explore the effects of *Foxg1* on OPC proliferation; and (4) another 24 mice from the same groups (8 mice per group) were sacrificed to investigate the effects of *Foxg1* on remyelination after 5 weeks of CPZ administration and another 2 weeks of recovery with normal chow. All mice received the same amount of chow each day.

In the OPC proliferation study, the mice were intraperitoneally injected with 5-bromo-2'-deoxyuridine (BrdU, Sigma-Aldrich, St. Louis, MO, USA) (50 mg/kg, 10 mg/mL dissolved in normal saline) twice a day for 7 consecutive days from week 3 to week 4, and then sacrificed (Fig. 3A). To assess OPC differentiation, mice were fed a CPZ-containing diet for 1 week after BrdU administration for 7 consecutive days (Fig. 4A).

Morris Water Maze

The Morris water maze test (MWM) was used to evaluate spatial location learning and memory as described in previous studies [20, 21]. All data were recorded using a computerized video system (EthoVision 3.1, Noldus Instruments, Wageningen, Gelderland, the Netherlands).

Histology and Immunofluorescence

Luxol fast blue staining and degrees of demyelination in three non-serial sections from each mouse were assessed semi-quantitatively in a blinded manner, as described previously [22]. The demyelination was scored as follows: 0, none; 1, rare foci; 2, a few areas; and 3, large (confluent) areas of demyelination.

For immunofluorescence, the brain sections were blocked with 5% bovine serum albumin (BSA) and 0.3% Triton X-100 (KeyGen Biotech, Nanjing, Jiangsu, China) in 0.01 mol/L phosphate-buffered saline (PBS) for 30 min at 37°C, followed by incubation with primary antibodies overnight at 4°C. The primary antibodies used were anti-CNPase (1:200, Santa Cruz, Dallas, Texas, USA), anti-MAG (1:300, Santa Cruz), anti-Nestin (1:500, Abcam, Cambridge, UK), anti-MBP (1:800, Abcam), and anti-BrdU (1:500, Abcam), anti-O4 (1:200, Sigma-Aldrich, St. Louis, MO, USA), anti-Foxg1 (1:500, Sigma-Aldrich), and anti-NG2 (1:200, Millipore, Bedford, MA, USA). The sections were treated with the appropriate FITC- or TRITC-conjugated secondary antibodies (1:200, Abcam) overnight at 4°C and then counterstained with 4',6-diamidino-2-phenylindole (DAPI). Finally, the sections were mounted with anti-fade mounting medium. The slides for BrdU staining were pretreated with solution containing 50% formamide, 280 mM NaCl, and 30 mM sodium citrate at 65°C for 2 h, incubated with 2 M HCl at 37°C for 30 min, and rinsed with 0.1 mol/L boric acid (pH 8.5) at room temperature for 10 min [2].

Image Acquisition and Quantification

Fluorescent images were captured using a confocal laser scanning microscope (Olympus FV10i, Tokyo, Japan) with appropriate excitation wavelengths. The digital images were measured using Image-Pro Plus 6.0 software (Media Cybernetics, Rockville, MD, USA). In the statistical analysis, at least 6 representative fields from randomly-selected images were acquired from each sample by a blinded observer, and then the average cell count/integrated optical density values were calculated [23]. To measure the proportion of OPCs in different differentiation stages *in vitro*, each dish was scanned with a 20 × objective lens in 600 μm × 450 μm format in the *x*–*y* direction. The number of NG2/GFP, O4/GFP or CNPase/GFP double-positive cells among GFP-positive cells in each field was counted by a blinded observer [2].

Primary Culture of Rat OPCs

The rat OPC proliferation culture was maintained as previously described [24, 25]. Isolated OPCs were plated at 10,000 cells/cm^2 on poly-L-lysine-coated flasks and cultured in DMEM/F12 medium supplemented with 2% B27, 10 ng/mL platelet-derived growth factor AA (PDGF-AA, Gibco, Grand Island, NY, USA), and 10 g/mL basic fibroblast growth factor (bFGF, Gibco) for 3 days; then, the medium was replaced with DMEM/F12 medium without PDGF-AA and bFGF for 1 day to generate preOLs. For oligodendrocyte differentiation, 10% fetal bovine serum (FBS) was added to the preOL medium and cultured for 7 days. The medium was changed every 2 days.

Quantitative Real-Time Polymerase Chain Reaction (qRT-PCR)

Genomic RNA was extracted with TRIzol reagent (Invitrogen, Carlsbad, CA, USA) according to the manufacturer's instructions and as previously described [26]. The sense and antisense primers for GSK-3β were as follows: forward: 5′-TCCCTCAAATTAAGGCACATC-3′ and reverse: 5′-CACGGTCTCCAGTATTAGCATC-3′. The expression level of 18S ribosomal RNA (rRNA) served as an internal control for the samples, and was assessed using the following sense and antisense primers: forward: 5′-CCTGGATACCGCAGCTAGG A-3′ and reverse: 5′-

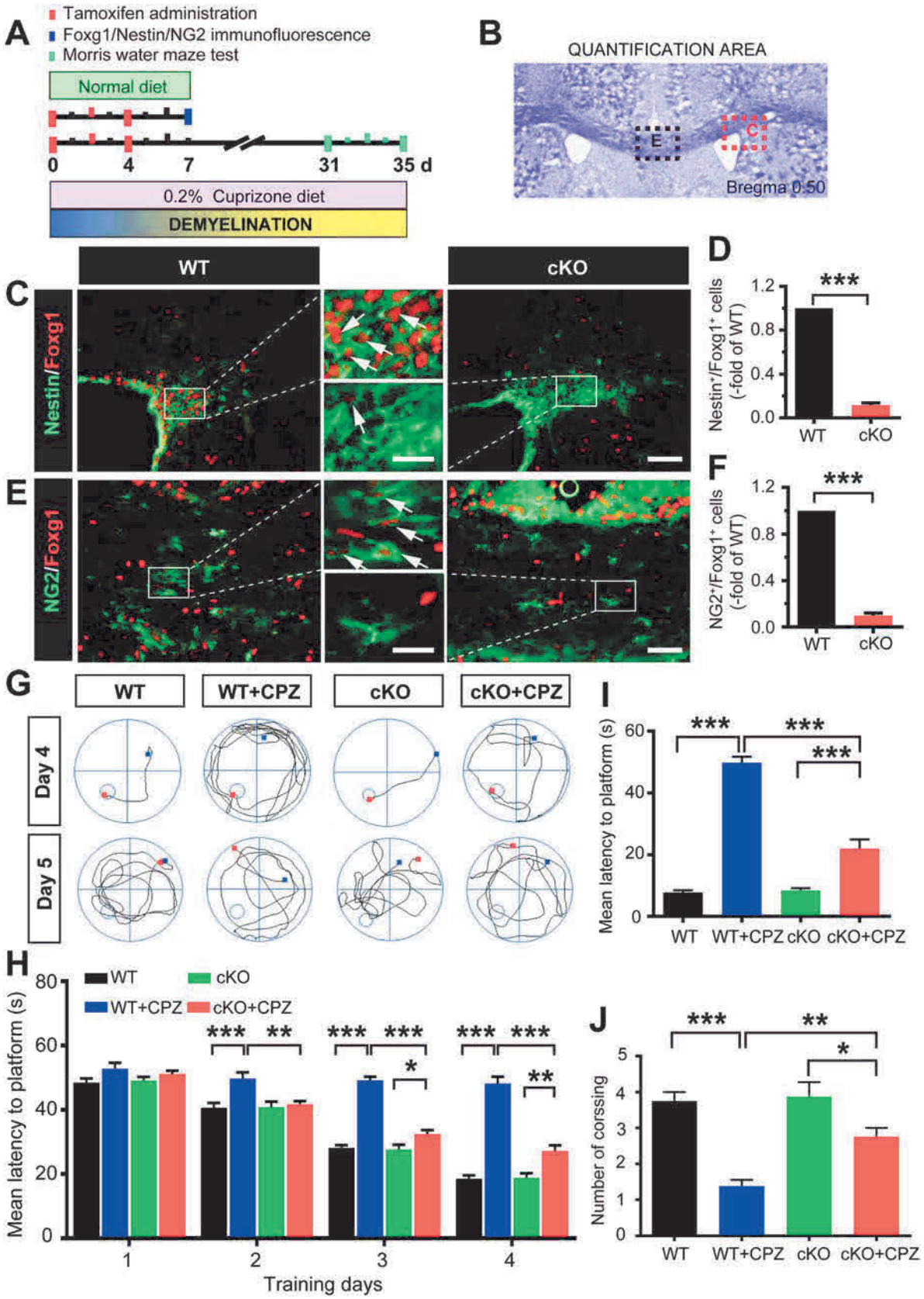
A
Tamoxifen administration
Foxg1/Nestin/NG2 immunofluorescence
Morris water maze test
Normal diet
0
4
7
31
35 d
0.2% Cuprizone diet
DEMYELINATION
B
QUANTIFICATION AREA
E
C
Bregma 0.50
C
WT
cKO
Nestin/Foxg1
D
Nestin+/Foxg1+ cells (-fold of WT)
***
WT
cKO
E
NG2/Foxg1
F
NG2+/Foxg1+ cells (-fold of WT)
***
WT
cKO
G
WT
WT+CPZ
cKO
cKO+CPZ
Day 4
Day 5
I
Mean latency to platform (s)
***
***
***
WT
WT+CPZ
cKO
cKO+CPZ
H
WT
cKO
WT+CPZ
cKO+CPZ
Mean latency to platform (s)
Training days
J
Number of corssing
***
**
*
WT
WT+CPZ
cKO
cKO+CPZ

◀**Fig. 1** *Foxg1* cKO relieves CPZ-induced learning and memory impairments in mice. **A** Schematic of the cuprizone (CPZ) and tamoxifen (TM) administration time points during experiment. Adult 7-week-old mice were fed a diet containing 0.2% CPZ for 5 weeks (demyelination phase); TM was intraperitoneally injected (3 times, 24 h apart) from day 0 after feeding the CPZ diet; mice were sacrificed immediately after the Morris water maze (MWM) test. **B** Image showing the measured region in the coronal sections in **C**, **D** (red dashed box) and **E**, **F** (black dashed box). **C**, **D** Effect of *Foxg1* knockout on neural stem cells assessed by Nestin/Foxg1 immunofluorescence staining (**C**) and quantitative analysis (**D**). **E**, **F** Effect of *Foxg1* knockout on oligodendrocyte precursor cells assessed by NG2/Foxg1 immunofluorescence staining (**E**) and quantitative analysis (**F**). **G** Representative tracking from each group of mice in the MWM test on days 4 and 5 (small circles, location of the platform; blue and red points, start and end locations of the mouse, respectively). **H** Average latency to find a hidden platform during the first 4 days of training in the directional navigation experiment. **I** Latency to find the platform on day 5 when the platform was removed. **J** Number of crossings in the spatial exploration experiment on day 5 of the MWM (white arrows in **C** and **E**, representative double-labeled positive cells). $n = 8$ per group. Data are presented as the mean ± SEM. $^{*}P < 0.05$, $^{**}P < 0.01$, $^{***}P < 0.001$, Student's *t*-test in **D**, **F**; one-way ANOVA with Tukey's *post hoc* test in **H**–**J**. Scale bars, 25 μm in **C**, **E**; 10 μm in the enlarged images.

GCGGCGCAATACGAATGCCCC-3′. The relative level of *Foxg1* mRNA expression was calculated according to the standard $2^{-\Delta\Delta Ct}$ method by normalization to the 18S rRNA mRNA level.

Western Blot Analysis

Western blot analysis was performed as previously described [27, 28]. Total protein was extracted from cultured rat OPCs using cell lysis buffer supplemented with proteinase and phosphatase inhibitors. The nuclear proteins were extracted using a commercial kit (Thermo Fisher Scientific, Waltham, MA, USA). Protein samples were separated on 10% SDS-PAGE gels and transferred to nitrocellulose membranes. The primary antibodies were anti-Foxg1 (1:800, Sigma-Aldrich), anti-GSK-3β (1:600, Sigma-Aldrich), anti-β-actin (1:1000, Santa Cruz), anti-β-catenin (1:500, Abcam), and anti-histone H3 (1:1000, Sigma-Aldrich). The band intensity was quantified using ImageJ software (NIH, Bethesda, MD, USA). Values were normalized to the β-actin/histone H3 level.

Lentiviral Vector Production

A lentivirus encoding small hairpin RNA (shRNA) for Foxg1 was designed and synthesized by GeneChem Co., Ltd (Shanghai, China). The *Foxg1* locus on chromosome 2 and its 200-bp flanking sequences were amplified by PCR from genomic rat DNA and inserted into the GV248 vector (the functional element is Ubi-EGFP-MCS-IRES-puromycin). The shRNA sequence for *Foxg1* was 5′-TCGGGCCAAGCTAGCCTTTAA-3′. To generate the construct, the scrambled sequence 5′-TTCTCCGAACGTGTCACGT-3′ was inserted. In the scrambled sequence, the nucleotides were randomly added with no target sequence tracks. Preparations of the recombinant lentivirus were made by transient co-transfection of HEK 293T cells accompanied by proper transfer vectors and lentiviral helper plasmids (20 μg of pGC-LV, 15 μg of pHelper 1.0, and 10 μg of pHelper 2.0) using Lipofectamine 2000 (Invitrogen, Waltham, MA, USA) according to the manufacturer's instructions. OPCs were transfected with lentiviral *Foxg1* shRNA 72 h before experiments.

EdU Labeling of OPCs

For EdU labeling, 3.5×10^4 cells were seeded into each well of a 48-well plate in DMEM/F-12 medium (1:1) supplemented with 10% FBS. Twenty-four hours later, EdU (RiboBio, Guangzhou, China) was added to the medium at 10 μmol/L. Another 24 h later, the cells were fixed with 4% paraformaldehyde for 30 min. For EdU staining, the cells were then incubated with freshly-made 1× Apollo®567 reaction cocktail for 30 min at room temperature in the dark. Then, the cells were incubated in 0.5% Triton X-100 in PBS for 10 min at room temperature. After washing twice with PBS, the cells were fixed in methanol and then stained with Hoechst 33342. The percentage of EdU-positive cells was calculated as the number of Apollo®567-stained cells/the number of Hoechst 33342-stained cells.

Statistical Analysis

Data were analyzed with SPSS software version 19.0 (IBM, Armonk, NY, USA) and are expressed as the mean ± SEM. *T*-tests or one-way analysis of variance (ANOVA) followed by the Newman-Keuls or Tukey's HSD post tests were used for comparisons between two or multiple groups, respectively. Statistical significance was set at $P < 0.05$.

Results

Conditional Ablation of *Foxg1* Ameliorates Behavioral Deficits and Demyelination Induced by CPZ

On the first day (day 0) of CPZ treatment, the mice were intraperitoneally injected with TM to induce *Foxg1* gene

knockout (Fig. 1A). The results showed that, compared with control littermates, Foxg1 expression on neural stem cells in the subventricular zone (Fig. 1C, D) or OPCs in the corpus callosum region (Fig. 1E, F) was significantly reduced in *Foxg1*-cKO mice on day 7 after TM injection. Studies have shown that CPZ administration results in a decline in learning and memory in mice [29, 30]. The MWM test showed that *Foxg1* cKO significantly shortened the prolonged mean latency from day 2 to day 4 (Fig. 1G, H), and it significantly decreased the latency to the platform on day 5 (Fig. 1G, I). The crossing number of *Foxg1*-cKO mice was clearly increased compared with the WT+CPZ mice (Fig. 1J). These results suggested that *Foxg1* cKO significantly alleviates the learning and memory impairments induced by CPZ in mice.

LFB staining showed that myelin was intact in the corpus callosum of WT mice, but it had almost entirely disappeared in the WT+CPZ mice (Fig. 2A). The demyelination score was significantly lower in the *Foxg1* cKO+CPZ group than in the WT+CPZ group (Fig. 2D). The statistical data from the myelin basic protein (MBP) immunofluorescence staining was consistent with the LFB staining results (Fig. 2B, E). These results indicated that demyelination induced by CPZ is significantly relieved by the absence of *Foxg1*.

Foxg1 cKO Decreases Proliferation but Promotes the Differentiation of OPCs in CPZ-Induced Demyelination

BrdU labeling was used to assess cell proliferation (Fig. 3A) and differentiation (Fig. 4A) in the corpus callosum, and the results showed that the number of BrdU-positive cells was significantly lower in the *Foxg1* cKO+CPZ group than the WT+CPZ group (Fig. 3C, D). Furthermore, the increase in percentage of $NG2^+$ cells (Fig. 3E, F) and $O4^+$ cells (Fig. 3J) cells in the WT+CPZ group was prevented by *Foxg1*-cKO treatment. The

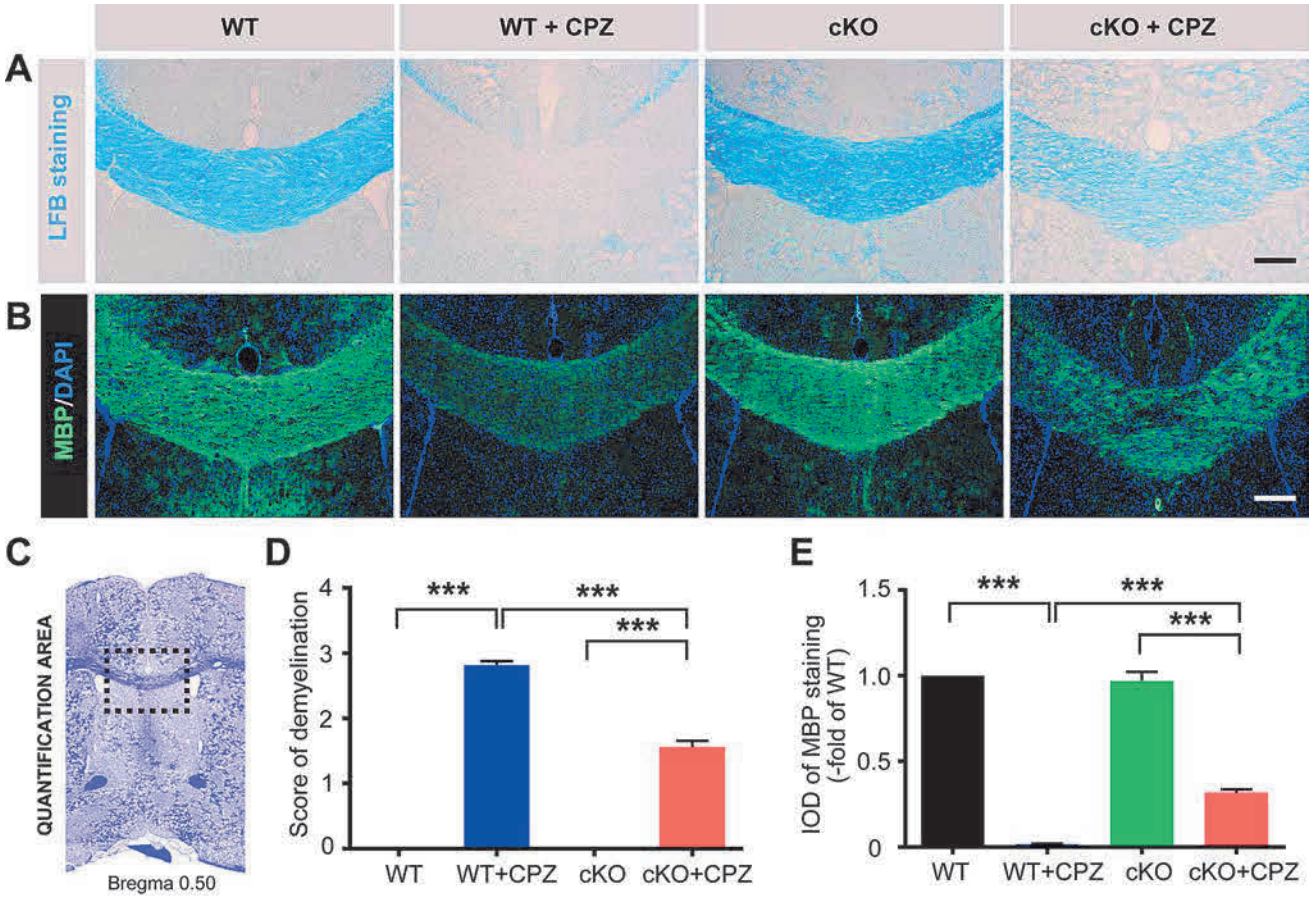

Fig. 2 Conditional ablation of *Foxg1* alleviates demyelination induced by cuprizone (CPZ) in mice. **A** Representative images of LFB staining showing demyelination in the corpus callosum (CC) of each group. **B** Representative images of NG2 immunofluorescence staining in the CC of each group. **C** Image showing the measured region (black dashed box) in the coronal sections in **A**, **B**. and **D** The degree of demyelination was analyzed in sections as in **A**. **E** Quantification of the MBP fluorescence measured as integrated optical density (IOD) in each group from sections as in **B**. $n = 8$ per group; data are presented as the mean ± SEM; $^{***}P < 0.001$, one-way ANOVA with Tukey's *post hoc* test; scale bars, 100 μm.

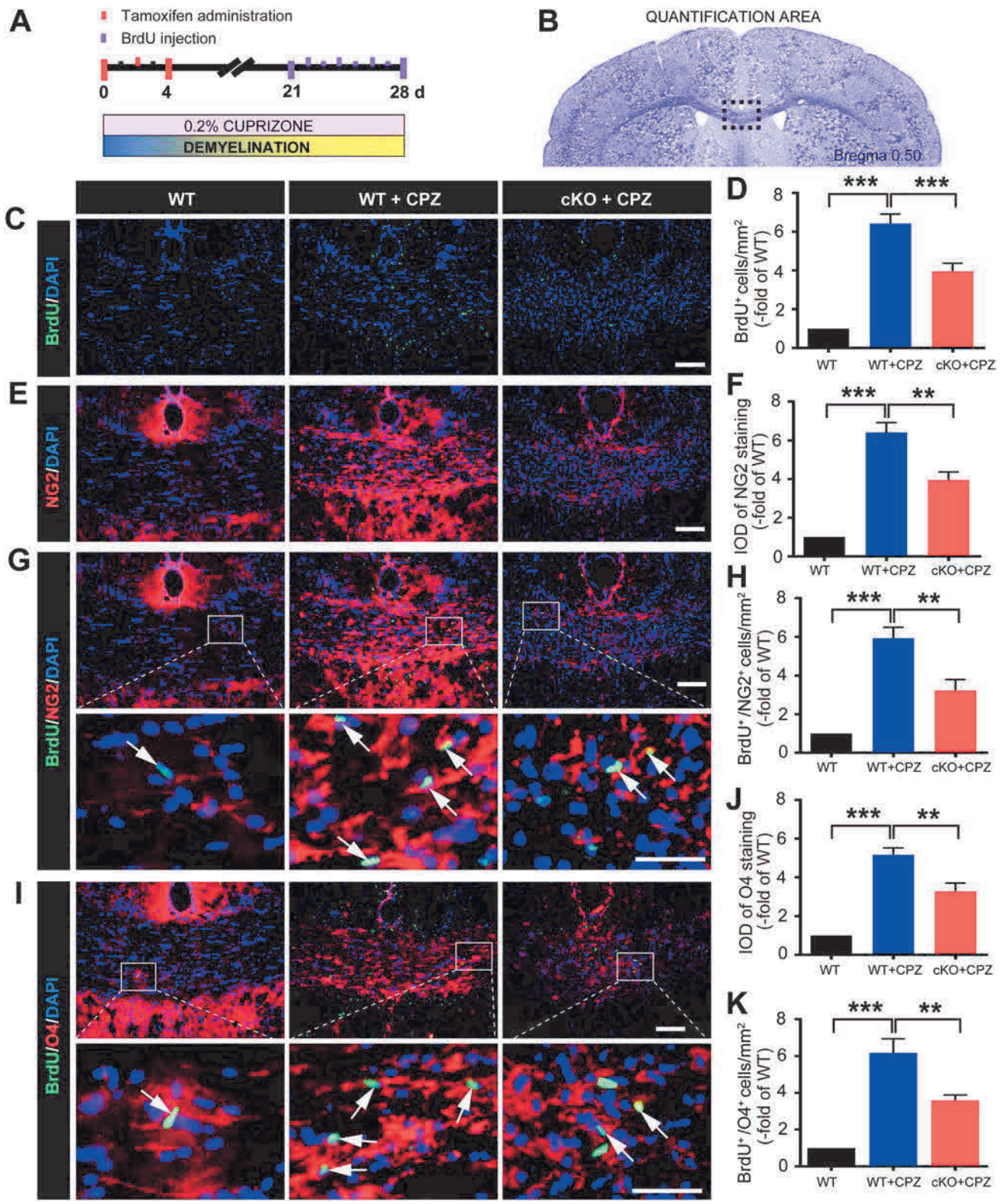
A
Tamoxifen administration
BrdU injection
0
4
21
28 d
0.2% CUPRIZONE
DEMYELINATION
B
QUANTIFICATION AREA
Bregma 0.50
C
WT
WT + CPZ
cKO + CPZ
BrdU/DAPI
D
BrdU+ cells/mm2 (-fold of WT)
E
NG2/DAPI
F
IOD of NG2 staining (-fold of WT)
G
BrdU/NG2/DAPI
H
BrdU+ /NG2+ cells/mm2 (-fold of WT)
I
BrdU/O4/DAPI
J
IOD of O4 staining (-fold of WT)
K
BrdU+ /O4+ cells/mm2 (-fold of WT)
***
**
WT
WT+CPZ
cKO+CPZ

◀**Fig. 3** Conditional knockout of *Foxg1* decreases the proliferation of oligodendrocyte precursor cells in the corpus callosum (CC) of mice induced with cuprizone (CPZ). **A** Schematic of CPZ and BrdU administration time points during the experiment. Adult 7-week-old mice were fed a diet containing 0.2% CPZ for 4 weeks (demyelination phase) to assess the proliferation of intrinsic OPCs; Tamoxifen (TM) was intraperitoneally injected (3 times, 24 h apart) from day 0 after starting the CPZ diet; BrdU was intraperitoneally injected twice a day for 7 consecutive days, and then the mice were sacrificed. **B** Image showing the measured region (black dashed box) in coronal sections as in **C**–**K**. **C** Immunofluorescence staining of BrdU in the CC of each group. **D** Quantitative analysis of $BrdU^+$ cells as in **C**. **E** Immunofluorescence staining of NG2 in the CC of each group. **F** Quantitative analysis of $NG2^+$ cells as in **E**. **G**, **H** Immunofluorescence staining of BrdU/NG2 (**G**) and quantitative analysis (**H**) in the CC of each group. **I** Immunofluorescence staining of BrdU/O4 in the CC of each group. **J**, **K** Quantitative analysis of $O4^+$ cells (**J**) and $BrdU^+/O4^+$ cells as in **I**. White arrows, representative double-labeled positive cells; $n = 8$ per group; data are presented as the mean ± SEM; $^{**}P < 0.01$, $^{***}P < 0.001$, one-way ANOVA with Tukey's *post hoc* test; scale bars, 50 μm in **C**, **E** and the upper panels in **G**, **I**; 20 μm in the lower panels of **G**, **I**.

number of proliferating OPCs, indicated by $NG2^+/BrdU^+$ (Fig. 3G, H) or $BrdU^+/O4^+$ (Fig. 3I, K), was also decreased; however, the number of new mature oligodendrocytes labeled with $BrdU^+/MBP^+$ (Fig. 4C, D), $BrdU^+/CNPase^+$ (Fig. 4E, F), and $BrdU^+/MAG^+$ (Fig. 4G, H) differentiated from the OPCs was significantly higher in the *Foxg1* cKO+CPZ group than in the WT+CPZ group. These data suggested that *Foxg1* cKO decreases the production or proliferation of OPCs but promotes their differentiation.

Foxg1 cKO Facilitates Myelination and the Recovery of Cognitive Function During Remyelination

To study the role of *Foxg1* in the regeneration of OLs after CPZ-induced myelin sheath injury, TM was administered on day 1 of CPZ withdrawal (Fig. 5A). Behavioral results showed that the average latency was significantly longer in the WT+CPZ than the WT group; however, *Foxg1* deletion in CPZ-treated mice clearly decreased the latency (Fig. 5B, C). In the spatial exploration experiment on day 5, the number of platform crossings was significantly higher in the *Foxg1* cKO+CPZ than the WT+CPZ group (Fig. 5D). These results suggested that *Foxg1* cKO significantly promotes the recovery of learning and memory after CPZ withdrawal in mice.

After 2 weeks of feeding without CPZ, the demyelination score was decreased (Fig. 5F, G) and the fluorescence intensity of MBP significantly enhanced (Fig. 5H, I) in the *Foxg1*-cKO mice. These results indicated that *Foxg1* deficiency favors myelin repair after CPZ-induced demyelinating injury.

Foxg1 cKO Inhibits Proliferation but Promotes the Differentiation of OPCs *In Vitro*

In vitro, GFP-tagged shRNA knockdown of *Foxg1* using lentiviral transfection was required to confirm its function in the proliferation and differentiation of cultured OPCs. The results of immunofluorescence staining (Fig. 6A, B) and Western blotting (Fig. 6D) demonstrated that *Foxg1* knockdown strongly decreased the expression of Foxg1 in primary cultured rat OPCs. The lentiviral transfection efficiency was defined by GFP fluorescence (Fig. 6C). The results of EdU staining showed that the number of EdU^+ cells was significantly smaller in the *Foxg1* shRNA than the control group (Fig. 6E, F). These results indicated that, to a certain extent, knockdown of *Foxg1* decreases the proliferation of OPCs *in vitro*, suggesting that *Foxg1* participates in the regulation of OPC proliferation.

To confirm whether *Foxg1* regulates OPC differentiation, we downregulated the level of *Foxg1* in OPCs and analyzed the number of immature and mature OLs. In contrast to the control group, most of the cells in the shRNA group were labeled with CNPase (Fig. 6I), and only a few were labeled with NG2 (Fig. 6G) or O4 (Fig. 6H). The number of O4-positive cells was significantly lower and CNPase-positive cells significantly higher in the *Foxg1* shRNA than in the Ctrl group (Fig. 6J), suggesting that *Foxg1* plays a negative regulatory role during OPC differentiation into OLs.

Foxg1 May Participate in the Proliferation and Differentiation of OPCs Through the Wnt Signaling Pathway

To explore whether *Foxg1* influences Wnt signal activation, we assessed the expression of GSK-3β and β-catenin. The results showed that the level of GSK-3β mRNA (Fig. 7A) and protein (Fig. 7B) was significantly higher in the *Foxg1* shRNA than in the control group, while the expression of β-catenin was significantly decreased in *Foxg1*-knockdown OPCs (Fig. 7C). The GSK-3β inhibitor SB216763 reversed the decrease in β-catenin induced by *Foxg1* knockdown (Fig. 7C). Moreover, SB216763 treatment also clearly increased the number of EdU^+ cells (Fig. 7D, E) and the proportions of $NG2^+$ (Fig. 7F, I) and $O4^+$ cells (Fig. 7G, I) and decreased the proportion of CNPase (Fig. 7H, I) when compared with the *Foxg1* shRNA group. These results indicated that *Foxg1* might be involved in the proliferation and differentiation of OPCs through the Wnt signaling pathway.

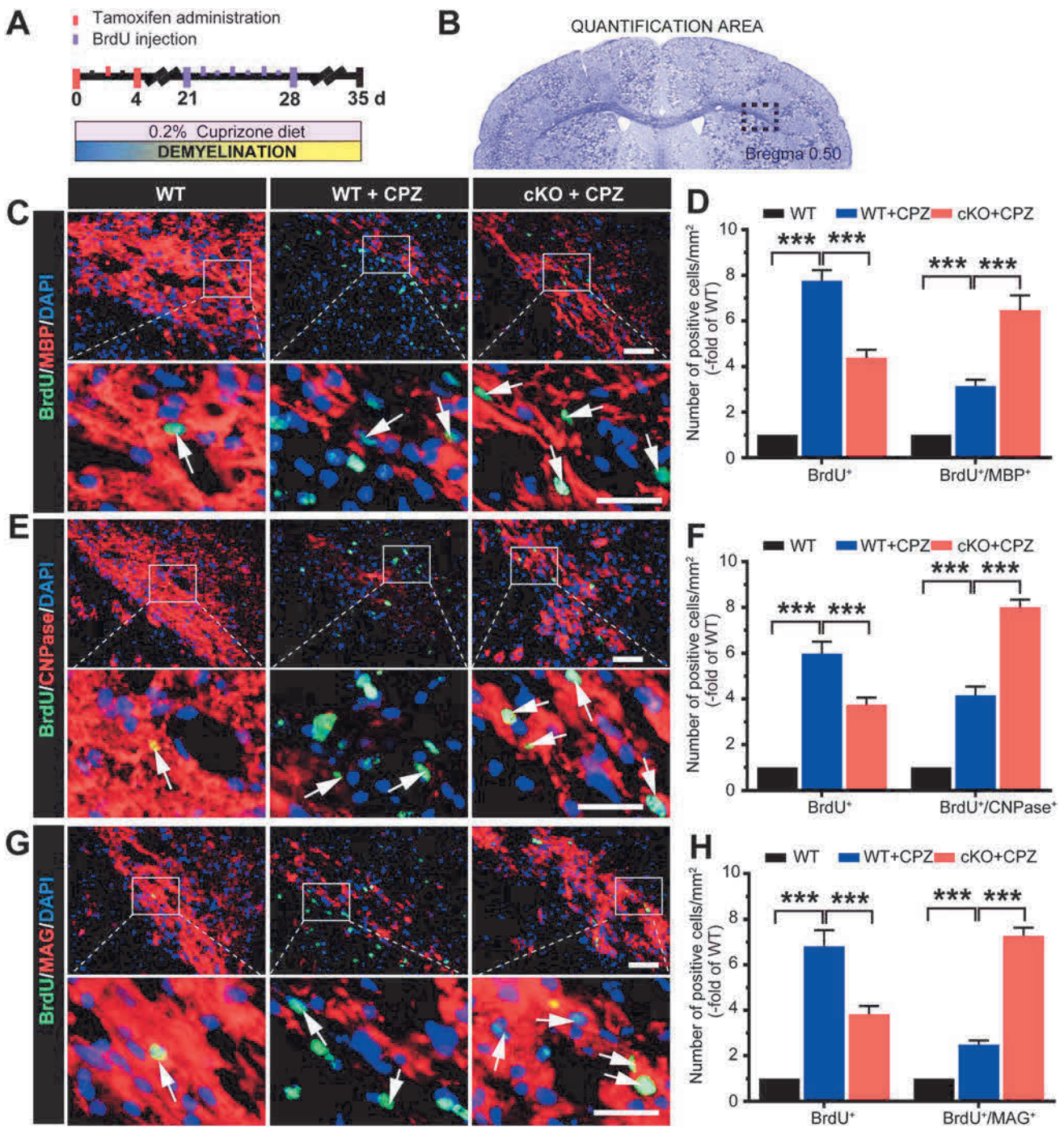

Fig. 4 Conditional knockout of *Foxg1* promotes the differentiation of oligodendrocyte precursor cells in the corpus callosum (CC) of mice induced by CPZ. **A** Schematic of cuprizone (CPZ) and BrdU administration time points during the experiment. Adult 7-week-old mice were fed a diet containing 0.2% CPZ for 5 weeks (demyelination phase); Tamoxifen (TM) was intraperitoneally injected (3 times, 24 h apart) from day 0 after feeding on a CPZ diet; BrdU was intraperitoneally injected twice a day for 7 consecutive days, and the mice were sacrificed on day 35. **B** Image showing the measured region (black dashed box) in coronal sections as in **C**–**H**. **C**–**H** Immunofluorescence double-labeled staining and quantitative analysis of BrdU/MBP (**C**, **D**), BrdU/CNPase (**E**, **F**), and BrdU/MAG (**G**, **H**) in the CC of *Foxg1*-cKO mice. White arrows indicate representative double-labeled positive cells; $n = 8$ per group; data are presented as the mean ± SEM; $^{**}P < 0.01$, $^{***}P < 0.001$, one-way ANOVA with Tukey's *post hoc* test; scale bars, 20 μm in the upper panel; 10 μm in the lower panel.

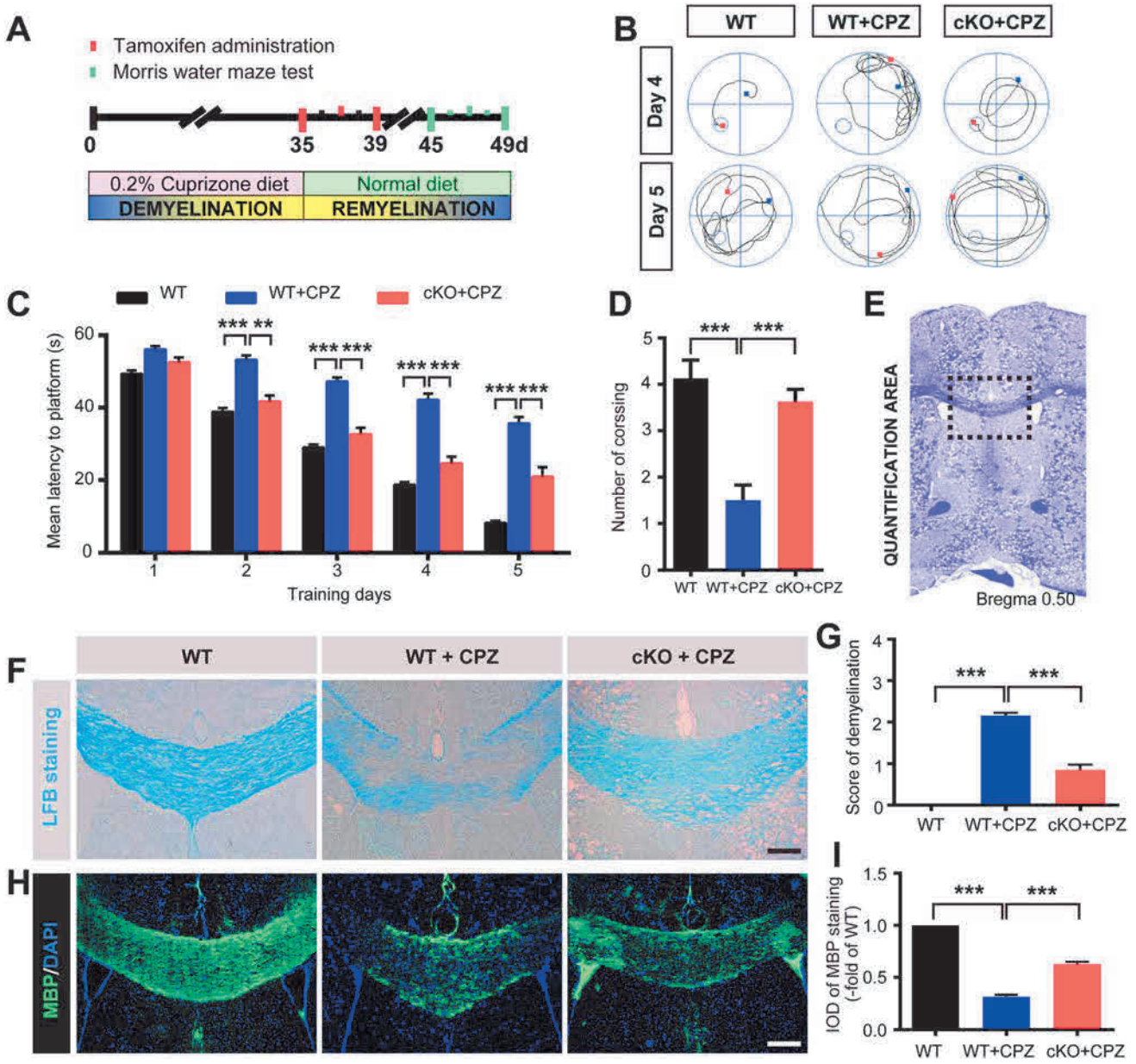

Fig. 5 *Foxg1* cKO promotes the recovery of cognitive function and remyelination after CPZ withdrawal in mice. **A** Timeline of the experimental design. Adult 7-week-old mice were fed a diet containing 0.2% cuprizone (CPZ) for 5 weeks (demyelination phase), followed by a normal diet for 2 weeks (remyelination phase); Tamoxifen (TM) was intraperitoneally injected (3 times, 24 h apart) after CPZ withdrawal; mice were sacrificed immediately after the Morris water maze (MWM) test. **B** Representative tracking in each group in the MWM test on days 4 and 5 (small circles, location of the platform; blue and red points, start and end locations, respectively). **C** Average latency for each group to find a hidden platform over the first 4 days of training in the directional navigation experiment and on day 5 when the platform was removed. **D** Number of crossings in each group in the spatial exploration experiment on day 5 of the MWM. **E** Image showing the measured region (black dashed box) in coronal sections as in **F**–**I**. **F** Representative images of LFB staining for demyelination in the corpus callosum in each group. **G** Analysis of the degree of demyelination as in **F**. **H**, **I** MBP immunofluorescence (**H**) and analysis of integrated optical density (IOD) (**I**) in each group. $n = 8$ per group; data are presented as the mean ± SEM; $^{**}P < 0.01$, $^{***}P < 0.001$, one-way ANOVA with Tukey's *post hoc* test; scale bars, 50 μm.

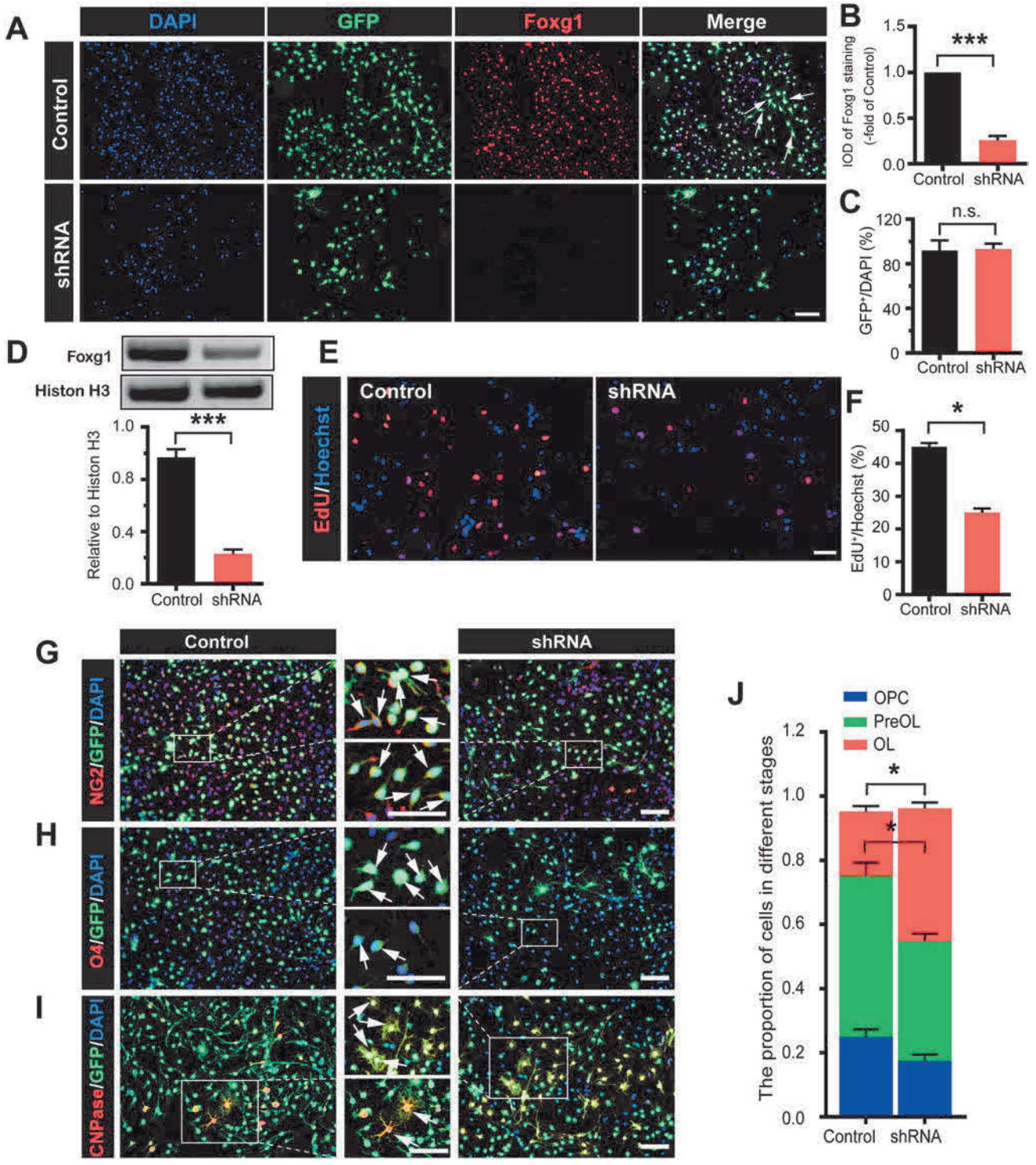

Fig. 6 Knockdown of *Foxg1* decreases proliferation while promoting the differentiation of OPCs *in vitro*. **A** *Foxg1* knockdown decreases the expression of Foxg1 in primary cultured rat OPCs. Cells transfected with a lentiviral GFP-tagged vector inserted into a scrambled sequence (Control) or lentiviral GFP-tagged *Foxg1* shRNA (shRNA) for 3 days and immunostained with anti-Foxg1 antibody. **B** Quantification of Foxg1 fluorescence integrated optical density (IOD) as in **A**. **C** The transfection efficiency as defined by GFP fluorescence. **D** Western blots and quantitative analyses of Foxg1 protein expression in primary cultured rat OPCs. **E**, **F** Representative images of EdU-positive proliferating cells (**E**) and quantitative analysis (**F**) of Control and *Foxg1* shRNA-treated OPCs. **G**–**I** Representative images of NG2 (**G**), O4 (**H**), and CNPase (**I**) staining in each group of cells. **J** Cell proportions at different stages during the differentiation of OPCs. White arrows, representative double-labeled positive cells; $n = 6$ per group; data are presented as the mean ± SEM; $^{*}P < 0.05$, $^{***}P < 0.001$, n.s. not significant, Student's *t*-test; scale bars, 40 μm.

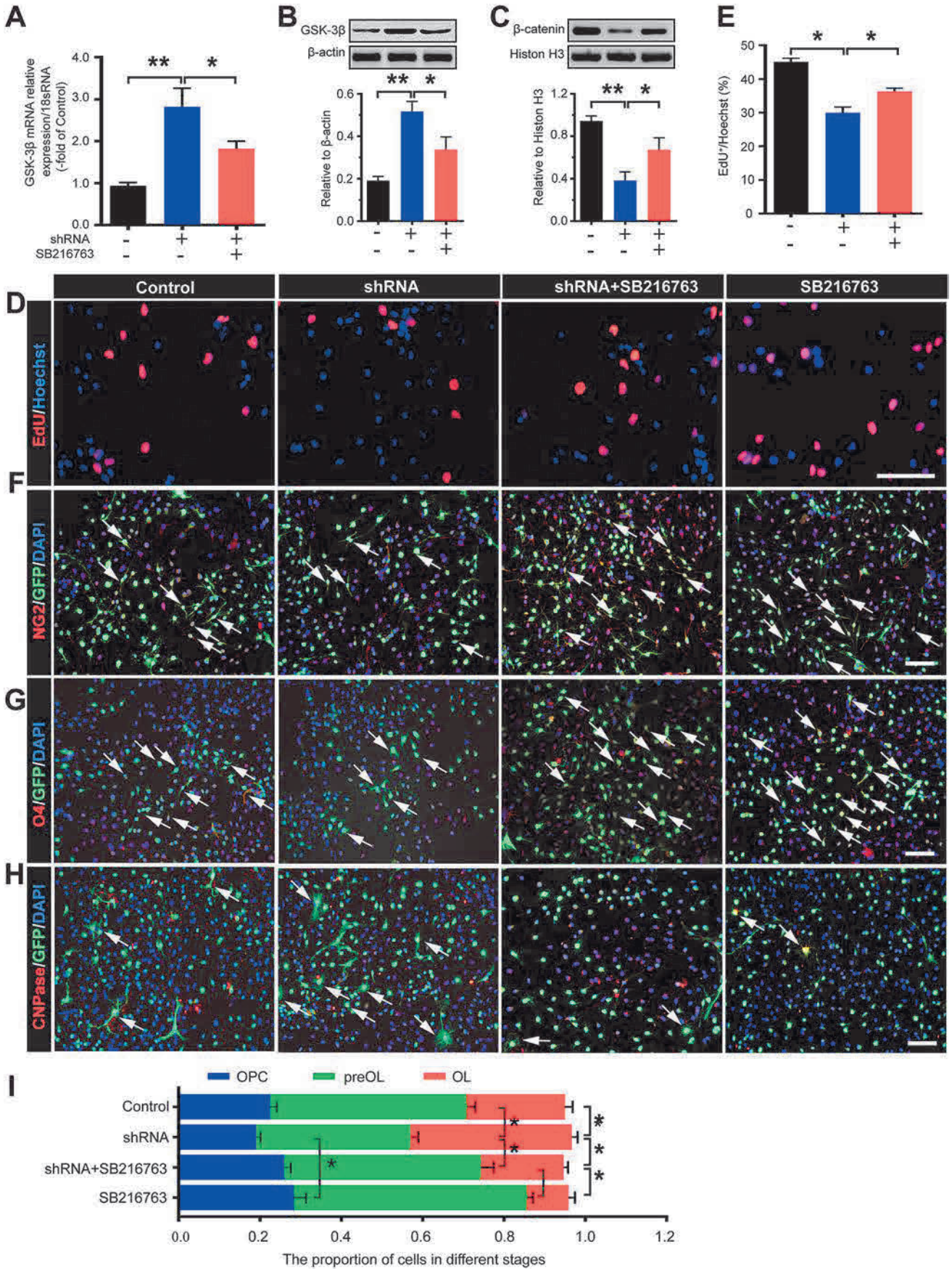
A
GSK-3β mRNA relative expression/18sRNA (-fold of Control)
shRNA
SB216763
B
GSK-3β
β-actin
Relative to β-actin
C
β-catenin
Histon H3
Relative to Histon H3
E
EdU+/Hoechst (%)
Control
shRNA
shRNA+SB216763
SB216763
D
EdU/Hoechst
F
NG2/GFP/DAPI
G
O4/GFP/DAPI
H
CNPase/GFP/DAPI
I
OPC
preOL
OL
Control
shRNA
shRNA+SB216763
SB216763
The proportion of cells in different stages

◀**Fig. 7** *Foxg1* regulates the proliferation and differentiation of OPCs by the Wnt signaling pathway. **A** GSK-3β mRNA expression in each group of cells assessed by qRT-PCR. **B**, **C** Western blots and quantitative analyses of the protein expression of GSK-3β (**B**) and nuclear β-catenin (**C**) in each group of cells. **D**, **E** EdU staining (**D**) and quantitative analysis (**E**) in each group of cells. **F**, **G** Representative images of NG2 (**F**) and O4 (**G**) immunofluorescence staining in each group of cells. **H** Representative images of CNPase immunofluorescence staining in each group of cells cultured in DMEM/F12 medium containing 10% FBS without PDGF-AA and bFGF for 7 days. **I** Cell proportions at different stages during the differentiation of OPCs. White arrows, representative double-labeled positive cells; $n = 6$ for each group; data are presented as the mean ± SEM; $^{*}P < 0.05$, $^{**}P < 0.01$, one-way ANOVA with Tukey's *post hoc* test; scale bars, 40 μm.

Discussion

As described in previous reports, *Foxg1* is abundantly expressed in the CNS [31] and plays pivotal roles in organogenesis through the regulation of proliferation and the specification of cell fate [32]. However, the role of *Foxg1* in the oligodendroglial lineage and the underlying mechanisms remain unclear. Therefore, the present study was designed to determine the effect of *Foxg1* and the mechanisms underlying the regulation of the Wnt signaling pathway following CPZ-induced demyelination.

CPZ is a copper chelator that impacts cell metabolism and leads to oligodendrocyte death and demyelination accompanied by weight loss and behavioral disorders [33]. The CPZ-fed C57BL/6 mouse model has been increasingly used to study demyelination and remyelination in the CNS [33, 34]. The present results are consistent with previous reports [35, 36], demonstrating that we successfully replicated the CPZ-induced demyelination model in the ICR strain of mice [37]. However, for the first time, we found that conditional knockout of *Foxg1* in NSPCs reversed the demyelination and spatial learning and memory impairments; moreover, a more evident remyelination was found after CPZ withdrawal. It has been reported that different subcellular localizations of *Foxg1* control the machinery that causes cell differentiation, replication, and bioenergetics. A fraction of *Foxg1* is recruited to mitochondria and plays a major role in neuronal survival, differentiation, and plasticity [38]. In addition, dietary triheptanoin rescues oligodendrocyte loss in a mouse model of Canavan disease [39], as well as the functional and molecular abnormalities in $Foxg1^{+/-}$ mice [40]. Thus, it should be noted that the food used in our study was a normal diet. To induce demyelination, 0.2% (w/w) CPZ was mixed into ground standard rodent chow. In addition, each group of mice received the same amount of chow. Thus, we confirmed that *Foxg1* might participate in the repair of myelin sheath damage in mice with CPZ-induced demyelination.

Oligodendrocytes are derived from OPCs [41], which populate the CNS starting from embryonic development [42, 43]. Previous studies [44, 45] have demonstrated that demyelinating injury induces OPC proliferation; however, studies on the differentiation of OPCs into mature oligodendrocytes and remyelination are limited. The mechanisms underlying the effect of *Foxg1* on the regulation of demyelination and remyelination remain to be clarified. Here, we found that CPZ administration increased the number of OPCs, which indicated that CPZ injury initiates the endogenous repair process and promotes the production of OPCs from neural stem cells of the subventricular zone region and migration to the injured area [46]. In the CPZ-induced demyelinated mouse corpus callosum, OPC proliferation was decreased by *Foxg1* cKO. Moreover, double labeling using BrdU and cell-specific markers showed that *Foxg1* cKO promoted OPC differentiation into mature OLs. Previous research has demonstrated that *Foxg1* may be necessary for maintenance of the NSC pool in the CNS and that genetic inactivity of *Foxg1* promotes both gliogenesis and neurogenesis [11]. NSCs are maintained in a quiescent state in the adult CNS [47]. Although it has been reported that *Foxg1* cKO in nestin-positive NSCs promotes neurogenesis and gliogenesis [11], it did not markedly change the myelin sheath and behavior in mice fed a normal diet in our study. We conclude that the change was so mild that there was no marked qualitative difference between the groups. However, the CPZ diet induced very serious demyelination accompanied by a change in the stem cell niche and OPC proliferation, and under this pathological situation, *Foxg1* cKO clearly promoted OPC differentiation. *In vitro*, purified primary OPCs were used to assess the effects of *Foxg1* inhibition on OPC proliferation and differentiation. It has been demonstrated that the loss of *Foxg1* leads to cycle exit and promotes the differentiation of premature cells [48, 49]. Consistent with previous reports [9–11], *Foxg1* knockdown inhibited the proliferation and promoted the differentiation of OPCs under normal culture conditions. As a result, the number of OPCs in the CPZ-treated corpus callosum area was reduced due to accelerated differentiation. The differentiated mature OLs encapsulated the axons of the neurons to form new myelin sheaths, thereby alleviating the myelin damage caused by CPZ or accelerating remyelination.

The Wnt/β-catenin signaling pathway plays an important role in regulating cell proliferation and differentiation [50–52]. Studies have shown that inhibition of GSK-3β expression in the Wnt signaling pathway inhibits the differentiation of OPCs while promoting their proliferation [53, 54]. Here, we found a significant increase in GSK-3β at the mRNA and protein levels in OPCs after *Foxg1* knockdown. We used 10 μmol/L SB216763 to inhibit the function of GSK-3β [55, 56], and found that this treatment

reversed the effect of *Foxg1* on OPC proliferation and differentiation and the nuclear level of β-catenin. These results are in agreement with reports in the literature [15]. Together with the results of the *in vivo* experiments performed here, it can be concluded that conditional knockout or knockdown of *Foxg1* effectively facilitates the differentiation of OPCs into OLs and promote the recovery of damaged myelin, and the Wnt/β-catenin signaling pathway is involved in this process. Given the increasing importance of glia-glia crosstalk and the inflammatory microenvironment in demyelination or remyelination [57–59], future studies are needed to focus on the microglia, astrocytes, and even the interaction between microglia, astrocytes, and oligodendrocytes, to further clarify the role of the Wnt/β-catenin signaling pathway in CPZ-induced demyelination or remyelination.

In summary, the present study provides evidence that, in CPZ-induced demyelinating mice, *Foxg1* knockout inhibits the proliferation but promotes the differentiation of OPCs into mature OLs by regulating the activity of the Wnt/β-catenin signaling pathway, which ultimately reduces the severity of demyelination and promotes remyelination. Therefore, *Foxg1* might be a promising novel target to enhance endogenous remyelination in patients with demyelinating diseases such as MS. Further experiments are required to investigate the precise targets of *Foxg1* in the Wnt/β-catenin signaling pathway and its interactions with other types of glial cells involved in demyelinating diseases in the CNS.

Acknowledgements We sincerely thank Professor Chunjie Zhao from the Medical School of Southeast University for providing the *Foxg1* cKO mice. This work was supported by the National Natural Science Foundation of China (81771337 and 81271345), the National Key R&D Program of China (2017YFA0104202), the Natural Science Foundation of Jiangsu Province (BK20161174), the Natural Science Foundation of the Jiangsu Higher Education Institutions of China (18KJB180028), and the Six Talent Peaks Project in Jiangsu Province (2015 to RY).

Conflict of interest The authors have no conflicts of interest to declare.

References

1. Lu F, Yin D, Pu Y, Liu W, Li Z, Shao Q, *et al.* Shikimic acid promotes oligodendrocyte precursor cell differentiation and accelerates remyelination in mice. Neurosci Bull 2019, 35: 434–446.
2. Fan HB, Chen LX, Qu XB, Ren CL, Wu XX, Dong FX, *et al.* Transplanted miR-219-overexpressing oligodendrocyte precursor cells promoted remyelination and improved functional recovery in a chronic demyelinated model. Sci Rep 2017, 7: 41407.
3. Amaral AI, Tavares JM, Sonnewald U, Kotter MR. Oligodendrocytes: Development, physiology and glucose metabolism. Adv Neurobiol 2016, 13: 275–294.
4. Pan Y, Jiang Z, Sun D, Li Z, Pu Y, Wang D, *et al.* Cyclin-dependent kinase 18 promotes oligodendrocyte precursor cell differentiation through activating the extracellular signal-regulated kinase signaling pathway. Neurosci Bull 2019, 35: 802–814.
5. Murphy DB, Wiese S, Burfeind P, Schmundt D, Mattei MG, Schulz-Schaeffer W, *et al.* Human brain factor 1, a new member of the fork head gene family. Genomics 1994, 21: 551–557.
6. Eagleson KL, Schlueter McFadyen-Ketchum LJ, Ahrens ET, Mills PH, Does MD, Nickols J, *et al.* Disruption of Foxg1 expression by knock-in of cre recombinase: effects on the development of the mouse telencephalon. Neuroscience 2007, 148: 385–399.
7. Boggio EM, Pancrazi L, Gennaro M, Lo Rizzo C, Mari F, Meloni I, *et al.* Visual impairment in FOXG1-mutated individuals and mice. Neuroscience 2016, 324: 496–508.
8. Perche O, Haddad G, Menuet A, Callier P, Marcos M, Briault S, *et al.* Dysregulation of FOXG1 pathway in a 14q12 microdeletion case. Am J Med Genet A 2013, 161A: 3072–3077.
9. Martynoga B, Morrison H, Price DJ, Mason JO. Foxg1 is required for specification of ventral telencephalon and region-specific regulation of dorsal telencephalic precursor proliferation and apoptosis. Dev Biol 2020, 15: 107–121.
10. Brunetti-Pierri N, Paciorkowski AR, Ciccone R, Della Mina E, Bonaglia MC, Borgatti R, *et al.* Duplications of FOXG1 in 14q12 are associated with developmental epilepsy, mental retardation, and severe speech impairment. Eur J Hum Genet 2011, 19: 102–107.
11. Tian CX, Gong YF, Yang Y, Shen W, Wang K, Liu JH, *et al.* Foxg1 has an essential role in postnatal development of the dentate gyrus. J Neurosci 2012, 32: 2931–2949.
12. Gallo V, Deneen B. Glial development: the crossroads of regeneration and repair in the CNS. Neuron 2014, 83: 283–308.
13. Feigenson K, Reid M, See J, Crenshaw EB, Grinspan JB. Wnt signaling is sufficient to perturb oligodendrocyte maturation. Mol Cell Neurosci 2009, 42: 255–265.
14. Caspi M, Zilberberg A, Eldar-Finkelman H, Rosin-Arbesfeld R. Nuclear GSK-3beta inhibits the canonical Wnt signalling pathway in a beta-catenin phosphorylation-independent manner. Oncogene 2008, 27: 3546–3555.
15. Zhou L, Shao CY, Xu SM, Ma J, Xie YJ, Zhou L, *et al.* GSK3beta promotes the differentiation of oligodendrocyte precursor cells via beta-catenin-mediated transcriptional regulation. Mol Neurobiol 2014, 50: 507–519.
16. Han X, Gu X, Zhang Q, Wang Q, Cheng Y, Pleasure SJ, *et al.* FoxG1 directly represses dentate granule cell fate during forebrain development. Front Cell Neurosci 2018, 12: 452.
17. Li T, Wang J, Wang H, Yang Y, Wang S, Huang N, *et al.* The deletion of dicer in mature myelinating glial cells causes progressive axonal degeneration but not overt demyelination in adult mice. Glia 2018, 66: 1960–1971.
18. Liu M, Liu X, Wang L, Wang Y, Dong F, Wu J, *et al.* TRPV4 inhibition improved myelination and reduced glia reactivity and inflammation in a cuprizone-induced mouse model of demyelination. Front Cell Neurosci 2018, 12: 392.

19. Liu S, Ren C, Qu X, Wu X, Dong F, Chand YK, *et al.* miR-219 attenuates demyelination in cuprizone-induced demyelinated mice by regulating monocarboxylate transporter 1. Eur J Neurosci 2017, 45: 249–259.
20. Dong F, Wang S, Wang Y, Yang X, Jiang J, Wu D, *et al.* Quercetin ameliorates learning and memory via the Nrf2-ARE signaling pathway in d-galactose-induced neurotoxicity in mice. Biochem Biophys Res Commun 2017, 491: 636–641.
21. Qi DS, Tao JH, Zhang LQ, Li M, Wang M, Qu R, *et al.* Neuroprotection of Cilostazol against ischemia/reperfusion-induced cognitive deficits through inhibiting JNK3/caspase-3 by enhancing Akt1. Brain Res 2016, 1653: 67–74.
22. Liu Y, Dong F, Guo R, Zhang Y, Qu X, Wu X, *et al.* Hydrogen-rich saline ameliorates experimental autoimmune encephalomyelitis in C57BL/6 mice via the Nrf2-ARE signaling pathway. Inflammation 2019, 42: 586–597.
23. Dong F, Yao R, Yu H, Liu Y. Neuroprotection of Ro25-6981 Against ischemia/reperfusion-induced brain injury via inhibition of autophagy. Cell Mol Neurobiol 2017, 37: 743–752.
24. Lai Q, Du W, Wu J, Wang X, Li X, Qu X, *et al.* H3K9ac and HDAC2 activity are involved in the expression of monocarboxylate transporter 1 in oligodendrocyte. Front Mol Neurosci 2017, 10: 376.
25. Wang XQ, Yao RQ, Liu X, Huang JJ, Qi DS, Yang LH. Quercetin protects oligodendrocyte precursor cells from oxygen/glucose deprivation injury in vitro via the activation of the PI3K/Akt signaling pathway. Brain Res Bull 2011, 86: 277–284.
26. Li L, Chen HZ, Wang M, Chen FF, Gao J, Sun S, *et al.* NCAM-140 Translocation into lipid rafts mediates the neuroprotective effects of GDNF. Mol Neurobiol 2017, 54: 2739–2751.
27. Bowler EH, Smith-Vidal A, Lester A, Bell J, Wang Z, Bell CG, *et al.* Deep proteomic analysis of Dnmt1 mutant/hypomorphic colorectal cancer cells reveals dysregulation of epithelial-mesenchymal transition and subcellular re-localization of Beta-Catenin. Epigenetics 2020, 15: 107–121.
28. Qu X, Guo R, Zhang Z, Ma L, Wu X, Luo M, *et al.* bFGF protects pre-oligodendrocytes from oxygen/glucose deprivation injury to ameliorate demyelination. Cell Mol Neurobiol 2015, 35: 913–920.
29. Franco-Pons N, Torrente M, Colomina MT, Vilella E. Behavioral deficits in the cuprizone-induced murine model of demyelination/remyelination. Toxicol Lett 2007, 169: 205–213.
30. Xiao L, Xu H, Zhang Y, Wei Z, He J, Jiang W, *et al.* Quetiapine facilitates oligodendrocyte development and prevents mice from myelin breakdown and behavioral changes. Mol Psychiatry 2008, 13: 697–708.
31. Pauley S, Lai E, Fritzsch B. Foxg1 is required for morphogenesis and histogenesis of the mammalian inner ear. Dev Dyn 2006, 235: 2470–2482.
32. Solomon KS, Logsdon JM, Jr., Fritz A. Expression and phylogenetic analyses of three zebrafish FoxI class genes. Dev Dyn 2003, 228: 301–307.
33. Torkildsen O, Brunborg LA, Myhr KM, Bo L. The cuprizone model for demyelination. Acta Neurol Scand Suppl 2008, 188: 72–76.
34. Zendedel A, Beyer C, Kipp M. Cuprizone-induced demyelination as a tool to study remyelination and axonal protection. J Mol Neurosci 2013, 51: 567–572.
35. Hoyos HC, Marder M, Ulrich R, Gudi V, Stangel M, Rabinovich GA, *et al.* The role of Galectin-3: From oligodendroglial differentiation and myelination to demyelination and remyelination processes in a cuprizone-induced demyelination model. Adv Exp Med Biol 2016, 949: 311–332.
36. Zhang Y, Yin L, Zheng N, Zhang L, Liu J, Liang W, *et al.* Icariin enhances remyelination process after acute demyelination induced by cuprizone exposure. Brain Res Bull 2017, 130: 180–187.
37. Pringproa K, Sathanawongs A, Khamphilai C, Sukkarinprom S, Oranratnachai A. Intravenous transplantation of mouse embryonic stem cells attenuates demyelination in an ICR outbred mouse model of demyelinating diseases. Neural Regen Res 2016, 11: 1603–1609.
38. Pancrazi L, Di Benedetto G, Colombaioni L, Della Sala G, Testa G, Olimpico F, *et al.* Foxg1 localizes to mitochondria and coordinates cell differentiation and bioenergetics. Proc Natl Acad Sci U S A 2015, 112: 13910–13915.
39. Francis JS, Markov V, Leone P. Dietary triheptanoin rescues oligodendrocyte loss, dysmyelination and motor function in the nur7 mouse model of Canavan disease. J Inherit Metab Dis 2014, 37: 369–381.
40. Testa G, Mainardi M, Olimpico F, Pancrazi L, Cattaneo A, Caleo M, *et al.* A triheptanoin-supplemented diet rescues hippocampal hyperexcitability and seizure susceptibility in FoxG1(+/−) mice. Neuropharmacology 2019, 148: 305–310.
41. Simons M, Nave KA. Oligodendrocytes: Myelination and axonal support. Cold Spring Harb Perspect Biol 2015, 8: a020479.
42. Liu X, Lu Y, Zhang Y, Li Y, Zhou J, Yuan Y, *et al.* Slit2 regulates the dispersal of oligodendrocyte precursor cells via Fyn/RhoA signaling. J Biol Chem 2012, 287: 17503–17516.
43. Kessaris N, Fogarty M, Iannarelli P, Grist M, Wegner M, Richardson WD. Competing waves of oligodendrocytes in the forebrain and postnatal elimination of an embryonic lineage. Nat Neurosci 2006, 9: 173–179.
44. Kremer D, Aktas O, Hartung HP, Kury P. The complex world of oligodendroglial differentiation inhibitors. Ann Neurol 2011, 69: 602–618.
45. Kuhlmann T, Miron V, Cui Q, Wegner C, Antel J, Bruck W. Differentiation block of oligodendroglial progenitor cells as a cause for remyelination failure in chronic multiple sclerosis. Brain 2008, 131: 1749–1758.
46. Emery B. Regulation of oligodendrocyte differentiation and myelination. Science 2010, 330: 779–782.
47. Sozmen EG, DiTullio DJ, Rosenzweig S, Hinman JD, Bridges SP, Marin MA, *et al.* White matter stroke induces a unique oligo-astrocyte niche that inhibits recovery. J Neurosci 2019, 39: 9343–9359.
48. Yu J, Li C, Ding Q, Que J, Liu K, Wang H, *et al.* Netrin-1 ameliorates blood-brain barrier impairment secondary to ischemic stroke via the activation of PI3K pathway. Front Neurosci 2017, 11: 700.
49. Bai L, Mei X, Shen Z, Bi Y, Yuan Y, Guo Z, *et al.* Netrin-1 improves functional recovery through autophagy regulation by activating the AMPK/mTOR signaling pathway in rats with spinal cord injury. Sci Rep 2017, 7: 42288.
50. Liu Z, Wu C, Xie N, Wang P. Long non-coding RNA MEG3 inhibits the proliferation and metastasis of oral squamous cell carcinoma by regulating the WNT/beta-catenin signaling pathway. Oncol Lett 2017, 14: 4053–4058.
51. Song H, Shi L, Xu Y, Xu T, Fan R, Cao M, *et al.* BRD4 promotes the stemness of gastric cancer cells via attenuating miR-216a-3p-mediated inhibition of Wnt/beta-catenin signaling. Eur J Pharmacol 2019, 852: 189–197.
52. Zhang H, Qi Y, Geng D, Shi Y, Wang X, Yu R, *et al.* Expression profile and clinical significance of Wnt signaling in human gliomas. Oncol Lett 2018, 15: 610–617.
53. Ye P, Hu Q, Liu H, Yan Y, D'Ercole A J. beta-catenin mediates insulin-like growth factor-I actions to promote cyclin D1 mRNA expression, cell proliferation and survival in oligodendroglial cultures. Glia 2010, 58: 1031–1041.
54. Azim K, Butt AM. GSK3beta negatively regulates oligodendrocyte differentiation and myelination *in vivo*. Glia 2011, 59: 540–553.
55. Heyd F, Lynch KW. Phosphorylation-dependent regulation of PSF by GSK3 controls CD45 alternative splicing. Mol Cell 2010, 40: 126–137.
56. Martin M, Rehani K, Jope RS, Michalek SM. Toll-like receptor-mediated cytokine production is differentially regulated by glycogen synthase kinase 3. Nature Immunology 2005, 6: 777–784.

57. Tepavcevic V, Kerninon C, Aigrot MS, Meppiel E, Mozafari S, Arnould-Laurent R*, et al.* Early netrin-1 expression impairs central nervous system remyelination. Ann Neurol 2014, 76: 252–268.
58. Rajasekharan S, Bin JM, Antel JP, Kennedy TE. A central role for RhoA during oligodendroglial maturation in the switch from netrin-1-mediated chemorepulsion to process elaboration. J Neurochem 2010, 113: 1589–1597.
59. He X, Li Y, Lu H, Zhang Z, Wang Y, Yang GY. Netrin-1 overexpression promotes white matter repairing and remodeling after focal cerebral ischemia in mice. J Cereb Blood Flow Metab 2013, 33: 1921–1927.

Neurosci. Bull. January, 2021, 37(1):31–44
https://doi.org/10.1007/s12264-020-00519-1

www.neurosci.cn
www.springer.com/12264

ORIGINAL ARTICLE

Respiratory Control by Phox2b-expressing Neurons in a Locus Coeruleus–preBötzinger Complex Circuit

Na Liu[1,2] · Congrui Fu[3] · Hongxiao Yu[1] · Yakun Wang[1] · Luo Shi[1] · Yinchao Hao[1] · Fang Yuan[1] · Xiangjian Zhang[4] · Sheng Wang[1]

Received: 1 December 2019 / Accepted: 12 March 2020 / Published online: 28 May 2020

Abstract The locus coeruleus (LC) has been implicated in the control of breathing. Congenital central hypoventilation syndrome results from mutation of the paired-like homeobox 2b (Phox2b) gene that is expressed in LC neurons. The present study was designed to address whether stimulation of Phox2b-expressing LC ($Phox2b^{LC}$) neurons affects breathing and to reveal the putative circuit mechanism. A Cre-dependent viral vector encoding a Gq-coupled human M3 muscarinic receptor (hM3Dq) was delivered into the LC of Phox2b-Cre mice. The hM3Dq-transduced neurons were pharmacologically activated while respiratory function was measured by plethysmography. We demonstrated that selective stimulation of $Phox2b^{LC}$ neurons significantly increased basal ventilation in conscious mice. Genetic ablation of these neurons markedly impaired hypercapnic ventilatory responses. Moreover, stimulation of $Phox2b^{LC}$ neurons enhanced the activity of preBötzinger complex neurons. Finally, axons of $Phox2b^{LC}$ neurons projected to the preBötzinger complex. Collectively, $Phox2b^{LC}$ neurons contribute to the control of breathing most likely *via* an LC–preBötzinger complex circuit.

Keywords Locus coeruleus · Phox2b · Hypercapnic ventilatory response · Chemoreceptor · Neural circuit

Introduction

Congenital central hypoventilation syndrome (CCHS) is a rare genetic respiratory disease. The patients manifest obvious hypoventilation during sleep but normal or mild hypoventilation during wakefulness. More than 90% of CCHS patients carry a heterozygous mutation of the paired-like homeobox 2b (Phox2b) gene [1]. Accumulated evidence indicates that the response to hypercapnia is markedly reduced in animal models and CCHS patients, and this is most likely attributable to abnormal structure and function of central respiratory chemoreceptors [1–4]. In addition, mice carrying heterozygous mutation of Phox2b exhibit not only a reduced number of retrotrapezoid nucleus (RTN) neurons but also a blunted hypercapnic ventilatory response (HCVR) [5]. During wakefulness, both volitional and metabolic pathways are active in determining the minute ventilation (MV) necessary to maintain eucapnia; with sleep onset, the primary determinant of ventilation depends on the metabolic pathway that must recruit respiratory chemoreceptors. Interestingly, Phox2b is densely expressed in the RTN and nucleus tractus solitarius (NTS), as well as the locus coeruleus (LC), all of which are thought to be central respiratory chemoreceptor candidates [6].

Recently, several lines of experiments have demonstrated the physiological role of brainstem Phox2b-containing neurons in the control of breathing. In anesthetized

Na Liu, Congrui Fu and Hongxiao Yu have contributed equally to this work.

✉ Sheng Wang
wangsheng@hebmu.edu.cn

[1] Department of Physiology, Hebei Medical University, Shijiazhuang 050017, China

[2] Department of Physiology, Cangzhou Medical College, Cangzhou 061000, China

[3] School of Nursing, Hebei Medical University, Shijiazhuang 050000, China

[4] Hebei Key laboratory of Vascular Homeostasis and Hebei Collaborative Innovation Center for Cardio-cerebrovascular Disease, Shijiazhuang 050000, China

rodents, optogenetic stimulation of Phox2b-containing RTN neurons potentiates breathing [7]; in contrast, selective ablation of these neurons inhibits the central respiratory chemoreflex [8]. In addition, the majority of Phox2b-containing RTN neurons exhibit robust CO_2/H^+ sensitivity [9]. Our recent findings demonstrated that in conscious mice, chemogenetic stimulation of Phox2b-expressing NTS neurons produces a long-lasting increase in basal ventilation *via* a significant increase in respiratory frequency (RF) [10]; genetic ablation of these neurons significantly attenuates the HCVR [11]. Moreover, a subset of Phox2b-expressing NTS neurons also display CO_2/H^+ sensitivity *in vitro* [11]. These respiratory effects of Phox2b-expressing neurons in the RTN and NTS are reminiscent of a presumably similar role in the LC.

The LC, a noradrenergic nucleus in the pons, sends/receives widespread projections to/from many brain regions to regulate sleep/wake states, attention, and arousal [12–14], as well as breathing [15, 16]. For instance, the HCVR is significantly inhibited in rats with proportional loss of LC noradrenergic neurons, suggesting an important contribution of LC neurons to the central respiratory chemoreflex [15, 16]. Moreover, a notable loss of LC neurons occurs in CCHS patients and a Phox2b mutant mouse model [17, 18]. However, it remains incompletely understood whether activation of $Phox2b^{LC}$ neurons regulates basal pulmonary ventilation. In addition, the possible circuit mechanism underlying such an effect has not yet been determined.

Here, we used a chemogenetic approach to assess whether selective stimulation of $Phox2b^{LC}$ neurons affects basal ventilation, and to address whether $Phox2b^{LC}$ neurons are required for the HCVR. Finally, we attempted to reveal the circuit mechanism responsible for the control of breathing by $Phox2b^{LC}$ neurons.

Materials and Methods

Animals

Phox2b-Cre, Phox2b-EGFP-Jx101, and C57BL/6 J mice were used in the present study. Phox2b-Cre mice were provided by the Jackson Laboratory (Stock Number: 016223) on a C57BL/6 J genetic background. Phox2b-EGFP-Jx101 transgenic mice were supplied by the Mutant Mouse Regional Resource Center (University of California at Davis, USA) and designed by the Gene Expression Nervous System Atlas Project research group at Rockefeller University. Both mouse lines have been verified in our laboratory [10, 11]. Mice were housed at a controlled temperature and humidity under a fixed 12-h light/12-h dark cycle, with *ad libitum* access to food and water. The animal use was conducted in compliance with the Guide for the Care and Use of Laboratory Animals. The experimental protocol was approved by the Animal Care and Ethics Committee of Hebei Medical University (Hebmu-2017002).

Viral Vectors and Stereotaxic Surgery

The Cre-dependent adeno-associated viral vectors (AAVs) were from Shanghai Taitool Bioscience Co., Ltd. For surgery, male adult Phox2b-Cre transgenic mice (25 g–30 g) were anesthetized with pentobarbital sodium (60 μg/g, i.p.). Depth of anesthesia was assessed by an absence of corneal and hindpaw withdrawal reflexes. Additional anesthetic was administered as necessary (30% of the initial dose). All surgical procedures were carried out under strict aseptic conditions. After anesthesia, the mouse was placed prone on a stereotaxic apparatus (RWD Life Science Co., Ltd, Shenzhen, China) and body temperature was maintained at 37°C using a heating pad and a blanket. After shaving and cleaning the skin, an incision was made to expose the skull, and then small holes were drilled over the LC region. Viral vectors were bilaterally microinjected into the LC (stereotaxic coordinates: – 5.3 mm from bregma, ± 0.8 mm lateral from midline, and – 4.0 mm vertical from cortical surface) *via* a glass micropipette connected to a syringe pump (Harvard Apparatus, Holliston, MA) based on the Mouse Brain in Stereotaxic Coordinates [19]. The pipette was retained *in situ* for at least 5 min after injections to allow sufficient diffusion of virus. After surgery, the mice received injections of ampicillin (125 mg/kg, i.p.) and the analgesic ketorolac (4 mg/kg, i.p.). Mice were caged individually and given 4 weeks to recover before breathing measurements and histological experiments.

Chemogenetic Stimulation and Breathing Measurements

The protocol for chemogenetic stimulation has been described in detail [10]. Shortly, a Cre-dependent viral vector (AAV-EF1α-DIO-hM3Dq-mCherry; titer, 10^{12} virus molecules per milliliter; 100 nL per injection; total volume: 200 nL) encoding a gene cassette for expression of a mutated human Gq-coupled M3 muscarinic receptor (hM3Dq), a type of designer receptor exclusively activated by designer drugs (DREADD), was microinjected into the LC region based on the above stereotaxic coordinates. An equal volume of the control vector AAV-EF1α-DIO-mCherry (titer, 10^{12}/mL) was also microinjected. Four weeks after virus injections, breathing parameters were measured in conscious, freely-moving mice by whole-body plethysmography (EMKA Technologies, Paris, France) as

previously described [10]. Briefly, mice were allowed to adapt to a recording chamber for at least 2 h before the testing protocol. Mice were exposed to room air (21% O_2) throughout experiments. A mass flow regulator provided quiet, smooth, and constant flow through the recording chamber (0.5 L/min). Air-flow signals were recorded, amplified, digitized, and analyzed using IOX software (EMKA Technologies) to determine breathing parameters over sequential 20 s epochs (about 50 breaths) during periods of behavioral quiescence and regular breathing. The breathing parameters RF (breaths/min), tidal volume (TV, μL/g), and MV (μL/g per minute), were consecutively collected and read out in a real-time mode. MV was calculated as the product of RF and TV, normalized to body weight (g). For chemogenetic stimulation of $Phox2b^{LC}$ neurons, clozapine-N-oxide (CNO, 1 mg/kg), an activator of hM3Dq, was intraperitoneally injected into hM3Dq-transduced mice and breathing parameters were continuously collected for 4 h. At the end of the experiments, mice were sacrificed with an overdose of pentobarbital and transcardially perfused for histology.

Assessment of HCVR

The microinjection protocol was used as described above. For genetic ablation of $Phox2b^{LC}$ neurons, the Cre-dependent AAV vector encoding a genetically-engineered Casp3 gene (AAV-CAG-DIO-taCasp3-TEVp; titer, 10^{13}/mL; 50 nL per injection; total volume: 100 nL) or an equal volume of control vector (AAV-CAG-DIO-mCherry) was bilaterally microinjected into the LC of Phox2b-Cre mice. To verify ablation of $Phox2b^{LC}$ neurons, quantitative PCR (qPCR) was performed as described previously [10]. In brief, after anesthesia, the LC tissue was rapidly dissected out and placed in lysate solution, followed by reverse transcription (Super Script III First-Strand Synthesis System, ThermoFisher Scientific, Waltham, MA, USA). The products were amplified and analyzed using the ABI Quant Studio 6 flex system (1 cycle at 50°C for 2 min; 1 cycle at 95°C for 2 min; 40 cycles at 95°C for 10 s, 60°C for 30 s, and 72°C for 1 min). GAPDH was used as an internal reference. The following primers were used: GAPDH forward: 5′-GCAAATTCAACGGCACAGTCAAGG-3′, reverse: 5′-TCTCGTGGTTCACACCCATCACAA-3′; Phox2b forward: 5′-TACGCCGCAGTTCCATACAAACTC-3′, reverse: 5′-TCTTTGAGCTGCGCGCTTGTGAAG-3′. The HCVR was assessed 4 weeks after vector microinjection. For analysis of the HCVR, mice were sequentially exposed to 100% O_2, 2% CO_2, 5% CO_2, and 8% CO_2 for 7 min (balanced O_2; each separated by 5 min of 100% O_2). The peak value of each breathing parameter in response to different concentrations of CO_2 was calculated using 60 s epochs (about 150 breaths). Hypercapnic exposure was conducted under the condition of hyperoxia to largely reduce the contribution of peripheral chemoreceptors to the HCVR.

Histology

The immunofluorescence protocol has been described [10]. In brief, under deep anesthesia with urethane (1.8 g/kg, i.p.), mice were perfused transcardially with 50 mL cold saline, followed by 4% phosphate-buffered paraformaldehyde (pH 7.4). Each mouse was decapitated and the brainstem was dissected out, stored in 4% perfusion fixative at 4°C for 24 h–48 h, and then immersed in 30% sucrose in phosphate-buffer saline (PBS) for at least 2 days. Coronal sections were cut at 25 μm on a freezing cryostat (CM1950; Leica Microsystems, Germany) and blocked for 1 h at room temperature in 5% BSA with 0.25% Triton X-100 in PBS. Sections were incubated with primary antibodies against Phox2b (1:200, sc-376997; Santa Cruz Biotechnology, Inc., Santa Cruz, CA), tyrosine hydroxylase (TH, 1:1000, AB152; Millipore, Billerica, MA, USA), cFos (1:400, #2250; Cell Signaling Technology, Danvers, MA), or EGFP (1:1000, ab13970; Abcam, Cambridge, MA) overnight at 4°C. After rinsing with PBS for 15 min, appropriate fluorescently-conjugated secondary antibodies were applied for 1 h at room temperature, followed by rinsing with PBS again. Finally, the sections were mounted on slides with Vectashield Antifade Mounting Medium (Vector Laboratories, Burlingame, CA) and visualized using a fluorescence (DM6000B, Leica, Germany) or confocal microscope (LSM800, Carl Zeiss, Germany). Note that the Phox2b antibody was validated in our prior studies [10, 11].

For cFos-based histological analysis of CNO-stimulated LC neurons, the hM3Dq-transduced mice exposed to room air were injected with CNO (1 mg/kg, i.p.) or an equal volume of saline. After 120 min, each mouse was anesthetized and perfused transcardially with fixative for subsequent histological processing. For cFos-based evaluation of the proportion of CO_2-activated mCherry-transduced LC neurons, each mouse was placed in a chamber and exposed to 100% O_2 or 8% CO_2 (balance O_2) for 50 min, followed by 100% O_2 for 60 min, followed by histological examination. To calculate the proportion of CO_2- or CNO-stimulated mCherry-transduced neurons in the LC, cells were counted in 6 coronal sections from each mouse. The rostrocaudal location of each section was determined (bregma: – 5.26 mm to – 5.80 mm) according to the Mouse Brain in Stereotaxic Coordinates [19]. For cFos-based analysis of whether chemogenetic stimulation of $Phox2b^{LC}$ neurons affected the neuronal activity in the preBötzinger complex (preBötC), transcardial perfusion and histological protocols were performed 120 min after injection of CNO or

saline in hM3Dq-transduced mice. To count putative cFos-expressing preBötC neurons, 5 consecutive coronal sections (bregma: – 6.72 mm to – 7.20 mm, each separated by 90 μm) were collected for histology. The Phox2b staining was conducted together with cFos to easily locate the preBötC contour. Cells were counted manually on a fluorescence or confocal microscope to obtain the total number of labeled neurons of interest.

Tracing of Phox2b^{LC} Neurons

To determine whether the axons of Phox2b^{LC} neurons project to the preBötC, the anterograde tracing virus AAV-EF1α-DIO-mCherry (titer, 10^{12}/mL; 100 nL per injection; total volume: 200 nL) was bilaterally microinjected into the LC of Phox2b-Cre mice. After successful transduction of mCherry, histological examination was carried out to check the distribution of Phox2b^{LC} neuronal axons in the preBötC. For retrograde tracing of Phox2b^{LC} neurons, AAV_{retro}-EF1α-DIO-EGFP (titer, 10^{13}/mL; 50 nL per injection; total volume: 100 nL) was microinjected into the preBötC of Phox2b-Cre mice (bregma coordinates: anteroposterior, – 6.8 mm; mediolateral, ± 1.2 mm; dorsoventral, – 4.65 mm). Four weeks after microinjection, EGFP-expressing neurons were visualized in the LC using a confocal microscope (Zeiss LSM800, Germany). EGFP-labeled neurons were manually counted in 6 sections from 9 mice (bregma: – 5.26 mm to – 5.80 mm, each separated by 90 μm).

Statistics

Statistical analysis was performed using Prism 8 (GraphPad, La Jolla, CA). All data are presented as the mean ± SEM. Two-group comparisons were analyzed using two-tailed Student's *t* test. The differences among groups were compared using two-way ANOVA with Bonferroni's *post hoc* test. Differences with $P < 0.05$ were considered statistically significant.

Results

Expression of Phox2b in LC Neurons

To validate the presence of Phox2b in LC neurons in adult mice, immunofluorescence staining was used in C57BL/6 J and Phox2b-EGFP mice. Here, we checked the co-expression of Phox2b and TH (a specific marker of LC neurons [20]). To that end, the immunoreactivity for Phox2b (Phox2b$^+$) and TH (TH$^+$) was examined in C57BL/6 J mice ($n = 7$) and both markers were found to be co-localized in most of the LC neurons (Fig. 1A). Based on the cell counts, Phox2b$^+$TH$^+$ neurons (643 ± 32) accounted for approximately 50% of total number of TH$^+$ neurons (1274 ± 66). In addition, using the Phox2b-EGFP mouse line, it has been reported that a large number of EGFP-expressing neurons are Phox2b$^+$ in the NTS, RTN, and LC [9, 11, 21]. Here, co-expression of TH (red) and EGFP (green) was also confirmed in adult Phox2b-EGFP mice (Fig. 1B). Altogether, these data confirm the presence of Phox2b in LC neurons in adult mice.

Validation of the Chemogenetic Approach

The chemogenetic approach has been widely used to manipulate specific cell types and modulate rodent behavior [10, 22]. Here, to selectively stimulate Phox2b^{LC} neurons, a Cre-inducible AAV vector encoding hM3Dq-mCherry was bilaterally microinjected into the LC of Phox2b-Cre mice (Fig. 2A), followed by immunofluorescence staining for validation. As shown in Fig. 2B, cell counts were obtained from each mouse ($n = 5$), and the number of neurons with immunoreactivity for both mCherry and Phox2b (mCherry$^+$Phox2b$^+$) accounted for approximately 92% of the total mCherry$^+$ neurons and for approximately 50% of the total Phox2b$^+$ neurons (Fig. 2C, D), showing that a large number of hM3Dq-mCherry-transduced neurons were Phox2b$^+$. To further determine the selective activation of Phox2b^{LC} neurons, hM3Dq-transduced mice in an awake state were injected with CNO or an equal volume of saline, followed by tissue fixation and immunohistochemical staining (Fig. 3A). cFos-immunoreactive neurons (cFos$^+$) represented the activation of Phox2b^{LC} neurons. Clearly, according to the cell counts, the number of cFos$^+$mCherry$^+$ neurons in CNO-injected mice was greater than that in saline-injected mice (192 ± 25 *versus* 22 ± 8, CNO *vs* saline, $n = 4$ for each group, $P < 0.001$, Fig. 3B, C). Hence, CNO was able to selectively activate most of the Phox2b^{LC} neurons.

Chemogenetic Activation of Phox2b^{LC} Neurons Increases Basal Ventilation

Next, we performed a gain-of-function experiment using chemogenetics to test the effect of Phox2b^{LC} neuronal stimulation on respiratory function in conscious mice. Four weeks after viral injections, whole-body plethysmography (Fig. 4A) was used to measure the respiratory parameters RF, TV and MV during exposure to room air in the CNO and saline groups. Intraperitoneal injection of CNO produced a long-lasting increase in RF (Fig. 4B) and MV (Fig. 4D), with an insignificant change in TV (Fig. 4C). The RF markedly increased 45 min after CNO injection, remained elevated for approximately 105 min and gradually declined to the control level after 150 min (162 ± 7 *vs*

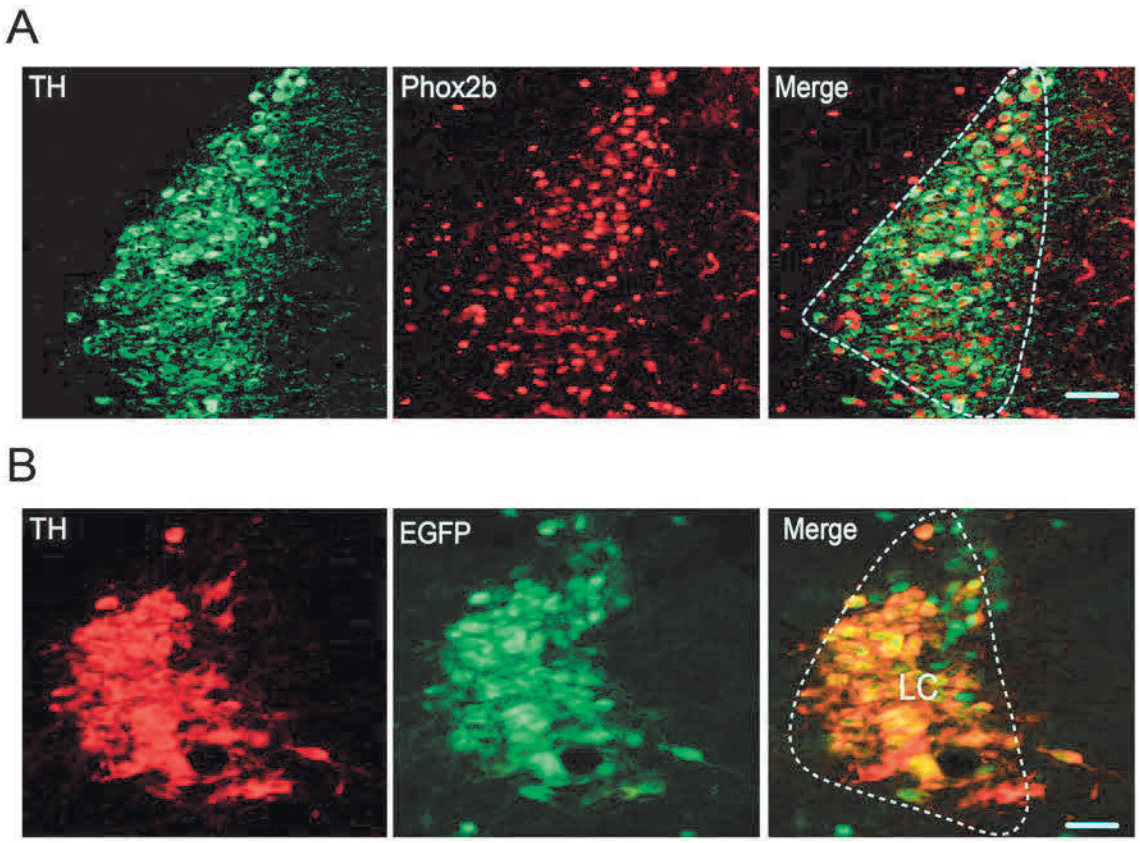

Fig. 1 Expression of Phox2b in LC neurons. Photomicrographs showing the co-expression of TH and Phox2b in LC neurons from adult C57BL/6 J (**A**) and Phox2b-EGFP (**B**) mice. The contour of LC is roughly indicated by dashed lines. Scale bars, 50 μm.

116 ± 8 breaths/min, CNO *vs* saline at approximately 75 min, $P < 0.0001$; Fig. 4B). Similarly, compared with the saline injection, the CNO injection generated a similar increase in MV, which persisted for approximately 105 min (1767 ± 82 *vs* 1168 ± 72 μL/g per minute, CNO *vs* saline at approximately 75 min, $P < 0.0001$, Fig. 4D). Administration of saline resulted in no significant increases in any breathing parameter. In control vector-injected mice (mCherry expression only), neither CNO nor saline injections caused significant changes in breathing parameters (data not shown). Collectively, we concluded that activation of Phox2b^{LC} neurons significantly increases the basal ventilation *via* an increase in RF rather than TV.

Chronic Ablation of Phox2b^{LC} Neurons Attenuates the HCVR

LC neurons have been thought to serve as a central respiratory chemoreceptor candidate [3, 23]. To further determine the role of Phox2b^{LC} neurons in the regulation of the HCVR, a loss-of-function experiment was carried out by ablation of Phox2b^{LC} neurons using a genetic approach as previously reported [10, 24]. As shown in Fig. 5A, the AAV-CAG-DIO-taCasp3-TEVp (AAV-CAG-DIO-mCherry for control) was bilaterally microinjected into the LC of Phox2b-Cre mice 4 weeks before breathing measurement. First, the effectiveness of Phox2b^{LC} neuron ablation was assessed using the unilateral injection of Casp3-containing virus into the LC, the other side being intact. The number of Phox2b^{LC} neurons on the injected side was lower than that on the control side (Fig. 5B). Quantitative analysis demonstrated that the Phox2b mRNA level in LC neurons from Casp3-transduced mice decreased by approximately 40% compared with that from mCherry-transduced mice (Fig. 5C). After validation of Phox2b^{LC} neuron ablation, we then tested the effect of bilateral ablation of Phox2b^{LC} neurons on the HCVR. Mice were sequentially exposed to 100% O_2, 2% CO_2, 5% CO_2, and 8% CO_2 and the breathing parameters were measured. During exposure to 100% O_2 and 2% CO_2, no statistical differences in RF, TV, and MV were found between the two groups. During exposure to 5% CO_2, ablation of Phox2b^{LC} neurons significantly reduced the TV and MV but not RF compared with the control group (TV: 10.0 ± 0.4 *vs* 13.9 ± 0.7 μL/g, $P < 0.0001$; MV: 2258 ± 90 *vs* 3266 ± 209 μL/g per minute, $P < 0.001$, Casp3 *vs* mCherry group, $n = 11$ for Casp3, $n = 9$ for mCherry; Fig. 5E). When 8% CO_2 was inhaled, RF, TV,

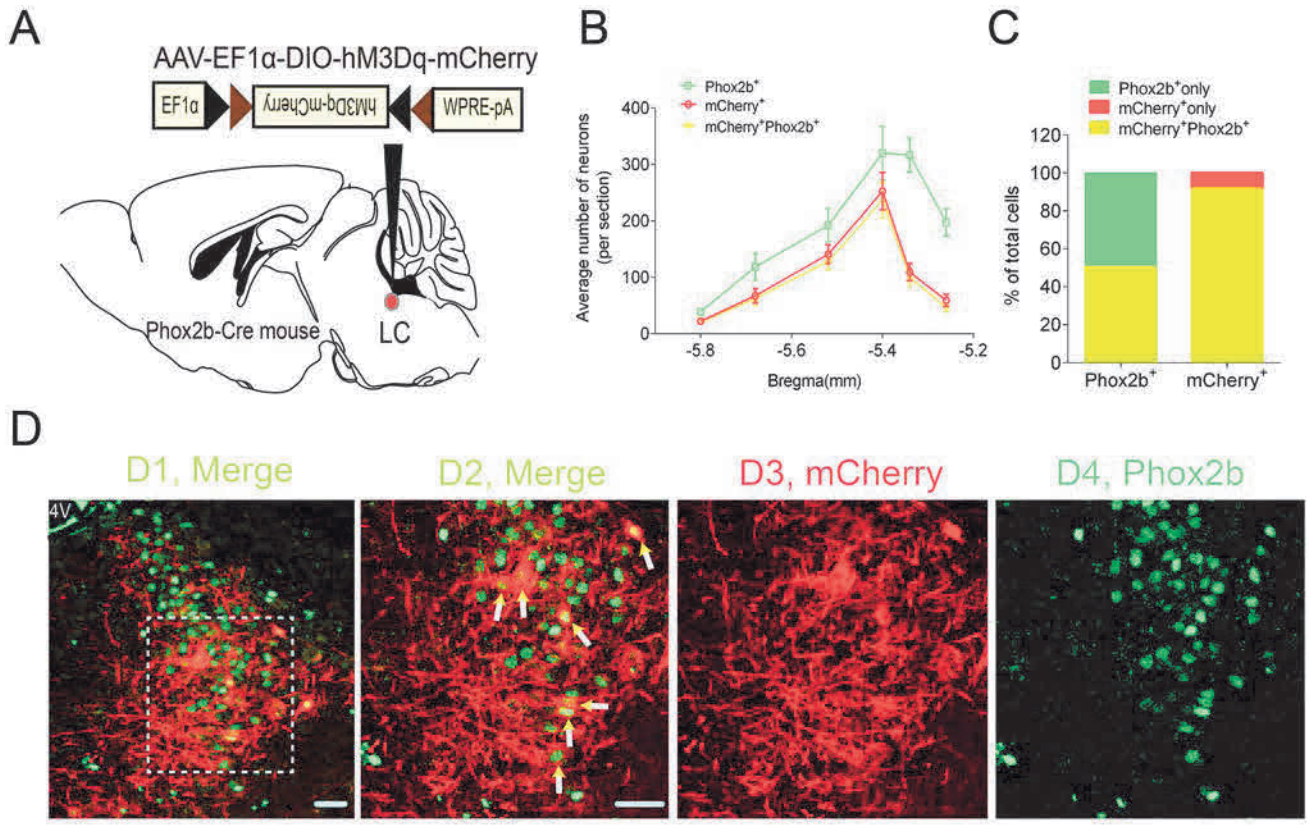

Fig. 2 Validation of hM3Dq-mCherry expression in Phox2b-Cre mice. **A** Schematic diagram showing the microinjection of viral vectors encoding hM3Dq-mCherry into the LC of Phox2b-Cre mice. **B** Rostrocaudal distribution of $Phox2b^+$, $mCherry^+$ and $mCherry^+$ $Phox2b^+$ neurons in the LC. Bilateral cell counts from 6 coronal sections (25 μm) from each mouse ($n = 5$). **C** Numbers of $mCherry^+Phox2b^+$ neurons account for approximately 92% of the total number of $mCherry^+$ neurons and for approximately 50% of $Phox2b^+$ neurons. **D1–4** Representative images of co-expression of Phox2b and mCherry. **D2** Enlargement of outlined area in D1. Arrows indicate $mCherry^+Phox2b^+$ neurons. **D3**, **4** Immunoreactivity for mCherry (red) and Phox2b (green). Scale bars, 50 μm; 4 V, fourth ventricle.

and MV all clearly decreased (RF: 257 ± 5 *vs* 281 ± 9 breaths/min, $P < 0.05$; TV: 13.5 ± 0.6 *vs* 18.1 ± 1.2 μL/g, $P < 0.0001$; MV: 3474 ± 188 *vs* 5093 ± 366 μL/g per minute, $P < 0.0001$; Casp3 *vs* mCherry group; Fig. 5F). Therefore, proportional ablation of $Phox2b^{LC}$ neurons significantly attenuated the HCVR.

CO_2 Sensitivity of $Phox2b^{LC}$ Neurons

The role of $Phox2b^{LC}$ neurons in the HCVR is associated with the intrinsic sensitivity to CO_2/H^+. To address whether $Phox2b^{LC}$ neurons exhibit CO_2 sensitivity, Phox2b-Cre mice injected with the AAV-EF1α-DIO-mCherry were exposed to 100% O_2 and 8% CO_2 and the immunoreactivity to cFos was examined to denote CO_2-activated cells. Fig. 6A shows immunofluorescence images of mCherry and cFos expression in the LC. The number of $cFos^+mCherry^+$ neurons was greater in mice treated with 8% CO_2 than with 100% O_2 (49 ± 4 *vs* 10 ± 1, 8% CO_2 *vs* 100% O_2, $n = 3$ per group, $P < 0.01$; Fig. 6B, C). Normalized data showed that $cFos^+mCherry^+$ neurons stimulated with 8% CO_2 accounted for approximately 18% of all $cFos^+$ neurons and for approximately 17% of all $mCherry^+$ neurons (Fig. 6D). These data suggest that a subgroup of $Phox2b^{LC}$ neurons is activated by CO_2 and most likely participates in the HCVR.

Stimulation of $Phox2b^{LC}$ Neurons Activates preBötC Neurons

preBötC neurons are the kernel of the respiratory central pattern generator (rCPG) [25]. It has been speculated that central respiratory chemoreceptors contribute to the control of breathing by activating the rCPG [25–27]. Therefore, we sought to address whether the stimulation of $Phox2b^{LC}$ neurons enhances the activity of preBötC neurons as represented by cFos-immunoreactivity. When hM3Dq-mCherry was successfully transduced into $Phox2b^{LC}$ neurons, CNO or saline was injected intraperitoneally, followed by immunofluorescence staining. Cell counts in 5

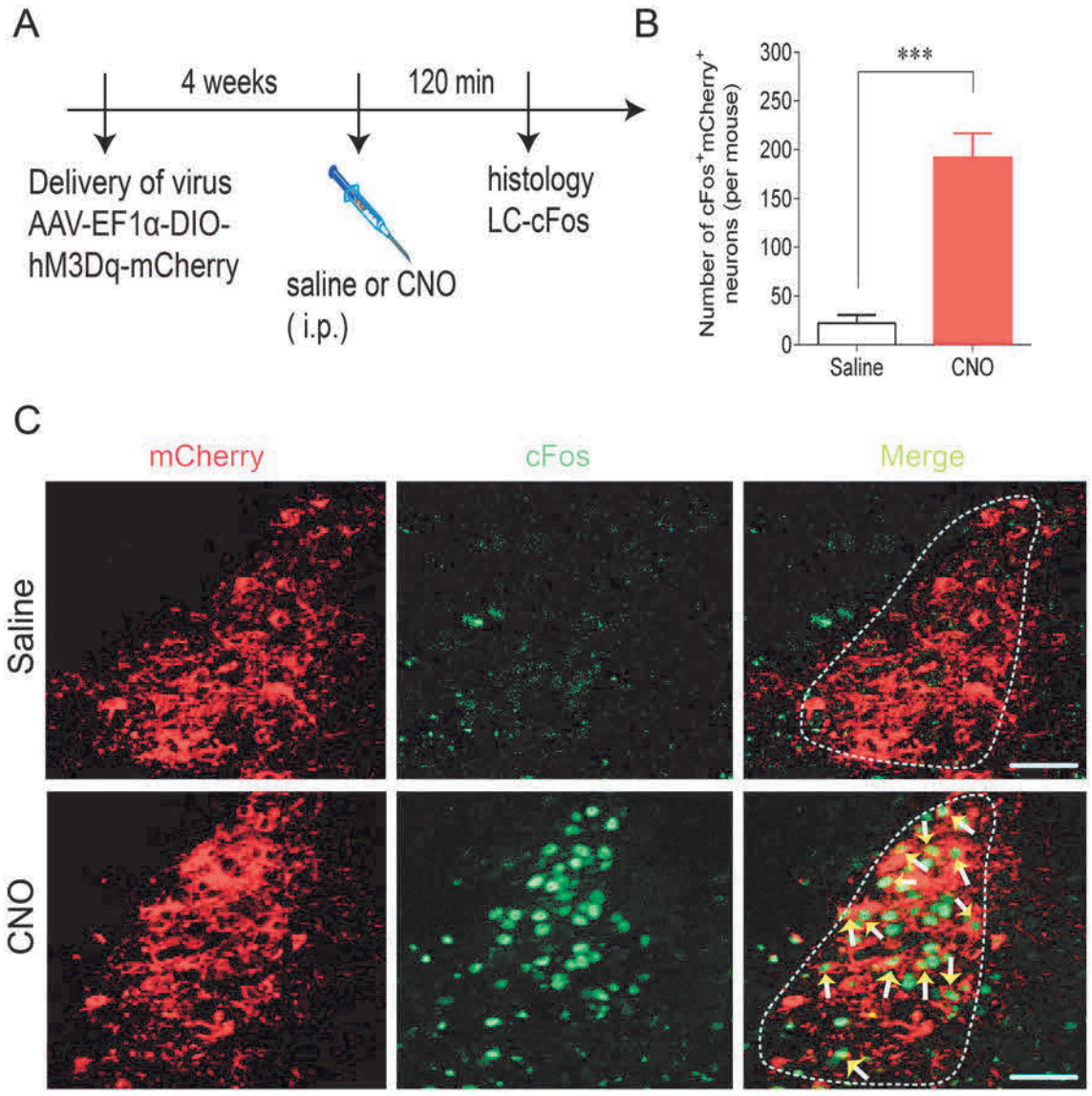

Fig. 3 Histomolecular verification of Phox2b^{LC} neuron activation. **A** Schematic of infection of Phox2b-Cre mice with AAV-EF1α-DIO-hM3Dq-mCherry by intraperitoneal injection of CNO or saline. **B** Numbers of cFos^{+}mCherry^{+} neurons in CNO (1 mg/kg)-injected mice relative to saline-injected mice. Cell counts are from 6 coronal sections from each mouse (n = 4 per group) (***$P < 0.001$, unpaired t test). **C** Representative photomicrographs showing mCherry^{+} (red) and cFos^{+} (green) neurons in the LC. Immunoreactivity for cFos indicates CNO-activated neurons (arrows). Scale bars, 50 μm.

coronal sections per mouse showed that the number of cFos^{+} neurons in the preBötC was greater in the CNO group than in the saline group (100 ± 7 *vs* 33 ± 2, CNO *vs* saline, $P < 0.001$, Fig. 7B, C). Note that due to a lack of adequately specific markers, cFos-labeled neurons were chosen based on the anatomically defined preBötC. Nevertheless, the present results suggest that stimulation of Phox2b^{LC} neurons can activate putative preBötC neurons.

Projection of Phox2b^{LC} Neurons to the preBötC

Having confirmed activation of the downstream preBötC neurons by Phox2b^{LC} neurons, we then attempted to dissect a putative direct pathway between the LC and preBötC. First, AAV-EF1α-DIO-mCherry was injected into the LC of Phox2b-Cre mice to map the axonal projection of Phox2b^{LC} neurons (Fig. 8A); immunofluorescence images demonstrated a dense distribution of putative axon terminals in the preBötC region (Fig. 8B). Because the viral vector used for anterograde tracing does not act transsynaptically [28], it can be concluded that these axons in

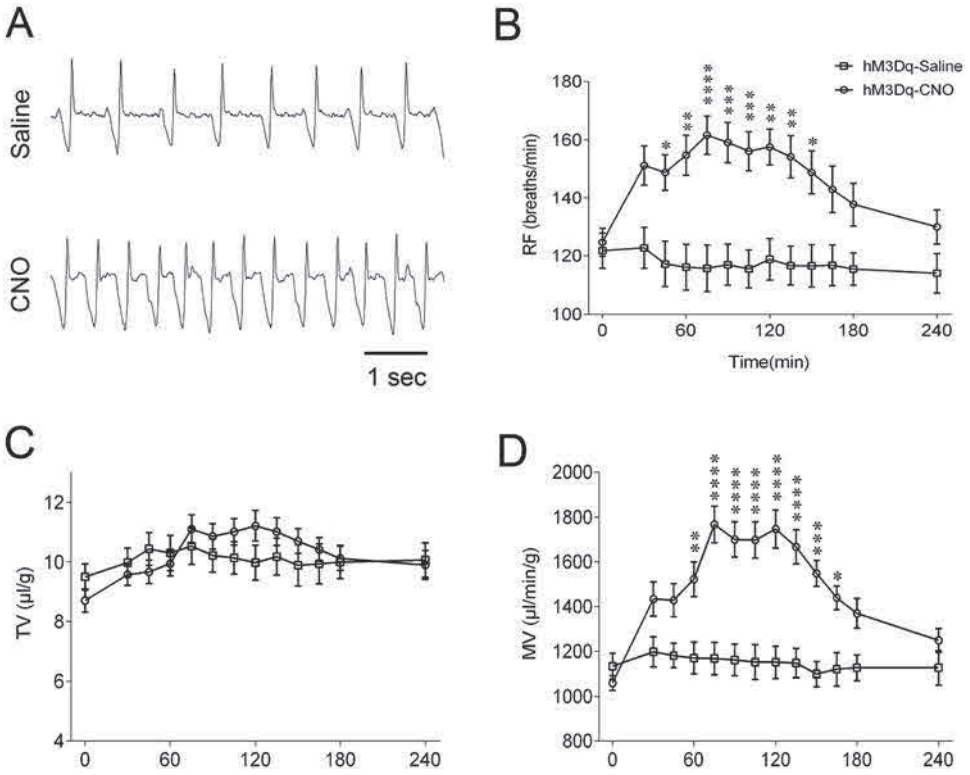

Fig. 4 Chemogenetic stimulation of Phox2b^{LC} neurons increases basal ventilation. **A** Typical traces of respiratory flow recording from hM3Dq-transduced Phox2b-Cre mice with intraperitoneal injection of saline or CNO. **B**–**D** Effects of Phox2b^{LC} neuron stimulation on breathing parameters. Administration of CNO, but not saline, produced marked increases in RF (**B**) and MV (**D**) but not TV (**C**) (n = 15 for saline group, n = 24 for CNO group; $^{*}P < 0.05$, $^{**}P < 0.01$, $^{***}P < 0.001$, $^{****}P < 0.0001$, saline *vs* CNO, two-way ANOVA with Bonferroni's *post hoc* test).

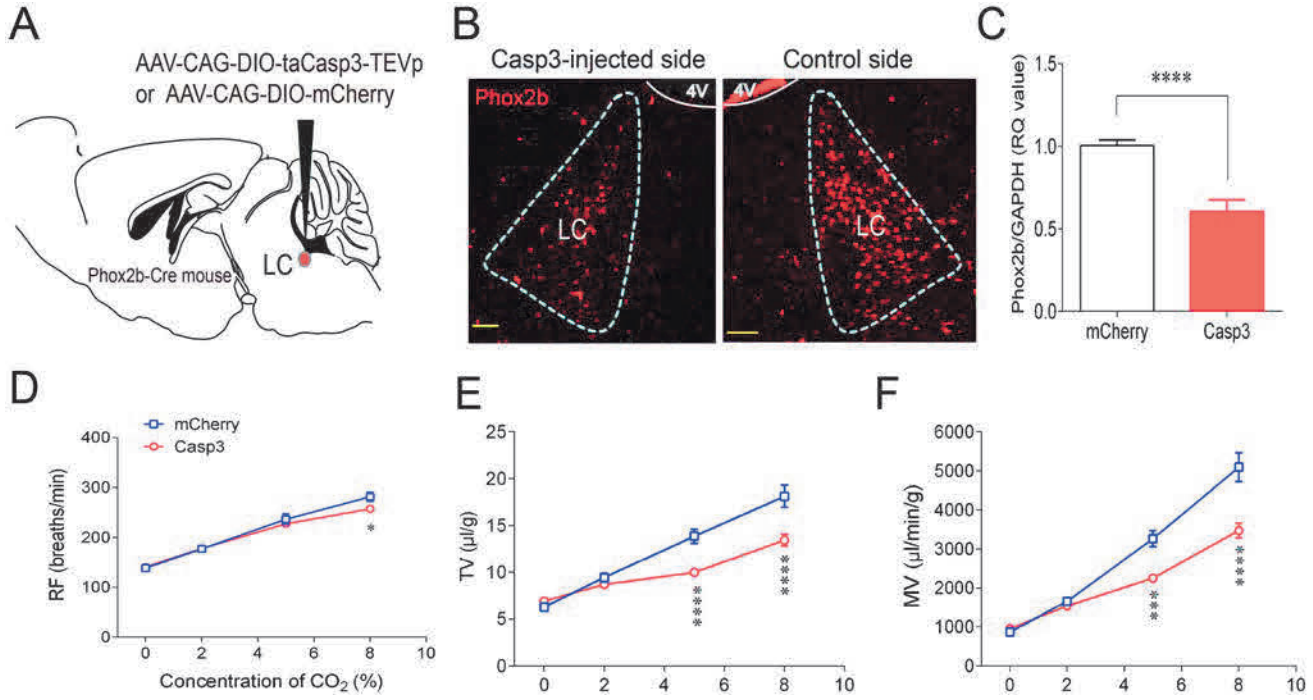

Fig. 5 Ablation of Phox2b^{LC} neurons impairs the HCVR. **A** Schematic diagram illustrating the microinjection of AAV-CAG-DIO-taCasp3-TEVp or AAV-CAG-DIO-mCherry (control virus) into the LC of Phox2b-Cre mice. **B** Immunofluorescence images showing that the number of Phox2b^{LC} neurons in the Casp3-injected side was significantly reduced compared to the control side of the LC in the same mouse (4 V, fourth ventricle; scale bars, 50 μm). **C** qPCR results for the levels of Phox2b mRNA in Casp3-transduced mice relative to mCherry-transduced mice (n = 14 samples from 7 mice for mCherry group, n = 10 samples from 5 mice for Casp3 group; $^{****}P < 0.0001$, unpaired t test). **D**–**F** Effects of bilateral ablation of Phox2b^{LC} neurons on breathing parameters during exposure to different concentrations of CO_2 (n = 9 for mCherry group, n = 11 for Casp3 group; $^{*}P < 0.05$, $^{***}P < 0.001$, $^{****}P < 0.0001$, two-way ANOVA with Bonferroni's *post hoc* test).

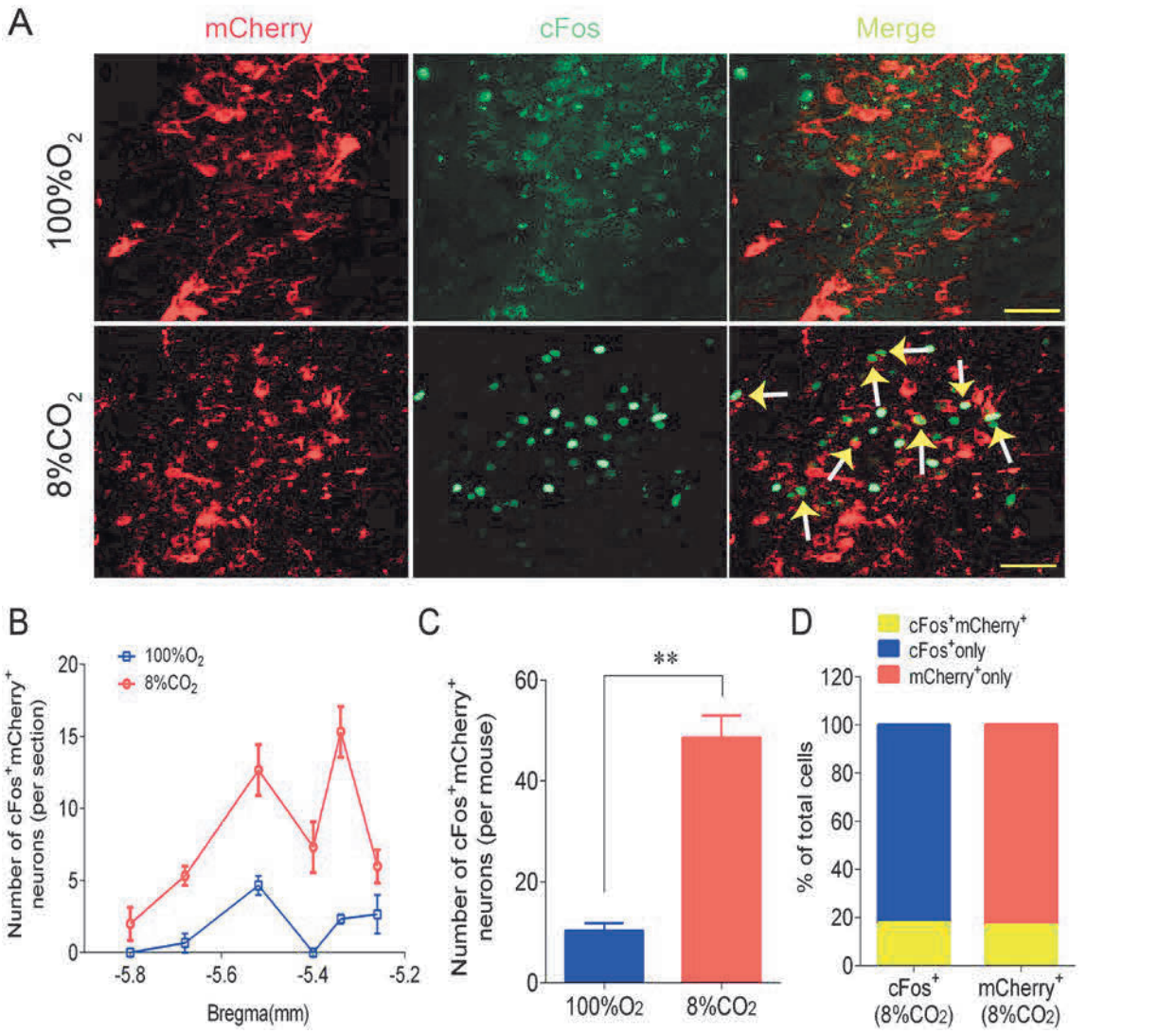

Fig. 6 CO_2 sensitivity of Phox2b^{LC} neurons. **A** Photomicrographs showing cFos$^+$ and mCherry$^+$ LC neurons in mCherry-injected mice exposed to 100% O_2 or 8% CO_2; immunoreactivity for cFos represents CO_2-activated neurons (arrows indicate mCherry$^+$cFos$^+$ neurons; scale bars, 50 μm). **B** Rostrocaudal distribution of cFos$^+$mCherry$^+$ neurons (6 coronal sections per mouse; n = 3 mice per group). **C** Numbers of cFos$^+$mCherry$^+$ neurons in mice exposed to 8% CO_2 and 100% O_2 (**$P < 0.01$, unpaired t test). **D** Percentages of cFos$^+$mCherry$^+$ neurons in the total number of cFos$^+$ and mCherry$^+$ neurons when challenged by 8% CO_2.

the preBötC originated from the somata of Phox2b^{LC} neurons. Second, AAV$_{retro}$-EF1α-DIO-EGFP, which is a retrograde tracer that infects neurons through axon terminals, was injected into the preBötC in Phox2b-Cre mice 4 weeks before histological examination (Fig. 8C); some EGFP-labeled neuronal somata, which projected axons to the preBötC, were found in the LC (Fig. 8D). Based on cell counts, EGFP$^+$Phox2b$^+$ neurons accounted for > 84% of the total number of EGFP$^+$ neurons (Fig. 8E). These data provide neuroanatomical evidence for an LC–preBötC pathway by which activation of Phox2b^{LC} neurons may increase pulmonary ventilation and HCVR.

Discussion

Noradrenergic neurons in the LC are thought to be central respiratory chemoreceptor candidates and they provide a CO_2-dependent excitatory drive to respiratory networks. However, the circuit mechanism underlying such an effect remains to be defined. In this paper, we used a chemogenetic approach in a transgenic mouse model to demonstrate that selective activation of Phox2b-expressing neurons, a putative subgroup of noradrenergic neurons in the LC, produced a long-lasting increase in basal MV *via* an increase in RF rather than TV in conscious mice. In addition, we used a genetic approach to proportionally ablate Phox2b^{LC} neurons, which resulted in an impaired

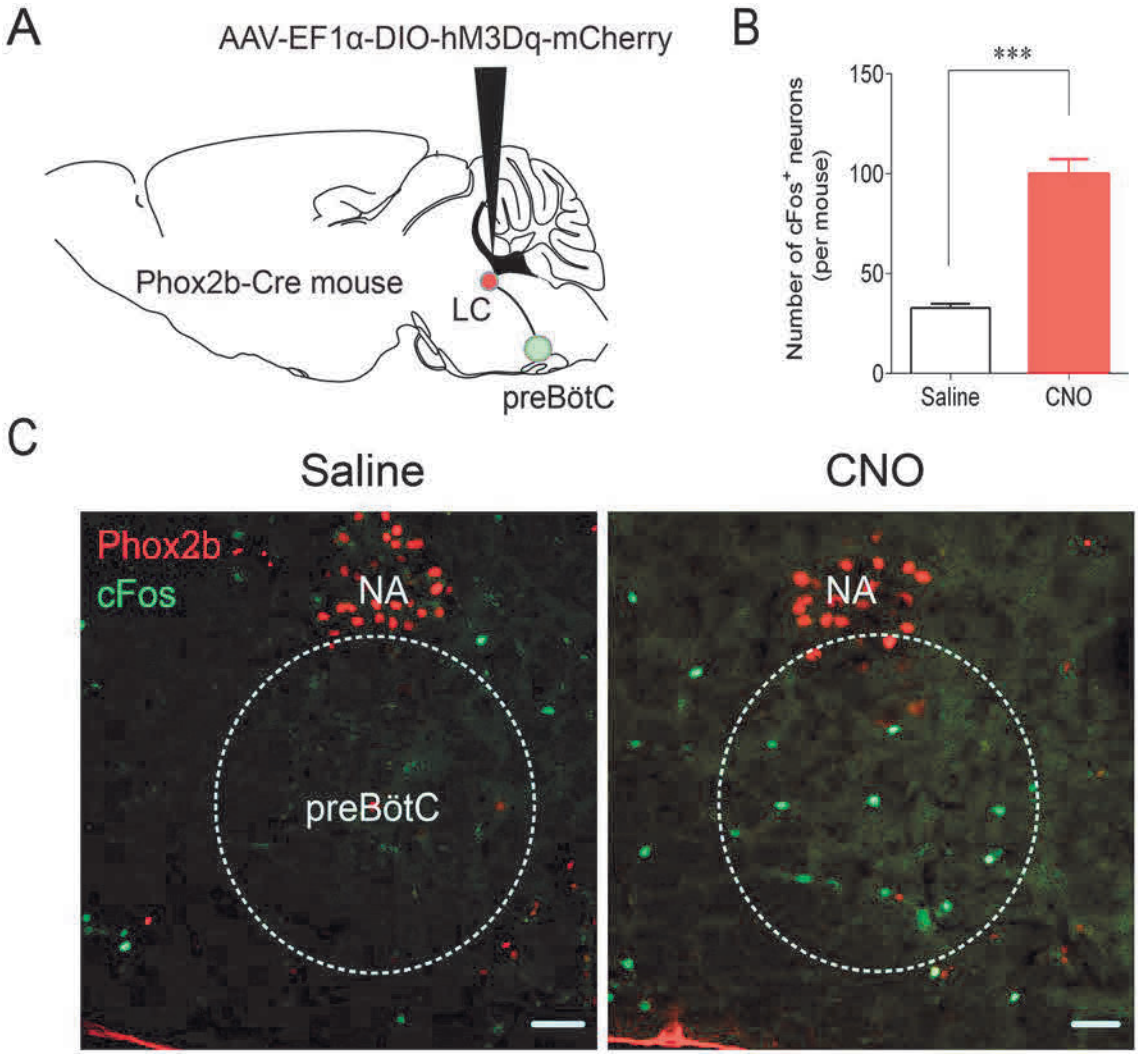

Fig. 7 Effect of Phox2b^{LC} neuron stimulation on the activity of preBötC neurons. **A** Schematic of microinjection of virus into the LC. After successful transduction of hM3Dq-mCherry in Phox2b^{LC} neurons, CNO or saline was intraperitoneally injected 2 h before histological examination for cFos labeling. **B** Numbers of cFos^{+} neurons in the preBötC in the CNO-injected and saline-injected groups (n = 4 for saline group, n = 6 for CNO group; ***$P < 0.001$, unpaired t test). **C** Photomicrographs showing cFos^{+} neurons (green) in mice treated with saline or CNO. The NA neurons were labeled by Phox2b (red). NA, nucleus ambiguus; scale bars, 50 μm.

HCVR. This phenomenon was most likely due to the CO_2-activation of a subset of Phox2b^{LC} neurons. Finally, an anatomically-defined LC–preBötC pathway is suggested to mediate the above effect of Phox2b^{LC} neurons.

Activation of Phox2b^{LC} Neurons Increases Basal Ventilation

In the present study, selective stimulation of Phox2b^{LC} neurons significantly increased basal pulmonary ventilation. This is supported by the following evidence. First, although the expression of Phox2b in adult rodents remains controversial [29, 30], our data, using Phox2b-Cre and Phox2b-EGFP mouse lines that have been validated, in combination with prior observations [6, 31], provide convincing evidence of Phox2b expression in the LC. Second, we found that > 90% of hM3Dq-transduced LC neurons were Phox2b^{+}, in favor of a significant contribution of Phox2b^{LC} neurons. Third, the majority of hM3Dq-expressing Phox2b^{LC} neurons were clearly activated by CNO. Of note, in addition to affecting breathing, stimulation of Phox2b^{LC} neurons probably had other biological effects that were not tested here, but this does not exclude the possibility that stimulation of non-Phox2b^{LC} neurons increases basal ventilation.

Interestingly, gain-of-function experiments indicate that in conscious mice, chemogenetic stimulation of either Phox2b^{LC} here, or Phox2b-expressing NTS neurons in our recent study [10], considerably increased basal ventilation *via* an RF increase, consistent with the prior report

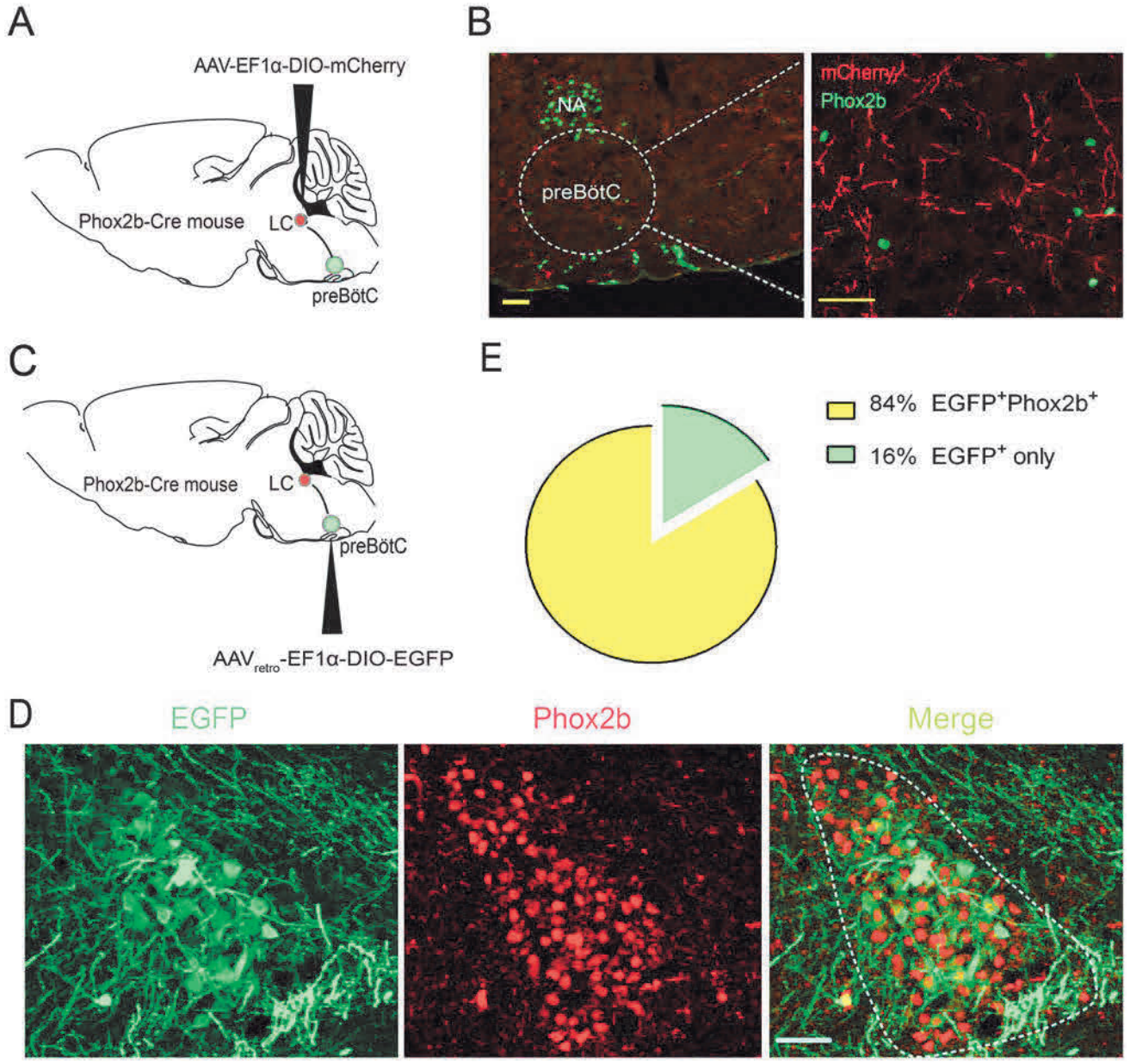

Fig. 8 Projection of Phox2b^{LC} neurons to the preBötC. **A** Schematic of anterograde virus injection into the LC of Phox2b-Cre mice. **B** Photomicrographs showing that mCherry-labeled axons of Phox2b^{LC} neurons project to the preBötC region. Left: dashed line, contour of the preBötC; right: enlarged image showing Phox2b-labeled NA and RTN neurons (green). Scale bars, 50 μm. **C** Schematic of retrograde virus injection into the preBötC in Phox2b-Cre mice. **D** Confocal images showing the cell bodies of EGFP-expressing neurons in the LC, most of which are Phox2b^{+}. **E** Cell counts showing that > 84% of EGFP neurons (n = 9 mice) projecting to the preBötC are Phox2b^{+} (scale bars, 50 μm).

demonstrating that RF is dramatically increased by photostimulation of Phox2b-expressing hindbrain neurons in a neonatal hindbrain–spinal cord preparation [32]. In these experiments, the basal MV increased *via* RF rather than TV, reflecting that at rest the RF appears to be the initial factor of respiratory mobilization, in line with the concept that the mobilization of RF is least costly in humans at rest [33]. Actually, the breathing pattern at rest has evolved to be a very economical mechanism, producing adequate ventilation at minimal cost. It has also been proposed that metabolic/chemical stimuli (e.g. hypercapnia and hypoxia) normally result in an increase in both RF and TV [34], as also supported by our present and prior findings [10, 11]. Although some studies have proposed the concept of differential control of RF and TV when challenged by different stressors [35], the underlying mechanism remains to be thoroughly investigated.

Ablation of Phox2b^{LC} Neurons Reduces the HCVR

The central respiratory chemoreflex is a crucial homeostatic mechanism to maintain normal blood gases [36]. Several studies have shown that the LC contains chemosensitive neurons that are recruited to mediate the ventilatory response to CO_2/H^+ [3, 23, 37]. For instance, proportional lesioning of LC noradrenergic neurons significantly blunts the HCVR *via* either a reduced TV [15] or RF [16]. Similar to these studies, our findings also demonstrated that selective lesioning of Phox2b^{LC} neurons, a subgroup of LC noradrenergic neurons, markedly attenuated the HCVR, primarily *via* a decreased TV. In addition, when destroying Phox2b-expressing neurons from any of the RTN, NTS, and LC, the HCVR was significantly reduced, strongly suggesting that a subgroup or most of the Phox2b-expressing neurons in these three regions are central chemoreceptor. Moreover, the basal ventilation remained unchanged, suggesting that when the central respiratory chemoreceptors from any of the RTN, NTS and LC were chemically or genetically lesioned, the remaining two centers most likely were able to compensate for the impaired respiratory function.

The HCVR largely relies on the normal function of central respiratory chemoreceptors. The molecular CO_2/H^+ sensors of central respiratory chemoreceptors differ in different brainstem regions. In the RTN, Phox2b-expressing neurons regulate breathing *via* recruiting TASK-2 channels and G-protein-coupled receptor 4 to sense the pH change [38]. In the NTS, acid-sensitive ion channels and background K^+ channels are suggested to mediate the pH-sensitive responses of Phox2b-expressing neurons *in vitro* [11]. Several studies have proposed that the chemosensitivity of LC neurons is mediated by different ion channels, including large conductance Ca^{2+}-activated K^+ channels [39], 4-aminopyridine-sensitive channels [40], and L-type Ca^{2+} channels [41]. In the present study, a small proportion of Phox2b^{LC} neurons was activated by CO_2, in support of the contribution of these neurons to the HCVR. However, we did not provide the ionic mechanism underlying the CO_2 sensitivity of Phox2b^{LC} neurons. Note that the pH-sensitive Phox2b^{LC} neurons may not contribute to the HCVR. Although the overwhelming number of LC neurons are TH-positive, actually these neurons may belong to different subsets that are responsible for different physiological functions.

The LC–preBötC Pathway

Metabolic regulation of breathing is mainly dependent on respiratory chemoreceptors, which are important for maintaining O_2 and CO_2 homeostasis, particularly during sleep [3, 42]. It has been proposed that central respiratory chemoreceptors provide an excitatory drive for the rCPG that is responsible for generating the eupneic rhythm. For example, the preBötC has been shown to receive direct synaptic transmission from RTN and NTS neurons [27, 43]; moreover, LC neurons have extensive connections with breathing-related brain regions, such as the NTS [44], parabrachial nucleus [45], and dorsal raphe nuclei [46], as well as the preBötC [13]. In the present study, we revealed the anatomical and functional relationships between Phox2b^{LC} neurons and the preBötC. Anatomically, both anterograde and retrograde viral tracing supported the conclusion that there is a direct projection of Phox2b^{LC} neurons to the preBötC. Functionally, stimulation of Phox2b^{LC} neurons enhanced the activity of putative preBötC neurons according to cFos analysis. Note that in the present study, cFos-labeled neurons in the preBötC region were anatomically defined. These neurons may not be responsible for the inspiratory rhythm and need to be functionally identified using *in vivo* or *in vitro* electrophysiological approaches. In addition, due to a lack of adequately specific markers of the breathing-related preBötC neurons, only cFos labeling was used here. These results reveal a circuit mechanism of the present gain-of-function and loss-of-function outcomes.

The LC has been implicated in attention, arousal, and panic/anxiety, and LC neuronal activity is highly state-dependent [47]. Taking these into account, some portion of the effect of Phox2b^{LC} neuron stimulation on ventilatory responses may well be directly through the LC-preBötC pathway, but another portion probably resulted from the consequence of behavioral arousal, suggesting an additive respiratory effect. In addition, exposure to CO_2 may not only increase pulmonary ventilation but also generate hypercapnia-elicited arousal [48] and a robust fear response in terms of behavior in mice, and panic symptom ratings in healthy volunteers and panic disorder patients [49]. Hence, some portion of the effect of ablation of Phox2b^{LC} neurons on the HCVR may be ascribed to the reduced respiratory drive to the preBötC due to the loss of pH-sensitive LC neurons, but another portion is likely due to the inhibition of hypercapnia-induced behavioral arousal or fear/panic. Based on the above analysis, in addition to the proposed LC–preBötC pathway to interpret the present results, other possible circuit mechanisms remain to be revealed.

Clinical Relevance and Conclusion

Heterozygous mutation of Phox2b is the leading cause of CCHS. One of the most important issues is to address the physiological role of Phox2b-containing cells. Interestingly, selective stimulation of Phox2b-expressing neurons from the RTN, NTS, and LC activates breathing in both

conscious and anesthetized mice, while ablation of these neurons significantly attenuates the central respiratory chemoreflex. These results shed light on the etiological mechanism underlying CCHS, and meanwhile provide central targets for potential clinical intervention. On the other hand, in addition to sustaining life, breathing may influence high-order behavior and thinking. For example, the LC–preBötC pathway contributes to the regulation of calm and arousal behaviors [13]. The present findings suggest that the effect of LC on breathing may also influence high-order behavior, but this awaits to be addressed.

In summary, the present study reveals that chemogenetic stimulation of $Phox2b^{LC}$ neurons increases basal pulmonary ventilation. In addition, a group of these neurons are required for the HCVR. The LC–preBötC pathway, as a circuit mechanism, is responsible for the control of breathing by $Phox2b^{LC}$ neurons. These findings help to better understand the pathogenic mechanisms underlying sleep-related hypoventilation or apnea.

Acknowledgements This work was supported by the National Natural Science Foundation of China (31971058 and 31571174), and the Youth Fund for Scientific and Technological Research in Higher Education Institutions of Hebei Province (QN2019019) and the Youth Science and Technology Talent Support Program of Natural Science in Hebei Medical University (CYQD201907).

Conflict of interest The authors claim that there are no conflicts of interest.

References

1. Zaidi S, Gandhi J, Vatsia S, Smith NL, Khan SA. Congenital central hypoventilation syndrome: An overview of etiopathogenesis, associated pathologies, clinical presentation, and management. Auton Neurosci 2018, 210: 1–9.
2. Moreira TS, Takakura AC, Czeisler C, Otero JJ. Respiratory and autonomic dysfunction in congenital central hypoventilation syndrome. J Neurophysiol 2016, 116: 742–752.
3. Guyenet PG, Stornetta RL, Bayliss DA. Central respiratory chemoreception. J Comp Neurol 2010, 518: 3883–3906.
4. Ramanantsoa N, Gallego J. Congenital central hypoventilation syndrome. Respir Physiol Neurobiol 2013, 189: 272–279.
5. Hernandez-Miranda LR, Ibrahim DM, Ruffault PL, Larrosa M, Balueva K, Muller T, *et al.* Mutation in LBX1/Lbx1 precludes transcription factor cooperativity and causes congenital hypoventilation in humans and mice. Proc Natl Acad Sci U S A 2018, 115: 13021–13026.
6. Pattyn A, Morin X, Cremer H, Goridis C, Brunet JF. The homeobox gene Phox2b is essential for the development of autonomic neural crest derivatives. Nature 1999, 399: 366–370.
7. Abbott SB, Stornetta RL, Fortuna MG, Depuy SD, West GH, Harris TE, *et al.* Photostimulation of retrotrapezoid nucleus phox2b-expressing neurons *in vivo* produces long-lasting activation of breathing in rats. J Neurosci 2009, 29: 5806–5819.
8. Takakura AC, Moreira TS, Stornetta RL, West GH, Gwilt JM, Guyenet PG. Selective lesion of retrotrapezoid Phox2b-expressing neurons raises the apnoeic threshold in rats. J Physiol 2008, 586: 2975–2991.
9. Wang S, Shi Y, Shu S, Guyenet PG, Bayliss DA. Phox2b-expressing retrotrapezoid neurons are intrinsically responsive to H^+ and CO_2. J Neurosci 2013, 33: 7756–7761.
10. Fu C, Shi L, Wei Z, Yu H, Hao Y, Tian Y, *et al.* Activation of Phox2b-expressing neurons in the nucleus tractus solitarii drives breathing in mice. J Neurosci 2019, 39: 2837–2846.
11. Fu C, Xue J, Wang R, Chen J, Ma L, Liu Y, *et al.* Chemosensitive Phox2b-expressing neurons are crucial for hypercapnic ventilatory response in the nucleus tractus solitarius. J Physiol 2017, 595: 4973–4989.
12. Carter ME, Yizhar O, Chikahisa S, Nguyen H, Adamantidis A, Nishino S, *et al.* Tuning arousal with optogenetic modulation of locus coeruleus neurons. Nat Neurosci 2010, 13: 1526–1533.
13. Yackle K, Schwarz LA, Kam K, Sorokin JM, Huguenard JR, Feldman JL, *et al.* Breathing control center neurons that promote arousal in mice. Science 2017, 355: 1411–1415.
14. Li L, Feng X, Zhou Z, Zhang H, Shi Q, Lei Z, *et al.* Stress accelerates defensive responses to looming in mice and involves a locus coeruleus-superior colliculus projection. Curr Biol 2018, 28: 859–871.e855.
15. Biancardi V, Bicego KC, Almeida MC, Gargaglioni LH. Locus coeruleus noradrenergic neurons and CO_2 drive to breathing. Pflugers Arch 2008, 455: 1119–1128.
16. Li A, Nattie E. Catecholamine neurones in rats modulate sleep, breathing, central chemoreception and breathing variability. J Physiol 2006, 570: 385–396.
17. Nobuta H, Cilio MR, Danhaive O, Tsai HH, Tupal S, Chang SM, *et al.* Dysregulation of locus coeruleus development in congenital central hypoventilation syndrome. Acta Neuropathol 2015, 130: 171–183.
18. Harper RM, Kumar R, Macey PM, Harper RK, Ogren JA. Impaired neural structure and function contributing to autonomic symptoms in congenital central hypoventilation syndrome. Front Neurosci 2015, 9: 415.
19. Paxinos G, Watson G. The Mouse Brain in Stereotaxic Coordinates. 2th ed. San Diego: Academic Press, 2001:124–129.
20. Berridge CW, Waterhouse BD. The locus coeruleus-noradrenergic system: modulation of behavioral state and state-dependent cognitive processes. Brain Res Brain Res Rev 2003, 42: 33–84.
21. Lazarenko RM, Milner TA, Depuy SD, Stornetta RL, West GH, Kievits JA, *et al.* Acid sensitivity and ultrastructure of the retrotrapezoid nucleus in Phox2b-EGFP transgenic mice. J Comp Neurol 2009, 517: 69–86.
22. Gomez JL, Bonaventura J, Lesniak W, Mathews WB, Sysa-Shah P, Rodriguez LA, *et al.* Chemogenetics revealed: DREADD occupancy and activation *via* converted clozapine. Science 2017, 357: 503–507.
23. Gargaglioni LH, Hartzler LK, Putnam RW. The locus coeruleus and central chemosensitivity. Respir Physiol Neurobiol 2010, 173: 264–273.
24. Zhao Z, Wang L, Gao W, Hu F, Zhang J, Ren Y, *et al.* A central catecholaminergic circuit controls blood glucose levels during stress. Neuron 2017, 95: 138–152 e5.
25. Del Negro CA, Funk GD, Feldman JL. Breathing matters. Nat Rev Neurosci 2018, 19: 351–367.
26. Guyenet PG. Regulation of breathing and autonomic outflows by chemoreceptors. Compr Physiol 2014, 4: 1511–1562.
27. Feldman JL, Del Negro CA, Gray PA. Understanding the rhythm of breathing: so near, yet so far. Annu Rev Physiol 2013, 75: 423–452.
28. Zhao F, Jiang HF, Zeng WB, Shu Y, Luo MH, Duan S. Anterograde trans-synaptic tagging mediated by adeno-associated virus. Neurosci Bull 2017, 33: 348–350.

29. Fan Y, Chen P, Raza MU, Szebeni A, Szebeni K, Ordway GA, *et al.* Altered expression of Phox2 transcription factors in the locus coeruleus in major depressive disorder mimicked by chronic stress and corticosterone treatment *in vivo* and *in vitro*. Neuroscience 2018, 393: 123–137.
30. Kang BJ, Chang DA, Mackay DD, West GH, Moreira TS, Takakura AC, *et al.* Central nervous system distribution of the transcription factor Phox2b in the adult rat. J Comp Neurol 2007, 503: 627–641.
31. Fan Y, Huang J, Duffourc M, Kao RL, Ordway GA, Huang R, *et al.* Transcription factor Phox2 upregulates expression of norepinephrine transporter and dopamine beta-hydroxylase in adult rat brains. Neuroscience 2011, 192: 37–53.
32. Cregg JM, Chu KA, Dick TE, Landmesser LT, Silver J. Phasic inhibition as a mechanism for generation of rapid respiratory rhythms. Proc Natl Acad Sci U S A 2017, 114: 12815–12820.
33. Mead J. The control of respiratory frequency. Ann N Y Acad Sci 1963, 109: 724–729.
34. Nicolo A, Girardi M, Sacchetti M. Control of the depth and rate of breathing: metabolic vs. non-metabolic inputs. J Physiol 2017, 595: 6363–6364.
35. Tipton MJ, Harper A, Paton JFR, Costello JT. The human ventilatory response to stress: rate or depth? J Physiol 2017, 595: 5729–5752.
36. Guyenet PG, Bayliss DA. Neural control of breathing and CO_2 homeostasis. Neuron 2015, 87: 946–961.
37. Haxhiu MA, Yung K, Erokwu B, Cherniack NS. CO_2-induced c-fos expression in the CNS catecholaminergic neurons. Respir Physiol 1996, 105: 35–45.
38. Kumar NN, Velic A, Soliz J, Shi Y, Li K, Wang S, *et al.* PHYSIOLOGY. Regulation of breathing by CO_2 requires the proton-activated receptor GPR4 in retrotrapezoid nucleus neurons. Science 2015, 348: 1255–1260.
39. Imber AN, Patrone LGA, Li KY, Gargaglioni LH, Putnam RW. The role of Ca^{2+} and BK channels of locus coeruleus (LC) neurons as a brake to the CO_2 chemosensitivity response of rats. Neuroscience 2018, 381: 59–78.
40. Li KY, Putnam RW. Transient outwardly rectifying A currents are involved in the firing rate response to altered CO_2 in chemosensitive locus coeruleus neurons from neonatal rats. Am J Physiol Regul Integr Comp Physiol 2013, 305: R780–792.
41. Imber AN, Putnam RW. Postnatal development and activation of L-type Ca^{2+} currents in locus ceruleus neurons: implications for a role for Ca^{2+} in central chemosensitivity. J Appl Physiol (1985) 2012, 112: 1715–1726.
42. He C, Hu Z. Homeostasis of synapses: Expansion during wakefulness, contraction during sleep. Neurosci Bull 2017, 33: 359–360.
43. Li P, Janczewski WA, Yackle K, Kam K, Pagliardini S, Krasnow MA, *et al.* The peptidergic control circuit for sighing. Nature 2016, 530: 293–297.
44. Lopes LT, Patrone LG, Li KY, Imber AN, Graham CD, Gargaglioni LH, *et al.* Anatomical and functional connections between the locus coeruleus and the nucleus tractus solitarius in neonatal rats. Neuroscience 2016, 324: 446–468.
45. Arima Y, Yokota S, Fujitani M. Lateral parabrachial neurons innervate orexin neurons projecting to brainstem arousal areas in the rat. Sci Rep 2019, 9: 2830.
46. Uribe-Marino A, Angelica Castiblanco-Urbina M, Luciano Falconi-Sobrinho L, Dos Anjos-Garcia T, de Oliveira RC, Mendes-Gomes J, *et al.* The alpha- and beta-noradrenergic receptors blockade in the dorsal raphe nucleus impairs the panic-like response elaborated by medial hypothalamus neurons. Brain Res 2019: 146468.
47. Aston-Jones G, Bloom FE. Activity of norepinephrine-containing locus coeruleus neurons in behaving rats anticipates fluctuations in the sleep-waking cycle. J Neurosci 1981, 1: 876–886.
48. Aston-Jones G, Cohen JD. An integrative theory of locus coeruleus-norepinephrine function: adaptive gain and optimal performance. Annu Rev Neurosci 2005, 28: 403–450.
49. Leibold NK, van den Hove DL, Viechtbauer W, Buchanan GF, Goossens L, Lange I, *et al.* CO_2 exposure as translational cross-species experimental model for panic. Transl Psychiatry 2016, 6: e885.

Neurosci. Bull. January, 2021, 37(1):45–54
https://doi.org/10.1007/s12264-020-00577-5

www.neurosci.cn
www.springer.com/12264

ORIGINAL ARTICLE

Cutaneous Hypersensitivity as an Indicator of Visceral Inflammation *via* C-Nociceptor Axon Bifurcation

Yehong Fang[1,3] · Shu Han[2] · Xiaoxue Li[2] · Yikuan Xie[1,3] · Bing Zhu[2] · Xinyan Gao[2] · Chao Ma[1,3]

Received: 5 January 2020 / Accepted: 19 May 2020 / Published online: 9 September 2020

Abstract Pain on the body surface can accompany disorders in the deep tissue or internal organs. However, the anatomical and physiological mechanisms are obscure. Here, we provided direct evidence of axon bifurcation in primary C-nociceptive neurons that innervate both the skin and a visceral organ. Double-labeled dorsal root ganglion (DRG) neurons and Evans blue extravasation were observed in 3 types of chemically-induced visceral inflammation (colitis, urocystitis, and acute gastritis) rat models. In the colitis model, mechanical hypersensitivity and spontaneous activity were recorded *in vivo* from double-labeled C-nociceptive neurons in S1 or L6 DRGs. These neurons showed significantly enhanced responses to both somatic stimulation and colorectal distension. Our findings suggest that the branching of C-nociceptor axons contribute to cutaneous hypersensitivity in visceral inflammation. Cutaneous hypersensitivity on certain locations of the body surface might serve as an indicator of pathological conditions in the corresponding visceral organ.

Keywords Visceral inflammation · Cutaneous hypersensitivity · Axon bifurcation · C-nociceptor

Introduction

Visceral pain, involving thoracic, abdominal, and pelvic organs, is the most common type of chronic pain nowadays [1–3]. However, the poor understanding of its pathogenesis makes it difficult to manage. It is well recognized that visceral innervation is complex. Organs in the thoracic and abdominal cavities may be innervated by both the vagal and spinal nerves with central terminals in the brainstem and spinal cord, respectively. Meanwhile, some pelvic organs are innervated by the pelvic nerves, which terminate in the lumbosacral spinal cord [4, 5]. Unlike cutaneous pain that is well localized, visceral pain is diffuse and often referred to a distal superficial location [4, 6]. Therefore, it is necessary to find an indicator to help detect and locate visceral pain in order to treat visceral diseases better.

Previous studies indicated that virtually all second-order spinal dorsal horn neurons, like wide dynamic range neurons, receive both visceral and convergent somatic (non-visceral) input [7, 8]. Such viscerosomatic convergence onto second-order spinal neurons has long been considered the underlying structural basis for pain in somatic sites. *In vivo* animal studies, including single-fiber recordings and spinal extracellular recordings, have revealed that visceral nociceptors (mainly mechanoreceptors) can be sensitized by inflammation and the mediated pain can be relieved by nociceptive stimulation of the skin [9, 10]. However, these findings do not negate the

Yehong Fang, Shu Han and Xiaoxue Li have contributed equally to this work.

✉ Xinyan Gao
gaoxy@mail.cintcm.ac.cn

✉ Chao Ma
machao@ibms.cams.cn

[1] Institute of Basic Medical Sciences, Department of Human Anatomy, Histology and Embryology, Neuroscience Center, Chinese Academy of Medical Sciences, School of Basic Medicine, Peking Union Medical College, Beijing 100005, China

[2] Department of Physiology, Institute of Acupuncture and Moxibustion, China Academy of Chinese Medical Sciences, Beijing 100700, China

[3] Joint Laboratory of Anesthesia and Pain, Peking Union Medical College, Beijing 100730, China

possibility that DRG neurons also play a role in visceral inflammation and the referred visceral sensation.

The bifurcation and sensory convergence of DRG neurons have been described in various studies [11–13]. Electrophysiological recordings from DRG neurons showed that some responded to both somatic and visceral stimulation [4], suggesting the bifurcation of primary sensory axons. In this study, we provide direct evidence that the double-labeled DRG neurons innervate both the visceral organs and skin, and used *in vivo* electrophysiology and Evans blue extravasation to confirm that cutaneous hypersensitivity can be used as an indicator of visceral inflammation *via* C-nociceptive sensory axon bifurcation.

Methods

Animal

Adult female Sprague-Dawley rats (specific pathogen free, 180 g–220 g, provided by the National Institutes for Food and Drug Control, China) were used. Room temperature was maintained at 23 ± 2 °C, with 50%–65% relative humidity. Rats were kept on a 12 h light/12 h dark cycle with free access to food and water. All animal experiments were approved by the Institutional Animal Care and Use Committee in the Chinese Academy of Medical Sciences, Institute of Basic Medical Sciences (Approval Number#211-2014).

Animal Models

Colitis: The rat model (n = 52) of intestinal inflammation was established based on previous reports [14, 15]. Briefly, under general anesthesia (sodium pentobarbital, 50 mg/kg, i.p.; Sigma Aldrich, St. Louis, MO, USA), 100 mg/kg 2,4,6-trinitro benzene sulfonic acid (TNBS; P2297, Sigma Aldrich) dissolved in 50% ethanol were instilled into the rectum, while the control group received vehicle (50% ethanol) only. Rats showed signs of cutaneous mechanical hypersensitivity starting from day 1 after drug administration (Fig. 3J).

Urocystitis: The urocystitis model (n = 9) was established as previously reported [16], 300 μL of 1.5% H_2O_2 (Beijing Chemical Works, China) solution diluted in sterile saline was introduced into the bladder through the urethra *via* a polyethylene tube (PE-50), and kept for 30 min. Then the H_2O_2 solution was drained from the bladder by pressing the lower abdomen. The control group received 300 μL of sterile saline. Rats showed signs of cutaneous mechanical hypersensitivity starting from day 1 after drug administration (Fig. 3K).

Gastritis: The acute gastritis rat model (n = 11) was induced by intragastric administration of 1 mL of solution containing 60% ethanol plus 150 mmol/L HCL (inducer) as in a previous study [17].The control group received 1 mL sterile saline. Rats showed signs of cutaneous mechanical hypersensitivity starting from 30 min after drug administration (Fig. 3L).

All rats were examined by histological analysis. Distal colonic, vesical, and gastric tissues were harvested and stained with hematoxylin and eosin (H&E). Histopathological examination was performed with a light microscope (FV1000, Olympus, Tokyo, Japan). Tissue edema and mucosal epithelium with inflammatory cell infiltration indicated the successful establishment of rat models of visceral inflammation [18–20].

Fluorescent Labeling

Nine rats were used in this experiment. Under anesthesia, the muscular layer of the distal colon, urinary bladder, and stomach were each injected with 20 μL of the lipophilic tracer 1,1′-dioctadecyl-3,3,3′,3′-tetrame-thylindocarbocyanine perchlorate (DiI, 200 μg/mL, Sigma Aldrich) without evident DiI leakage. After 3 days, 15 μL of the B subunit of cholera toxin Alexa Fluor 488 (CTB-488, C-34775, Molecular Probes, Eugene, USA) was injected into the skin once at multiple sides around the root of the tail and back area (thoracic segments). One week later, under pentobarbital anesthesia (50 mg/kg, i.p.), the rats were transcardially perfused with PBS followed by 4% paraformaldehyde, then DRGs in the thoracic, lumbar, and sacral segments were harvested, post-fixed for 12 h, and cryoprotected in 30% sucrose overnight. The tissue was frozen and sectioned at 13 μm on a cryostat. We cut sections at 20 μm intervals and ultimately obtained ∼20 slices for each DRG. Then the sections were cover-slipped with Vectashield mounting medium with DAPI (Vector Laboratories, Burlingame, CA, USA) followed by examination under a fluorescence microscope (FV1000 and Olympus FluoView software; Olympus, Tokyo, Japan).

Evans Blue Extravasation

Evans blue extravasation was applied after establishing the colitis (n = 3), urocystitis (n = 3), and gastritis (n = 3) models. Briefly, under anesthesia (sodium pentobarbital, 50 mg/kg, i.p.), rats were slowly injected with 2 mL Evans blue (1%, Sigma Aldrich) into the caudal vein and perfused transcardially with 0.1 mol/L phosphate-buffered saline 30 min later. Finally, images of corresponding local skin of each rat were collected after depilation.

Assessment of Mechanical Pain Threshold in the Skin of Rats

Rats with colitis (n = 8), urocystitis (n = 6), and gastritis (n = 8) were used. Before all tests, rats were placed in a homemade square (20 cm × 10 cm) stainless-steel cage to habituate for 2 days and the hair was removed (root of the tail for colitis and urocystitis rats and thoracic back skin for gastritis rats). Habituation for 30 min was allowed before each test. The average threshold at –2 days and –1 day was defined as baseline. A calibrated electronic von Frey filament (Electronic von Frey 2390-5 Aesthesiometer; IITC Life Science, Woodland Hills, CA, USA) was applied to measure the mechanical threshold of each rat at different time points. The average of three repeated measurements was taken as the final threshold.

In Vivo Electrophysiological Recording

In vivo extracellular electrophysiological recordings of double-labeled (labeled by both DiI and CTB-488) L6 or S1 DRG neurons were performed in both normal (n = 10) and colitis (n = 15) rats. Specific surgical details and recording procedures were as previously reported [21, 22]. Briefly, rats were anesthetized with pentobarbital sodium (initial dose of 50 mg/kg i.p. followed by supplementary doses of 20 mg/kg as needed), the L6-S1 transverse process was removed, and a laminectomy was made from L5 to S2 to expose the S1 or L6 DRG. During surgery, oxygenated artificial cerebrospinal fluid (ACSF) at 35 °C was dripped onto the surface of the DRG, and then the perineurium and epineurium were carefully removed under a dissecting microscope. After the rat was transferred to the recording platform, a pool was made by attaching the skin to a metal ring and filling it with ACSF. Action potentials were

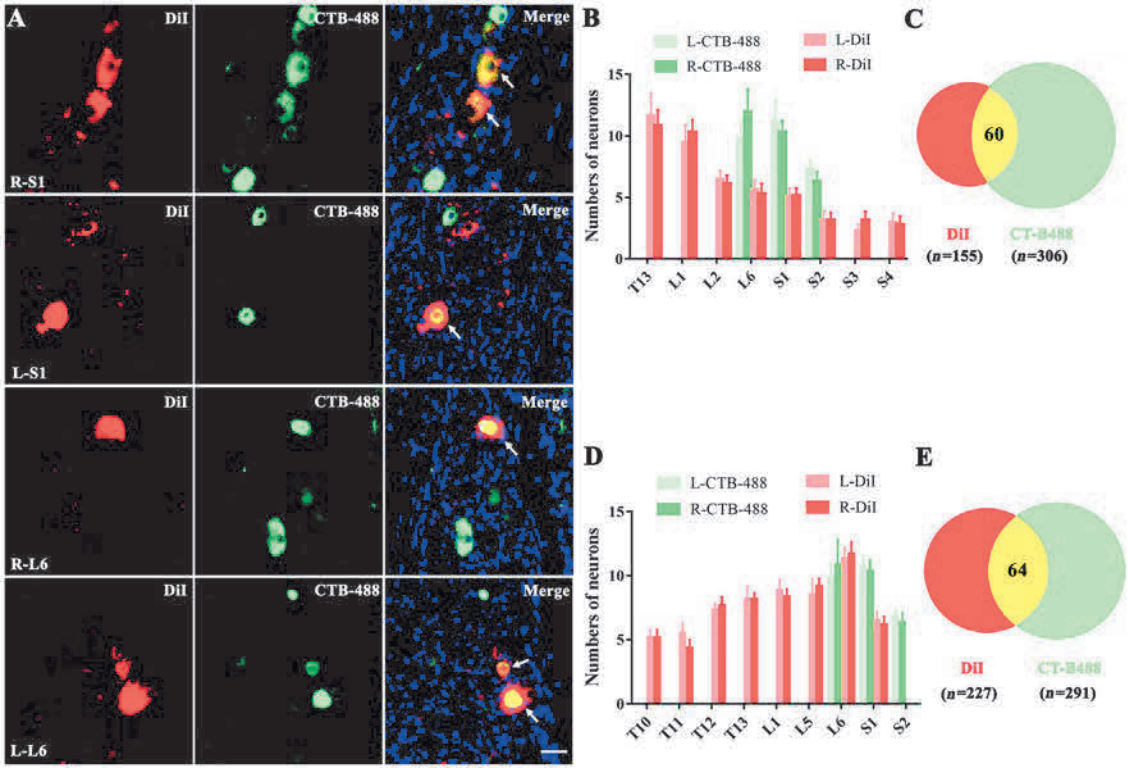

Fig. 1 Retrogradely labeled primary sensory neurons in dorsal root ganglia (DRGs) innervating both skin and distal colon/urinary bladder. **A** Representative images of sensory neurons in bilateral L6 and S1 DRGs after injection of DiI in the distal colon and CTB-488 in the skin around the root of the tail [red, DiI-positive colon afferent fibers; green, CTB-positive skin afferent fibers; yellow, double-labeled cells (white arrows); scale bar, 25 μm; CTB-488, cholera toxin subunit B (recombinant) Alexa Fluor 488; DiI, 1,1′-dioctadecyl-3,3,3′,3′-tetrame-thylindocar bocyanine perchlorate]. **B** Bar graph of the number of neurons labeled by DiI (distal colon) and CTB-488 (skin around the root of the tail) in bilateral T13, L1, L2, L6, and S1–S4 DRGs (T, thoracic; L, lumbar; S, sacral). **C** The Venn diagram showing the total number of DiI-labeled (red), CTB-488-labeled (green), and double-labeled (yellow) neurons in all DRGs (18 DRGs from 3 rats). **D** Numbers of neurons labeled by DiI (urinary bladder) and CTB-488 (skin around the root of the tail) in bilateral T10–13, L1, L5–6, and S1–2 DRGs. **E** Venn diagram showing the total number of DiI-labeled (red), CTB-488-labeled (green), and double-labeled (yellow) neurons in all DRGs (16 DRGs from 3 rats).

recorded extracellularly using a Multiclamp 700B amplifier (Molecular Devices, Sunnyvale, CA, USA) and Digidata 1440A (Molecular Devices, Sunnyvale, CA, USA).

To ensure that recorded neurons innervated both the inner colon and skin, we chose DiI-labeled neurons (under a fluorescence microscope) that responded to both distal colonic distension and nociceptive stimuli to the cutaneous receptive field. Axonal conduction velocity (CV) was determined by dividing the distance between the receptive field and the cell body by the latency of the action potential. A C-neuron was identified by a CV <2 m/s. The cutaneous receptive filed (RF) was identified by exploring the skin at the root of the tail using a handheld glass probe. Then various handheld stimuli were applied: cotton swab (for innocuous mechanical stimuli) and a von Frey filament with a fixed tip diameter (200 μm). For cutaneous and inner colonic stimuli, von Frey filaments were applied to the corresponding receptive field for 3 s at different forces (5 mN, 10 mN, 30 mN, and 50 mN) and the balloon in the distal colon was inflated for 10 s to a series of pressures (20 mmHg, 40 mmHg, and 60 mmHg). Spontaneous activity (SA) was defined as continuous discharge of a DRG neuron lasting for 3 min without any external stimulus. Once SA was detected, a series of stimuli, including wiping with a Q-tip, pinching with forceps, poking with an acupuncture needle, and 0.3% capsaicin, were applied to the cutaneous RF or non-RF (defined as the skin within a circle 1 cm in diameter around the RF). Each recording continued for at least another 5 min.

Statistical Analysis

Data are presented as the mean ± SEM. Student's *t*-test was used to test the difference between two groups. Difference among multiple groups were tested by one-way analysis of variance (ANOVA) followed by the Bonferroni *post hoc* test. A statistically significant difference was defined as a two-sided P value < 0.05. SPSS software (version 21.0) was used for statistical analysis.

Results

Dorsal Root Ganglion Neurons Innervate Both Visceral Organs and Skin

DRG neurons were double-labeled by injecting the fluorescent dye DiI into visceral organs (distal colon, urinary bladder and stomach) and CTB-488 into the corresponding skin (root of tail and thoracic back area). In colonic (n = 3) and urocystic (n = 3) rats, double-labeled neurons were limited to bilateral L6, S1, and S2 DRGs (Fig. 1A). Therefore, L6 and S1 DRGs were chosen for recording the electrophysiological activity of double-labeled neurons. DiI-labeled neurons (distal colon) were found in T13, L1–2, L6, and S1–4 DRGs, while CTB-488-labeled neurons (skin around the root of tail) were found in L6, S1, and S2 DRGs. Meanwhile, DiI-positive neurons (urinary bladder injection) were in the T10–13, L1, L5–6, and S1 DRGs. The number of labeled neurons did not significantly differ between the left and right DRGs in the two models (Fig. 1B, D). In addition, statistical analysis indicated that no more than 6 double-labeled neurons

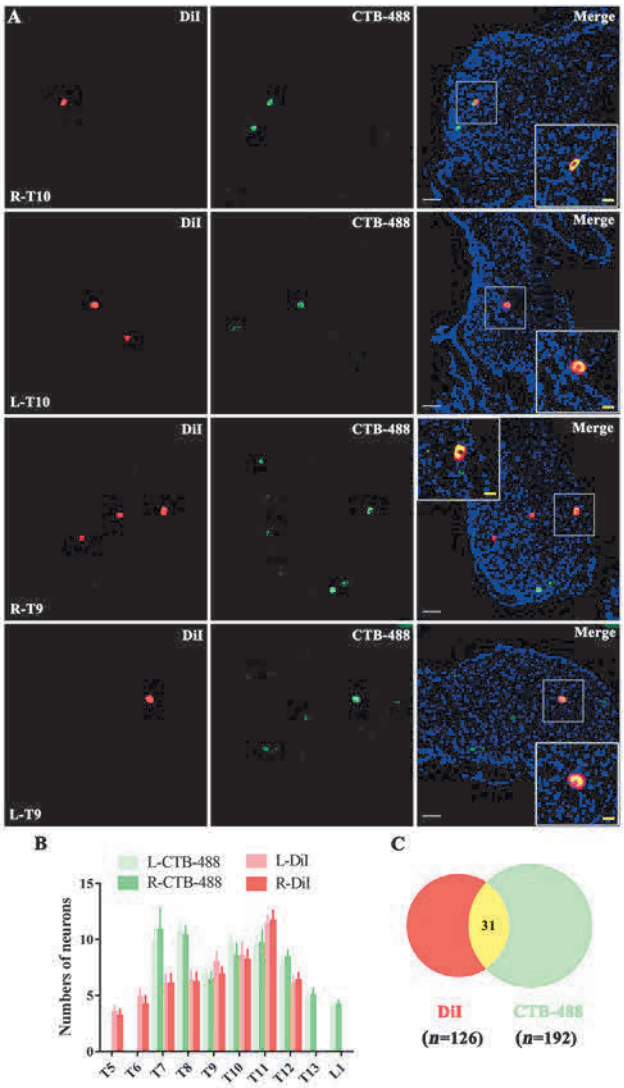

Fig. 2 Retrogradely labeled primary sensory neurons in DRGs innervating both skin and stomach. **A** Representative images of sensory neurons in bilateral T9 and T10 DRGs after injection of DiI into the stomach and CTB-488 into the thoracic back skin. Insets are higher magnification images. Scale bars, 100 μm (white); 25 μm (yellow). **B** Counts of DRG neurons labeled by DiI (stomach) and CTB-488 (back skin of thoracic segments) in bilateral T5–13 and L1 DRGs. **C** Venn diagram showing the total number of DiI-labeled (red), CTB-488-labeled (green), and double-labeled (yellow) neurons in all DRGs (30 DRGs from 3 rats).

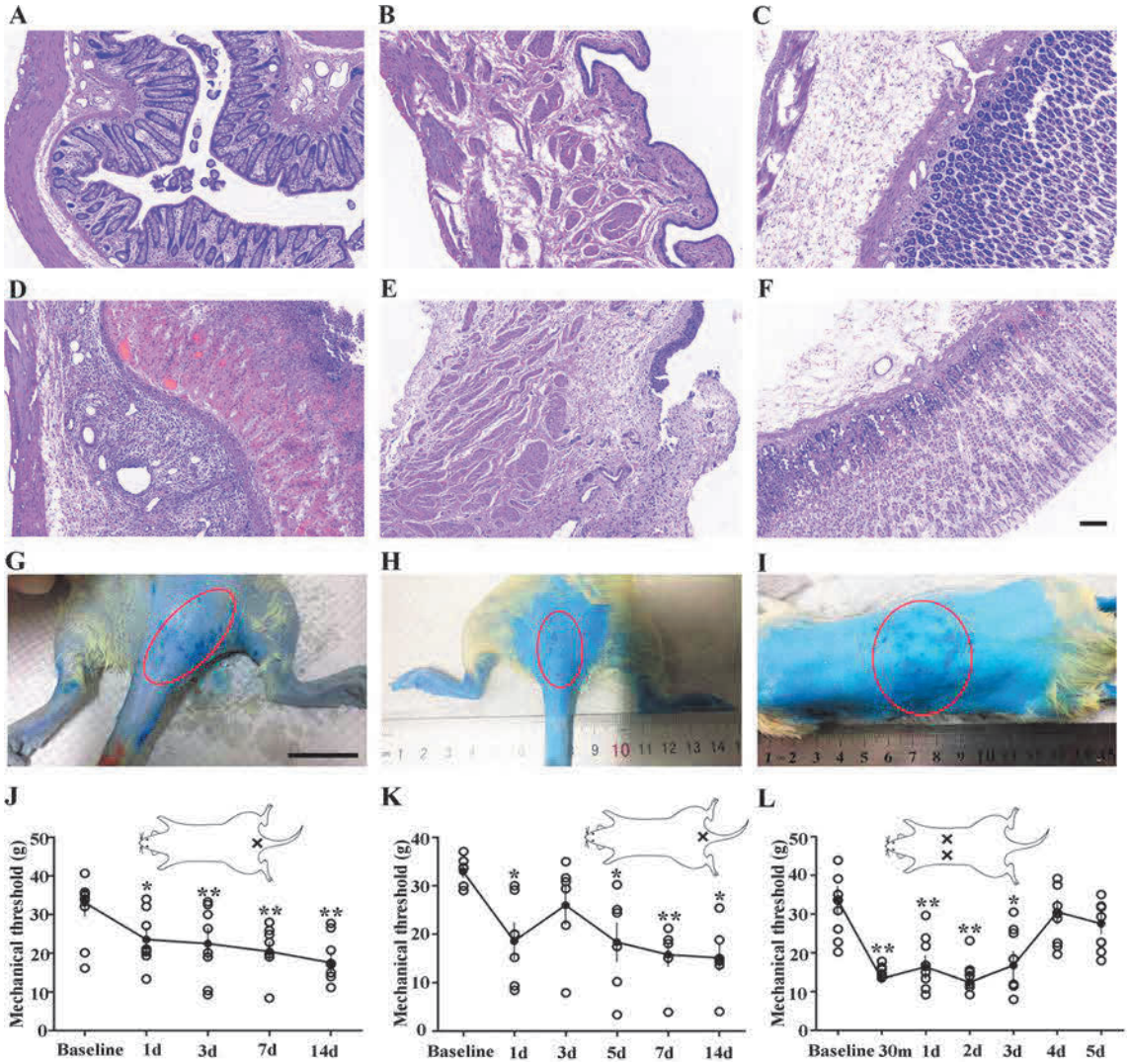

Fig. 3 Histological changes, Evans blue extravasation and mechanical pain assessment in rat models of colitis, urocystitis, and gastritis. **A–C** Representative microscopic images showing H&E staining in control tissue of distal colon, urinary bladder, and stomach. **D–F** Representative microscopic images showing H&E staining of distal colonic, vesical, and gastric tissue sections from rat models. Scale bars in A–F, 100 μm. **G** and **H** Representative images showing Evans blue extravasation (blue dots in red circles) mainly at the root of the tail in rats with both colitis ($n = 3$) and urocystitis ($n = 3$). Scale bar in G, 2 cm. **I** Massive Evans blue extravasation (blue dots in red circles) in the thoracic back skin of rats with gastritis ($n = 3$). **J–L** Mechanical hyperalgesia in rats with colitis ($n = 8$), urocystitis ($n = 6$), or gastritis ($n = 8$). **J** Mechanical threshold before (baseline) and at 1–14 days after intrarectal TNBS instillation. **K** Mechanical threshold before (baseline) and at 1–14 days after transurethral delivery of H_2O_2 into the bladder. **L** Mechanical threshold before (baseline) and 30 min to 5 days after intragastric administration of ethanol plus HCL. $^*P < 0.05$, $^{**}P < 0.01$ *vs.* baseline, Student's *t*-test.

(accounting for 0.08% of ~ 7000 neurons per DRG [23]) were found in each DRG either in colonic or urocystic rats. We found a total of 60 double-labeled neurons (from 18 DRGs) in 3 rats with colonic injection and 64 double-labeled neurons (from 16 DRGs) in 3 rats with urocystic injection (Fig. 1C, E). For the stomach ($n = 3$), DiI-labeled neurons were found in the T5–T12 DRGs while CTB-488-labeled neurons were found in the T7–13 and L1 DRGs. A total of 31 double-labeled neurons were found in the T7–11 DRGs, with no more than 3 neurons in each DRG (25 DRGs from 3 rats; Fig. 2A–C).

Colonic, Vesical, and Gastric Tissues in Rat Models

After intracolonic instillation of TNBS for 3–7 days, rats were emaciated (10% loss of body weight)and mortality was high (50%, 26 out of 52 survived) as reported previously [14]. Compared to H&E-staining of control tissue (Fig. 3A–C), an absence of part of the mucosal layer and inflammatory cell infiltration in the mucosal epithelium and muscular layer were observed in colonic tissue (Fig. 3D), while edema and inflammatory cell infiltration were observed in vesical tissue (Fig. 3E). In addition,

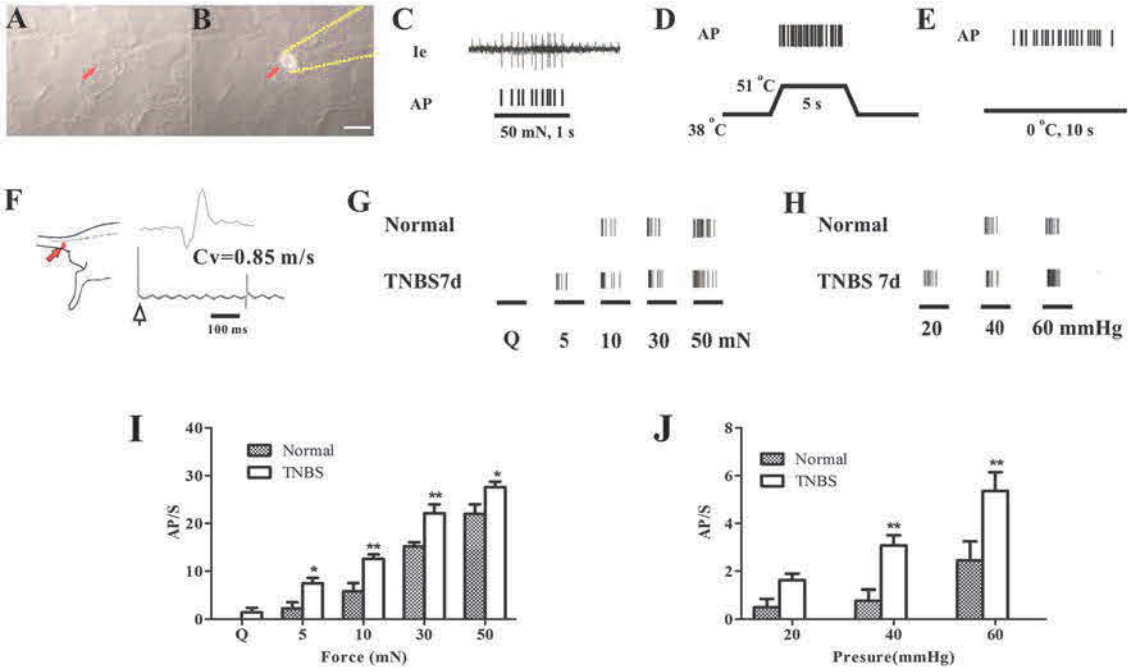

Fig. 4 Mechanical threshold of double-labeled C-nociceptive neurons in S1 and L6 DRGs from control and TNBS-treated rats. **A** Bright-field image of the surface of an S1 DRG; red arrow indicates a small neuron. **B** Fluorescence image of the same cell under recording by an extracellular glass electrode (orange dotted line). Scale bar for B and A, 20 μm. **C** Typical response of a double-labeled small neuron to 50 mN mechanical stimulation. Action potentials (APs) in the original recording (Ie) are indicated by corresponding tick marks below. **D** and **E** This neuron also responds to nociceptive warm (51 °C) and cold (0 °C) stimulation. **F**. Measurement of conduction velocity (CV) of recorded neuron by stimulation of the receptive field (RF, red arrow). **G** Responses of double-labeled C-nociceptive neurons to Q-tip wiping and von Frey filaments of several forces (5, 10 mN, 30 mN, and 50 mN) in control and TNBS-treated rats. **H** Responses of double-labeled C-nociceptive neurons to expansion of the distal colon by a balloon at several pressures (20 mmHg, 40 mmHg, and 60 mmHg) in control and TNBS-treated rats. **I** and **J**. Action potential discharge rate s (AP/s) of double-labeled C-nociceptive neurons evoked by mechanical stimulation (**I**) and balloon expansion (**J**) in control ($n = 6$) and TNBS-treated ($n = 7$) rats $^{*}P < 0.05$, $^{**}P < 0.01$, TNBS *vs.* normal group (**I** and **J**), one-way ANOVA with Bonferroni *post hoc* test.

intermittent rupture of the muscular layer and exuviation of urothelium were observed. Similar changes occurred in H&E-stained gastric tissue (Fig. 3F). The above results indicated that models of colitis, urocystitis, and gastritis had been successfully established.

Cutaneous Mechanical Hypersensitivity and Inflammation in the Model Rats

Cutaneous mechanical hypersensitivity and neuroinflammation have been described in animals with visceral pain [24, 25]. To confirm the location of sensitized areas on the skin, extravasation of Evans blue was performed. As Fig. 3G showed, Blue dots were observed in the skin at the root of the tail in rats with colitis, indicating the appearance of neuroinflammation in this site. And in rats with urocystitis, Evans blue was exuded at almost the same site around the root of the tail (Fig. 3H). Rats with gastritis provided the strongest evidence, with massive Evans blue extravasation on the thoracic back skin (Fig. 3I).

Mechanical hypersensitivity was assessed in the model rats (colitis, $n = 8$; urocystitis, $n = 6$; gastritis, $n = 8$). Compared to baseline, the cutaneous mechanical pain threshold of all the model rats declined significantly as early as 30 min after intervention and remained for up to 14 days in rats with colitis and urocystitis, and 3 days in those with gastritis (Fig. 3J–L).

In vivo electrophysiological recordings from the C-nociceptive neurons labeled with fluorescent dye showed RFs on both the skin and the colon. A total of 30 neurons were recorded from naïve rats ($n = 10$) and 32 from those with colitis ($n = 15$). These neurons showed significantly enhanced responses to expansion of the distal colon and mechanical, nociceptive, warm, or cold stimulation of the cutaneous RF (Fig. 4A–H), indicating both a cutaneous mechanical sensitization (5 mN, 2.20 ± 1.44 *vs.* 7.43 ± 1.13, $P < 0.05$; 10 mN, 5.80 ± 1.80 *vs.* 12.57 ± 0.98, $P < 0.01$; 30 mN, 15.20 ± 1.00 *vs.* 22.14 ± 1.89, $P < 0.01$; 50 mN, 22.00 ± 1.79 *vs.* 27.57 ± 1.20, $P < 0.05$, Fig. 4I) and visceral sensitization (40 mmHg, 3.08 ± 0.43 *vs.* 0.77 ±

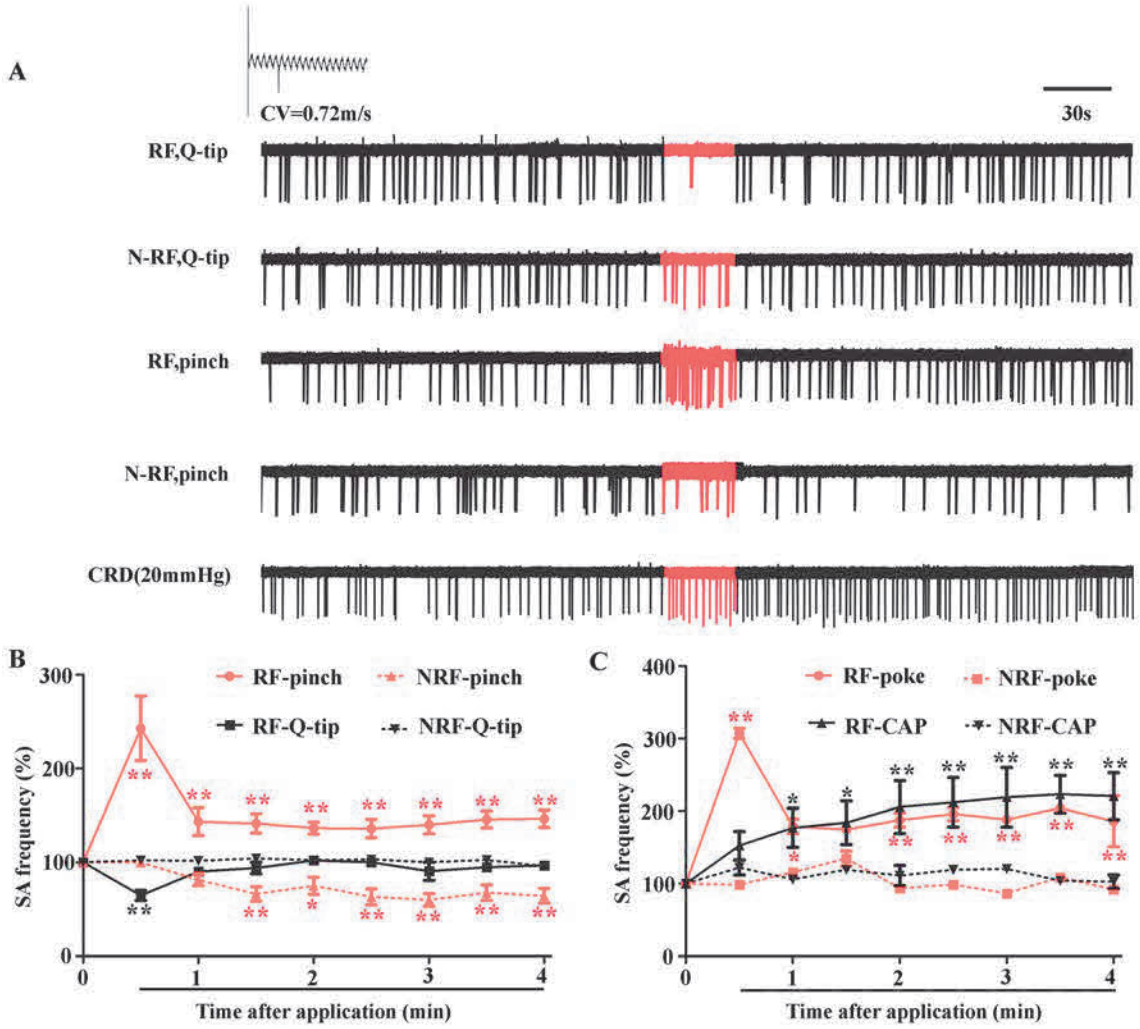

Fig. 5 Changes in spontaneous activity (SA) after different cutaneous stimuli in rat model of colitis. **A** An example of SA recorded in one S1 DRG neuron (conduction velocity, 0.72 m/s) changing with both non-nociceptive (Q-tip) and nociceptive (pinch) mechanical stimulation applied to both receptive field (RF) and non-RF areas (red, action potentials (APs) during 30-s stimulation). The neuron responds to both cutaneous stimulation and colorectal distention (CRD). **B** Quantification of SA frequency in L6 and S1 DRG neurons after application of a Q-tip ($n = 8$) and pinch ($n = 10$) to both RF and non-RF areas. Mean SA frequency within 3 min before application is defined as 100%. $^{*}P < 0.05$, $^{**}P < 0.01$, after application *vs* before application, one-way ANOVA. **C** Statistics of SA frequency after applying capsaicin (CAP, $n = 4$) and poking (poke, $n = 5$) to both RF and non-RF areas. $^{*}P < 0.05$, $^{**}P < 0.01$, after application *vs.* before application, one-way ANOVA.

0.46, $P < 0.01$; 60 mmHg, 5.36 ± 0.79 *vs.* 2.44 ± 0.80, $P < 0.01$, Fig. 4J).

Spontaneous Activity in Colitis Model and Changes After Diverse Cutaneous Stimulation

Spontaneous activity was recorded with an average frequency of 0.33 Hz (from 0.11 Hz to 0.55 Hz, data is not shown) in rats with colitis ($n = 15$), whereas no SA occurred in normal rats ($n = 10$). Application of a Q-tip to the cutaneous RF showed an immediate inhibitory effect on SA but recovered instantly once the stimulus was removed. However, a Q-tip had no effect when applied to the non-RF skin. On the other hand, SA frequency increased significantly when pinching the RF skin with forceps, but declined when pinching the non-RF skin (Fig. 5A, B). Increased SA frequency was also recorded when poking or smearing capsaicin on the RF skin, but not when poking or smearing capsaicin on the non-RF skin (Fig. 5C).

Discussion

Visceral pain and visceral sensation are diffuse in character and often refer to other non-visceral somatic organs such as skin [4]. Thus, it is sensible to regard cutaneous

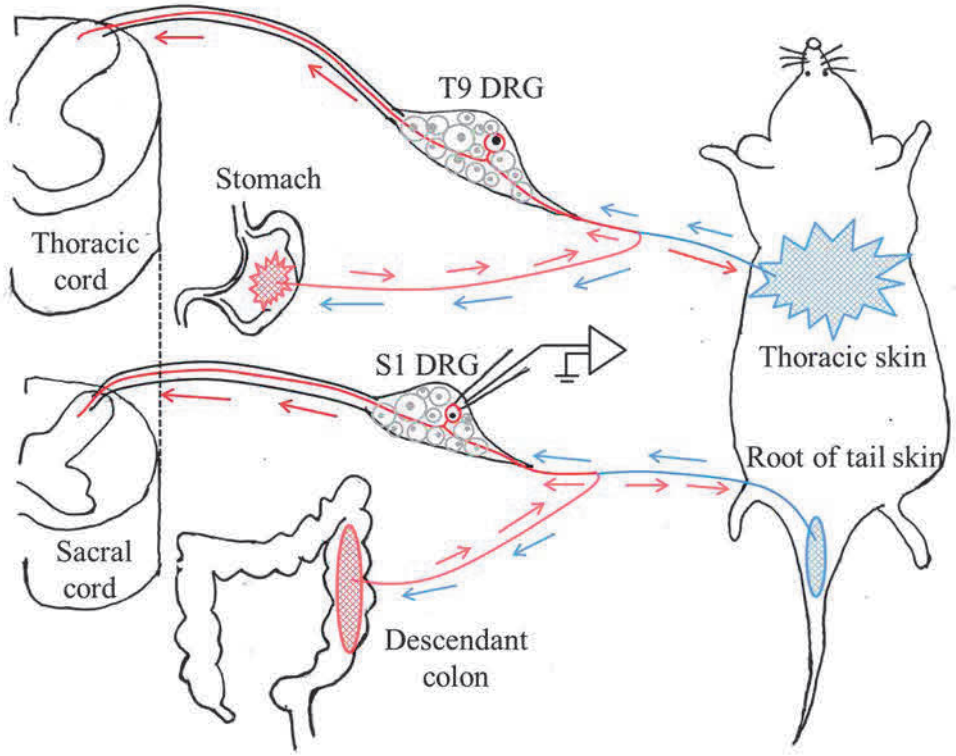

Fig. 6 Schematic showing how axon branching of C-nociceptive neurons in dorsal root ganglia (DRGs) contributes to cutaneous hypersensitivity *via* neurogenic inflammation that occurs commonly in visceral inflammatory pain. The inflammation of visceral organs (colon and stomach) leads to discharges of C-nociceptive neurons in DRGs and further results in neurogenic inflammation and cutaneous hypersensitivity, which in turn is an indicator of visceral pain.

hypersensitivity as an indicator of visceral pain. TNBS-induced colitis simulates, to an extent, the pathogenesis and clinical course of Crohn's disease [26, 27], was used in our study. We found that both cutaneous hypersensitivity and neuroinflammation appeared in this model. Moreover, our results indicated that sensory axon bifurcation may be the anatomical basis for this physiological phenomenon. We then verified this finding in both urocystitis and gastritis models and got similar results. In addition, to label DRG neurons innervating both visceral organs and skin, two kinds of fluorescent dye (DiI and CTB-488) were used. Data analysis of fluorescent labeling revealed the double-labeled neurons (≤ 6 neurons per DRG) accounted for $\sim 0.08\%$ of total neurons in each DRG examined. This rate is far below the rate of 1% reported in a previous study [23], which may be due in part to the small proportion of visceral innervation among all spinal afferents.

Cutaneous hypersensitivity appears in the case of visceral pathology, indicating that visceral and cutaneous sensations communicate and may interplay. Previous studies [8, 28–32] have revealed some of the reasons for this phenomenon. One explanation is that wide dynamic range neurons in the dorsal horn (usually located in laminae I and V) receive electrical signals from both visceral organs and cutaneous stimulation, which then are integrated in the spinal cord and may in return affect cutaneous sensation by antidromic activation of the dorsal roots (dorsal root reflex theory). These reverse discharges further induce peripheral vasodilation and cause the release of substance P, calcitonin gene-related peptide, and other inflammatory substances [33]. Our Evans blue extravasation experiments further confirmed this hypothesis.

Another explanation is DRG neuron coupled activation, which is also called the cross-depolarization theory [30–32]. This means once the primary neurons innervating visceral organs are activated, the neighboring neurons (that may innervate the skin) also become excited and sensitive. Gap junctions between neurons and astrocytes can transfer information between two neurons and make possible the appearance of cutaneous sensitization in the condition of visceral pain. This possibility will be further explored in future studies.

The bifurcation of axons in the peripheral nerve has been found in previous studies [23]. Pierau and colleagues [12] found that a number of DRG neurons respond to electrical stimulation of myelinated fibers in both the pudendal and sciatic nerves and this double-response can also be elicited when the dorsal roots are cut. These results are strong evidence that the peripheral processes of some ganglion cells dichotomize into different nerves innervating their respective target organs. The fluorescent labeling of DRG neurons and electrophysiological recording from them in our study also revealed that one double-labeled neuron can respond to both distal colonic distension and cutaneous stimulation. The inflammation of visceral organs leads to the discharge of C-nociceptive neurons in DRGs

and further results in neurogenic inflammation and cutaneous hypersensitivity, which in turn as an indicator of visceral pain (Fig. 6). Interestingly, the SA frequency of C-nociceptive neurons changed differently following nociceptive or non-nociceptive stimulation of the cutaneous RF or the skin adjacent to the RF (non-RF). To be specific, the SA was inhibited immediately by Q-tip wiping on the cutaneous RF while unreactive to touch of the non-RF area. This result supports the hypothesis that innocuous afferent input from touch of the skin may alleviate acute pain as described in previous studies [34, 35]. By comparison, the SA was accelerated and maintained for several minutes when the RF received nociceptive stimulation (pinch and poke) while reduced with stimulation of the non-RF. Unexpectedly, poking and capsaicin applied to the non-RF area failed to induce any significant change of SA. One explanation for these results might be that visceral pain is inhibited only if a large number of C-nociceptors in the non-RF skin are activated and adequate afferent signals are delivered to the spinal cord. This hypothesis will be further explored in future. Taken together, our findings suggest that axon branching of C-nociceptors contributes to cutaneous hypersensitivity in visceral inflammation, and cutaneous hypersensitivity at certain locations on the body surface might serve as an indicator of pathological conditions in the corresponding visceral organ.

Acknowledgements We thank Ms. Bo Yuan, Dr. Tao Wang, Dr. Fan Liu, and Dr. Huan Cui in the Department of Anatomy, Histology and Embryology, Institute of Basic Medical Sciences, Chinese Academy of Medical Sciences for technical assistance and Dr. Kun Liu and Dr. Shuya Wang from the Department of Physiology, Institute of Acupuncture and Moxibustion, China Academy of Chinese Medical Sciences, for technical assistance. This work was supported by Grants from the National Science Foundation of China (81771205, 91632113, 81973963, 81674085, and 81674075), the National Key Research and Development Program of China (2018YFC1704600), the Natural Science Foundation and Major Basic Research Program of Shanghai (16JC1420500 and 16JC1420502), and the Chinese Academy of Medical Sciences Innovation Fund for Medical Sciences (2017-I2M-3-008).

Conflict of interest The authors claim that there are no conflicts of interest.

References

1. Ananthakrishnan AN. Epidemiology and risk factors for IBD. Nat Rev Gastroenterol Hepatol 2015, 12: 205–217.
2. Elsenbruch S, Hauser W, Janig W. [Visceral pain]. Schmerz 2015, 29: 496–502.
3. Durazzo M, Gargiulo G, Pellicano R. Non-cardiac chest pain: a 2018 update. Minerva Cardioangiol 2018, 66: 770–783.
4. Gebhart GF, Bielefeldt K. Physiology of visceral pain. Compr Physiol 2016, 6: 1609–1633.
5. Cervero F. Sensory innervation of the viscera: peripheral basis of visceral pain. Physiological reviews 1994, 74.
6. Cervero F. Visceral pain: mechanisms of peripheral and central sensitization. Ann Med 1995, 27: 235–239.
7. Zain M, Bonin RP. Alterations in evoked and spontaneous activity of dorsal horn wide dynamic range neurons in pathological pain: A systematic review and analysis. Pain 2019.
8. Ness TJ, Gebhart GF. Interactions between visceral and cutaneous nociception in the rat. I. Noxious cutaneous stimuli inhibit visceral nociceptive neurons and reflexes. J Neurophysiol 1991, 66: 20–28.
9. Zhao JJ, Rong PJ, Shi L, Ben H, Zhu B. Somato stimulation and acupuncture therapy. Chin J Integr Med 2016, 22: 394–400.
10. Zhang R, Lao L, Ren K, Berman BM. Mechanisms of acupuncture-electroacupuncture on persistent pain. Anesthesiology 2014, 120: 482–503.
11. Armijo-Weingart L, Gallo G. It takes a village to raise a branch: Cellular mechanisms of the initiation of axon collateral branches. Mol Cell Neurosci 2017, 84: 36–47.
12. Pierau FK, Taylor DC, Abel W, Friedrich B. Dichotomizing peripheral fibres revealed by intracellular recording from rat sensory neurones. Neurosci Lett 1982, 31: 123–128.
13. Christianson JA, Liang R, Ustinova EE, Davis BM, Fraser MO, Pezzone MA. Convergence of bladder and colon sensory innervation occurs at the primary afferent level. Pain 2007, 128: 235–243.
14. Antoniou E, Margonis GA, Angelou A, Pikouli A, Argiri P, Karavokyros I, *et al.* The TNBS-induced colitis animal model: An overview. Ann Med Surg (Lond) 2016, 11: 9–15.
15. Zheng H, Chen M, Li Y, Wang Y, Wei L, Liao Z, *et al.* Modulation of gut microbiome composition and function in experimental colitis treated with Sulfasalazine. Front Microbiol 2017, 8: 1703.
16. Dogishi K, Okamoto K, Majima T, Konishi-Shiotsu S, Homan T, Kodera M, *et al.* A rat long-lasting cystitis model induced by intravesical injection of hydrogen peroxide. Physiol Rep 2017, 5.
17. Yang HJ, Kim MJ, Kwon DY, Kang ES, Kang S, Park S. Gastroprotective actions of Taraxacum coreanum Nakai water extracts in ethanol-induced rat models of acute and chronic gastritis. J Ethnopharmacol 2017, 208: 84–93.
18. Kankuri E, Asmawi MZ, Korpela R, Vapaatalo H, Moilanen E. Induction of iNOS in a rat model of acute colitis. Inflammation 1999, 23: 141–152.
19. Yang HJ, Kim MJ, Kwon DY, Kang ES, Kang S, Park S. Gastroprotective actions of Taraxacum coreanum Nakai water extracts in ethanol-induced rat models of acute and chronic gastritis. Journal of ethnopharmacology 2017, 208: 84–93.
20. Cayan S, Coşkun B, Bozlu M, Acar D, Akbay E, Ulusoy E. Botulinum toxin type A may improve bladder function in a rat chemical cystitis model. Urological research 2003, 30: 399–404.
21. Ma C, Donnelly DF, LaMotte RH. In vivo visualization and functional characterization of primary somatic neurons. J Neurosci Methods 2010, 191: 60–65.

22. Chen Z, Wang T, Fang Y, Luo D, Anderson M, Huang Q*, et al.* Adjacent intact nociceptive neurons drive the acute outburst of pain following peripheral axotomy. Sci Rep 2019, 9: 7651.
23. Lee S, Yang G, Xiang W, Bushman W. Retrograde double-labeling demonstrates convergent afferent innervation of the prostate and bladder. Prostate 2016, 76: 767–775.
24. Pinter E, Szolcsanyi J. Plasma extravasation in the skin and pelvic organs evoked by antidromic stimulation of the lumbosacral dorsal roots of the rat. Neuroscience 1995, 68: 603–614.
25. Verne GN, Robinson ME, Vase L, Price DD. Reversal of visceral and cutaneous hyperalgesia by local rectal anesthesia in irritable bowel syndrome (IBS) patients. Pain 2003, 105: 223–230.
26. Li C, Xi Y, Li S, Zhao Q, Cheng W, Wang Z*, et al.* Berberine ameliorates TNBS induced colitis by inhibiting inflammatory responses and Th1/Th17 differentiation. Mol Immunol 2015, 67: 444–454.
27. Luo X, Yu Z, Deng C, Zhang J, Ren G, Sun A*, et al.* Baicalein ameliorates TNBS-induced colitis by suppressing TLR4/MyD88 signaling cascade and NLRP3 inflammasome activation in mice. Sci Rep 2017, 7: 16374.
28. Clement CI, Keay KA, Podzebenko K, Gordon BD, Bandler R. Spinal sources of noxious visceral and noxious deep somatic afferent drive onto the ventrolateral periaqueductal gray of the rat. J Comp Neurol 2000, 425: 323–344.
29. Berkley KJ. A life of pelvic pain. Physiol Behav 2005, 86: 272–280.
30. Amir R, Devor M. Chemically mediated cross-excitation in rat dorsal root ganglia. J Neurosci 1996, 16: 4733–4741.
31. Amir R, Devor M. Functional cross-excitation between afferent A- and C-neurons in dorsal root ganglia. Neuroscience 2000, 95: 189–195.
32. Kim YS, Anderson M, Park K, Zheng Q, Agarwal A, Gong C*, et al.* Coupled activation of primary sensory neurons contributes to chronic pain. Neuron 2016, 91: 1085–1096.
33. Willis WD, Jr. Dorsal root potentials and dorsal root reflexes: a double-edged sword. Exp Brain Res 1999, 124: 395–421.
34. Arcourt A, Gorham L, Dhandapani R, Prato V, Taberner FJ, Wende H*, et al.* Touch receptor-derived sensory information alleviates acute pain signaling and fine-tunes nociceptive reflex coordination. Neuron 2017, 93: 179–193.
35. Choi JC, Kim J, Kang E, Lee JM, Cha J, Kim YJ*, et al.* Brain mechanisms of pain relief by transcutaneous electrical nerve stimulation: A functional magnetic resonance imaging study. Eur J Pain 2016, 20: 92–105.

Neurosci. Bull. January, 2021, 37(1):55–69
https://doi.org/10.1007/s12264-020-00563-x

www.neurosci.cn
www.springer.com/12264

ORIGINAL ARTICLE

Chronic Oral Administration of Magnesium-*L*-Threonate Prevents Oxaliplatin-Induced Memory and Emotional Deficits by Normalization of TNF-α/NF-κB Signaling in Rats

Xin Zhou[1] · Zhuo Huang[1] · Jun Zhang[1] · Jia-Liang Chen[3] · Pei-Wen Yao[1] · Chun-Lin Mai[1] · Jie-Zhen Mai[1] · Hui Zhang[2] · Xian-Guo Liu[1,4]

Received: 8 January 2020 / Accepted: 14 May 2020 / Published online: 28 August 2020

Abstract Antineoplastic drugs such as oxaliplatin (OXA) often induce memory and emotional deficits. At present, the mechanisms underlying these side-effects are not fully understood, and no effective treatment is available. Here, we show that the short-term memory deficits and anxiety-like and depression-like behaviors induced by intraperitoneal injections of OXA (4 mg/kg per day for 5 consecutive days) were accompanied by synaptic dysfunction and downregulation of the NR2B subunit of N-methyl-D-aspartate receptors in the hippocampus, which is critically involved in memory and emotion. The OXA-induced behavioral and synaptic changes were prevented by chronic oral administration of magnesium-*L*-threonate (L-TAMS, 604 mg/kg per day, from 2 days before until the end of experiments). We found that OXA injections significantly reduced the free Mg^{2+} in serum and cerebrospinal fluid (from ~ 0.8 mmol/L to ~ 0.6 mmol/L). The Mg^{2+} deficiency (0.6 mmol/L) upregulated tumor necrosis factor (TNF-α) and phospho-p65 (*p*-p65), an active form of nuclear factor-kappaB (NF-κB), and downregulated the NR2B subunit in cultured hippocampal slices. Oral L-TAMS prevented the OXA-induced upregulation of TNF-α and *p*-p65, as well as microglial activation in the hippocampus and the medial prefrontal cortex. Finally, similar to oral L-TAMS, intracerebroventricular injection of PDTC, an NF-κB inhibitor, also prevented the OXA-induced memory/emotional deficits and the changes in TNF-α, *p*-p65, and microglia. Taken together, the activation of TNF–α/NF–κB signaling resulting from reduced brain Mg^{2+} is responsible for the memory/emotional deficits induced by OXA. Chronic oral L-TAMS may be a novel approach to treating chemotherapy-induced memory/emotional deficits.

Keywords Magnesium-*L*-threonate · Oxaliplatin · Tumor necrosis factor-alpha · Nuclear factor-kappaB · Cognitive deficit · Hippocampus · Medial prefrontal cortex

Xin Zhou, Zhuo Huang and Jun Zhang have contributed equally to this work.

Electronic supplementary material The online version of this article (https://doi.org/10.1007/s12264-020-00563-x) contains supplementary material, which is available to authorized users.

✉ Hui Zhang
zhanghui@gd2h.org.cn

✉ Xian-Guo Liu
liuxg@mail.sysu.edu.cn

[1] Department of Physiology and Pain Research Center, Zhongshan School of Medicine, Sun Yat-sen University, Guangzhou 510080, China

[2] Department of Anesthesiology, Guangdong Second Provincial General Hospital, Guangzhou 510317, China

[3] Department of Urology, Third Affiliated Hospital of Sun Yat-sen University, Guangzhou 510630, China

[4] Guangdong Province Key Laboratory of Brain Function and Disease, Guangzhou 510080, China

Introduction

Chemotherapy-induced cognitive dysfunction and chemotherapy-induced mood disorders are common side-effects in cancer patients. The former is manifested as a decline in attention and visuospatial skills [1], and the latter as anxiety and depression [2]. These disorders often persist for a long period after the termination of chemotherapy, seriously reducing the quality of life and the ability of cancer survivors to work [3]. At present, the treatment of these side-effects is a major challenge in clinical practice.

To date, it is still unclear how anticancer agents with different chemical structures and anticancer mechanisms, such as oxaliplatin (OXA) [4], paclitaxel [5, 6], and vincristine [7, 8], have common side-effects – memory/emotional deficits. It has been shown that many anticancer agents, including OXA [9], paclitaxel [10], vinblastine [11], cisplatin [12], and cetuximab [13], result in hypomagnesemia in patients. Magnesium deficiency is associated with high levels of serum pro-inflammatory cytokines including TNF-α in humans [14]. These cytokines play important roles in the initiation of chemotherapy-induced memory [15] and emotional deficits [16]. NF-κB, a potent transcription factor for many inflammatory cytokines and chemokines, is involved in cancer genesis and treatment [17]. However, currently little is known about the role of NF-κB in chemotherapy-induced memory and emotional deficits. The causal link between Mg^{2+} deficiency and the activation of TNF-α/NF-κB signaling in the central nervous system after chemotherapy has not been clarified.

Previous work has shown that oral administration of magnesium-*L*-threonate (L-TAMS, also called MgT), which can elevate brain Mg^{2+}, improves hippocampus-dependent spatial learning in naïve rats [18] and in a mouse model of Alzheimer's disease [19]. Oral L-TAMS also prevents and restores the memory deficits induced by peripheral nerve injury [20] and enhances fear extinction, but does not affect the amygdala-dependent delay-cued fear memory [21]. Mechanistically, L-TAMS upregulates the NR2B subunit of N-methyl-D-aspartate receptors (NMDARs) and brain-derived neurotrophic factor, as well as improving synaptic plasticity/density in the hippocampus [18] and prefrontal cortex, but not in the amygdala [21]. A recent clinical trial indicated that the global cognitive ability of older adults can be improved by oral L-TAMS [22]. Furthermore, Mg^{2+} deficiency results in anxiety and depression in animals and humans [23]. However, whether oral L-TAMS can prevent chemotherapy-induced memory/emotional deficits remains unknown.

The present study was designed to test the hypothesis that OXA induces memory and emotional deficits by activation of TNF-α/NF-κB signaling *via* reducing Mg^{2+} in the brain, and to determine whether supplemental Mg^{2+} by chronic oral L-TAMS can prevent the Mg^{2+} deficiency and memory/emotional deficits induced by OXA.

Materials and Methods

Animals

Adult male Sprague-Dawley rats weighing 220–250 g and Sprague–Dawley rats 5–7 days old (~ 10 g) were purchased from the Institute for Experimental Animals of Sun Yat-sen University. The rats were housed in separate cages in a temperature-controlled room (24 ± 1°C) with 50%–60% humidity under a 12:12-h light/dark cycle in a specific pathogen-free environment, and permitted free access to sterile water and standard laboratory chow. All experimental procedures were approved by the Animal Care and Use Committee of Sun Yat-sen University and carried out under the guidelines on animal care and the ethical guidelines of the National Institutes of Health. Rats were randomly assigned to different experimental and control conditions.

Drug Administration

Oxaliplatin sulfate (Jinrui Pharmaceutical Co., Ltd, Hainan, China) dissolved in 5% glucose/H_2O to 1 mg/mL was intraperitoneally injected at 4 mg/kg/day for 5 consecutive days [24]. Control animals received an equivalent volume of 5% glucose/H_2O. Based on previous studies [18], L-TAMS (Neurocentria Inc., Walnut Creek, CA, USA) was administered *via* drinking water (604 mg/kg per day; 50 mg/kg per day elemental Mg^{2+}), initiated 2 days in advance of chemotherapy and continued until the end of the experiments. The average volume of drinking water (~ 30 mL/day) and daily food intake (containing 0.15% elemental Mg^{2+}) were monitored. Accordingly, the concentration of L-TAMS in the drinking water was adjusted to reach the appropriate target dose.

Experimental Design

Behavioral Tests

The novel object-recognition test (NORT) was applied to assess short-term memory as previously described [25]. Briefly, rats were tested in an open field apparatus made up of a circular arena 80 cm in diameter. In the first stage, each rat was placed in the arena for 5 min with two identical objects that served as "old objects". Ten minutes later, a new object replaced the less preferred old object. Each rat was allowed to explore the two different objects for 5 min. The recognition index was calculated as the ratio of time spent exploring the novel object over total exploration time.

The elevated plus-maze test (EPMT) was carried out in an EPM apparatus (RWD Life Science, Shenzhen, China) formed by 2 open arms and 2 closed arms surrounded by walls 30 cm high in a plus shape. Each rat was placed in the center of the maze and allowed to explore freely for 5 min. The anxiety-like behaviors were measured using TopScan3D software (Clever Sys Inc., Reston, VA, USA). The percentage of time and bouts in the open arms in

different groups were compared. A reduction of time and bouts in the open arms indicated anxiety-like behavior.

The forced swimming test (FST) was based on previous studies [26]. Rats were forced to swim for 6 min in a glass cylinder (25 cm in diameter and 55 cm high) containing 30 cm of water at 25 ± 1°C. In the last 4 min, the immobility time was used as an indicator of depression-like behavior.

Electrophysiological Recording

Frequency facilitation at CA3-CA1 synapses was measured in the hippocampus *in vivo*. After electrical stimulation of the Schaffer collateral–commissural pathway, field excitatory postsynaptic potentials (fEPSPs) were recorded from the stratum radiatum of CA1. The best placement of electrodes was based on electrophysiological criteria [27]. The recording electrode was positioned at 2.5 mm lateral to the midline, 3.4 mm posterior to bregma, and ∼ 2.2 mm below the dura. The stimulating electrode was positioned at 4.2 mm posterior to bregma, 3.8 mm lateral to the midline, and ∼ 4.7 mm below the dura. The baseline fEPSPs in CA1 were recorded following stimulation of CA3 with test stimuli (0.066 Hz, 0.2 ms duration). The intensity of the test stimulus was adjusted to produce 50%–55% of the maximum response. Conditioning stimuli at 2, 4, and 8 Hz at 20-min intervals were used to induce frequency facilitation in each rat. The intensity of the conditioning stimulus was identical to that of the test stimulus.

Measurement of Extracellular Free Magnesium

Blood was sampled from the left ventricle and centrifuged at 1000 *g* for 10 min to obtain serum. Cerebrospinal fluid (CSF) was collected from the occipital foramen. Free Mg^{2+} content in the fluids was measured by Calmagite chromometry [28].

Organotypic Hippocampal Slice Cultures

The method of organotypic culture of hippocampal slices from Sprague–Dawley rats 5–7 days old was as described previously [29]. Briefly, slices were cut at 300 μm and then cultured on porous (0.4 μm) insert membranes (Millipore, Billerica, MA). These membranes were transferred to 6-well culture trays in a humidified atmosphere (5% CO_2, 37°C) and maintained for 7 days before use. The culture medium consisted of 50% MEM (Eagle) with Glutamax-1, 25% Earle's balanced salt solution, 25% heat-inactivated horse serum, 6.5 mg/mL D-glucose, 50 μg/mL streptomycin, and 50 U/mL penicillin (all from Gibco, Grand Island, NY).

Intracerebroventricular (icv) Injection

Each rat, anesthetized with 10% chloral hydrate (0.4 mg/kg, i.p.), was placed in a stereotaxic frame and a cannula was implanted in a lateral cerebral ventricle at the following coordinates: 1.8 mm lateral to the midline, 1.2 mm posterior to bregma, and 3.7–4.3 mm below the skull. Seven days after the operation, pyrrolidine dithiocarbamic acid (PDTC, 10 ng/5 μL; Sigma) or artificial CSF was injected icv in a volume of 5 μL in 10 min (daily). The behavioral tests started 2 days after the last injection.

Western Blot

Under anesthesia with sodium pentobarbital (50 mg/kg, i.p.), hippocampus samples were harvested and immediately stored at –80°C until use. Total protein was extracted on ice in 15 mmol/L Tris buffer supplemented with proteinase inhibitors and phosphatase inhibitors. Protein samples were separated by sodium dodecyl sulfate-polyacrylamide gel electrophoresis and then transferred onto a PVDF membrane. After blocking, the blots were incubated with primary antibody against TNF-α (1:1000, rabbit; Bioworld Technology, Inc., Louis Park, MN), phosphorylated NF-κB p65 (Ser311) (1:1000, rabbit, Abcam, Cambridge, UK), NR2B (1:1000, rabbit, Abcam), and β-actin (1:1000, mouse; Cell Signaling Technology, Danvers, MA) overnight at 4°C. Horseradish peroxidase-conjugated IgG was applied for 1 h. Electrochemiluminescence was used to detect the immune complexes. Bands were quantified using a computer-assisted imaging analysis system (ImageJ; -National Institutes of Health, Bethesda, MD).

Immunohistochemistry

Rats were anesthetized and perfused through the ascending aorta with saline followed by 4% paraformaldehyde. Brains were removed and post-fixed in the same fixative for 1 h, then transferred to 30% sucrose for 3 days. Hippocampal sections (25 μm) were cut on a freezing microtome (CM3050S, Leica, Wetzlar, Germany) and processed for immunohistochemical staining. Sections were first blocked for 1 h and then incubated with primary antibody against TNF-α (1:200, Rabbit, Bioworld Technology), phosphorylated NF-κB p65 (Ser311,1:100, rabbit; Affinity Biosciences, OH), NeuN (1:400, mouse; Chemicon, Temecula, CA), GFAP (1:500, mouse, Abcam), and Iba1 (1:200, goat, Abcam) overnight at 4°C. Then the sections were incubated with Cy3-conjugated and Alexa-conjugated secondary antibodies for 1 h at room temperature, then mounted on coverslips with Fluoromount-G with DAPI (Southern Biotech, Birmingham, AL). Images of the stained sections were then captured with a Leica

fluorescence microscope (Leica DFC350 FX camera, Wetzlar, Germany) or Leica fluorescence microscope (Leica DM6B camera). All parameters such as exposure, gamma, and gain were fixed to ensure standardization between slices. ImageJ software was used to analyze the fluorescence intensity.

Statistical Analysis

All data are presented as the mean ± SEM. SPSS 17.0 (SPSS, Inc., Chicago, IL) was used to perform data analysis. The results from the behavioral tests, measurement of Mg^{2+} content, western blot, and immunohistochemistry, were analyzed with one-way or two-way ANOVA followed by Tukey's *post hoc* test. The electrophysiology was analyzed with two-way ANOVA followed by Tukey's *post hoc* test. $P < 0.05$ was considered a significant difference.

Results

Chronic Oral Magnesium-L-Threonate Prevents the Memory and Emotional Deficits Induced by Oxaliplatin

To determine if chronic oral administration of L-TAMS is capable of preventing the memory and emotional deficits induced by OXA, rats were randomly assigned into four groups: the OXA group receiving OXA injections (4 mg/kg per day, i.p., for 5 consecutive days) and drinking normal water; the OXA + L-TAMS group receiving L-TAMS in drinking water from 2 days before OXA injection until the end of the experiments; the L-TAMS group receiving L-TAMS and vehicle injections; and the control group drinking normal water and receiving vehicle injections. Two days after the termination of the OXA or vehicle injections, behavioral tests were applied to the different groups (Fig. 1A). We found that the recognition index for short-term memory assessed with the NORT (Fig. 1B) decreased and the immobility time with the FST (Fig. 1C) increased markedly compared to controls, indicating that the OXA injections impair short-term memory and induce depression-like behavior. Furthermore, the percentage of time and bouts in the open arms measured with the EPMT were significantly lower in the OXA group than in controls (Fig. 1D, E), while the total distance traveled and the average speed did not differ among the groups (Fig. 1F, G). The data indicated that the OXA injections also cause anxiety-like behaviors without affecting motor functions. Importantly, we found that oral L-TAMS completely prevented the OXA-induced memory deficits as well as the depression-like and anxiety-like behaviors, because the index of short-term memory, the immobility time, and the percentage of time and bouts in the open arms in the L-TAMS + OXA group were significantly higher than those in the OXA group and were not different from controls (Fig. 1B–E). L-TAMS had no effect on the memory and emotion indexes in the rats treated with vehicle (Fig. 1B–E).

Oral L-TAMS Prevents the Impairment of Synaptic Transmission and Downregulation of the NR2B Subunit in NMDARs in the Hippocampus Induced by OXA

An increasing number of studies have shown that the hippocampus, which is important for memory formation, also plays a role in emotion [30]. Our previous work showed that the working memory and short-term memory deficits induced by peripheral nerve injury are associated with impairment of frequency facilitation at hippocampal CA3–CA1 synapses [31], so we tested whether the same might be true in rats treated with OXA. As shown in Fig. 2, the amplitudes of fEPSPs at CA3–CA1 synapses were progressively enhanced with increased frequencies (2, 4, and 8 Hz) in controls, while the magnitudes of the facilitation induced by the same frequencies were significantly lower in the OXA group than in controls (Fig. 2B–D). Importantly, the magnitude of the facilitation in L-TAMS-treated rats was higher than that in those treated with OXA and did not differ from controls. These data indicate that OXA impairs sustained synaptic transmission, which may contribute to memory and emotional deficits, and the effects are prevented by L-TAMS.

Previous studies have shown that the expression of the NR2B but not the NR2A subunit of NMDARs in the hippocampus is important for synaptic plasticity and memory in numerous animal models [32]. Therefore, we measured the expression of NR2B in the hippocampus 5 days after the end of OXA injections and found that the NR2B levels were lower in the OXA group than in controls, while these in the L-TAMS+OXA group did not differ from controls (Fig. 2E). This NR2B down-regulation may contribute to the dysfunction of synaptic transmission. Interestingly, the effects were again prevented by the chronic administration of L-TAMS.

Oral Magnesium-L-Threonate Prevents the Mg^{2+} Deficiency Induced by OXA *In Vivo*, While Reducing Mg^{2+} Activates TNF-α/NF-κB Signaling and Downregulates NR2B in Cultured Hippocampal Slices

Our previous work showed that the free Mg^{2+} concentrations in serum and CSF are significantly reduced in

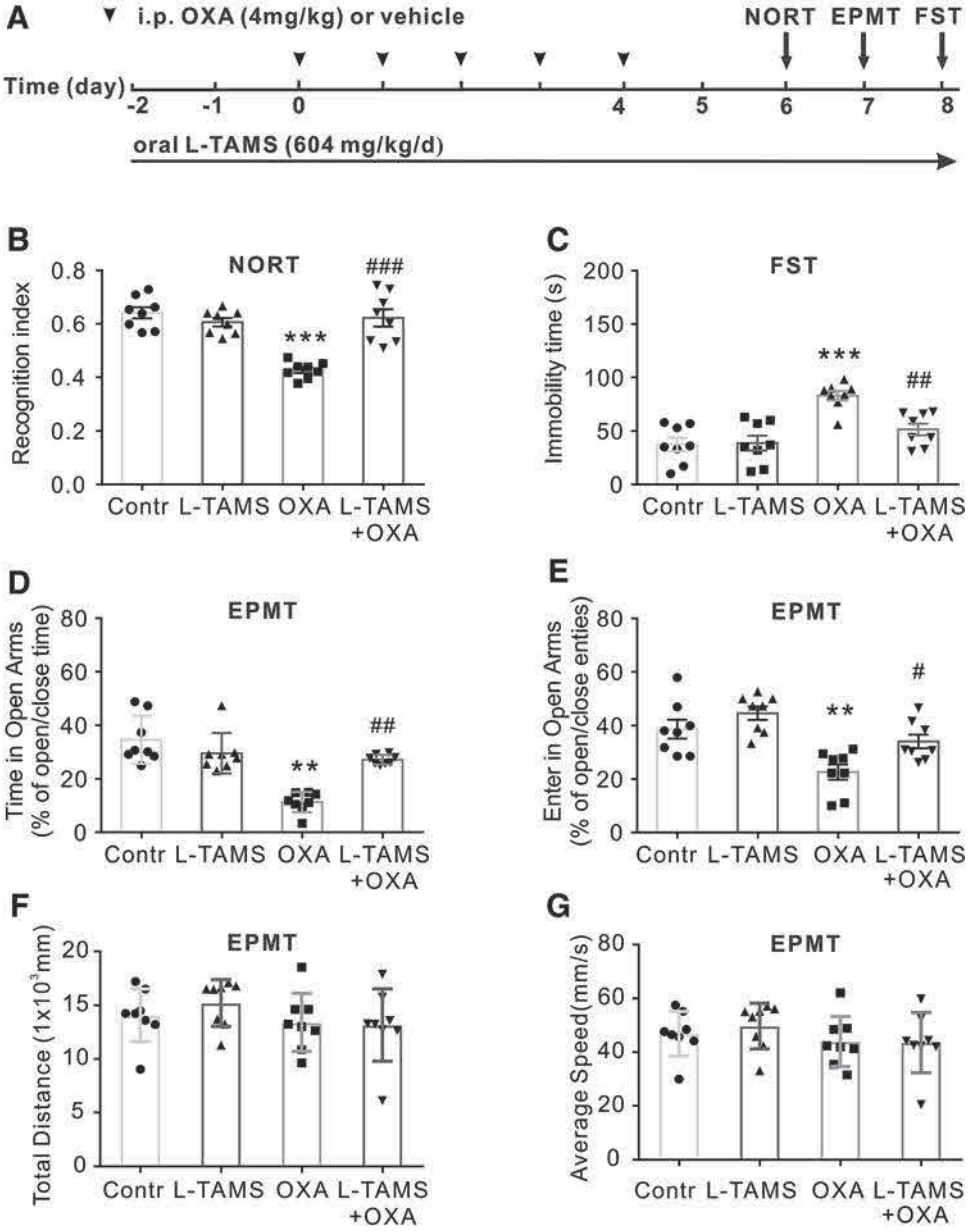

Fig. 1 Magnesium-L-threonate prevents the short-term memory and emotion deficiency induced by OXA. **A** Experiment schedule. **B** Recognition index in indicated groups, accessed with the novel object recognition test (NORT) ($n = 8$ per group). **C** Immobility time in each group measured in the forced swimming test (FST). Oral L-TAMS significantly suppressed the increased immobility time induced by OXA ($n = 8$ per group). **D**, **E** Injections of OXA reduced the percentage of time and entries into the open arms in the elevated plus-maze test (EPMT), and the effects were prevented by oral L-TAMS ($n = 8$ per group). **F**, **G** Total distance traveled and average speed did not differ among the groups in the EPMT ($n = 8$ per group). $^{*}P < 0.05$, $^{**}P < 0.01$, $^{***}P < 0.001$ *vs* Control (Contr); $^{\#}P < 0.05$, $^{\#\#}P < 0.01$, $^{\#\#\#}P < .001$, *vs* OXA (one-way ANOVA followed by Tukey's *post hoc* test).

vincristine-treated rats, and oral L-TAMS prevents Mg^{2+} deficiency [33]. In the present work, we found that injection of OXA for 5 consecutive days led to short-term memory deficits along with depression-like and anxiety-like behaviors 6–8 days after the onset of OXA treatment (1–3 days after termination of treatment). And the OXA-induced behavioral changes were prevented by supplementation with Mg^{2+}. These data suggest that the behavioral changes might be produced by Mg^{2+} deficiency. To confirm this, the extracellular free Mg^{2+} was measured 5 and 10 days after OXA injection. Indeed, we found that the free Mg^{2+} in both serum and CSF were significantly lower in the OXA group than in the controls (Fig. 3A, B). But no difference between the L-TAMS + OXA group and controls was detected at any time point. These results demonstrate that OXA also induces Mg^{2+} deficiency, which is prevented by oral L-TAMS.

We next investigated how Mg^{2+} deficiency in the brain causes memory/emotional deficits. A large amount of evidence has demonstrated that activation of the TNF-α/NF-κB signaling pathway plays a critical role in cognitive deficits [34], depression [35], and anxiety [36]. We therefore tested the hypothesis that Mg^{2+} deficiency in the brain leads to memory/emotional deficits by activation of TNF-α/NF-κB signaling. To do so, hippocampal slices were cultured in media containing normal (0.8 mmol/L) and lower (0.6 mmol/L) Mg^{2+}, as injection of OXA decreased free Mg^{2+} in the CSF from ~ 0.8 to

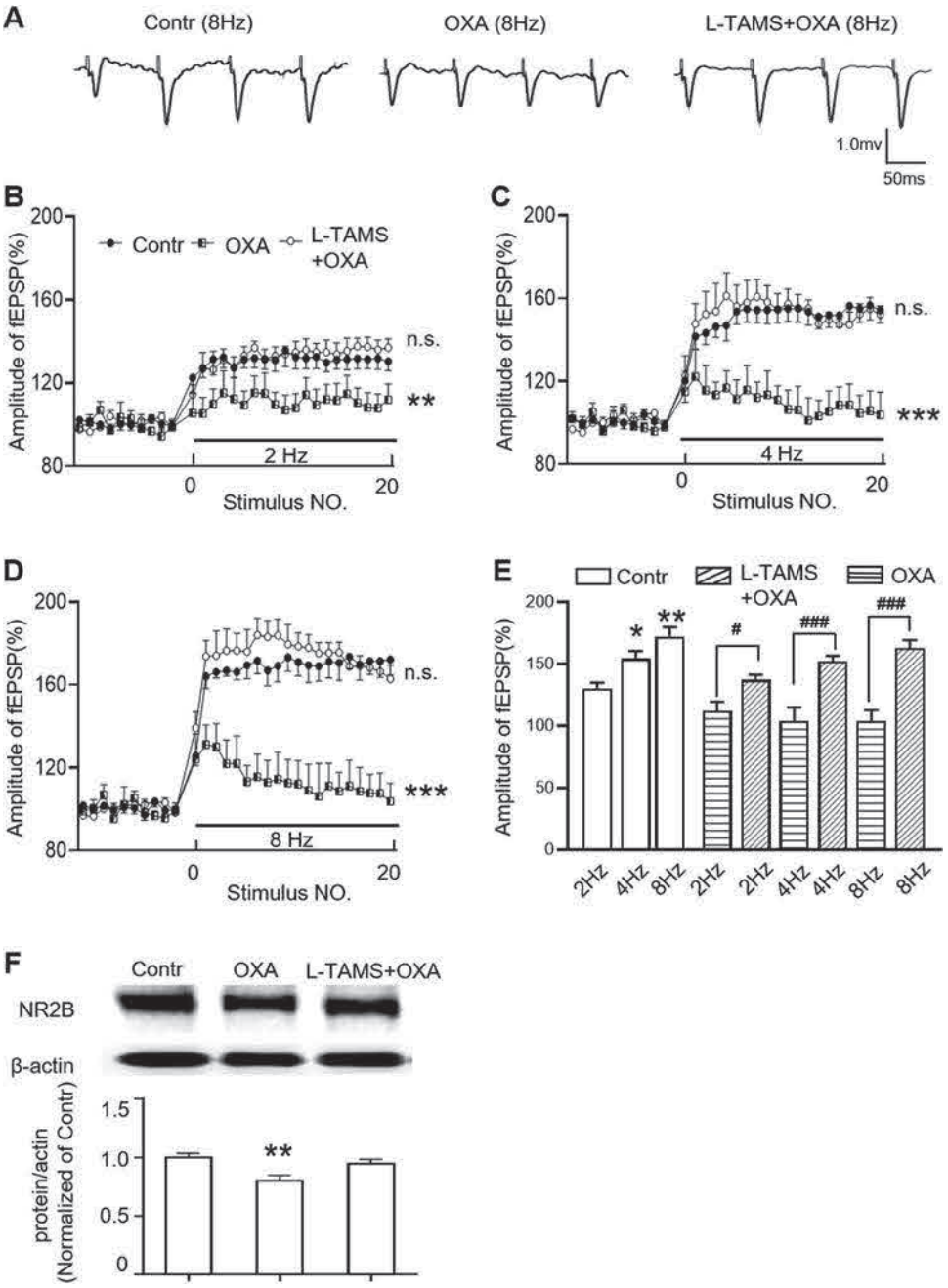

Fig. 2 Oral magnesium-L-threonate prevents the impairment of synaptic transmission and downregulation of NR2B induced by OXA. **A** Raw traces of fEPSPs at CA3–CA1 synapses evoked by the first 4 consecutive conditioning stimuli (8 Hz, 0.2 ms) in the indicated groups. **B**–**D** Facilitation of fEPSPs induced by 2, 4, and 8 Hz electrical stimuli. The magnitude of facilitation in the OXA group was significantly lower than in controls (Contr). The impairment of frequency facilitation was abolished by oral L-TAMS (n = 5–7 per group). Data are expressed as a percentage of baseline elicited by test stimuli at 0.066 Hz. The intensity of the conditioning stimulus was identical to that of the test stimulus in each experiment. **E** Amplitudes fEPSPs at CA1–CA3 evoked by the 20th conditioning stimulus in the different groups. **F** Representative blots and histogram showing the NR2B protein levels in the hippocampus in the indicated groups. Injection of OXA downregulated NR2B in the hippocampus, and the effects were prevented by oral L-TAMS (n = 5 per group). $^{**}P < 0.01$, $^{***}P < 0.001$, n. s. no significant difference compared to controls (Contr) (two-way ANOVA followed by Tukey's *post hoc* test).

$\sim$ 0.6 mmol/L (Fig. 3B). Western blots revealed that the levels of TNF-α and *p*-p65, an active form of NF-κB, were significantly higher in hippocampal slices cultured with 0.6 mmol/L Mg^{2+} on days 1 and 2 (Fig. 3C, D). Our previous work showed that vincristine downregulates NR2B in the hippocampus [33]. In the present work, we found that the level of NR2B was significantly reduced in hippocampal slices on day 2 but not on day 1 after culture in 0.6 mmol/L Mg^{2+} medium compared to that with 0.8 mmol/L medium. These data suggest that the downregulation of NR2B may result from the activation of TNF-α/NF-κB signaling.

In subsequent experiments, we used the OXA model to test whether oral L-TAMS is able to prevent the activation of TNF-α/NF-κB signaling and the resultant microglial activation in the hippocampus and medial prefrontal cortex (mPFC), which are important for memory and emotion [37, 38].

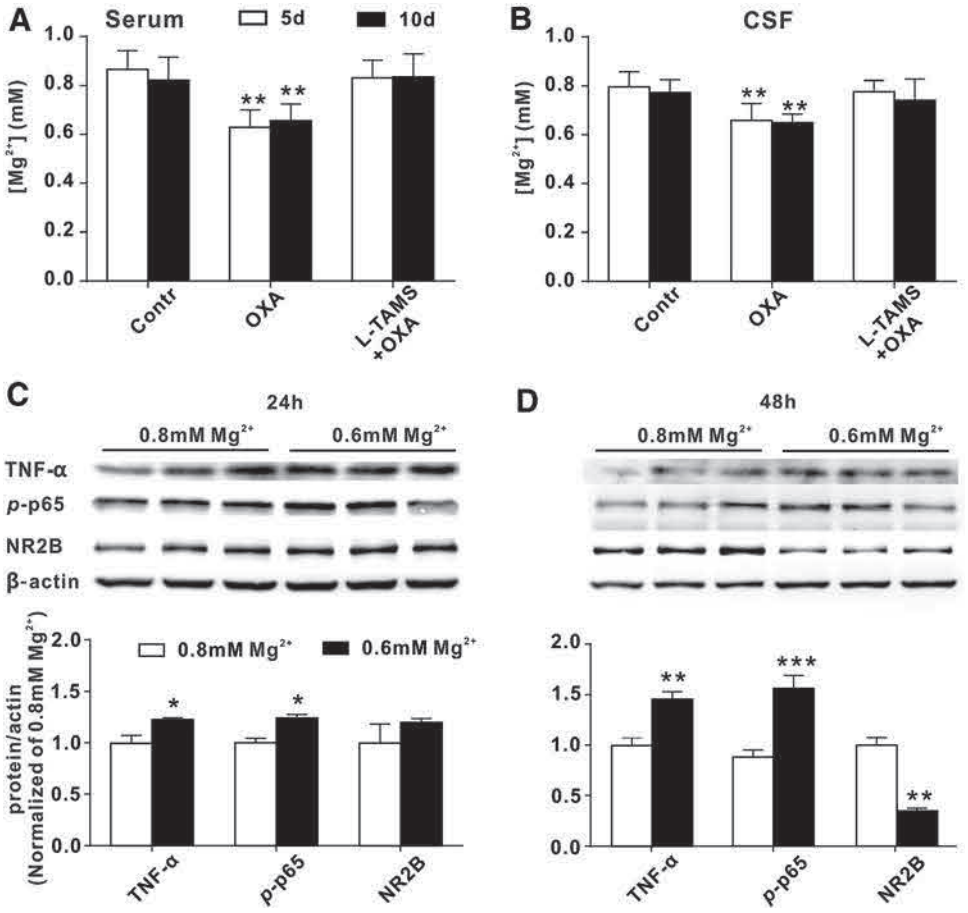

Fig. 3 Magnesium-L-threonate prevents the Mg^{2+} deficiency induced by OXA *in vivo*, while Mg^{2+} deficiency upregulates NF-κB/TNF-α and downregulates NR2B in cultured hippocampal slices. **A**, **B** Histograms of the free Mg^{2+} concentrations in serum and CSF in the indicated groups. OXA reduced free Mg^{2+} and the effects were prevented by L-TAMS (n = 6–8 per group). **C**, **D** Representative blots and histograms showing the protein levels of TNF-α, p-p65, and NR2B in hippocampal slices cultured in medium containing 0.6 mmol/L or 0.8 mmol/L free Mg^{2+} for 24 and 48 h. $^{*}P < 0.05$, $^{**}P < 0.01$, $^{***}P < 0.001$ *vs* 0.8 mmol/L free Mg^{2+} (one-way ANOVA followed by Tukey's *post hoc* test).

Oral Magnesium-L-Threonate Abolishes the OXA-Induced Activation of TNF-α/NF-κB and Microglial Activation in Both the Hippocampus and Medial Prefrontal Cortex *In Vivo*

Having shown that Mg^{2+} deficiency activates TNF-α/NF-κB signaling *in vitro*, we next investigated whether the OXA injections that reduce Mg^{2+} in CSF activate TNF-α-NF-κB signaling in the brain *in vivo*. Western blots revealed that the protein levels of both TNF-α and p-p65 in the hippocampus and mPFC increased progressively after OXA injection (Figs. 4A, B, 5A, B). The change in TNF-α reached a significant level on day 3 in the hippocampus and on day 5 in the mPFC, compared to controls (Fig. 4A, B). Of note, the TNF-α remained at these levels on days 7 and 10 after the onset of OXA injection in both regions (Fig. 4A, B). That is, TNF-α upregulation persisted for 3 and 6 days after the termination of OXA injections (see Fig, 1A for experimental schedule). Similarly, p-p65 was significantly upregulated in the hippocampus and mPFC from day 3 to day 10 after the first injection of OXA (Fig. 5A, B). These data indicate that the injection of OXA causes a long-lasting activation of TNF-α-NF-κB signaling in the hippocampus and mPFC. Importantly, we found that the levels of TNF-α and p-p65 in both regions in the L-TAMS + OXA group were significantly lower than those in the OXA group and did not differ from controls (Figs. 4A, B, 5A, B) at 10 days after OXA treatment. Similar results were obtained in the hippocampus and mPFC by immunostaining 10 days after the first OXA injection (Figs. 4C, 5C). These results indicate that oral L-TAMS normalizes the OXA-induced overexpression of TNF-α and p-p65 in the hippocampus and mPFC. Double-

Fig. 4 Oral L-TAMS blocks the OXA-induced TNF-α upregulation in both the hippocampus and mPFC. **A** Representative blots and histograms showing the expression of TNF-α in the hippocampus at different time points after the onset of OXA injections (n = 4 per group). The TNF-α upregulation induced by OXA is blocked by L-TAMS as measured on day 10 after the first OXA injection (n = 4 per group). **B** OXA injections also progressively upregulate TNF-α in the mPFC (n = 4 per group), and this overexpression is blocked by L-TAMS (n = 4 per group). **C** Representative immunofluorescent staining and histograms showing that L-TAMS prevents the upregulation of TNF-α induced by OXA in CA1 and the dentate gyrus (DG) of the hippocampus and the mPFC (n = 6 per group). **D** Double immunofluorescence staining showing that TNF-α (red) is co-localized with NeuN (green), but not with Iba1 (green) and GFAP (green) in the hippocampus and mPFC (arrowheads indicate co-localization). $^{*}P < 0.05$, $^{**}P < 0.01$, $^{***}P < 0.001$ *vs* controls (Contr) (one-way ANOVA followed by Tukey's *post hoc* test).

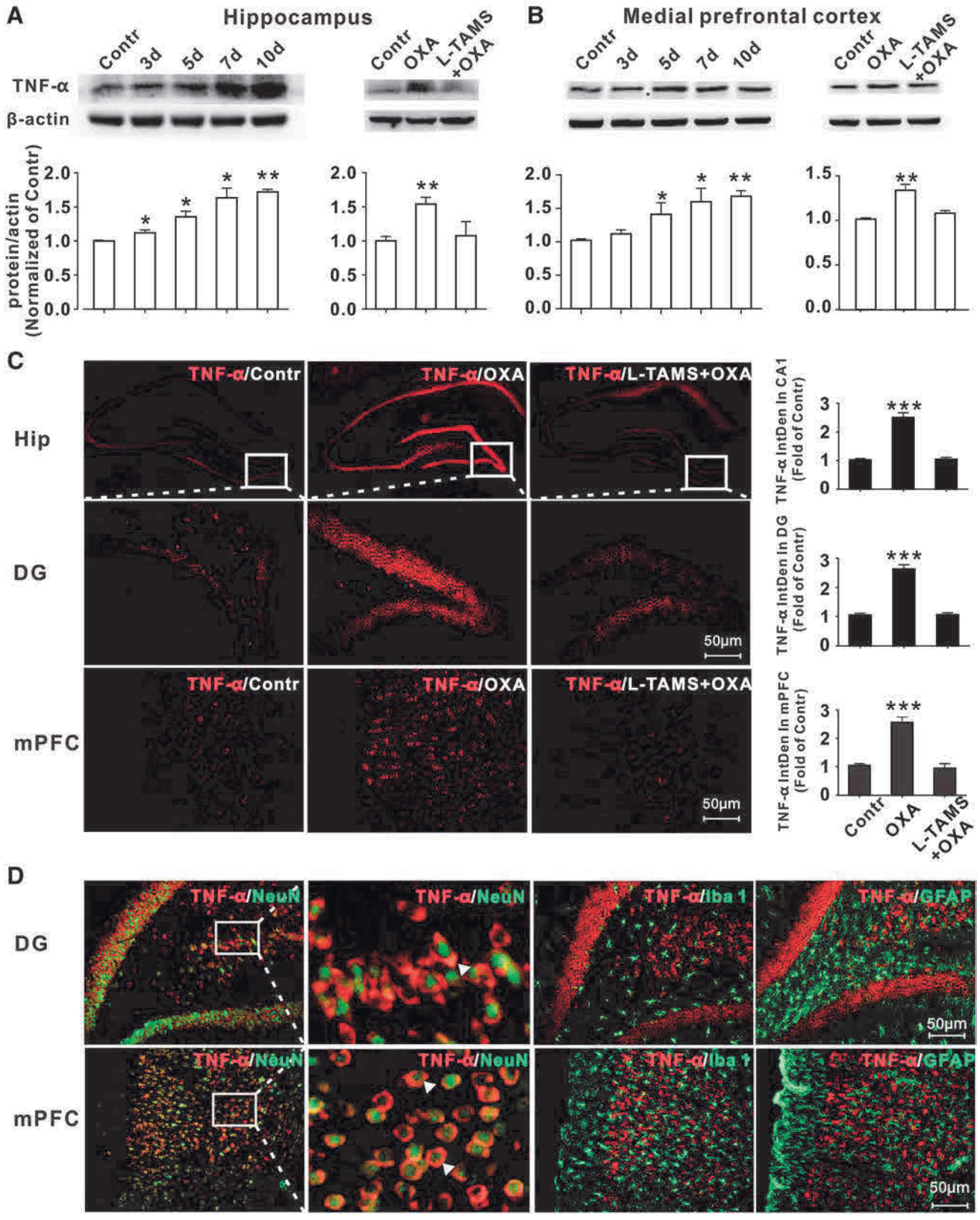
A
Hippocampus
Contr
3d
5d
7d
10d
TNF-α
β-actin
Contr
OXA
L-TAMS +OXA
protein/actin (Normalized of Contr)
B
Medial prefrontal cortex
C
Hip
DG
mPFC
TNF-α/Contr
TNF-α/OXA
TNF-α/L-TAMS+OXA
50μm
TNF-α IntDen in CA1 (Fold of Contr)
TNF-α IntDen in DG (Fold of Contr)
TNF-α IntDen in mPFC (Fold of Contr)
D
TNF-α/NeuN
TNF-α/Iba 1
TNF-α/GFAP

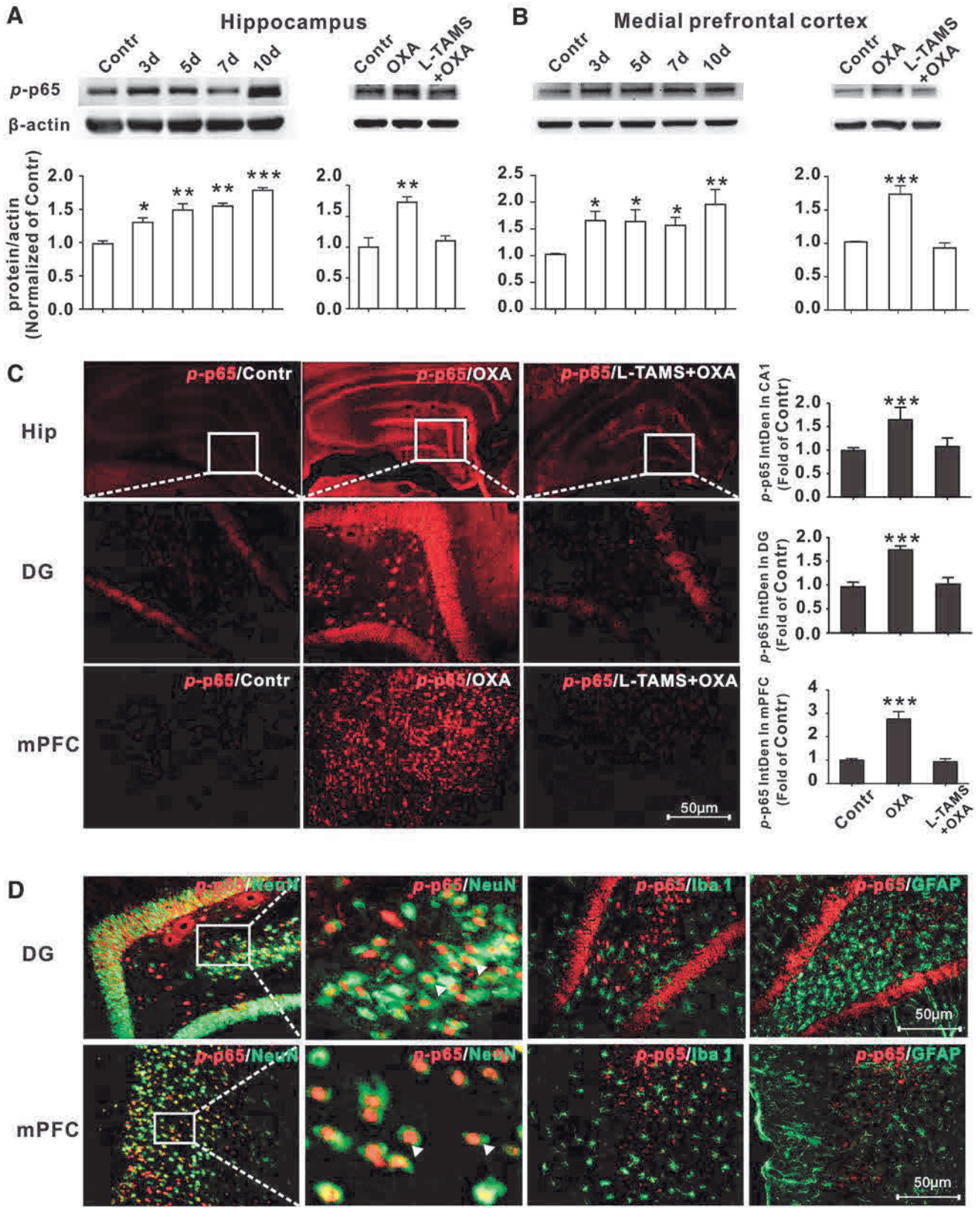
A
Hippocampus
Contr
3d
5d
7d
10d
Contr
OXA
L-TAMS +OXA
p-p65
β-actin
protein/actin (Normalized of Contr)
B
Medial prefrontal cortex
C
p-p65/Contr
p-p65/OXA
p-p65/L-TAMS+OXA
Hip
DG
mPFC
50μm
p-p65 IntDen In CA1 (Fold of Contr)
p-p65 IntDen In DG (Fold of Contr)
p-p65 IntDen In mPFC (Fold of Contr)
D
p-p65/NeuN
p-p65/Iba 1
p-p65/GFAP

◀**Fig. 5** L-TAMS prevents *p*-p65 upregulation in the hippocampus and mPFC induced by OXA. **A**, **B** Representative blots and histograms showing the levels of *p*-p65 in the hippocampus (**A**) and mPFC (**B**) at different time points after the onset of OXA injection in the indicated groups ($n = 4$ per group). The OXA-induced overexpression of *p*-p65 is blocked by L-TAMS in both regions at 10 days after the onset of OXA ($n = 4$ per group). **C** Representative immunofluorescent staining and histograms showing the OXA-induced *p*-p65 upregulation is completely blocked by co-administration of L-TAMS ($n = 6$ per group) in both regions ($n = 6$ per group). D Double immunofluorescence staining reveals that *p*-p65 (red) is co-localized with NeuN (green), but not with Iba1 (green) and GFAP (green) in the hippocampus and mPFC (arrowheads indicate co-immunostaining of *p*-p65 and cell markers). $^{*}P < 0.05$, $^{**}P < 0.01$, $^{***}P < 0.001$ *vs* controls (Contr) (one-way ANOVA followed by Tukey's *post hoc* test).

staining with these tissues harvested 10 days after OXA injection showed that both TNF-α and *p*-p65 co-localized with NeuN (a marker of the nuclei of neurons) but not with Iba1 (a microglia marker) and GFAP (an astrocyte marker) in the OXA group (Figs. 4D, 5D). These data indicate that chronic oral L-TAMS prevents the excessive activation of TNF-α–NF-κB signaling in neurons of the hippocampus and mPFC.

As microglial activation is critically involved in chemotherapy-induced cognitive impairment [39], we tested whether L-TAMS is also able to prevent OXA-induced microglial activation. Immunostaining showed that the number of microglia in the OXA group was markedly higher in CA1 and the DG of the hippocampus and in the mPFC than that in controls, while the control and L-TAM + OXA groups did not differ (Fig. 6A, B). Therefore, the microglial activation induced by OXA in the hippocampus and mPFC can be normalized by oral L-TAMS.

OXA-Induced Memory and Emotional Deficiency are Prevented by Inhibition of NF-κB

Thus far, we showed that OXA injections led to memory/emotional deficits and activation of TNF-α/NF-κB signaling in the hippocampus and mPFC by reducing brain Mg^{2+}, but causal links between the TNF-α/NF-κB activation and the abnormal behaviors in OXA-treated rats have not been established. To clarify this, the NF-κB inhibitor pyrrolidine dithiocarbamic acid (PDTC, 10 ng/5 μL) was injected icv 30 min before each OXA injection (Fig. 7A). The results showed that PDTC substantially prevented the short-term memory deficits and the anxiety-like and depression-like behaviors induced by OXA (Fig. 7B). Following the behavioral tests, the expression of *p*-p65 and TNF-α in the hippocampus and mPFC were assessed with western blots, which showed that the upregulation of *p*-p65 and TNF-α in both regions induced by OXA was completely prevented by PDTC (Fig. 8A, B). Furthermore, PDTC also prevented the OXA-induced microglial activation in the hippocampus and mPFC (Fig. S1). These data indicate that activation of TNF-α/NF-κB signaling is essential for OXA-induced memory, emotional deficiency, and microglial activation in the mPFC and hippocampus.

Discussion

In the present work, we showed that OXA injections induced memory and emotional deficits (Fig. 1) were accompanied by reduced Mg^{2+} in serum and CSF (Fig. 3A, B). Importantly, we found that oral L-TAMS prevented both the Mg^{2+} deficiency and the behavioral disorders induced by OXA (Figs. 1 and 3). OXA impaired frequency facilitation at CA3–CA1 synapses and downregulated the NR2B subunit of NMDARs in the hippocampus, and the effects were again prevented by oral L-TAMS. Mg^{2+} deficiency activated TNF-α/NF-κB signaling and downregulated NR2B in cultured hippocampal slices (Fig. 3C, D). Oral L-TAMS prevented the activation of TNF-α/NF-κB signaling and microglial activation in the hippocampus and mPFC induced by OXA (Figs 4, 5, 6). Finally, we showed that inhibition of NF-κB by icv injection of PDTC substantially prevented the behavioral and molecular changes induced by OXA (Figs. 7, 8, and S1). The data demonstrate that activation of TNF-α/NF-κB signaling resulting from Mg^{2+} deficiency may underlie the memory and emotional deficits induced by OXA, and these adverse effects are prevented by chronic oral L-TAMS. This study may provide a novel approach to treat chemotherapy-induced memory and emotional deficits.

Here, we used L-TAMS to supplement Mg^{2+} because a previous report [18] showed that only L-TAMS but not $MgCl_2$, Mg citrate, or Mg gluconate elevates Mg^{2+} in the CSF of rats. In patients, increasing the plasma Mg^{2+} by three-fold *via* intravenous infusion of $MgSO_4$ does not elevate Mg^{2+} in the CSF [40].

The Activation of TNF-α/NF-κB Signaling in Neurons Resulting from Mg^{2+} Deficiency may Underlie the OXA-induced Memory and Emotional Deficits

At present, the mechanisms underlying chemotherapy-induced memory/emotional deficits are unclear. As noted in the Introduction, many anti-cancer agents cause hypomagnesemia in patients. Consistent with this, our previous work in rats showed that vincristine (another anticancer agent) reduces the Mg^{2+} level in serum and CSF [33]. The present work showed that OXA also reduced Mg^{2+} in serum and CSF (Fig. 3A) and that supplementation of Mg^{2+} by oral L-TAMS prevented both the Mg^{2+} deficiency (Fig. 3A) and the memory/emotional deficits

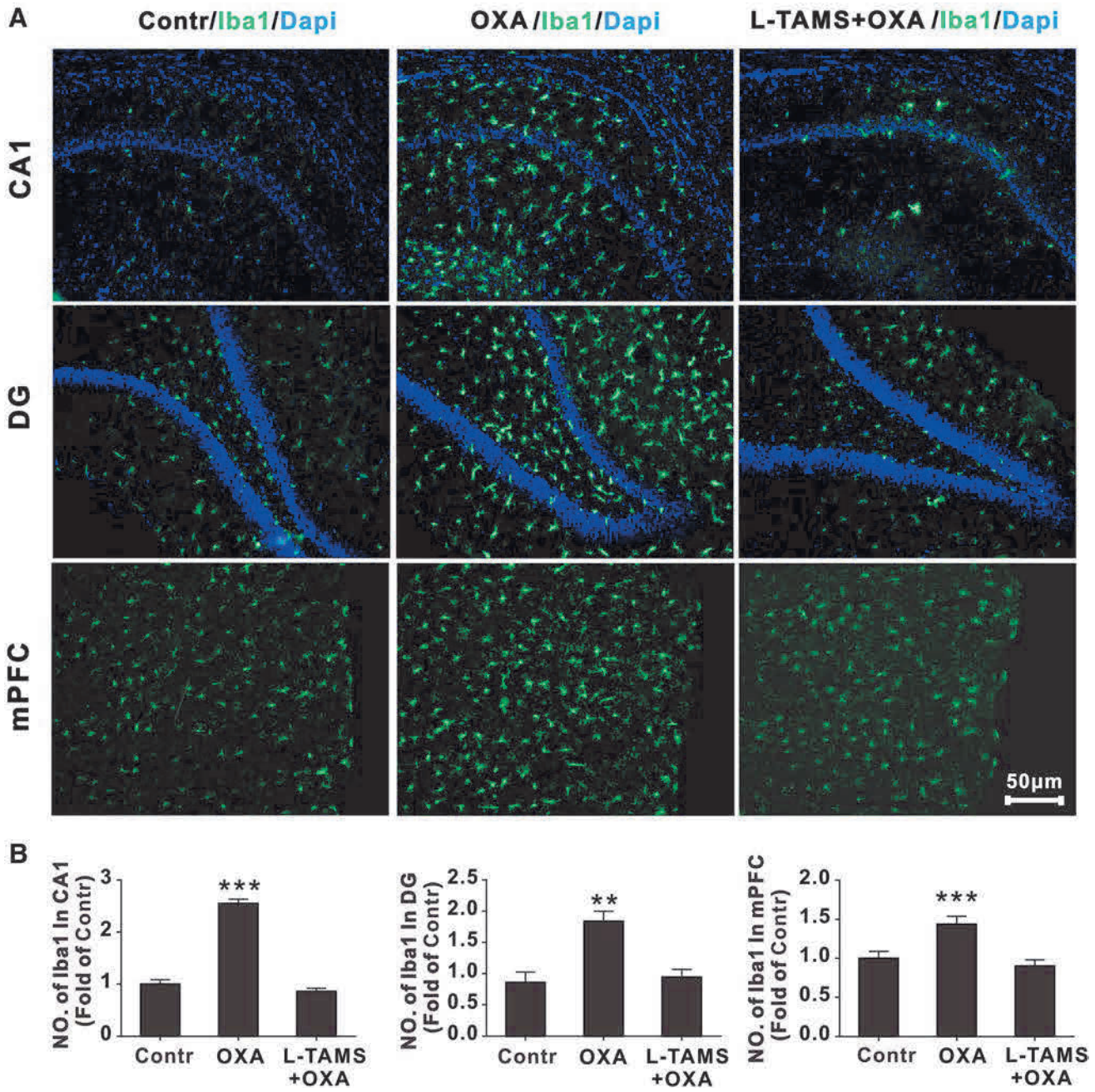

Fig. 6 Oral L-TAMS prevents the OXA-induced microglial activation in CA1 and the DG of the hippocampus and in mPFC. **A** Representative images of the immunofluorescence staining of Iba1 (a microglia marker) and DAPI in different groups as indicated. **B** Histograms showing summary data of Iba1 expression ($n = 6$ per group). $^{**}P < 0.01$, $^{***}P < 0.001$ *vs* controls (Contr) (one-way ANOVA followed by Tukey's *post hoc* test).

induced by OXA (Fig. 1). Therefore, we conclude that Mg^{2+} deficiency may be the root cause of OXA-induced cognitive dysfunction. Furthermore, we found that the memory and emotional deficits induced by OXA were accompanied by long-lasting activation of TNF-α/NF-κB signaling in neurons of the hippocampus and mPFC. Reducing Mg^{2+} in the medium (from 0.8 to 0.6 mmol/L in the CSF of control and OXA-treated rats) activated TNF-α/NF-κB signaling in cultured hippocampal slices, and the molecular and the behavioral changes induced by OXA were prevented by icv injection of an NF-κB inhibitor. Therefore, the activation of TNF-α/NF-κB in neurons resulting from Mg^{2+} deficiency is responsible for the OXA-induced memory and emotional deficits.

Previous reports [32, 41] have shown that dysfunction of the NR2B subunit of NMDARs is involved in memory deficits and depression. The present work showed that activation of TNF-α/NF-κB signaling was accompanied by

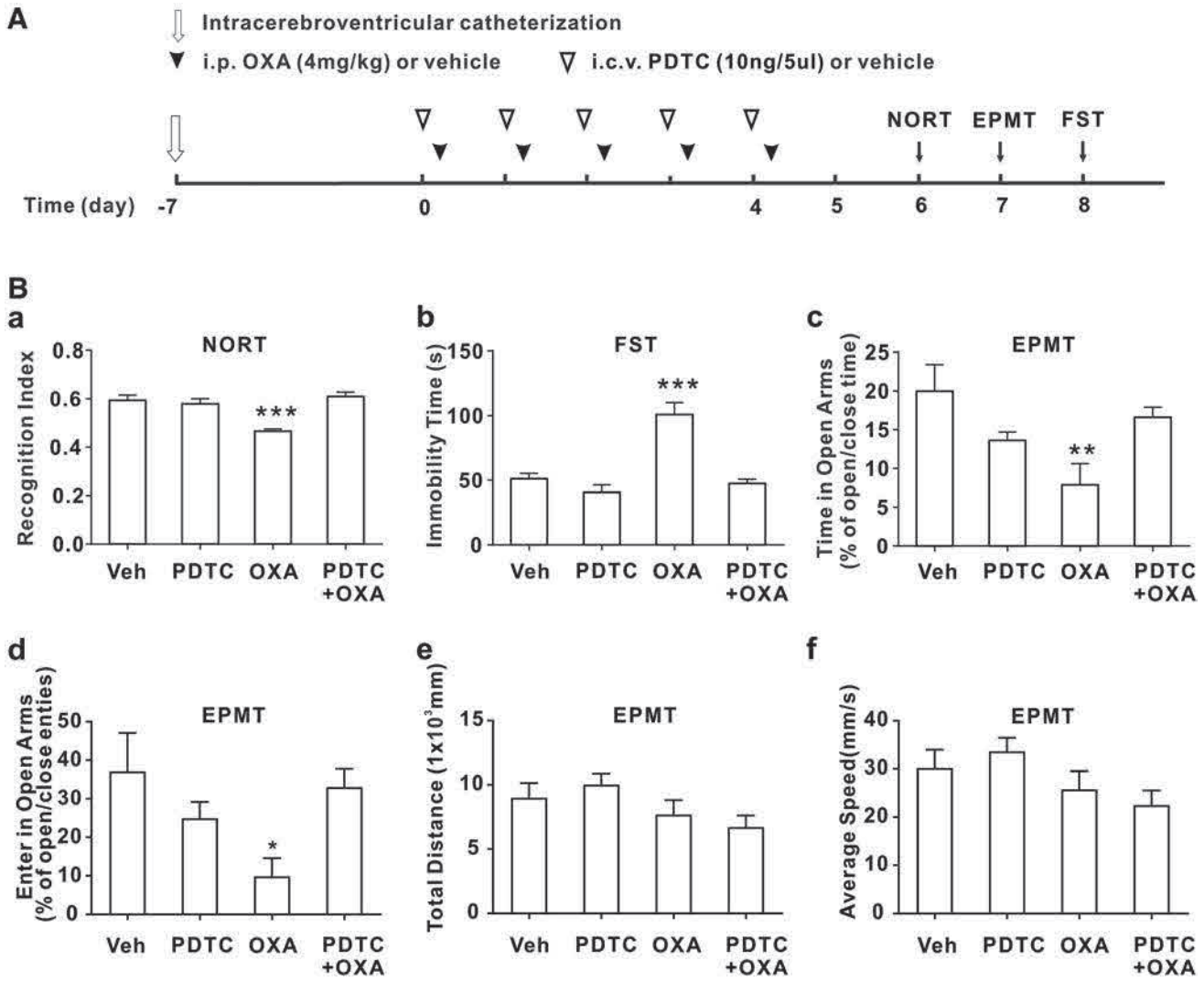

Fig. 7 The OXA-induced deficiency in memory and emotion is prevented by intracerebroventricular injection of the NF-κB inhibitor PDTC. **A** Experimental schedule. **B** A decrease in recognition index for short-term memory assessed with the NORT (a), an increase in immobility time with the FST (b), and a reduced time in open arms and bouts in the open arms with the EPMT (c, d) induced by i.p. injection of OXA were abolished by PDTC injection 30 min before each OXA injection ($n = 6$ per group). There was no difference in total distance traveled and average speed between groups in the EPMT (e, f). $^{**}P < 0.01$, $^{***}P < 0.001$ *vs* vehicle (Veh) group (one-way ANOVA followed by Tukey's *post hoc* test).

the downregulation of NR2B *in vivo*, and that in cultured hippocampal slices with lower Mg^{2+} the upregulation of TNF-α and NF-κB *p*-p65 was followed by downregulation of NR2B. These data indicate that the activation of TNF-α/NF-κB signaling resulting from Mg^{2+} deficiency may induce memory and emotional deficits *via* downregulation of NR2B.

We found that OXA also induced microglial activation, which is critical for chemotherapy-induced cognitive impairment [39]. Our previous work showed that vincristine activates TNF-α and NF-kB only in neurons but not in microglia in the spinal dorsal horn [33]. The present work showed that OXA also did the same in the hippocampus and mPFC. As TNF-α/NF-kB are not activated in microglia in the case of chemotherapy, the relationship between microglial activation and TNF-α/NF-κB might be indirect. We speculated that the release of inflammatory cytokines such as TNF-α from neurons may stimulate microglia. Conversely, the microglia may activate neuronal NF-κB *via* the release of gliotransmitters. The complicated neuron-glial interaction may contribute to the lasting TNF-α/NF-kB activation after the termination of OXA injection. Further studies are needed to clarify the mechanisms underlying the positive feedback.

Our finding that Mg^{2+} deficiency is the root cause of the memory and emotional deficits induced by OXA is clinically important, as it indicates that the mechanism underlying the side-effects is different from its anticancer

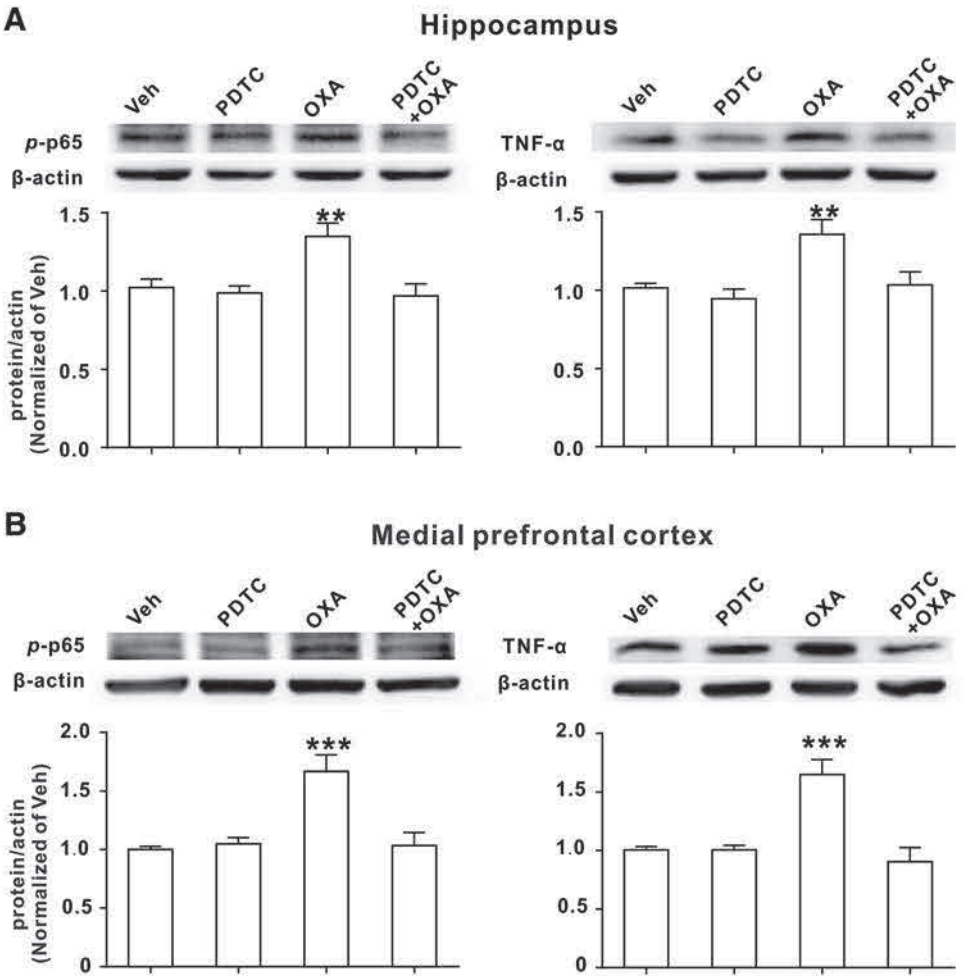

Fig. 8 OXA-induced upregulation of TNF-α and *p*-p65 in the hippocampus and mPFC are abolished by icv injection of PDTC. **A, B** Western blots and histograms showing the levels of *p*-p65 and TNF-α in the hippocampus (**A**, $n = 4$ per group) and mPFC (**B**, $n = 4$ per group) in the indicated groups. $^{***}P < 0.001$ *vs* vehicle (Veh) (one-way ANOVA followed by Tukey's *post hoc* test).

effect. In fact, accumulating evidence shows that NF-κB signaling plays critical roles in many aspects of cancers, such as cancer cell proliferation and survival, the epithelial-to-mesenchymal transition, and resistance to anticancer agents (see [17] for a review). Epidemiological studies have shown that high Mg^{2+} in drinking water reduces the risk of esophageal cancer [42] and liver cancer [43]. Therefore, Mg^{2+} supplementation may not only prevent the side-effects of chemotherapy but also be beneficial to the prevention and treatment of cancer. At present, how Mg^{2+} deficiency activates NF-κB signaling is unknown. As the second most abundant intracellular cation, Mg^{2+} is essential for more than 600 enzymatic reactions [44]. The dysfunction of some enzymes may be responsible for the activation of NF-κB. Further studies are needed to elucidate this issue.

We showed that an NF-κB inhibitor was also able to prevent the OXA-induced cognitive dysfunction (Fig. 7) and TNF-α upregulation in the hippocampus and mPFC (Fig. 8). However, TNF-α/NF-κB signaling has many physiological functions, such as memory storage [45] and immunity [17], so insufficient activation of the pathway may also impair these functions. It is difficult to regulate the pathway at a proper level *via* an NF-κB inhibitor. As noted above, anti-cancer agents lead to Mg^{2+} deficiency in both patients and in rats, and lowering extracellular Mg^{2+} leads to over-activation of TNF-α/NF-κB signaling. Accordingly, supplementary Mg^{2+} can normalize the pathway. Oral L-TAMS that can enhance brain Mg^{2+} may be a better way to prevent the chemotherapy-induced side-effects.

Impairment of Synaptic Transmission Contributes to the Chemotherapy-Induced Memory and Emotional Deficits

We found that the memory and emotional deficits induced by OXA were paralleled by impairment of frequency facilitation in synaptic transmission and downregulation of NR2B protein in the hippocampus. Both were prevented by oral L-TAMS. This is consistent with a previous report showing that L-TAMS improves memory and upregulates NR2B in the hippocampus of naïve rats [18]. It is well established that NR2B subunit-containing NMDARs at the

postsynaptic density are important for the strengthening of synaptic connections [46] and memory formation [32]. Furthermore, our previous work showed that the impairment of frequency facilitation at CA3–CA1 synapses is associated with a reduction of the density of presynaptic boutons [31]. Therefore, both presynaptic and postsynaptic impairment may cause a failure to follow repetitive afferent inputs in CA3–CA1 synapses, leading to the memory deficits induced by anticancer agents. Prevention of the synaptic dysfunction may contribute to the therapeutic effects of L-TAMS on the memory and emotional deficits induced by OXA.

In conclusion, the excessive activation of TNF-α/NF-κB signaling resulting from Mg^{2+} deficiency contributes to OXA-induced memory and emotional deficits. Supplementary Mg^{2+} by chronic oral L-TAMS is effective for preventing the TNF-α/NF-κB activation, and the memory and emotional deficits induced by OXA.

Acknowledgements This work was supported by the National Natural Science Foundation of China (31771166).

Conflict of interest The authors claim that there are no conflicts of interest.

References

1. Tannock IF, Ahles TA, Ganz PA, Van Dam FS. Cognitive impairment associated with chemotherapy for cancer: report of a workshop. J Clin Oncol 2004, 22: 2233–2239.
2. Ballenger JC, Davidson JR, Lecrubier Y, Nutt DJ, Jones RD, Berard RM*, et al.* Consensus statement on depression, anxiety, and oncology. J Clin Psychiatry 2001, 62 Suppl 8: 64–67.
3. Zhang J, Zhou Y, Feng Z, Xu Y, Zeng G. Longitudinal trends in anxiety, depression, and quality of life during different intermittent periods of adjuvant breast cancer chemotherapy. Cancer Nurs 2018, 41: 62–68.
4. Johnston IN, Tan M, Cao J, Matsos A, Forrest DRL, Si E*, et al.* Ibudilast reduces oxaliplatin-induced tactile allodynia and cognitive impairments in rats. Behav Brain Res 2017, 334: 109–118.
5. Hipkins J, Whitworth M, Tarrier N, Jayson G. Social support, anxiety and depression after chemotherapy for ovarian cancer: a prospective study. Br J Health Psychol 2004, 9: 569–581.
6. Hermelink K. Acute and late onset cognitive dysfunction associated with chemotherapy in women with breast cancer. Cancer 2011, 117: 1103; author reply 1103–1104.
7. Silberfarb PM. Chemotherapy and cognitive defects in cancer patients. Annu Rev Med 1983, 34: 35–46.
8. Gothelf D, Rubinstein M, Shemesh E, Miller O, Farbstein I, Klein A*, et al.* Pilot study: fluvoxamine treatment for depression and anxiety disorders in children and adolescents with cancer. J Am Acad Child Adolesc Psychiatry 2005, 44: 1258–1262.
9. Fountzilas E, Krishnan E, Janku F, Fu S, Karp DD, Naing A*, et al.* A phase I clinical trial of hepatic arterial infusion of oxaliplatin and oral capecitabine, with or without intravenous bevacizumab, in patients with advanced cancer and predominant liver involvement. Cancer Chemother Pharmacol 2018, 82: 877–885.
10. Konner J, Schilder RJ, DeRosa FA, Gerst SR, Tew WP, Sabbatini PJ*, et al.* A phase II study of cetuximab/paclitaxel/carboplatin for the initial treatment of advanced-stage ovarian, primary peritoneal, or fallopian tube cancer. Gynecol Oncol 2008, 110: 140–145.
11. Vogelzang NJ, Torkelson JL, Kennedy BJ. Hypomagnesemia, renal dysfunction, and Raynaud's phenomenon in patients treated with cisplatin, vinblastine, and bleomycin. Cancer 1985, 56: 2765–2770.
12. Hodgkinson E, Neville-Webbe HL, Coleman RE. Magnesium depletion in patients receiving cisplatin-based chemotherapy. Clin Oncol (R Coll Radiol) 2006, 18: 710–718.
13. Fakih M. Management of anti-EGFR-targeting monoclonal antibody-induced hypomagnesemia. Oncology (Williston Park) 2008, 22: 74–76.
14. Rodriguez-Moran M, Guerrero-Romero F. Elevated concentrations of TNF-alpha are related to low serum magnesium levels in obese subjects. Magnes Res 2004, 17: 189–196.
15. Meyers CA, Albitar M, Estey E. Cognitive impairment, fatigue, and cytokine levels in patients with acute myelogenous leukemia or myelodysplastic syndrome. Cancer 2005, 104: 788–793.
16. Yang M, Kim J, Kim JS, Kim SH, Kim JC, Kang MJ*, et al.* Hippocampal dysfunctions in tumor-bearing mice. Brain Behav Immun 2014, 36: 147–155.
17. Taniguchi K, Karin M. NF-kappaB, inflammation, immunity and cancer: coming of age. Nat Rev Immunol 2018, 18: 309–324.
18. Slutsky I, Abumaria N, Wu LJ, Huang C, Zhang L, Li B*, et al.* Enhancement of learning and memory by elevating brain magnesium. Neuron 2010, 65: 165–177.
19. Ying YL, Wei XH, Xu XB, She SZ, Zhou LJ, Lv J*, et al.* Overexpression of P2X7 receptors in spinal glial cells contributes to the development of chronic postsurgical pain induced by skin/muscle incision and retraction (SMIR) in rats. Exp Neurol 2014, 261: 836–843.
20. Wang J, Liu Y, Zhou LJ, Wu Y, Li F, Shen KF*, et al.* Magnesium L-threonate prevents and restores memory deficits associated with neuropathic pain by inhibition of TNF-alpha. Pain Physician 2013, 16: E563–575.
21. Abumaria N, Yin B, Zhang L, Li XY, Chen T, Descalzi G*, et al.* Effects of elevation of brain magnesium on fear conditioning, fear extinction, and synaptic plasticity in the infralimbic prefrontal cortex and lateral amygdala. J Neurosci 2011, 31: 14871–14881.
22. Liu G, Weinger JG, Lu ZL, Xue F, Sadeghpour S. Efficacy and safety of MMFS-01, a synapse density enhancer, for treating cognitive impairment in older adults: A randomized, double-blind, placebo-controlled trial. J Alzheimers Dis 2016, 49: 971–990.
23. Serefko A, Szopa A, Poleszak E. Magnesium and depression. Magnes Res 2016, 29: 112–119.
24. Zhang XL, Ding HH, Xu T, Liu M, Ma C, Wu SL*, et al.* Palmitoylation of delta-catenin promotes kinesin-mediated membrane trafficking of Nav1.6 in sensory neurons to promote neuropathic pain. Sci Signal 2018, 11.
25. Gui WS, Wei X, Mai CL, Murugan M, Wu LJ, Xin WJ*, et al.* Interleukin-1beta overproduction is a common cause for neuropathic pain, memory deficit, and depression following peripheral nerve injury in rodents. Mol Pain 2016, 12.
26. Detke MJ, Rickels M, Lucki I. Active behaviors in the rat forced swimming test differentially produced by serotonergic and noradrenergic antidepressants. Psychopharmacology (Berl) 1995, 121: 66–72.
27. Leung LW. Orthodromic activation of hippocampal CA1 region of the rat. Brain Res 1979, 176: 49–63.

28. Abernethy MH, Fowler RT. Micellar improvement of the calmagite complexiметric measurement of magnesium in plasma. Clin Chem 1982, 28: 520–522.
29. De Simoni A, My Yu L. Preparation of organotypic hippocampal slice cultures: interface method. Nature Protocols 2006, 1: 1439–1445.
30. Phelps EA. Human emotion and memory: interactions of the amygdala and hippocampal complex. Curr Opin Neurobiol 2004, 14: 198–202.
31. Ren WJ, Liu Y, Zhou LJ, Li W, Zhong Y, Pang RP*, et al.* Peripheral nerve injury leads to working memory deficits and dysfunction of the hippocampus by upregulation of TNF-alpha in rodents. Neuropsychopharmacology 2011, 36: 979–992.
32. Lee YS, Silva AJ. The molecular and cellular biology of enhanced cognition. Nat Rev Neurosci 2009, 10: 126–140.
33. Xu T, Li D, Zhou X, Ouyang HD, Zhou LJ, Zhou H*, et al.* Oral application of magnesium-L-threonate attenuates vincristine-induced allodynia and hyperalgesia by normalization of tumor necrosis factor-alpha/nuclear factor-kappaB signaling. Anesthesiol 2017, 126: 1151–1168.
34. Terrando N, Monaco C, Ma D, Foxwell BM, Feldmann M, Maze M. Tumor necrosis factor-alpha triggers a cytokine cascade yielding postoperative cognitive decline. Proc Natl Acad Sci U S A 2010, 107: 20518–20522.
35. Himmerich H, Fulda S, Linseisen J, Seiler H, Wolfram G, Himmerich S*, et al.* Depression, comorbidities and the TNF-alpha system. Eur Psychiatry 2008, 23: 421–429.
36. Fourrier C, Bosch-Bouju C, Boursereau R, Sauvant J, Aubert A, Capuron L*, et al.* Brain tumor necrosis factor-alpha mediates anxiety-like behavior in a mouse model of severe obesity. Brain Behav Immun 2019, 77: 25–36.
37. Euston DR, Gruber AJ, McNaughton BL. The role of medial prefrontal cortex in memory and decision making. Neuron 2012, 76: 1057–1070.
38. Belleau EL, Treadway MT, Pizzagalli DA. The impact of stress and major depressive disorder on hippocampal and medial prefrontal cortex morphology. Biol Psychiatry 2019, 85: 443–453.
39. Gibson EM, Monje M. Emerging mechanistic underpinnings and therapeutic targets for chemotherapy-related cognitive impairment. Curr Opin Oncol 2019.
40. McKee JA, Brewer RP, Macy GE, Borel CO, Reynolds JD, Warner DS. Magnesium neuroprotection is limited in humans with acute brain injury. Neurocrit Care 2005, 2: 342–351.
41. Li Y, Liu J, Liu X, Su CJ, Zhang QL, Wang ZH*, et al.* Antidepressant-like action of single facial injection of botulinum neurotoxin A is associated with augmented 5-HT levels and BDNF/ERK/CREB pathways in mouse brain. Neurosci Bull 2019, 35: 661–672.
42. Yang CY, Chiu HF, Tsai SS, Wu TN, Chang CC. Magnesium and calcium in drinking water and the risk of death from esophageal cancer. Magnes Res 2002, 15: 215–222.
43. Tukiendorf A, Rybak Z. New data on ecological analysis of possible relationship between magnesium in drinking water and liver cancer. Magnes Res 2004, 17: 46–52.
44. Romani AM. Cellular magnesium homeostasis. Arch Biochem Biophys 2011, 512: 1–23.
45. Meffert MK, Baltimore D. Physiological functions for brain NF-kappaB. Trends Neurosci 2005, 28: 37–43.
46. Shipton OA, Paulsen O. GluN2A and GluN2B subunit-containing NMDA receptors in hippocampal plasticity. Philos Trans R Soc Lond B Biol Sci 2014, 369: 20130163.

Neurosci. Bull. January, 2021, 37(1):70–80
https://doi.org/10.1007/s12264-020-00527-1

www.neurosci.cn
www.springer.com/12264

ORIGINAL ARTICLE

Dynamic Brain Responses Modulated by Precise Timing Prediction in an Opposing Process

Minpeng Xu[1,2] · Jiayuan Meng[1] · Haiqing Yu[1] · Tzyy-Ping Jung[1,3] · Dong Ming[1,2]

Received: 9 December 2019 / Accepted: 11 February 2020 / Published online: 16 June 2020

Abstract The brain function of prediction is fundamental for human beings to shape perceptions efficiently and successively. Through decades of effort, a valuable brain activation map has been obtained for prediction. However, much less is known about how the brain manages the prediction process over time using traditional neuropsychological paradigms. Here, we implemented an innovative paradigm for timing prediction to precisely study the temporal dynamics of neural oscillations. In the experiment recruiting 45 participants, expectation suppression was found for the overall electroencephalographic activity, consistent with previous hemodynamic studies. Notably, we found that N1 was positively associated with predictability while N2 showed a reversed relation to predictability. Furthermore, the matching prediction had a similar profile with no timing prediction, both showing an almost saturated N1 and an absence of N2. The results indicate that the N1 process showed a 'sharpening' effect for predictable inputs, while the N2 process showed a 'dampening' effect. Therefore, these two paradoxical neural effects of prediction, which have provoked wide confusion in accounting for expectation suppression, actually co-exist in the procedure of timing prediction but work in separate time windows. These findings strongly support a recently-proposed opposing process theory.

Keywords Expectation suppression · Predictive coding · Event-related potentials · Timing prediction

Introduction

Human perceptions are shaped by not only sensory inputs, but also prior knowledge stored in the brain [1, 2]. The ability to generate and utilize prediction is fundamental for survival [2, 3], and has been demonstrated to be indispensable in a wide range of mental processes [4–8]. However, the neural effect and underlying mechanism of prediction remains controversial.

Predictive coding, an influential theory of the neural process of prediction, proposes that the brain actively builds up predictive templates to shape perceptions, rather than being driven merely by bottom-up stimuli. It optimizes perceptions using prediction errors, i.e., differences between predictions and sensory inputs [9–11]. In this way, unexpected stimuli would induce more neural activity than expected stimuli, to address larger prediction errors. This is known as the 'dampening' effect, i.e. the neural representations is 'dampened' for predictable stimuli. The phenomenon of expectation suppression has been reported in both the electroencephalographic (EEG) and hemodynamic studies [12–16]. However, some studies have shown that even with lower brain responses, the expected stimuli have more salient neural representation than unexpected stimuli [17–21], which is beyond the 'dampening' account. This

Minpeng Xu and Jiayuan Meng contributed equally to this work.

Electronic supplementary material The online version of this article (https://doi.org/10.1007/s12264-020-00527-1) contains supplementary material, which is available to authorized users.

✉ Dong Ming
richardming@tju.edu.cn

[1] College of Precision Instruments and Optoelectronics Engineering, Tianjin University, Tianjin 300072, China

[2] Academy of Medical Engineering and Translational Medicine, Tianjin University, Tianjin 300072, China

[3] Swartz Center for Computational Neuroscience, University of California, San Diego, CA 92093, USA

unusual phenomenon was explained by Kok *et al.* as prediction actually 'sharpening' and not 'dampening' the neural representation [22]. The 'sharpening' account holds the view that, although the overall neural activity in response to expected information seems to be suppressed, the neurons encoding the expected information are not suppressed—it is the neurons not tuned to the expected information that are suppressed, making the expected features more salient and selective, concurrently resulting in lower neural responses [3]. Although some conflicting phenomena can be explained by the reversal of prediction-related representations by attention [23], we are still far from understanding the mechanism underlying the reported paradoxical effects of prediction.

Recently, increasing numbers of studies have realized that it may be misleading to stress only one effect of prediction during the whole predictive coding process [2, 3]. Clark *et al.* highlighted the duplex architecture of predictive coding theory [2], which assumes that at each prediction processing level, the representational and error signals are encoded by two functionally distinct units [1, 24–26], although how they interact over time remains unclear. Moreover, Friston proposed that prediction processing may dynamically evolve from sensory representation to error correction (or perceptual learning) [10]. Inspired by these assumptions, a recent opposing processing theory posited that perception is initially biased towards the expected information after the sensory representation, and no other process is needed if the inputs are sufficiently in line with current expectation, while error-correction would be conducted if the input is different enough from the expectation [27]. That means, the paradoxical 'sharpening' and 'dampening' effects of prediction may be reconciled by studying the neural signals at fine temporal resolution. Therefore, we set out to investigate the temporal dynamics of predictive timing processes to obtain experimental evidence associated with the 'sharpening' and 'dampening' effects, and to determine whether these conflicting effects are compatible during the dynamic process. To this end, we designed an innovative experimental paradigm to study the time course of neural oscillations under different precise timing prediction states, and found that the 'sharpening' and 'dampening' effects of prediction actually co-exist in the predictive timing process, but in distinct processing stages with an opposing trend.

Materials and Methods

Participants

Forty-five healthy individuals (23 females, 19–28 years old) participated in the current experiment. Forty-two were right-handed and other three were left-handed. All individuals had normal or corrected-to-normal vision, and were free from psychological or neurological diseases. The experimental procedures were approved by the Institutional Review Board at Tianjin University. All possible consequences of the study were explained, and written informed consent was given by all participants.

Stimulus

The double-flashes used in this study were presented by a 15×15 mm^2 LED placed at the eye level and 80 cm from the participant. The LED was driven by a chronometric FPGA platform (Cyclone II: EP2C8T144C8) with 20-ns resolution. The duration of each flash was 120 ms (Fig. 1). Each trial started with an auditory cue that lasted for 1,000 ms. Then there was a blank with a random duration selected from 1,000 ms, 1,500 ms, or 2,000 ms. Next, a double-flash appeared with unpredictable stimulus-onset asynchrony (SOA) of 400 ms, 600 ms, or 900 ms. Finally, there was a blank period between 1,600 ms and 2,600 ms before the next trial. A total of 30 trials were conducted in one session, and 16 sessions were conducted for each participant. Thus, there were 160 trials for each kind of double-flash.

Training Procedure

According to predictive coding theory, the construction of the perceptual template is a prerequisite for the brain's predictive processing [28–30]. Therefore, it is very important for participants to set up a precise template in their minds before testing its influences on sensory inputs. As the mental clock in the human brain is not very precise, and is relatively insensitive to sub-second time intervals without proper training [31], it is difficult for participants to set up a precise timing template only using recent ambiguous experiences, such as temporarily learning past repetitions [13, 32] or temporal associations [33]. For this reason, training sessions were necessary in this study. The precise timing template built up in the training sessions made the predictive processing in the formal experiment more stable and invariable across trials, and made this study sensitive and reliable.

All participants were trained for about three days before testing (the specific training time in each day differed

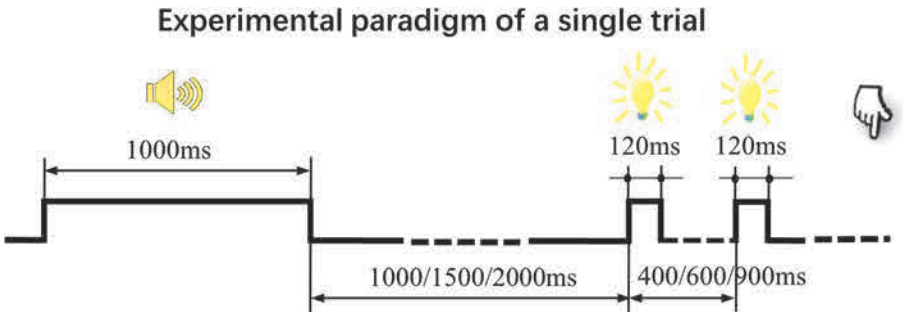

Fig. 1 Illustration of a single trial in the testing experiment. In each trial, a loudspeaker first sounds for 1,000 ms to alert the participant to the upcoming double-flash, followed by a random blank period (1,000 ms, 1,500 ms, or 2,000 ms). Then the LED in front of the participant flashes twice with an unpredictable SOA. Each participant was required to press different buttons to indicate their judgments.

among participants). The averaged task accuracy improved from 62.58% to 92.36%, and the average reaction time shortened from 998.60 ms to 509.32 ms (details in Fig. S1). Only when the participants achieved high enough accuracy (> 85%) for more than five training blocks, which indicated that the timing templates were stably stored in their minds, were they allowed to take part in the formal experiment.

Formal Experimental Procedure

In the formal experiment, each participant was required to conduct four different kinds of mental task. Specifically, they were required to (1) compare the actual double-flash with the SOA400 double-flash in their mind (under this instruction, the participants were only allowed to recall the SOA400 double-flash so that the SOA400 timing template was exclusively deployed as the initial predicative code. Therefore, the actual SOA400 double-flash absolutely matched the prediction, AMP); (2) compare the actual double-flash with the SOA600 timing template (under this instruction, the participants were only allowed to recall the SOA600 double-flash so that the SOA600 timing template was exclusively deployed as the initial predictive code. Therefore, the actual SOA400 double-flash mismatched the prediction, MMP); (3) determine which SOA the actual double-flash was from 400, 600, or 900 ms (under this instruction, the participants needed to concurrently recall SOA400, SOA600, and SOA900 double-flashes so that all three timing templates were deployed for the initial prediction state. Therefore, the actual SOA400 double-flash partially matched the prediction, PMP); and (4) indicate the onset of the second flash (under this instruction, no predictive code, NPC, was initially deployed). After each double-flash, each participant made a judgement by pressing a specific button as soon as possible. This study only focused on the brain responses to stimuli with the SOA400 double-flash, because the longer SOA raised the problem of information disclosure to participants after 400 ms.

There were 4 sessions for each mental task, and all the sixteen sessions were interleaved. In each session, the three kinds of double-flash were presented in a random order with equal probability, and no choice preference was found when participants made decisions (Fig. S2). Moreover, pressing a button with the right or left thumb was balanced across sessions. In particular, for AMP and MMP, each participant was required to use the right or left thumb to press the Match/Mismatch button in two sessions, and have an exchange in the other two sessions. For PMP, they were required to use the right thumb to press the SOA400 button in two sessions, and the left thumb to press the SOA400 button in the other two sessions. For NPC, they were required to use the right thumb to press the button in two sessions, and the left thumb to press the button in the other two sessions.

In addition, two points need to be further explained for a better understanding of the experimental paradigm. First, this study shaped the matching and mismatching processes of timing prediction by comparing the actual with the predicted time lapses, which was adapted from previous studies of feature-based prediction [30, 34]. Second, the current paradigm for shaping the timing prediction avoided the problem caused by using recent experiences of past stimulus repetitions. As the stimulus repetition would entail entrainment of neural oscillations which could influence the following neural process and response [33, 35, 36], it would disturb the natural predictive processing, making it impossible to decouple the top-down influence of timing prediction from the bottom-up influence of neural entrainment.

EEG Recording and Pre-processing

EEG was recorded by a Neuroscan Synamps2 system at a sample rate of 1000 Hz, and filtered by a low-pass filter at 200 Hz and a notch filter at 50 Hz. Sixty-four electrodes

were positioned on the scalp according to the International 10–20 system. We only focused on signals from the parietal and occipital regions. All channels were referenced to the tip of the nose and grounded to the frontal region. Eye-blinks were monitored by signals recorded at FP1 and FP2. The stored EEG data were then filtered by a ChebyshevII low-pass filter cutting at 45 Hz, and down-sampled to 200 Hz. EEG trials were segmented from − 900 ms to 2,100 ms after the second flash onset. Only correct trials with reaction latencies between 100 ms and 800 ms were considered in the subsequent analyses. For the first ERP, the baseline was corrected by subtracting the mean of 200 ms of data before the first flash onset, while for the second ERP, the baseline was corrected by subtracting the mean of 50 ms of data before the second flash onset to avoid the influence of contingent negative variations (CNVs).

ERP Amplitude and Latency Measurements

The predictive coding theory was originally proposed to explain the prediction mechanism in primary visual cortex [9]. Low-level sensory processing is an important issue for the prediction mechanism and has become a research topic of interest [12, 23, 37]. Therefore, we mainly focus on the ERPs of the posterior scalp locations where low-level visual processing predominately takes place. On the basis of grand averages, the time windows of the first N1 and N2 ERPs were defined as − 260 ms to − 225 ms and − 170 ms to − 105 ms, and those of the second N1 and N2 ERPs as 130 ms to 165 ms and 200 ms to 260 ms, respectively. In addition, as the durations of the N2 component varied with conditions, we also applied jack-knife-based scoring methods to measure the N2 components (AMP, 205 ms–225 ms; PMP, 205 ms–250 ms; MMP, 205 ms–275 ms; details in Fig. S3). The amplitude of each ERP component was calculated as the mean within the specified time window. The latency was measured as the time point before which 50% of the total component area occurred in the specified time window.

Inter-trial Coherence (ITC), Event-Related Spectral Perturbation (ERSP), and Evoked EEG Energy

ITC measures the consistency across trials of the EEG spectral phase at each frequency and time window [38]; it ranges from 0 to 1. The testing trials showed more phase coherence, so the ITC value was closer to 1. ERSP reflects the changes of event-related spectral power at each time-frequency point compared to the baseline of pre-stimulus spectral power in its corresponding frequency band [38]. For the first response, the baseline was the mean of 200 ms of data before the first flash onset, while for the second response, the baseline was the mean of 50 ms of data before the second flash onset. The evoked EEG energy was the sum of the ERSP values from 0 s to 2.4 s after the first flash onset, where the baseline was the mean of 200 ms of data before the first flash onset.

Statistical Tests

One-way repeated-measures ANOVA with Bonferroni correction was used to test the significance of behavioral differences among conditions. Two-way repeated-measures ANOVA (electrode × condition) was used to test the significance of the ERP, ITC, ERSP, and evoked EEG energy differences, and only the effects of condition are shown. Bonferroni correction was used for multiple comparisons of conditions. Paired *t*-tests were used to test the significance of ERP differences between AMP and NPC. All error bars show 95% within-participant confidence intervals of the mean difference between conditions.

Results

Behavioral Analyses

In this study, a participant's behavior could be influenced by two factors – task difficulty and prediction state – which were addressed separately. Since NPC was the easiest and simplest task, it elicited the highest response accuracy (99.89% ± 0.52%) and the shortest reaction time (RT, 268.25 ± 55.50 ms), which were significantly superior to AMP (accuracy, 97.33% ± 2.89%; RT, 398.60 ± 56.42 ms; both $P < 0.001$ after Bonferroni correction), PMP (accuracy, 92.94% ± 5.44%; RT, 494.21 ± 54.85 ms; both $P < 0.001$ after Bonferroni correction), and MMP (accuracy, 89.67% ± 7.66%; RT, 530.22 ± 57.45 ms; both $P < 0.001$ after Bonferroni correction) (Fig. 2A, B). From the number of options, PMP was the most difficult task because participants had to address three options, while there were only two options for AMP and MMP. However, the behavioral performance of MMP was, on the contrary, worse than that of PMP. Specifically, MMP had a longer RT ($P < 0.001$) and lower accuracy than PMP ($P = 0.105$ after Bonferroni correction). This can only be explained by a wrong prediction slowing the reaction, which indicated that the prediction state played a greater role than task difficulty here. In addition, AMP had significantly higher accuracy and a shorter RT than PMP (both $P < 0.001$ after Bonferroni correction) and MMP (both $P < 0.001$ after Bonferroni correction), which further demonstrated that a correct prediction speeds up the reaction [33]. Therefore, the prediction state indeed played a crucial role in responding

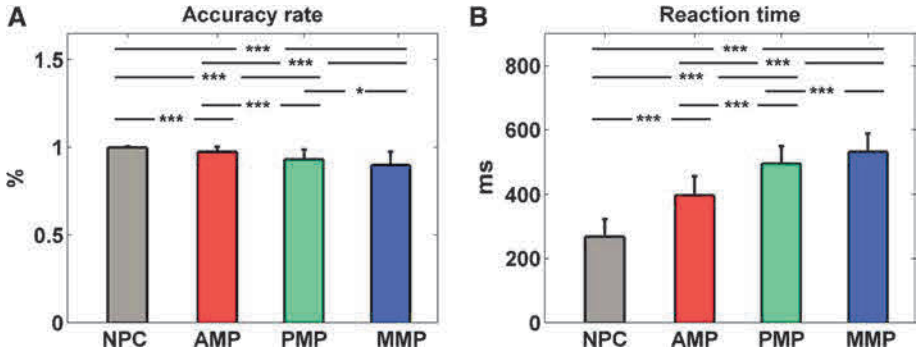

Fig. 2 Accuracy rate (**A**) and reaction time (**B**) for different conditions. Comparison of the evoked EEG energy of the whole predictive response. Evoked energies in the delta and theta bands were summed from 0 s to 2.4 s after the first flash onset. Vertical lines, error bars; $*P < 0.05$, $**P < 0.01$, $***P < 0.001$ after Bonferroni correction.

to the SOA400 double-flash. The setting of three but not two options for PMP was to rule out the risk that participants could mistakenly treat the task in the same way as AMP and MMP, because judging which one the SOA was from two options might be replaced by judging whether the SOA was familiar and expected or not, as the latter was easier, which required participants to remember only one SOA.

Analyses of Evoked EEG Energy

Expectation suppression (neural responses suppressed by correct compared to the incorrect predictions) has been widely demonstrated in blood-oxygen-level-dependent (BOLD) imaging studies [12, 14, 30]. However, electrophysiological evidence is still lacking. Here, we measured the evoked EEG energy of the whole predictive response to the SOA400 double-flash (the background EEG energy estimated by the baseline before the first flash was removed from the total energy of the brain responses after stimulus onset) to assess the degree of neural activation for different conditions. We found that the predictive response under matching prediction induced significantly less energy than that under mismatching prediction (F (2,88) = 5.607, P = 0.005), especially in the low-frequency band (< 13 Hz). Specifically, the evoked energy for AMP was smaller than MMP (AMP *vs* PMP P = 0.012 after Bonferroni correction; Fig. 3). However, there were no significant differences among the three conditions for the other frequency bands (details in supplementary materials). Therefore, the overall neural activation in the early sensory regions was suppressed for the correct compared to the incorrect prediction, in line with the BOLD studies.

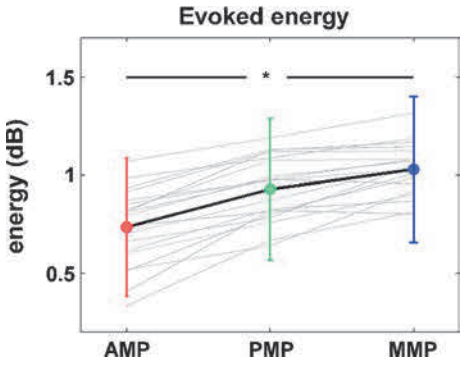

Fig. 3 Analyses on the evoked EEG energy of brain responses.

ERP Analyses

We compared the posterior ERPs of AMP, PMP, and MMP, and found the variations of N1 and N2 induced by the second flash were relevant to the process of timing prediction. To be specific, the SOA400 double-flash elicited two successive ERPs with a time interval of 400 ms (Fig. 4A). Since the upcoming moment of the first flash was unpredictable for all conditions, their responses would be the same. As expected, the first grand average ERPs following the first flash did not markedly differ across the three conditions, and their topographies were remarkably similar (Fig. 4D, F). Component analyses demonstrated no significant differences among the three conditions for the first N1 (F (2,88) = 0.793, P = 0.456) and N2 (F (2,88) = 0.776, P = 0.463) potentials in the posterior area. However, the grand average ERPs following the second flash showed considerable differences after removal of their different baselines caused by distinct CNVs (Fig. 4B, the reason for removing the CNVs is explained in the discussion). Topographic analyses revealed that the second N1 component was the largest for AMP on the whole posterior scalp, medium for PMP, and smallest for MMP, which were positively related to predictability (Fig. 4E). On the contrary, the second N2 component was largest for MMP, medium for PMP, and smallest for AMP, which were negatively related to the predictability (Fig. 4G). Component analyses further demonstrated that the two potentials had an opposite changing trend, i.e. decreasing N1 but increasing N2 against unpredictability (Fig. 4H, I). Such amplitude changes among the three conditions were significant for both N1 (F (2,88) = 5.367, P = 0.006; AMP *vs* MMP: P = 0.009; AMP *vs* PMP: P = 0.537; PMP *vs* MMP:

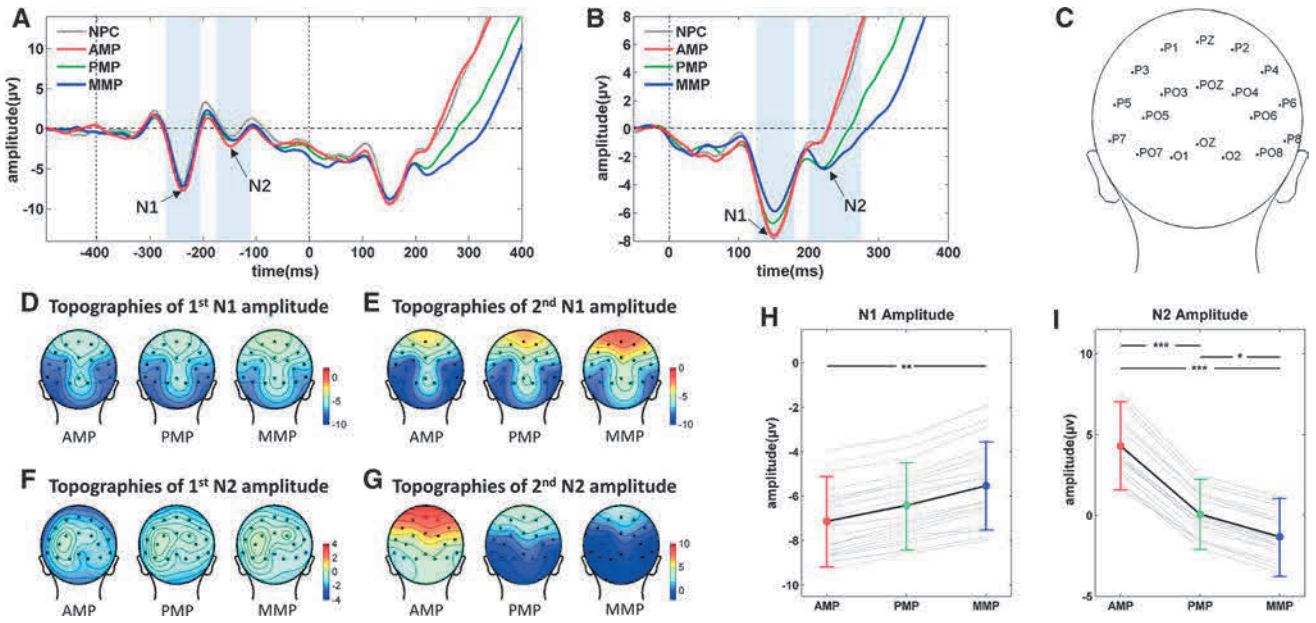

Fig. 4 ERP analyses. **A** Grand average ERPs induced by the SOA400 double-flash, across participants and electrodes on the posterior scalp under NPC, AMP, PMP, and MMP conditions (time zero is defined as the moment when the second flash is triggered). **B** Grand average ERPs induced by the second flash of the SOA400 double-flash (baseline averaged between − 50 ms and 0 ms is removed). **C** Names and locations of electrodes used. **D–G** Amplitude topographies of the first N1 (**D**), second N1 (**E**), first N2 (**F**), and second N2 (**G**) under distinct conditions. **H** N1 amplitudes induced by the second flash for AMP, PMP, and MMP (small dots, amplitude at each electrode; large dots, average amplitude). **I** N2 amplitudes induced by the second flash for AMP, PMP, and MMP. Vertical lines, error bars; $^{*}P < 0.05$, $^{**}P < 0.01$, $^{***}P < 0.001$ (*post hoc* tests after Bonferroni correction).

$P = 0.071$ all after Bonferroni correction) and N2 (F (2,88) = 40.907, $P < 0.001$; PMP *vs* MMP: $P = 0.035$; others: $P < 0.001$, all after Bonferroni correction). Then the second posterior scalp ERPs of AMP were compared to those of the NPC. Since the NPC had no timing prediction and needed no comparisons between the predictive code and sensory input, it was the least influenced by the top-down factors, which could act as a baseline for studying the neural effects of timing prediction. The two ERP waveforms were almost identical; no statistical difference was found in both the amplitudes (N1: T (44) = 0.307, $P = 0.760$; N2: T (44) = − 0.620, $P = 0.539$) and latencies (N1: T (44) = 1.366, $P = 0.179$; N2: T (44) = 0.878, $P = 0.385$) (Fig. 5A–E).

The above phenomena indicated that both N1 and N2 were modulated by prediction but in different manners. Specifically, compared to the baseline of NPC, the amplitude decreased for N1 while increasing for N2 with the increase of unpredictability, i.e., concurrent changes of N1 and N2 in opposite trends with the modulation of precise timing prediction.

It should be noted that a slow positive waveform followed the N2 component. It might be argued that this waveform was caused by the button-press, so the N2 variation recorded here was also due to the button-press rather than by timing prediction. However, this is not the case. First, if the N2 variation was caused by the button-press, the N2 latency would be closely associated with the RT. As the RT of NPC was the shortest of all ($P < 0.001$), accordingly, it should have much shorter latency than the other conditions. However, the N2 latencies of NPC and AMP were almost identical ($P = 0.385$), regardless of the significant differences in RT. Correlation analysis further showed no correlation between the N2 latency and RT ($r < 0.01$, $P = 0.96$; Fig. 5F), indicating that the N2 variations were not caused by the button-press. Second, the component analyzed here occurred in the early sensory processing stage (200 ms–260 ms after target onset), of which the defined temporal window was similar to the typical error-related component reported in a previous study [39], rather than that caused by the button-press or its preparation, which mainly emerged at the late sensory processing stage as a slow waveform [40, 41]. In addition, in order to further confirm that the N2 component measured here was dissociated from the subsequent slow waveform, we also applied the jackknife-based scoring method [42, 43], which defined the N2 time window according to the length of the negative-going component (AMP, 205 ms–225 ms; PMP, 205 ms–250 ms; MMP, 205 ms–275 ms) and obtained similar results (details in Fig. S3).

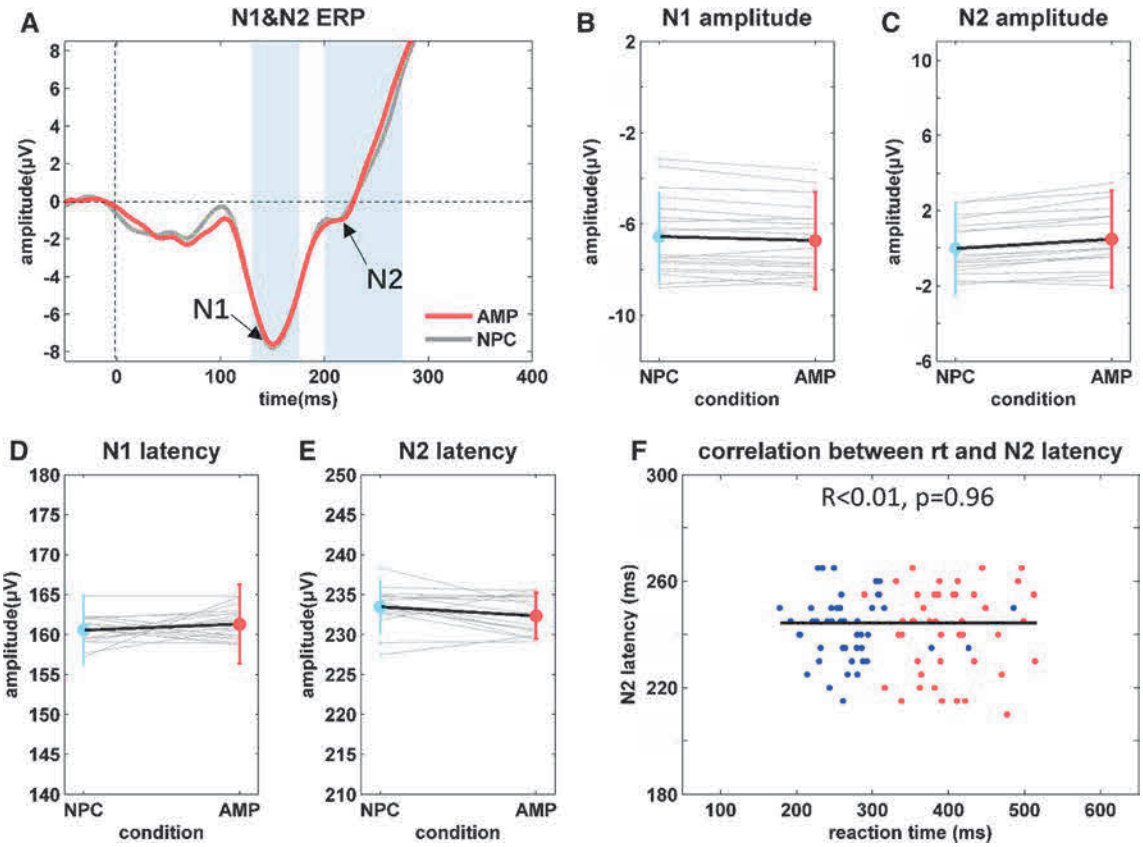

Fig. 5 Second ERPs for NPC and AMP. **A** Grand averages of the second ERP for NPC and AMP. **B**, **C** Comparison of the second N1 (**B**) and N2 (**C**) amplitude under NPC and AMP conditions (small dots, average N1/N2 amplitude at each electrode across all participants; large dots, average across all participants and all electrodes in the posterior area; vertical lines, error bars). **D**, **E** Comparison of the latency of the second N1 (**D**) and N2 (**E**) components. **F** Correlation analysis between RT and N2 latency (blue dots, RT and N2 latency in the NPC condition for each person; red dots, those in the AMP condition).

ITC and ERSP Analyses

Next, we analyzed the second posterior ERP using the ITC and ERSP techniques (Fig. 6A, C). As a result, both ITC and the evoked power of N1 in the theta band decreased from AMP to PMP to MMP, consistent with the above ERP results. Specifically, the theta-band ITC had a significant decreasing trend from AMP to PMP to MMP (Fig. 6B; F (2,88) = 15.827; $P < 0.001$; AMP *vs* PMP: $P = 0.031$; others: $P < 0.001$, all after Bonferroni correction). However, for the first N1, the theta band ITC showed no significant differences among conditions (F (2,88) = 1.021; $P = 0.364$). Furthermore, no significant differences in ITC were found in the other frequency bands for both the first and second N1 components (Fig. S4). The ERSP results were similar to those with ITC. The theta-band ERSP of the second N1 was largest for AMP, medium for PMP, and smallest for MMP (Fig. 6D); the differences were significant (F (2, 88) = 7.550; $P = 0.001$; AMP *vs* PMP: $P = 0.027$; AMP *vs* MMP: $P = 0.002$; PMP *vs* MMP: $P = 0.998$; all after Bonferroni correction). However, there was neither a significant ERSP difference in the theta band for the first N1 (F (2, 88) = 1.183; $P = 0.311$) nor in other frequency bands for both the first and second N1 components (Fig. S5). Here, we could not analyze ITC and ERSP of the second N2 because the small N2 components were smeared by the following large P3 potentials due to the restricted resolution of time-frequency transformation. Therefore, greater theta-band neural activity would be elicited during the sensory matching process for a matching prediction than a mismatching prediction.

Discussion

Consistent with previous BOLD studies, in this study we found the phenomenon of expectation suppression, i.e. the evoked EEG energy was lower for the matching than the mismatching prediction. Furthermore, the dynamic process of timing prediction was revealed by ERP analyses. As a result, compared to the control condition of no timing prediction, the N1 potential maintained almost the same

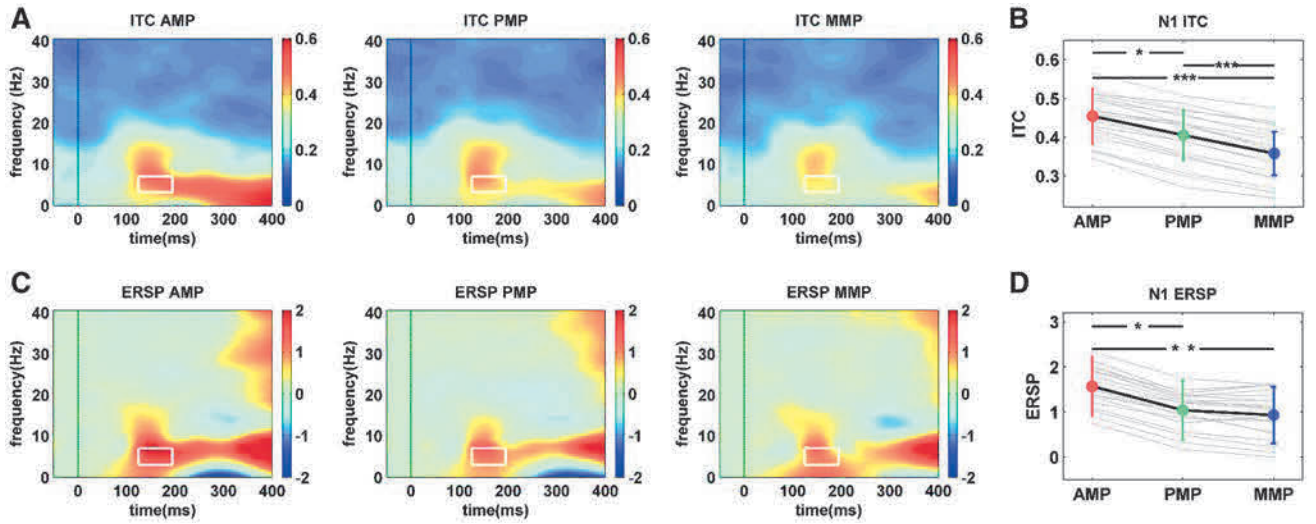

Fig. 6 Time-frequency decomposition analyses. **A** ITC for AMP, PMP, and MMP (white boxes, theta-band N1). **B** Comparison of N1 ITC in the theta band. **C** ERSP for AMP, PMP, and MMP (white boxes, theta-band N1). **D** Comparison of the N1 ERSP in the theta band. Vertical lines, error bars; $*P < 0.05$, $**P < 0.01$, $***P < 0.001$ (*post hoc* tests after Bonferroni correction).

profile for the expected condition but was suppressed for the unexpected condition. This indicates that prediction 'sharpens' the expected sensory input during the N1 period. However, N2 was enhanced for the unexpected compared to the expected condition. This indicates that prediction 'dampens' the expected sensory information and encodes the prediction error. Therefore, underlying the phenomenon of expectation suppression, the 'sharpening' and 'dampening' effects work together but in separate time windows, providing direct neural evidence for the opposing process theory [27].

Attention Cannot Account for Our Results

We found an enhanced N1 in the matching prediction compared to the mismatching prediction. As attention has a facilitatory effect similar to prediction [44] and can be oriented in time [45], it may be argued that the enhanced matching N1 can be alternatively accounted for by temporal attention, rather than solely by timing prediction. It is possible that participants may orient attention to the predicted moment they need to discriminate, so more attentional resources would be allocated to the second flash of SOA400 for AMP than others. However, we argue this is not the case. Actually, participants paid equal attention to the second flash for all conditions, for four reasons. First, as the brain measures sub-second intervals by an automatic timing system which can measure time without attentional modulation [46], the participants would maintain the same attentional level during the whole double-flash, i.e. the second flash attracted as much attention as the first flash for each trial. As the first ERPs of the three conditions had the same profile, we can conclude that the participants were at the same attentional level for the first flash. Therefore, their attentional level would also be the same for the second flash. Second, according to previous studies [47, 48], if more attention was paid to the second flash for AMP, its visual N1 would be larger than that of the NPC. However, the two conditions had almost the same profiles for the second ERPs. Therefore, it was not for AMP to enhance but for PMP and MMP to attenuate the second N1, which showed a sharpening effect of prediction. Third, it has been demonstrated that the alpha band oscillation is closely relevant to the allocation of attention [49–51], while the theta oscillation is relevant to timing prediction [49, 52]. The ITC and ERSP results only showed significant differences in the theta band among conditions (Fig. 5), but not in the alpha band (ITC: F (2,88) = 1.654, P = 0.288; ERSP: F (2,88) = 1.358, P = 0.302), which indicated there were no differences in attention but differences of prediction deployed on the second flash for the three conditions. Fourth, this study not only included the condition of no timing prediction, but also the condition where participants knew there were only three kinds of stimuli and were required to react to the stimuli as fast as possible (PMP condition). As participants had known the content of stimuli and needed to press the button as quickly as possible in PMP, if attention does play a leading role in this process, the SOA400 would be the first moment on which they would allocate more attention. If so, the PMP N1 would be larger than that of other prediction-related conditions. However, the PMP N1 induced by SOA400 was smaller, which goes against the assumption of attentional modulation. In sum, the enhanced matching N1 cannot be accounted for by an attentional effect.

Dynamic Process of Brain Responses Modulated by Precise Timing Prediction

We investigated the dynamic neural responses to the identical double-flash with different timing predictions. Clearly, the CNVs in the midst of a double-flash differed among conditions (Fig. 4A). Previous studies have suggested that the CNV is closely relevant to temporal expectation [53]. However, recent findings have demonstrated that the timing of intervals does not depend on increasing neural activity but is more relevant to evoked potentials [54]. Therefore, we only focused on the evoked potential on which the precise timing template would be imposed. By studying the neural signatures of the evoked responses, we found that the successive N1 and N2 components were modulated by timing prediction but in opposite tendencies. Such modulations reflect the interactive process of the underlying representational and error signals during the predictive brain response. Predictive coding theory states that the external sensory input is matched with the internal perceptual template, resulting in a residual error signal to adjust the initial predictive state [9, 10]. Although previous evidence has demonstrated the existence of representational and error signals [1, 24–26, 55], evidence for the temporal dynamics of the two signals is still lacking. The results of our study show how the two signals wax and wane over time. Compared to the control condition of no timing prediction, a mismatching prediction attenuates the posterior N1 but enhances the following N2, while a matching prediction has no significant effect on the profiles. As N1 is linked to visual discrimination processes [56] and N2 is referred to as a mismatch detector [39], the results indicate that the representational signal during the N1 period is inhibited for unexpected sensory input but maintained for expected sensory input, while an error signal during the N2 period is produced for the unexpected sensory input but absent for the expected sensory input. This finding can help shed light on the neural mechanism of expectation suppression, as discussed below.

Reconciling the 'Sharpening' and 'Dampening' Accounts for Expectation Suppression

The neural effect of prediction is still poorly understood. Although the phenomenon of expectation suppression has been widely reported in previous studies, its underlying neural mechanism is still under debate. Currently, there are two paradoxical accounts for how the brain suppresses the neural response to predictable sensory input. The 'dampening' account proposes that the predictive templates in higher regions are able to dampen or 'explain away' the predictable sensory inputs in lower regions. Therefore, compared to mismatching prediction, matching prediction needs to address fewer inconsistent signals between predictive templates and sensory inputs. Accordingly, the neural activation would be lower for matching prediction than mismatching prediction [12–14, 57]. However, the 'sharpening' account holds the view that the suppressed neural activity of matching prediction is formed mainly by suppressing the neurons encoding the unpredicted, rather than those encoding the predicted information [3, 58], making the predicted information more salient and distinctively represented in a specific area of cortex [22]. We investigated the dynamic process of brain response modulated by the precise timing prediction, and found the phenomenon of expectation suppression by calculating the evoked EEG energy, which was in line with the BOLD studies. By analyzing the dynamic ERP process, we found the representational signal was significantly suppressed for mismatching prediction during the N1 period, which supported the 'sharpening' account. Furthermore, the error signal was almost absent for matching prediction during the N2 period, which supported the 'dampening' account. The results indicate that the neural representation of predicted information is sharpened during the N1 period and dampened during the N2 period. Therefore, the 'sharpening' and 'dampening' effects, which seem to contradict each other, are compatible during the dynamic prediction process. They work together but in separate time windows. These findings fit nicely with a recent proposed notion of opposing perceptual processes [27], which claims that the expected and unexpected events are addressed separately in time by applying Bayesian ('sharpening') and cancellation ('dampening') models, sequentially.

In sum, by using an innovative experimental paradigm, we investigated the fine temporal evolution of the evoked neural responses associated with precise timing prediction. We not only found the phenomenon of expectation suppression as in previous studies, but also found the 'sharpening' and 'dampening' effects of prediction in distinct processing stages with an opposing trend. These results provide direct neural evidence for the opposing processing theory, which is a potential theoretical resolution for the 'sharpening' and 'dampening' effects of prediction.

Acknowledgements This work was supported by the National Key Research and Development Program of China (2017YFB1300302), the National Natural Science Foundation of China (81925020 and 61976152), and the Young Elite Scientist Sponsorship Program of the China Association for Science and Technology (2018QNRC001).

Conflict of interest The authors declare no conflict of interest.

References

1. Egner T, Monti JM, Summerfield C. Expectation and surprise determine neural population responses in the ventral visual stream. J Neurosci 2010, 30: 16601–16608.
2. Clark A. Whatever next? Predictive brains, situated agents, and the future of cognitive science. Behav Brain Sci 2013, 36: 181–204.
3. de Lange FP, Heilbron M, Kok P. How do expectations shape perception? Trends Cogn Sci 2018, 22: 764–779.
4. Adams RA, Shipp S, Friston KJ. Predictions not commands: active inference in the motor system. Brain Struct Funct 2013, 218: 611–643.
5. Cope TE, Sohoglu E, Sedley W, Patterson K, Jones PS, Wiggins J, *et al.* Evidence for causal top-down frontal contributions to predictive processes in speech perception. Nat Commun 2017, 8: 2154.
6. Pine A, Sadeh N, Ben-Yakov A, Dudai Y, Mendelsohn A. Knowledge acquisition is governed by striatal prediction errors. Nat Commun 2018, 9: 1673.
7. Summerfield C, de Lange FP. Expectation in perceptual decision making: neural and computational mechanisms. Nat Rev Neurosci 2014, 15: 745–756.
8. Sun H, Ma X, Tang L, Han J, Zhao Y, Xu X, *et al.* Modulation of beta oscillations for implicit motor timing in primate sensorimotor cortex during movement preparation. Neurosci Bull 2019, 35: 826–840.
9. Rao RPN, Ballard DHJNN. Predictive coding in the visual cortex: a functional interpretation of some extra-classical receptive-field effects. Nat Neurosci 1999, 2: 79–87.
10. Friston K. A theory of cortical responses. Philos Trans R Soc Lond B Biol Sci 2005, 360: 815–836.
11. Friston K. The free-energy principle: a unified brain theory? Nat Rev Neurosci 2010, 11: 127–138.
12. Alink A, Schwiedrzik CM, Kohler A, Singer W, Muckli L. Stimulus predictability reduces responses in primary visual cortex. J Neurosci 2010, 30: 2960–2966.
13. Barne LC, Claessens PME, Reyes MB, Caetano MS, Cravo AM. Low-frequency cortical oscillations are modulated by temporal prediction and temporal error coding. Neuroimage 2017, 146: 40–46.
14. Blank H, Davis MH. Prediction errors but not sharpened signals simulate multivoxel fMRI patterns during speech perception. PLoS Biol 2016, 14: e1002577.
15. Ullsperger M, Fischer AG, Nigbur R, Endrass T. Neural mechanisms and temporal dynamics of performance monitoring. Trends Cogn Sci 2014, 18: 259–267.
16. Richter D, Ekman M, Lange FPDJJoN. Suppressed sensory response to predictable object stimuli throughout the ventral visual stream. J Neurosci 2018, 38:7452–7461.
17. Bueti D, Bahrami B, Walsh V, Rees G. Encoding of temporal probabilities in the human brain. J Neurosci 2010, 30: 4343–4352.
18. Doherty JR, Rao A, Mesulam MM, Nobre AC. Synergistic effect of combined temporal and spatial expectations on visual attention. J Neurosci 2005, 25: 8259–8266.
19. Jaramillo S, Zador AM. The auditory cortex mediates the perceptual effects of acoustic temporal expectation. Nat Neurosci 2011, 14: 246–251.
20. Kok P, Brouwer GJ, van Gerven MA, de Lange FP. Prior expectations bias sensory representations in visual cortex. J Neurosci 2013, 33: 16275–16284.
21. Kouider S, Long B, Le Stanc L, Charron S, Fievet AC, Barbosa LS, *et al.* Neural dynamics of prediction and surprise in infants. Nat Commun 2015, 6: 8537.
22. Kok P, Jehee JF, de Lange FP. Less is more: expectation sharpens representations in the primary visual cortex. Neuron 2012, 75: 265–270.
23. Kok P, Rahnev D, Jehee JF, Lau HC, de Lange FP. Attention reverses the effect of prediction in silencing sensory signals. Cereb Cortex 2012, 22: 2197–2206.
24. de Gardelle V, Waszczuk M, Egner T, Summerfield C. Concurrent repetition enhancement and suppression responses in extrastriate visual cortex. Cereb Cortex 2013, 23: 2235–2244.
25. de Gardelle V, Stokes M, Johnen VM, Wyart V, Summerfield C. Overlapping multivoxel patterns for two levels of visual expectation. Front Hum Neurosci 2013, 7: 158.
26. Miller EK, Desimone R. Parallel neuronal mechanisms for short-term memory. Science 1994, 263: 520–522.
27. Press C, Kok P, Yon D. The perceptual prediction paradox. Trends Cogn Sci 2020, 24: 13–24.
28. Ekman M, Kok P, de Lange FP. Time-compressed preplay of anticipated events in human primary visual cortex. Nat Commun 2017, 8: 15276.
29. Kok P, Mostert P, de Lange FP. Prior expectations induce prestimulus sensory templates. Proc Natl Acad Sci U S A 2017, 114: 10473–10478.
30. Summerfield C, Egner T, Greene M, Koechlin E, Mangels J, Hirsch J. Predictive codes for forthcoming perception in the frontal cortex. Science 2006, 314: 1311–1314.
31. Bueti D, Lasaponara S, Cercignani M, Macaluso E. Learning about time: plastic changes and interindividual brain differences. Neuron 2012, 75: 725–737.
32. Arnal LH, Doelling KB, Poeppel D. Delta-beta coupled oscillations underlie temporal prediction accuracy. Cereb Cortex 2015, 25: 3077–3085.
33. Stefanics G, Hangya B, Hernadi I, Winkler I, Lakatos P, Ulbert I. Phase entrainment of human delta oscillations can mediate the effects of expectation on reaction speed. J Neurosci 2010, 30: 13578–13585.
34. Summerfield C, Koechlin E. A neural representation of prior information during perceptual inference. Neuron 2008, 59: 336–347.
35. Calderone DJ, Lakatos P, Butler PD, Castellanos FX. Entrainment of neural oscillations as a modifiable substrate of attention. Trends Cogn Sci 2014, 18: 300–309.
36. Lakatos P, Karmos G, Mehta AD, Ulbert I, Schroeder CE. Entrainment of neuronal oscillations as a mechanism of attentional selection. Science 2008, 320: 110–113.
37. Melloni L, Schwiedrzik CM, Muller N, Rodriguez E, Singer W. Expectations change the signatures and timing of electrophysiological correlates of perceptual awareness. J Neurosci 2011, 31: 1386–1396.
38. Delorme A, Makeig S. EEGLAB: an open source toolbox for analysis of single-trial EEG dynamics including independent component analysis. J Neurosci Methods 2004, 134: 9–21.
39. Folstein JR, Van PCJP. Influence of cognitive control and mismatch on the N2 component of the ERP: a review. Psychophysiology 2008, 45: 152–170.
40. Brunia CHM, Damen EJP. Distribution of slow brain potentials related to motor preparation and stimulus anticipation in a time estimation task. Electroencephalogr Clin Neurophysiol 1988, 69: 234–243.
41. Luck SJ, Kappenman ES (Eds). The Oxford Handbook of Event-Related Potential Components. Oxford Library of Psychology 2008.
42. Stahl J, Gibbons HJP. The application of jackknife-based onset detection of lateralized readiness potential in correlative approaches. Psychophysiology 2004, 41: 845–860.

43. Miller J, Patterson AT, Ulrichb R. Jackknife-based method for measuring LRP onset latency differences. Psychophysiology 1998, 35: 99–115.
44. Summerfield C, Egner T. Expectation (and attention) in visual cognition. Trends Cogn Sci 2009, 13: 403–409.
45. Nobre AC, van Ede F. Anticipated moments: temporal structure in attention. Nat Rev Neurosci 2018, 19: 34–48.
46. Buhusi CV, Meck WH. What makes us tick? Functional and neural mechanisms of interval timing. Nat Rev Neurosci 2005, 6: 755–765.
47. Hillyard SA, Anllo-Vento L. Event-related brain potentials in the study of visual selective attention. Proc Natl Acad Sci U S A 1998, 95: 781–787.
48. Stormer VS, McDonald JJ, Hillyard SA. Cross-modal cueing of attention alters appearance and early cortical processing of visual stimuli. Proc Natl Acad Sci U S A 2009, 106: 22456–22461.
49. Arnal LH, Giraud AL. Cortical oscillations and sensory predictions. Trends Cogn Sci 2012, 16: 390–398.
50. Capilla A, Schoffelen JM, Paterson G, Thut G, Gross J. Dissociated alpha-band modulations in the dorsal and ventral visual pathways in visuospatial attention and perception. Cereb Cortex 2014, 24: 550–561.
51. Klimesch W. alpha-band oscillations, attention, and controlled access to stored information. Trends Cogn Sci 2012, 16: 606–617.
52. Cravo AM, Rohenkohl G, Wyart V, Nobre AC. Endogenous modulation of low frequency oscillations by temporal expectations. J Neurophysiol 2011, 106: 2964–2972.
53. van Rijn H, Kononowicz TW, Meck WH, Ng KK, Penney TB. Contingent negative variation and its relation to time estimation: a theoretical evaluation. Front Integr Neurosci 2011, 5: 91.
54. Kononowicz TW, van Rijn H. Decoupling interval timing and climbing neural activity: a dissociation between CNV and N1P2 amplitudes. J Neurosci 2014, 34: 2931–2939.
55. Ni B, Wu R, Yu T, Zhu H, Li Y, Liu Z. Role of the hippocampus in distinct memory traces: timing of match and mismatch enhancement revealed by intracranial recording. Neurosci Bull 2017, 33: 664–674.
56. Mangun GR, Hillyard SA. Modulations of sensory-evoked brain potentials indicate changes in perceptual processing during visual-spatial priming. J Exp Psychol Hum Percept Perform 1991, 17: 1057–1074.
57. Summerfield C, Trittschuh EH, Monti JM, Mesulam MM, Egner T. Neural repetition suppression reflects fulfilled perceptual expectations. Nat Neurosci 2008, 11: 1004–1006.
58. Chalk M, Marre O, Tkacik G. Toward a unified theory of efficient, predictive, and sparse coding. Proc Natl Acad Sci U S A 2018, 115: 186–191.

Neurosci. Bull. January, 2021, 37(1):81–93
https://doi.org/10.1007/s12264-020-00579-3

www.neurosci.cn
www.springer.com/12264

ORIGINAL ARTICLE

Distinct Effects of Social Stress on Working Memory in Obsessive-Compulsive Disorder

Qianqian Li[1,2] · Jun Yan[1,2] · Jinmin Liao[1,2] · Xiao Zhang[1,2] · Lijun Liu[1,2] · Xiaoyu Fu[1,2] · Hao Yang Tan[5,6] · Dai Zhang[1,2,3,4] · Hao Yan[1,2]

Received: 12 December 2019 / Accepted: 13 May 2020 / Published online: 1 October 2020

Abstract Stress might exaggerate the compulsion and impair the working memory of patients with obsessive-compulsive disorder (OCD). This study evaluated the effect of stress on the cognitive neural processing of working memory in OCD and its clinical significance using a "number calculation working memory" task. Thirty-eight patients and 55 gender- and education-matched healthy controls were examined. Stress impaired the performance of the manipulation task in patients. Healthy controls showed less engagement of the medial prefrontal cortex and striatum during the task under stress *versus* less stress, which was absent in the patients with OCD. The diagnosis × stress interaction effect was significant in the right fusiform, supplementary motor area, precentral cortex and caudate. The failure of suppression of the medial prefrontal cortex and striatum and stress-related hyperactivation in the right fusiform, supplementary motor area, precentral cortex, and caudate might be an OCD-related psychopathological and neural response to stress.

Keywords Working memory · Acute stress · Obsessive-compulsive disorder · Functional magnetic resonance imaging

Qianqian Li and Jun Yan have contributed to this work.

Electronic supplementary material The online version of this article (https://doi.org/10.1007/s12264-020-00579-3) contains supplementary material, which is available to authorized users.

✉ Dai Zhang
daizhang@bjmu.edu.cn

✉ Hao Yan
hao_y@bjmu.edu.cn

[1] Peking University Sixth Hospital, Beijing 100191, China

[2] Peking University Institute of Mental Health, National Health Commission Key Laboratory of Mental Health (Peking University), National Clinical Research Center for Mental Disorders (Peking University Sixth Hospital), Beijing 100191, China

[3] Tsinghua University-Peking University Joint Center for Life Sciences, Beijing 100871, China

[4] PKU-IDG/McGovern Institute for Brain Research, Peking University, Beijing 100871, China

[5] Lieber Institute for Brain Development, Baltimore, MD 21205, USA

[6] Department of Psychiatry and Behavioral Sciences, Johns Hopkins University School of Medicine, Baltimore, MD 21205, USA

Introduction

Obsessive-compulsive disorder (OCD) is a chronic and disabling mental disease [1, 2] characterized by the presence of obsessions (repeated thoughts) or compulsions (repeated behaviors to neutralize anxiety), or both [3]. The World Health Organization ranks it as one of the ten most disabling conditions by lost income and reduced quality of life [4].

Stress is one of the main risk factors for the formation of the disorder [5], and previous studies have indicated that OCD patients have an impaired stress response [6]. The neuropsychological theories of OCD suggest that it might be a disorder of imbalance between goal-directed behavior and maladaptive habits [7]. The excessive habit formation or habit dysregulation might result in the compulsions in OCD, which can be exaggerated by stress [8]. Moreover, stress impairs working memory (WM) and cognitive flexibility; this has been confirmed by meta-analysis of the main neuropsychological assessments in OCD patients [9].

Meanwhile, WM has been found to shape and moderate the balance between the goal-directed and habitual systems as one of the core cognitive abilities [10, 11].

Accumulating evidence from neuroimaging studies has suggested a certain extent of spatial overlap between the neural mechanism of OCD, the stress effect, and the WM process [12]. The well-known neuropathological model suggests that the function of the cortical-striatal-thalamo-cortical (CSTC) loop is impaired in OCD [13–15]. Banca *et al*. found that, during effective symptom provocation, OCD patients show reduced activation in the ventromedial prefrontal cortex (vmPFC) and caudate nucleus, and increased activation in regions of the pre-supplementary motor area (pre-SMA) and putamen, which have also been implicated in goal-directed behavioral control and habit learning, respectively [16]. A visuospatial WM study suggested an inefficient fronto-parietal executive network and increased connectivity between frontal regions and the amygdala in OCD [17]. Moreover, meta-analysis of the brain responses to the stress of trauma revealed hyperactivation in the amygdala, insula, and precuneus cortex and hypoactivation in the anterior cingulate cortices and vmPFC [18, 19]. Some studies have indicated that stress leads to changes in the neuroendocrine and limbic brain, resulting in mental diseases such as depression and post-traumatic stress disorder [20, 21]. However, how stress influences the neural processing related to the cognitive deficits of WM in OCD and the clinical correlations remain unknown.

Therefore, in the current study, a new event-related "number calculation working memory" task which integrated interpersonally competitive stress into the WM process was used to investigate the stress effect on WM in OCD. This newly designed task differs from the Montreal Imaging Stress Task (MIST) [22] which consists of mental arithmetic under social evaluating stress but not WM. Based on our previous work in a large sample of healthy adult Han Chinese individuals [23], the task-related activity included the prefrontal-parietal system and stress-related suppression of the medial prefrontal cortex (mPFC) and striatum. Therefore, in view of the neuropathological theory of OCD, we hypothesized that the regions of the CSTC circuit, frontal-parietal executive, and stress-related networks might respond differentially to the WM task under stress in patients with OCD *versus* healthy controls.

Materials and Methods

Ethics Statement

The Ethics Committee of the Peking University Sixth Hospital approved the study. All participants were given detailed information regarding the purpose and procedures of the study. Only patients who could consent were invited to participate. All the participants enrolled gave written consent.

Participants

In total, 125 individuals participated in the study: 58 patients with OCD and 67 healthy controls (HCs). The patients were recruited from either the inpatient or outpatient department of Peking University Sixth Hospital. Patients all met the Diagnostic and Statistical Manual of Mental Disorders, 4th Edition, Text Revision (DSM-IV-TR) diagnostic criteria of OCD, without other comorbidities in the DSM-IV-TR Axis I Disorders (including depression), and were evaluated by two psychiatrists using the Structured Clinical Interview for DSM-IV-TR Axis I Disorders, Patient Edition (SCID-I/P). The exclusion criteria were any comorbidity of other SCID-I diagnoses, electroconvulsive therapy within six months, or a history of severe medical illness. All HCs were recruited from the local community by advertisement and assessed by psychiatrists using the SCID-I, Non-Patient Edition to exclude any mental disorder. Participants were excluded if they had: a history of neurological disease, a history of > 5 min loss of consciousness, or magnetic resonance imaging (MRI) contraindications.

The Yale-Brown Obsessive Compulsive Symptom Checklist Scale and Severity Scale (YBOCS-CS/YBOCS-SS) [24], Hamilton Anxiety Scale (HAMA) and Hamilton Depression Scale (HAMD), and four factors were used to assess the symptom severity and dimensions in patients. In the 38 patients included in the final analysis, 24 were taking one or more antidepressants and 14 were drug-naïve. All medication doses were transformed into Imipramine equivalents (mg/day) [25] (see Tables 1 and S1 for details).

Working Memory Paradigm

We applied a new event-related "number calculation working memory" task from previous work, which comprised alternating competitive and non-competitive blocks (NumComp-task) [23] (Fig. 1). The participants received task training before MRI scanning to ensure that they understood the task well.

During the trials with competition (C), participants were led to believe that they were playing a number calculation game against a competitor of similar age and gender, and were judged based on timing and accuracy. The NumComp-task had two sessions: 14 competitive trials and 14 non-competitive trials in total. To induce social stress, participants received more negative feedback of "you lost" (5/7) among the 14 competitive trials. During the non-

Table 1 Demographics and clinical data of the obsessive-compulsive disorder patients (OCD) and healthy controls (HC).

Variables	OCD (n = 38)*	HC (n = 55)*	t/χ^2	P value
Gender (F/M)	14/24	30/25	2.83	0.09**
Age (years)	27.1 ± 6.1	23.6 ± 2.9	3.25	0.02†
Edu (years)	15.7 ± 2.7	16.4 ± 1.6	− 1.32	0.19†
Imipramine equivalents (mg/day)	232.6 ± 128.8			
Course (months)	77.0 ± 47.1			
YBOSC-TS	21.9 ± 13.8			
YBOSS-TS	23.0 ± 7.8			
HAMAS	12.0 ± 7.6			
HAMDS	8.9 ± 6.2			

*Unless otherwise indicated, data are the mean ± SD; **Pearson χ^2 (categorical data); †independent-sample t-test (parametric data); YBOSC-TS, Yale-Brown Symptom Checklist total score; YBOSS-TS, Yale-Brown severity scale total score; HAMAS, Hamilton Anxiety Scale total score; HAMDS, Hamilton Depression Scale total score.

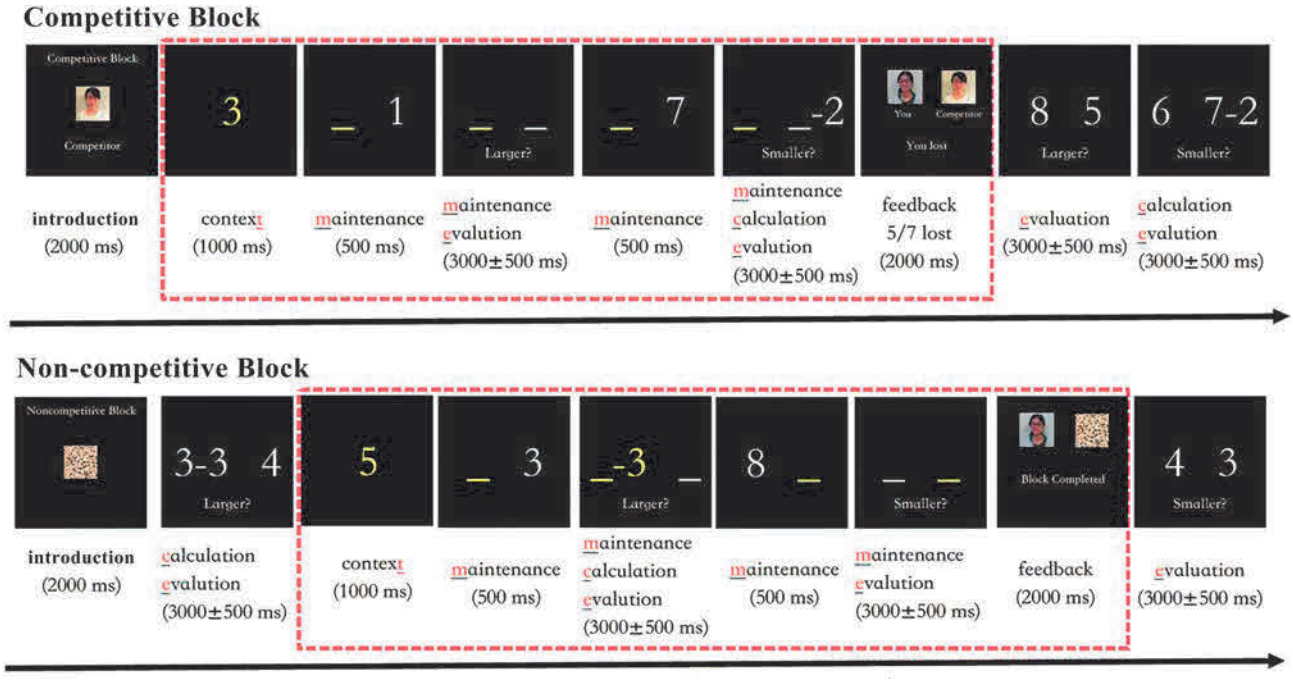

Fig. 1 The event-related numerical WM task paradigm.

competitive (NC) trials, the participants played the game with no competitor and received a neutral response.

For each trial under the WM conditions, the participants were presented with two numbers from 1 to 9 successively to encode into WM and subsequently had to be maintained. Then they were asked which of the two results was "larger" or "smaller" as instructed (maintenance evaluation, ME) or had to perform mental arithmetic (subtraction) on one of the numbers before giving a response to the "larger" or "smaller" comparison (maintenance calculation evaluation, MCE). Further details of the NumComp-task are available in the supplementary material.

The NumComp-task had competitive and non-competitive blocks. For WM (enclosed in red dashes), participants encoded 2 integer numbers in yellow or white presented over 1 s and to be retained in WM (underlined in the same color, yellow or white) across an interval of 3–5 s. In maintenance trials, participants responded to which of the two numbers was "larger" or "smaller" within 2.5–3.5 s. In the manipulation trials, participants had to do mental arithmetic on one of the two numbers in yellow or white before the "larger" or "smaller" evaluation within 2.5–3.5 s. These two kinds of trials were embedded within equal numbers of competitive or non-competitive blocks. Two blocks were counterbalanced in 2 runs. Each run

took ~ 10 min. All the instructions were originally in Chinese. All "competitors" were of the same gender and age. The interspersed fixation was between each complete competitive block and a noncompetitive block and was not shown.

Image Acquisition

Imaging data were acquired using a 3.0-Tesla GE scanner (Discovery MR750) at the Center for Neuroimaging, Peking University Sixth Hospital. Foam pads were used to minimize head motion. A gradient echo sequence was used to acquire blood oxygen level-dependent (BOLD) functional MRI (fMRI) images, and each volume consisted of 33 axial slices covering the entire cerebrum and cerebellum with the following parameters: thickness/gap = 4.2 mm/0 mm, TR/TE = 2000/30 ms, flip angle = 90°, field of view = 22.4 cm × 22.4 cm, matrix = 64 × 64. Three dummy scans were acquired at the beginning of the fMRI scanning.

Image Processing and Analyses

We excluded participants with an accuracy rate < 50% in any WM conditions (8 OCDs), those with head motion > 3 mm translation or 3° rotation (8 OCDs and 6 HCs), and those with image artifacts or did not complete the task (4 OCDs and 6 HCs) for quality control. In total, 93 participants (38 OCDs and 55 HCs) were included in the final analysis (Table 1).

The fMRI imaging data were pre-processed using MatLab 2016b and SPM12 (http://www.fil.ion.ucl.ac.uk/spm). Functional images for each participant was slice-timing corrected, realigned to the first volume in the time series, and corrected for head motion. Images were then spatially normalized into standard stereotaxic space (Montreal Neurological Institute template) using fourth-degree B-spline interpolation. Spatial smoothing was applied with a Gaussian filter set at 8 mm full-width at half-maximum. Each task-evoked stimulus was modelled as a separate delta function and convolved with a canonical hemodynamic response function; ratio normalized to the whole-brain global mean to control for systematic differences in global activity, and temporally filtered using a high-pass filter of 128 s. Each task-evoked stimulus event was modelled for correctly-performed trials in the general linear model of the first-level analysis of the image data. Incorrect responses and residual movement parameters were also modelled as regressors of no interest [26].

The planned contrasts of interest for a second-level random effect within-group analysis using one-sample t-tests were brain activity in the maintenance (ME) or manipulation (MCE) task conditions under non-competitive (NC) and competitive (C) condition at $P < 0.05$, whole-brain family-wise error (FWE) corrected.

For the diagnosis effect (group difference) on brain activity in each WM condition (ME or MCE) under competitive or non-competitive condition, the significance level was set as an uncorrected $P < 0.001$, with a cluster sizes ≥ 86 voxels (688 mm^3) for ME_C, ≥ 94 voxels (752 mm^3) for ME_NC, ≥ 83 voxels (664 mm^3) for MCE_C, and ≥ 103 voxels (824 mm^3) for MCE_NC with independent-sample *t*-tests, which corresponded to a corrected $P < 0.05$ determined by 5000 Monte Carlo simulations using AlphaSim correction within the grey matter mask in DPABI_V4.0 (http://rfmri.org/dpabi). The inter-subject variability was treated as a random effect, controlled for age, gender, and years of education.

For the stress effect indicated as brain activity during the maintenance or manipulation task conditions under competition *versus* non-competition in the HC and OCD groups, the significance level was set as an uncorrected $P < 0.001$, with cluster sizes ≥ 125/124 voxels (1000/992 mm^3) for HC and ≥ 137/229 voxels (1096/1832 mm^3) for OCD with one-sample *t*-tests, which corresponded to a corrected $P < 0.05$ determined by 5000 Monte Carlo simulations using AlphaSim correction within the grey matter mask in DPABI_V4.0 (http://rfmri.org/dpabi). The imipramine equivalent was included as a covariate to control for the medication effect in the OCD within-group analysis.

The contrast images of the competitive or non-competitive condition were subsequently subjected to a flexible 2 × 2 analysis of variance (ANOVA) to explore the brain activity of the diagnosis × stress interaction effect separately in the ME and MCE conditions. The significance level was set at an uncorrected $P < 0.001$, with cluster sizes ≥ 38 voxels (304 mm^3) for maintenance and ≥ 95 voxels (760 mm^3) for manipulation, which corresponded to a corrected $P < 0.05$ determined by 5000 Monte Carlo simulations using AlphaSim correction within the grey matter mask in DPABI_V4.0 (http://rfmri.org/dpabi). Around the peak coordinates, an 8 mm radius sphere was created using DPABI_V4.0 as the region of interest (ROI) of each area showing a significant interaction effect, and then the contrast values of the ROIs from the corresponding contrast images of each task and condition in each group were extracted for a two-way repeated measures ANOVA and a simple main effect analysis using GraphPad Prism 7.0 (https://www.graphpad.com). The significance level of the ANOVA and simple main effect analysis in GraphPad Prism 7.0 was set at $P < 0.05$, false discovery rate (FDR) correction.

Statistical Analyses of Clinical and Behavioral Data

Demographic and clinical data were analyzed with a standard statistical package (IBM SPSS 21.0, Chicago, IL), using the *t*-test and χ^2 test. Task behavioral data (accuracy rate and reaction time) of the two groups under stress and non-stress condition were analyzed with GraphPad Prism 7.0 using two-way repeated measures ANOVA. If the diagnosis × stress interaction effect was significant, a simple main effect analysis was applied as a *post hoc* analysis in GraphPad Prism 7.0. If the brain activity of diagnosis × stress interaction effect was significant in ME or MCE conditions, the stress-related contrast values of the ROI of the interaction effect from the corresponding contrast images of each task condition (ME or MCE under competitive *versus* non-competitive contrast images) in the OCD group were extracted and correlated to the clinical variables (Y-BOCS, HAMA, and HAMD) and task behavioral performance. The significance level of the *t*-test and χ^2 test was set at $P < 0.05$. The significance level of the two-way repeated measures ANOVA, simple main effect, and correlation analysis was set at $P < 0.05$, with FDR correction.

Results

Behavioral Performance

In terms of the accuracy rate of maintenance, we only found significant main effects of stress (competitive *vs* non-competitive, $F = 38.47$, $P < 0.0001$). The accuracy was higher during the competitive than the non-competitive condition in OCDs ($t = 3.48$, $q = 0.0008$, FDR correction) and HCs ($t = 5.52$, $q < 0.0001$, FDR correction) (Fig. 2A and Table S2). As for the accuracy rate in the manipulation task, the main effect of diagnosis (OCD *vs* HC, $F = 4.89$, $P = 0.03$) and the interaction effects of diagnosis × stress ($F = 7.47$, $P = 0.008$) were significant. The accuracy was lower in OCDs than in HCs only during the competitive condition ($t = 3.32$, $q = 0.001$, FDR correction) and the accuracy was lower under the competitive than the non-competitive condition only in OCDs ($t = 2.57$, $q = 0.01$, FDR correction) (Fig. 2C and Table S2–S3).

In terms of reaction time in the maintenance and manipulation tasks, the main effects of diagnosis ($F = 4.87$, $P = 0.03$, ME; $F = 8.54$, $P = 0.004$, MCE) and stress ($F = 5.02$, $P = 0.03$, only in ME) were significant and there was no significant diagnosis × stress interaction effect (Table S2). The reaction time was longer in OCDs than that in HCs during both the competitive ($t = 2.20$, $q = 0.043$, FDR correction, ME; $t = 3.31$, $q = 0.002$, FDR correction, MCE) and non-competitive ($t = 2.06$, $q = 0.043$, FDR correction, ME; $t = 2.27$, $q = 0.03$, FDR correction, MCE) conditions. The reaction time was shorter under the competitive than the non-competitive ME condition. However, there was no significant stress effect within each group (Fig. 2B and Fig. 2D).

Brain Activation

WM-Related Brain Activation

During each of the WM maintenance and manipulation tasks under the competitive or non-competitive condition in both OCDs and HCs, regions in the prefrontal, parietal, temporal, occipital, and cerebellar cortices, and the striatum were robustly activated, along with well-established deactivation in areas of the default mode network (DMN) during the cognitive task, including the mPFC and posterior cingulate cortex ($P < 0.05$, whole-brain FWE correction for multiple comparisons, see Figs. 3 and 4, left).

There was no significant between-group difference in the brain activity in WM maintenance or manipulation under competitive and non-competitive conditions.

Stress Effect on Brain Activity in Each Group

In terms of stress effects on WM maintenance and manipulation, a pattern of less engagement of the basal ganglia (less activation) and mPFC (more deactivation), more activation of the cerebellum was found during maintenance and manipulation under competitive *versus* non-competitive conditions in HCs ($P < 0.05$, AlphaSim correction for multiple comparisons, see Fig. 3, right, and Table S4).

The pattern of reduced engagement of the basal ganglia and mPFC in HCs was absent from the OCDs. Taking the WM manipulation for example, the more activated regions included the dorsal and ventral anterior cingulate, superior temporal lobe, bilateral hippocampus, bilateral thalamus, and bilateral SMA which are implicated in the neural processing of goal-directed behavioral control, habit learning, and stress; while the less deactivated regions included the medial frontal gyrus and bilateral temporal cortex, which are implicated in the DMN ($P < 0.05$, AlphaSim correction for multiple comparisons, see Fig. 4, right, and Table S5).

Diagnosis and Stress Interaction Effects

For the WM manipulation task, we found a significant diagnosis × stress interaction effect in the right fusiform cortex, right supplementary motor area (SMA), right

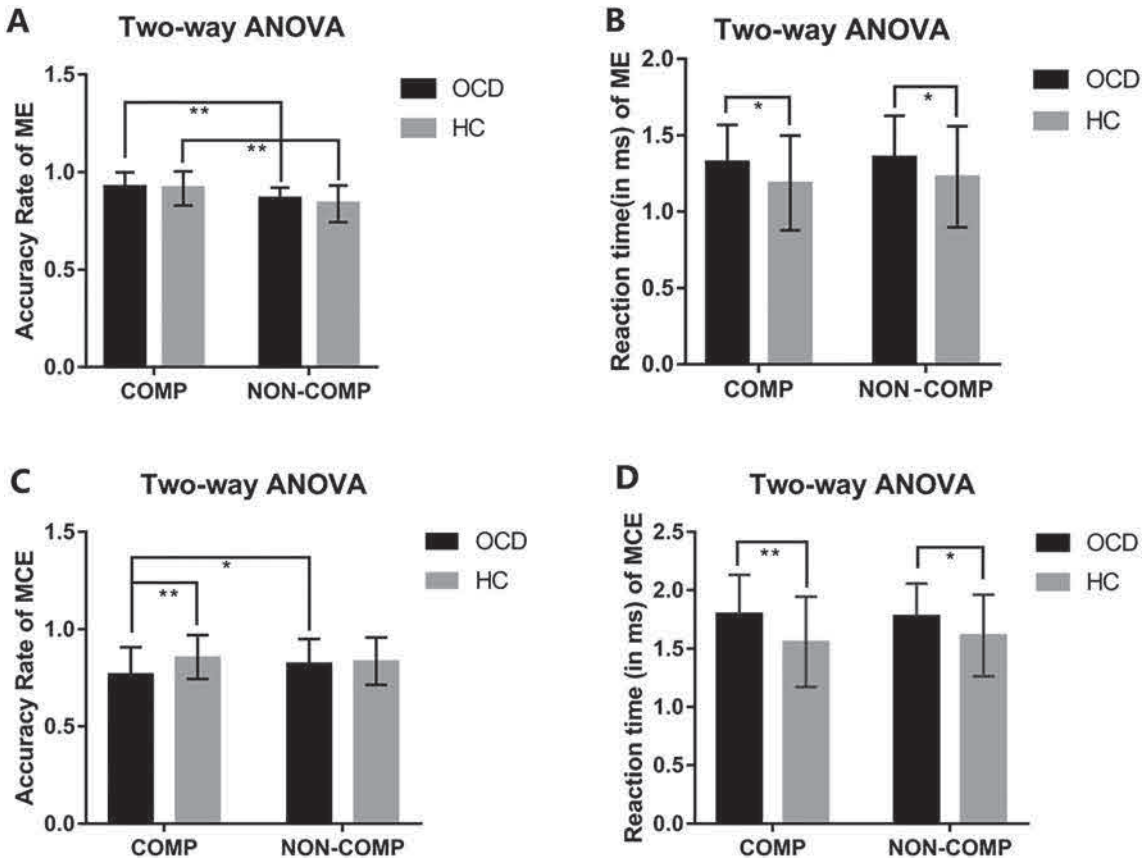

Fig. 2 Results of two-way ANOVA of diagnosis and stress and multiple comparisons in behavioral performance. **A** Stress has the main effect on accuracy rate in the ME task. The accuracy rate is higher under competition than non-competition in both groups. **B**, **D** Diagnosis has the main effect on average reaction time in the ME and MCE tasks. The average reaction time is longer in OCDs than HCs under both competitive and non-competitive conditions. **C** Stress and diagnosis have an interaction effect on accuracy rate in the MCE task. The accuracy rate is lower in OCDs than HCs only under the competitive condition and the accuracy rate is lower under competitive than non-competitive conditions only in OCDs. ME, maintenance evaluation; MCE, maintenance calculation evaluation; C, competition; NC, non-competition $*P < 0.05$, $**P < 0.01$.

precentral cortex, and right caudate ($P < 0.05$, AlphaSim correction for multiple comparisons, Fig. 5A and Table 2). The contrast values of the four ROIs in WM manipulation under competitive or non-competitive conditions of each group were extracted for further analysis. The activation of all four areas was significantly higher under competitive than non-competitive conditions only in OCDs (fusiform, $t = 4.66$, $q < 0.0001$; SMA, $t = 4.63$, $q < 0.0001$; precentral cortex, $t = 4.37$, $q < 0.0001$; caudate, $t = 2.83$, $q = 0.01$; FDR correction; Fig. 5B–E and Tables S6–S10). The activation of the right caudate was lower under competitive *versus* non-competitive conditions only in HCs ($t = 2.53$, $q = 0.01$, FDR correction; Fig. 5E and Table S10). In conclusion, the stress effect on brain activity differed between OCDs and HCs. The right fusiform, SMA, precentral cortex, and caudate had increased stress-related activity in OCDs, but not in HCs, while the right caudate had decreased stress-related activity in HCs.

No significant brain activity of diagnosis × stress interaction effect was found for WM maintenance.

Correlation Analysis

Correlation analyses were carried out between the stress-related activity of the brain regions with a significant diagnosis × stress interaction and the stress-related behavioral measures in OCDs. Considering the stress effect was only significant in accuracy rate but not in reaction time in OCDs (Fig. 2), the measure of the task performance only included the accuracy rate difference between manipulation under competitive and non-competitive condition.

In the OCD patients, the severity of obsessions and compulsions was positively correlated with their anxiety and depression symptoms (Table S11). Behavioral performance of the maintenance and manipulation tasks was significantly correlated with symptom severity (worse symptoms of depression correlated with faster responses),

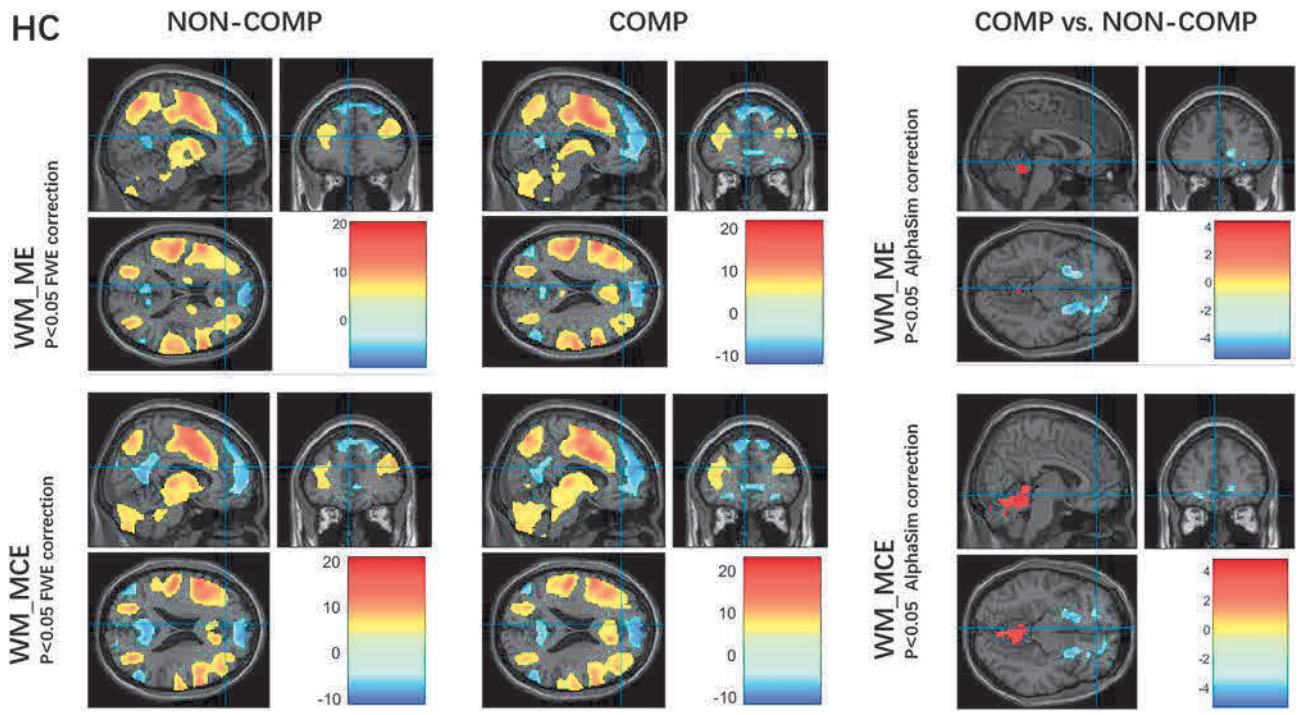

Fig. 3 Working memory-related brain activity and stress effect in the HC group. **A** Activity in the working memory task under competition and non-competition (left, $P < 0.05$, FWE correction, cluster size > 5 voxels). **B** Activity of competitive *versus* non-competitive conditions group under different task patterns (right, $P < 0.05$, AlphaSim correction for multiple comparisons). ME, maintenance evaluation; MCE, maintenance calculation evaluation; COMP, competition; NON-COMP, non-competition; FWE, whole-brain family-wise error corrected.

and more severe obsession symptoms were associated with a lower accuracy rate: obsession severity factors were negatively correlated with the accuracy rate in the manipulation task under stress ($r = –0.479$, $P < 0.01$; $r = –0.358$, $P < 0.05$) (Table S12).

In terms of the correlation between the neural activation of the stress effect with the symptoms and task performance, only significantly negative correlations were found with the clinical symptom severity (Table S13), such as a stress-related activation change in the right fusiform and SMA showing negative correlations with the obsession interference score and time score, respectively ($r = –0.465$, $P < 0.01$; $r = –0.353$, $P < 0.05$); and no significant correlation with the accuracy rate difference.

However, no correlation survived the FDR correction.

Discussion

We investigated the effect of stress on the neural processing associated with cognitive changes of WM in OCD and its relationship with the clinical variables. Stress impaired the WM behavioral performance in OCDs but not in HCs, specifically in more difficult WM manipulation. OCD patients showed a WM activation pattern similar to that of HCs: increased WM-related activity in the prefrontal-parietal-striatum network and decreased activity in the DMN, consistent with previous studies in HCs [22, 26–28]. The stress effect on the WM-related activity pattern in OCDs (a failure to suppress the DMN) differed from HCs (more deactivation in the mPFC along with less activation in the striatum). The diagnosis effect under each task condition (ME or MCE) and each stress condition (competitive or noncompetitive) on the activity was not significant, while the diagnosis and stress interaction effect on activation was significant in the right fusiform, SMA, precentral cortex, and right caudate only in the WM manipulation. OCD patients had stress-related hyperactivity in the right fusiform, SMA, precentral cortex, and right caudate, and HCs had stress-related suppression in the right caudate. Further, the clinical symptoms in OCD were associated with their task performance and the stress-related changes of brain activation.

Task Performance and Stress Effect

OCD patients performed worse than HCs but this was only indicated by the longer reaction time in WM maintenance and manipulation and worse accuracy in WM manipulation under stress. Under stress, the task performance was

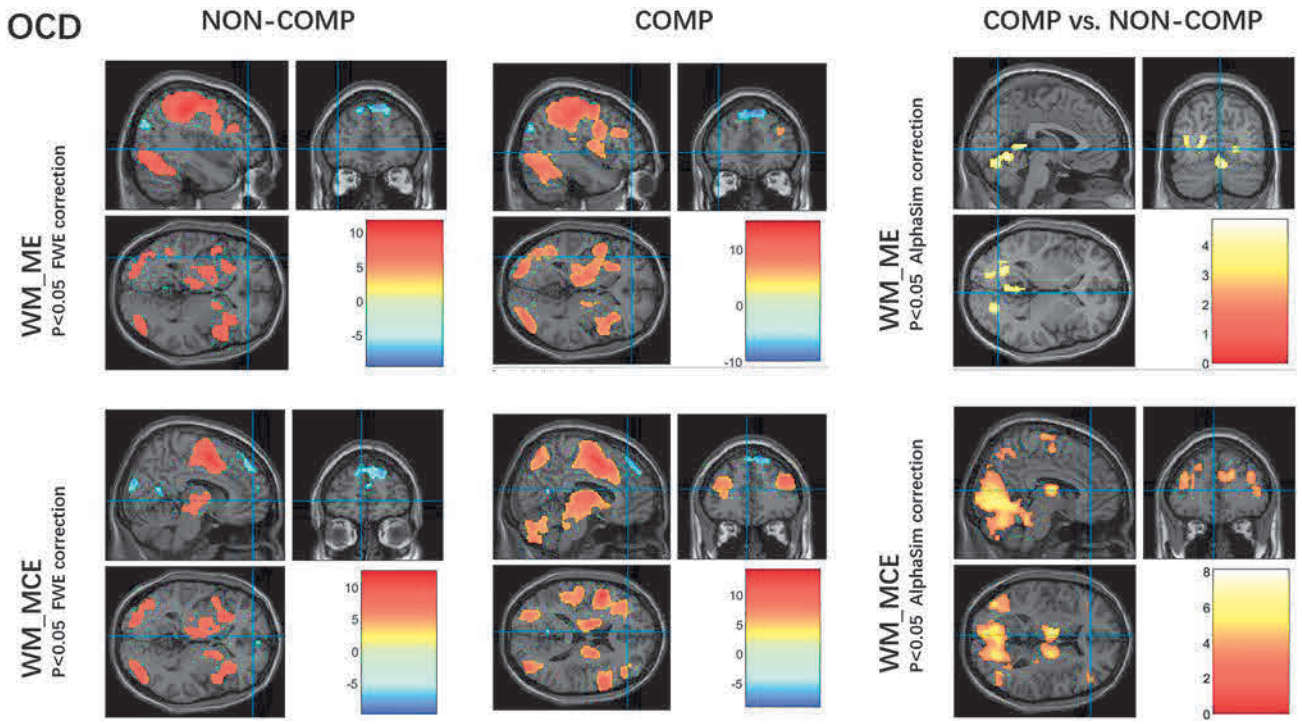

Fig. 4 Working memory-related brain activity and stress effect in the OCD group. **A** Activity of working memory task under competition and non-competition (left, $P < 0.05$, FWE correction, cluster size > 5 voxels). **B** Activity of competitive *versus* non-competitive conditions under different task patterns (right, $P < 0.05$, AlphaSim correction for multiple comparisons). ME, maintenance evaluation; MCE, maintenance calculation evaluation; COMP, competition; NON-COMP, non-competition; FWE, whole-brain family-wise error corrected.

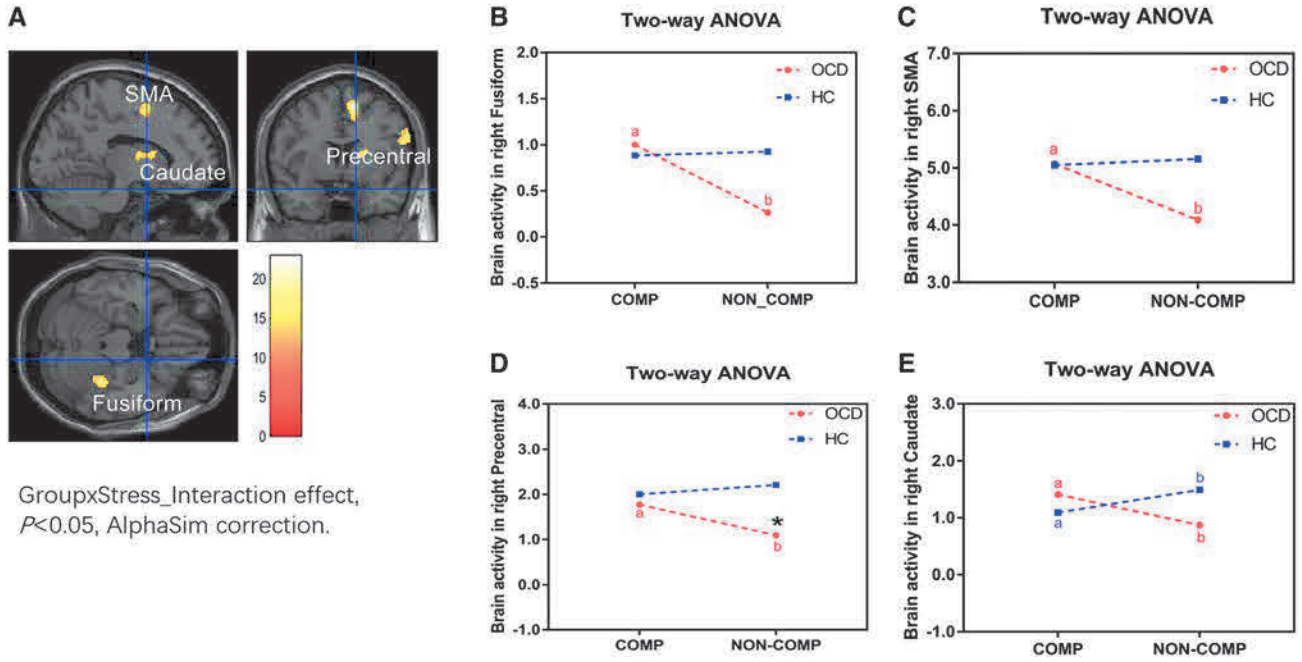

Fig. 5 Interaction effect of diagnosis and stress in brain areas. **A** The right fusiform, supplementary motor area, precentral, and right caudate are areas of the diagnosis and stress interaction effect. **B**–**E** Activation of the right fusiform (**B**), supplementary motor area (**C**), precentral (**D**), and right caudate (**E**) is higher under competitive than non-competitive condition only in OCDs; a, b, activation of the right caudate is lower under competitive than non-competitive conditions only in HCs; *under the non-competitive condition, the BOLD signal in the right precentral is higher in HCs than OCDs.

Table 2 The diagnosis × stress interaction effect in brain areas in the manipulation task (MCE) ($P < 0.05$, AlphaSim correction).

Variables	Cluster Size	Structure (aal)	Peak MNI coordinates			Peak intensity
	130	Fusiform_R (aal)	32	− 36	− 20	4.36
	158	Supp_Motor_Area_R (aal)	8	4	56	4.34
	164	Precentral_R (aal)	62	4	28	3.96
		Precentral_R (aal)	54	4	24	3.67
	227	Caudate_R (aal)	18	18	2	3.79
		Caudate_R (aal)	14	10	12	3.69
		Caudate_R (aal)	14	0	12	3.62

improved in WM maintenance and intact in the more difficult WM manipulation in HCs, while in OCDs under stress, the performance was also improved in WM maintenance but impaired in WM manipulation. Previous meta-analysis of the neuropsychology of OCD only found small negative mean effect sizes for WM across studies, which suggested that OCD patients perform worse than controls to a relatively small extent [9]. Although few previous studies have explored the role of acute stress in WM in OCD patients, several studies of HCs have shown that stress tends to increase the accuracy of WM [29, 30]. A previous meta-analysis implied that the overall influence of acute stress on WM is deleterious, depending on stress severity, WM load, and percentage of male participants [31]. Although no significant between-group difference in the brain activity was found in WM maintenance or manipulation under stress and non-stress, the behavioral findings in the current study suggested that WM in patients with OCD was impaired to a less severe extent, consistent with the previous findings, and might be more vulnerable to stress than HCs.

Brain Activation

Less Engagement of the mPFC and Limbic System in HCs Under Stress

In the HCs, the stress effect on WM activations included less involvement of the mPFC (more deactivation) and the striatum (less activation) and increased activity in the cerebellum. The finding of less activation in the striatum is consistent with previous work on HCs in which stress increased activity in prefrontal and parietal cortex [29] and reduced activity in limbic areas including the ventral striatum, hypothalamus, amygdala, and hippocampus [32]. Moreover, Kogler *et al*. found psychosocial stress-related deactivation in the striatum and activation in the superior temporal cortex in a meta-analysis of neuroimaging studies [33]. The mPFC plays an important role in processing information about stressors and regulating the corresponding behavioral responses [34–36]. Van Leeuwen *et al*. investigated the responses to an emotional stimulus after inducing acute stress in healthy adults and the healthy siblings of patients with schizophrenia. They found that the HCs, but not the siblings of schizophrenics, showed reduced deactivation in the mPFC, middle cingulate gyrus, posterior cingulate gyrus, precuneus, and superior temporal cortex following stress; these were consistent with the regions of the DMN [37]. Thus, we assumed that suppression of the mPFC might be a reassignment of neural resources to the stress response by suppressing self-referential processes and salience detection as well [37]. However, conflicting studies have found that, after inducing stress, the dorsolateral PFC is less activated and the medial orbitofrontal cortex within the DMN is less deactivated than under the non-stress condition [38, 39]. The reason could be that an overly strong stress induced higher cortisol levels or other possible confounding factors that made the finding different from the previous [29] and our findings.

Failure to Suppress the Default Mode Network in OCD Patients Under Stress

OCD patients showed a pattern different from the HCs: regions in the DMN, including the mPFC and bilateral temporal cortex were more involved (less deactivation) under competitive *versus* non-competitive conditions. A recent study investigated the deactivated pattern of the DMN in OCDs and HCs under a transition from a resting to a non-resting context. They indicated that OCDs had a failure to suppress the DMN activity even during the emotion-provoking stimulus [40]. Using the same MIST task, Lord *et al*. reported less deactivation in the mPFC and orbitofrontal cortex induced by stress in postpartum OCD patients [41]. A deficit of DMN suppression has also been found in schizophrenia and depression during WM tasks [42–44], and failure of the DMN suppression is associated with a worse behavioral performance in schizophrenia and depression [42]. Thus, less suppression of the DMN under stress could be a common neural response to stress in OCD, schizophrenia, and depression and might be correlated with worse behavioral performance.

Previous studies have generally suggested that the DMN supports an internal model for the self-referential process [45, 46]. DMN suppression plays an important role in external goal-directed cognition tasks by suppressing certain internal activity such as daydreaming and self-referential thought [42]. A study of large-scale brain networks considered that the networks are dynamically-shifting and resource re-allocated by neurobiological modulators to adapt to acute stress [20]. Previous functional connectivity studies of OCD reported dysconnectivity within the DMN and between networks for salience, frontoparietal and the DMN [47], and reduced connectivity within DMN subsystems [48]. Therefore, a failure of DMN suppression during cognition and under stress might be one of the neural mechanisms underlying the cognitive impairment induced by stress in OCDs.

Stress-Related Hypersensitivity in OCD

An interaction effect of diagnosis and stress was found both on behavioral performance and neural response only in WM manipulation, indicating that WM deficits in OCD are load-dependent and can be influenced by stress. Activations in the right fusiform, SMA, precentral cortex, and right caudate were significantly higher in the OCD group after inducing stress.

The Fusiform Gyrus

The lateral part of the fusiform gyrus was named as the fusiform face area (FFA) because of its specific role in face processing [49]. Few studies have investigated the function of the FFA in OCD patients. However, increased fMRI activity in the FFA has been found in schizophrenia to compensate for the damaged basic integration capability during spatial frequency-degraded face processing [50]. The FFA is hyperactivated and has greater connectivity with the amygdala in social anxiety disorder when handling the fearful face [51]. Moreover, several previous studies in healthy adults have also found interpersonal competition-related hyperactivation in the right fusiform and suggested its role in the social interaction process [52–54]. Thus, we assumed that the hyperactivity of the right fusiform in OCD was compensation to process the relevant information of the WM task under interpersonally competitive stress.

The Supplementary Motor Area

The right SMA showed greater activation after inducing stress in OCD patients under the manipulation task and was negatively correlated with the severity of obsession. De Vries *et al*. reported hyperactivity of the pre-SMA in OCD patients during a higher-level n-back task [17] and a response inhibition task [55]. They also found that right pre-SMA activation is negatively correlated with illness severity, suggesting that hyperactivity of the pre-SMA is a candidate endophenotype of OCD. The SMA, pre-SMA and the supplementary eye field compose the supplementary motor complex (SMC), which links cognition to action [56]. Studies of macaque monkeys has provided the most evidence for the anatomy and connections between the SMC and the basal ganglia (including direct, indirect, and hyper-direct pathways similar to the CSTC circuit) [56]. Lesion studies of the SMC reported difficulty in task-switching that resulted in compulsivity [57, 58]. Thus, we assumed that the SMC takes part in the neuropathological mechanism of OCD and is activated in compensation for the stress response.

The Precentral Gyrus

The primary motor cortex is included in the precentral gyrus and is responsible for motor responses. Previous studies have found hyperactivity of the precentral gyrus in emotional regulation-related tasks in mood and anxiety disorders and high-risk individuals [59–61]. Thus, the finding of significantly lower activation of the precentral gyrus in OCDs compared with HCs under non-competitive conditions but significant hyperactivity after inducing stress in OCDs is consistent with the results of previous research and might be a compensatory mechanism for stress response.

The Caudate

Caudate dysfunction is one of the most consistent findings in OCD. Previous work on the brain morphology of OCD patients consistently found increased volume in the caudate [62, 63]. Resting-state functional connectivity (FC) studies of OCD patients found that the decreased FC between the ventrolateral PFC and the caudate is associated with decreased cognitive flexibility [64]. A symptom provocation study reported reduced activation in the caudate nucleus [65], while activation of the caudate is considered to contribute to goal-directed behavior [66, 67]. Few previous studies have explored stress-related activation of the subcortical regions during WM in OCD patients. However, several studies have reported stress-related hyperactivity in the caudate in depressed patients, reflecting hypersensitivity to stress [44, 68]. Thus, according to the pathological model of OCD, acute stress might induce the compensatory upregulation of activity in the caudate to increase goal-directed action and to improve WM performance in OCD.

The four brain regions discussed above are associated with the pathological circuit of OCD [56, 69] and might

also be involved in social stress processes [70]. Thus, we assumed that their activation is compensatory upregulation for the stress response. However, more research is needed to verify the existence of an OCD-specific stress network.

Clinical Implications

The accuracy rate was negatively correlated with the OCD symptom severity score, especially the accuracy rate in WM manipulation under stress, and the reaction time of all task conditions was negatively correlated with the scores on the HAMA and HAMD, which indicated that neural dysfunction related to the psychopathology of OCD is associated with the WM network dysfunction. The previous meta-analysis of resting-state fMRI showed that the frontoparietal regions are the commonly impaired circuits in both the assumed OCD model and executive and WM networks [36, 47], consistent with the behavioral findings in the current study. The contrasts of compensatory upregulation of the four areas were negatively correlated with OCD symptom severity, which indicate that patients with less severe symptoms are better able to compensate.

Limitations and Future Directions

This study has several potential limitations. First, given the limited sample size, we could not further explore the stress effect on different subtypes of OCD or gender to investigate the relationship between clinical heterogeneity and neural responses to stress. Second, more than half of the patients were taking antidepressants during fMRI scanning. Although we included medication dosage as confounding, it may still have influenced brain activity. It is necessary to recruit drug-naive patients in future. Third, the OCD and HC groups were well matched in demography but for age. However, we tried to remove the linear effect from all the findings and most of the participants in both groups were in their twenties. Therefore, age was less likely to be the main factor causing a between-group difference. Nevertheless, a future study with a larger sample of OCD patients and including other neuropsychiatric disorders is necessary to verify the current findings and explore their specificity over diseases. Fourth, the relationship between altered neural activity and symptoms did not conform to the expected direction, although some previous study have reported similar findings [55]. Besides, no correlation findings survived FDR correction in the current study. Therefore, we should treat all the correlation findings with caution before they are verified with further evidence.

Conclusion

The study provides evidence that OCD patients are more vulnerable to acute stress, which affects their WM-related neuro-mechanisms. The failure of suppression of the mPFC and striatum and stress-related hyperactivation of the right fusiform, SMA, precentral, and right caudate might be OCD-related psychopathological and neural responses to stress.

Acknowledgements This work was supported by the National Natural Science Foundation of China (81771443, 81370032, 81601171, and 91432304). We thank National Center for Protein Sciences at Peking University in Beijing, China, for assistance with MRI data acquisition.

Conflict of interest The authors claim that there are no conflicts of interest.

References

1. Pauls DL. The genetics of obsessive-compulsive disorder: a review. Dialogues Clin Neurosci 2010, 12: 149–163.
2. Pauls DL, Abramovitch A, Rauch SL, Geller DA. Obsessive-compulsive disorder: an integrative genetic and neurobiological perspective. Nat Rev Neurosci 2014, 15: 410–424.
3. Veale D, Roberts A. Obsessive-compulsive disorder. BMJ 2014, 348: g2183.
4. Bobes J, González MP, Bascarán MT, Arango C, Sáiz PA, Bousoño M. Quality of life and disability in patients with obsessive-compulsive disorder. Eur Psychiatry 2001, 16: 239–245.
5. Brander G, Pérez-Vigil A, Larsson H, Mataix-Cols D. Systematic review of environmental risk factors for Obsessive-Compulsive Disorder: a proposed roadmap from association to causation. Neurosci Biobehav Rev 2016, 65: 36–62.
6. Kanehisa M, Kawashima C, Nakanishi M, Okamoto K, Oshita H, Masuda K, *et al*. Gender differences in automatic thoughts and cortisol and alpha-amylase responses to acute psychosocial stress in patients with obsessive-compulsive personality disorder. J affect disord 2017, 217: 1–7.
7. Robbins TW, Vaghi MM, Banca P. Obsessive-Compulsive Disorder: Puzzles and Prospects. Neuron 2019, 102: 27–47.
8. Schwabe L, Wolf OT. Stress prompts habit behavior in humans. J Neurosci 2009, 29: 7191–7198.

9. Abramovitch A, Abramowitz JS, Mittelman A. The neuropsychology of adult obsessive-compulsive disorder: a meta-analysis. Clin Psychol Rev 2013, 33: 1163–1171.
10. Dolan RJ, Dayan P. Goals and habits in the brain. Neuron 2013, 80: 312-325.
11. Liu S, Schad DJ, Kuschpel MS, Rapp MA, Heinz A. Music and Video Gaming during Breaks: Influence on Habitual versus Goal-Directed Decision Making. PLoS One 2016, 11: e150165.
12. Zou S, Li CT. High-Throughput Automatic Training System for Spatial Working Memory in Free-Moving Mice. Neurosci Bull 2019, 35: 389–400.
13. Menzies L, Chamberlain SR, Laird AR, Thelen SM, Sahakian BJ, Bullmore ET. Integrating evidence from neuroimaging and neuropsychological studies of obsessive-compulsive disorder: the orbitofronto-striatal model revisited. Neurosci Biobehav Rev 2008, 32: 525–549.
14. Pauls DL, Abramovitch A, Rauch SL, Geller DA. Obsessive–compulsive disorder: an integrative genetic and neurobiological perspective. Nat Rev Neurosci 2014, 15: 410–424.
15. Saxena S, Rauch SL. Functional neuroimaging and the neuroanatomy of obsessive-compulsive disorder. Psychiatr Clin North Am 2000, 23: 563–586.
16. Banca P, Voon V, Vestergaard MD, Philipiak G, Almeida I, Pocinho F, *et al*. Imbalance in habitual versus goal directed neural systems during symptom provocation in obsessive-compulsive disorder. Brain 2015, 138: 798–811.
17. de Vries FE, de Wit SJ, Cath DC, van der Werf YD, van der Borden V, van Rossum TB, *et al*. Compensatory frontoparietal activity during working memory: an endophenotype of obsessive-compulsive disorder. Biol Psychiatry 2014, 76: 878–887.
18. Etkin A, Wager TD. Functional neuroimaging of anxiety: a meta-analysis of emotional processing in PTSD, social anxiety disorder, and specific phobia. Am J Psychiatry 2007, 164: 1476–1488.
19. Stark EA, Parsons CE, Van Hartevelt TJ, Charquero-Ballester M, McManners H, Ehlers A, *et al*. Post-traumatic stress influences the brain even in the absence of symptoms: A systematic, quantitative meta-analysis of neuroimaging studies. Neurosci Biobehav Rev 2015, 56: 207–221.
20. Hermans EJ, Henckens MJAG, Joëls M, Fernández G. Dynamic adaptation of large-scale brain networks in response to acute stressors. Trends Neurosci 2014, 37: 304–314.
21. de Kloet ER, Joëls M, Holsboer F. Stress and the brain: from adaptation to disease. Nat Rev Neurosci 2005, 6: 463–475.
22. Dedovic K, Renwick R, Mahani NK, Engert V, Lupien SJ, Pruessner JC. The montreal imaging stress task: using functional imaging to investigate the effects of perceiving and processing psychosocial stress in the human brain. J Psychiatry Neurosci 2005, 30: 319–325.
23. Zhang X, Yan H, Yu H, Zhao X, Shah S, Dong Z, *et al*. Childhood urbanization affects prefrontal cortical responses to trait anxiety and interacts with polygenic risk for depression. bioRxiv 2019: 246876.
24. Goodman WK, Price LH, Rasmussen SA, Mazure C, Fleischmann RL, Hill CL, *et al*. The yale-brown obsessive compulsive scale. I. development, use, and reliability. Arch Gen Psychiatry 1989, 46: 1006–1011.
25. Hayasaka Y, Purgato M, Magni LR, Ogawa Y, Takeshima N, Cipriani A, *et al*. Dose equivalents of antidepressants: Evidence-based recommendations from randomized controlled trials. J Affect Disord 2015, 180: 179–184.
26. Tan HY, Chen Q, Goldberg TE, Mattay VS, Meyer-Lindenberg A, Weinberger DR, *et al*. Catechol-o-methyltransferase Val158-Met modulation of prefrontal parietal striatal brain systems during arithmetic and temporal transformations in working memory. J Neurosci 2007, 27: 13393–13401.
27. Tan HY, Chen AG, Kolachana B, Apud JA, Mattay VS, Callicott JH, *et al*. Effective connectivity of AKT1-mediated dopaminergic working memory networks and pharmacogenetics of antidopaminergic treatment. Brain 2012, 135: 1436–1445.
28. Rahm B, Kaiser J, Unterrainer JM, Simon J, Bledowski C. fMRI characterization of visual working memory recognition. Neuroimage 2014, 90: 413–422.
29. Weerda R, Muehlhan M, Wolf OT, Thiel CM. Effects of acute psychosocial stress on working memory related brain activity in men. Hum Brain Mapp 2010, 31: 1418–1429.
30. Yuen EY, Liu W, Karatsoreos IN, Feng J, McEwen BS, Yan Z. Acute stress enhances glutamatergic transmission in prefrontal cortex and facilitates working memory. Proc Natl Acad Sci U S A 2009, 106: 14075–14079.
31. Shields GS, Sazma MA, Yonelinas AP. The effects of acute stress on core executive functions: a meta-analysis and comparison with cortisol. Neurosci Biobehav Rev 2016, 68: 651–668.
32. Pruessner JC, Dedovic K, Khalili-Mahani N, Engert V, Pruessner M, Buss C, *et al*. Deactivation of the limbic system during acute psychosocial stress: evidence from positron emission tomography and functional magnetic resonance imaging studies. Biol Psychiatry 2008, 63: 234–240.
33. Kogler L, Müller VI, Chang A, Eickhoff SB, Fox PT, Gur RC, *et al*. Psychosocial versus physiological stress — Meta-analyses on deactivations and activations of the neural correlates of stress reactions. Neuroimage 2015, 119: 235–251.
34. Amat J, Paul E, Zarza C, Watkins LR, Maier SF. Previous experience with behavioral control over stress blocks the behavioral and dorsal raphe nucleus activating effects of later uncontrollable stress: role of the ventral medial prefrontal cortex. J Neurosci 2006, 26: 13264–13272.
35. Rozeske RR, Der-Avakian A, Bland ST, Beckley JT, Watkins LR, Maier SF. The medial prefrontal cortex regulates the differential expression of morphine-conditioned place preference following a single exposure to controllable or uncontrollable stress. Neuropsychopharmacology 2009, 34: 834–843.
36. Arnsten AFT. Stress signalling pathways that impair prefrontal cortex structure and function. Nat Rev Neurosci 2009, 10: 410–422.
37. van Leeuwen J, Vink M, Fernandez G, Hermans EJ, Joels M, Kahn RS, *et al*. At-risk individuals display altered brain activity following stress. Neuropsychopharmacology 2018, 43: 1954–1960.
38. Qin S, Hermans EJ, van Marle HJF, Luo J, Fernández G. Acute psychological stress reduces working memory-related activity in the dorsolateral prefrontal cortex. Biol Psychiatry 2009, 66: 25–32.
39. Luettgau L, Schlagenhauf F, Sjoerds Z. Acute and past subjective stress influence working memory and related neural substrates. Psychoneuroendocrinology 2018, 96: 25–34.
40. Gonçalves ÓF, Soares JM, Carvalho S, Leite J, Ganho-Ávila A, Fernandes-Gonçalves A, *et al.* Patterns of Default Mode Network Deactivation in Obsessive Compulsive Disorder. Sci Rep 2017, 7: 44468.
41. Lord C, Steiner M, Soares CN, Carew CL, Hall GB. Stress response in postpartum women with and without obsessive-compulsive symptoms: an fMRI study. J Psychiatry Neurosci 2012, 37: 78–86.
42. Anticevic A, Cole MW, Murray JD, Corlett PR, Wang XJ, Krystal JH. The role of default network deactivation in cognition and disease. Trends Cogn Sci 2012, 16: 584–592.
43. Anticevic A, Repovs G, Barch DM. Working memory encoding and maintenance deficits in schizophrenia: neural evidence for activation and deactivation abnormalities. Schizophr Bull 2013, 39: 168–178.

44. Ming Q, Zhong X, Zhang X, Pu W, Dong D, Jiang Y, *et al*. State-independent and dependent neural responses to psychosocial stress in current and remitted depression. Am J Psychiatry 2017, 174: 971–979.
45. Buckner RL, Andrews-Hanna JR, Schacter DL. The brain's default network: anatomy, function, and relevance to disease. Ann N Y Acad Sci 2008, 1124: 1–38.
46. Raichle ME. The brain's default mode network. Annu Rev Neurosci 2015, 38: 433–447.
47. Gürsel DA, Avram M, Sorg C, Brandl F, Koch K. Frontoparietal areas link impairments of large-scale intrinsic brain networks with aberrant fronto-striatal interactions in OCD: a meta-analysis of resting-state functional connectivity. Neurosci Biobehav Rev 2018, 87: 151–160.
48. Beucke JC, Sepulcre J, Eldaief MC, Sebold M, Kathmann N, Kaufmann C. Default mode network subsystem alterations in obsessive–compulsive disorder. Br J Psychiatry 2014, 205: 376–382.
49. Loffler G, Yourganov G, Wilkinson F, Wilson HR. fMRI evidence for the neural representation of faces. Nat Neurosci 2005, 8: 1386–1391.
50. Silverstein SM, All SD, Kasi R, Berten S, Essex B, Lathrop KL, *et al*. Increased fusiform area activation in schizophrenia during processing of spatial frequency-degraded faces, as revealed by fMRI. Psychol Med 2010, 40: 1159–1169.
51. Frick A, Howner K, Fischer H, Kristiansson M, Furmark T. Altered fusiform connectivity during processing of fearful faces in social anxiety disorder. Transl Psychiatry 2013, 3: e312.
52. Assaf M, Kahn I, Pearlson GD, Johnson MR, Yeshurun Y, Calhoun VD, *et al*. Brain activity dissociates mentalization from motivation during an interpersonal competitive game. Brain Imaging Behav 2009, 3: 24–37.
53. Piva M, Zhang X, Noah JA, Chang SWC, Hirsch J. Distributed neural activity patterns during human-to-human competition. Front Hum Neurosci 2017, 11: 571.
54. Polosan M, Baciu M, Cousin E, Perrone M, Pichat C, Bougerol T. An fMRI study of the social competition in healthy subjects. Brain Cogn 2011, 77: 401–411.
55. de Wit SJ, de Vries FE, van der Werf YD, Cath DC, Heslenfeld DJ, Veltman EM, *et al*. Presupplementary motor area hyperactivity during response inhibition: a candidate endophenotype of obsessive-compulsive disorder. Am J Psychiatry 2012, 169: 1100–1108.
56. Nachev P, Kennard C, Husain M. Functional role of the supplementary and pre-supplementary motor areas. Nat Rev Neurosci 2008, 9: 856–869.
57. Husain M, Parton A, Hodgson TL, Mort D, Rees G. Self-control during response conflict by human supplementary eye field. Nat Neurosci 2003, 6: 117–118.
58. Parton A, Nachev P, Hodgson TL, Mort D, Thomas D, Ordidge R, *et al*. Role of the human supplementary eye field in the control of saccadic eye movements. Neuropsychologia 2007, 45: 997–1008.
59. Picó-Pérez M, Radua J, Steward T, Menchón JM, Soriano-Mas C. Emotion regulation in mood and anxiety disorders: A meta-analysis of fMRI cognitive reappraisal studies. Prog Neuropsychopharmacol Biol Psychiatry 2017, 79: 96–104.
60. Hardee JE, Cope LM, Munier EC, Welsh RC, Zucker RA, Heitzeg MM. Sex differences in the development of emotion circuitry in adolescents at risk for substance abuse: a longitudinal fMRI study. Soc Cogn Affect Neurosci 2017, 12: 965–975.
61. Saarimäki H, Gotsopoulos A, Jääskeläinen IP, Lampinen J, Vuilleumier P, Hari R, *et al.* Discrete neural signatures of basic emotions. Cereb Cortex 2016, 26: 2563–2573.
62. Boedhoe PS, Schmaal L, Abe Y, Ameis SH, Arnold PD, Batistuzzo MC, *et al*. Distinct subcortical volume alterations in pediatric and adult OCD: a worldwide meta- and mega-analysis. Am J Psychiatry 2017, 174: 60–69.
63. Tan L, Fan Q, You C, Wang J, Dong Z, Wang X, *et al*. Structural changes in the gray matter of unmedicated patients with obsessive-compulsive disorder: a voxel-based morphometric study. Neurosci Bull 2013, 29: 642–648.
64. Vaghi MM, Vértes PE, Kitzbichler MG, Apergis-Schoute AM, van der Flier FE, Fineberg NA, *et al*. Specific frontostriatal circuits for impaired cognitive flexibility and goal-directed planning in obsessive-compulsive disorder: evidence from resting-state functional connectivity. Biol Psychiatry 2017, 81: 708–717.
65. Fineberg NA, Apergis-Schoute AM, Vaghi MM, Banca P, Gillan CM, Voon V, *et al*. Mapping compulsivity in the DSM-5 obsessive compulsive and related disorders: cognitive domains, neural circuitry, and treatment. Int J Neuropsychopharmacol 2018, 21: 42–58.
66. Jahanshahi M, Obeso I, Rothwell JC, Obeso JA. A fronto-striato-subthalamic-pallidal network for goal-directed and habitual inhibition. Nat Rev Neurosci 2015, 16: 719–732.
67. Gremel CM, Costa RM. Orbitofrontal and striatal circuits dynamically encode the shift between goal-directed and habitual actions. Nat Commun 2013, 4: 2264.
68. Admon R, Holsen LM, Aizley H, Remington A, Whitfield-Gabrieli S, Goldstein JM, *et al*. Striatal hypersensitivity during stress in remitted individuals with recurrent depression. Biol Psychiatry 2015, 78: 67–76.
69. Schultz RT, Grelotti DJ, Klin A, Kleinman J, Van der Gaag C, Marois R, *et al*. The role of the fusiform face area in social cognition: implications for the pathobiology of autism. Philos Trans R Soc Lond B Biol Sci 2003, 358: 415–427.
70. Alcalá-López D, Smallwood J, Jefferies E, Van Overwalle F, Vogeley K, Mars RB, *et al*. Computing the social brain connectome across systems and states. Cereb Cortex 2018, 28: 2207–2232.

Neurosci. Bull. January, 2021, 37(1):94–98
https://doi.org/10.1007/s12264-020-00558-8

www.neurosci.cn
www.springer.com/12264

LETTER TO THE EDITOR

Gray Matter-Based Age Prediction Characterizes Different Regional Patterns

Nianming Zuo[1,2,3,4] · Tianyu Hu[1,2,3] · Hao Liu[1,2,3] · Jing Sui[1,2,3,5] · Yong Liu[1,2,3,5] · Tianzi Jiang[1,2,3,4,5,6,7]

Received: 5 March 2020 / Accepted: 31 May 2020 / Published online: 19 August 2020

Dear Editor,

The brain experiences ongoing changes across different ages to support brain development and functional reorganization. During the span of adulthood, although the brain has matured from a neurobiological perspective, it is still continuously shaped by external factors such as habits, the family setting, socioeconomic status, and the work environment [1]. In contrast to chronological age (CA), brain (or biological) age (BA) is conceptualized as an important index for characterizing the aging process and neuropsychological state, as well as individual cognitive performance. Growing evidence indicates that BA can be assessed by neuroimaging techniques, including MRI [2]. Due to their short collection time, stable image features, and (usual) availability during clinical diagnosis, T1-weighted MRIs are considered the first choice for estimating BA, with structural features including local/global volumes of gray matter (GM) and white matter (WM), geometrical characteristics of the cerebral cortex, and distinctions between GM and WM at the boundary [3].

There are two elusive questions in T1-weighted MRI-based BA prediction. The first is how to improve prediction accuracy. At present, research is either limited by relatively poor accuracy or by incomplete age span datasets. Currently, the mean average error (MAE) for a full adult age span dataset for a single site is >4 years. As expected, reports based on multi-site data are usually much less accurate. For example, Valizadeh and colleagues [4] comprehensively tested a variety of feature extractions based on multi-site T1 images and prediction algorithms, and demonstrated varying prediction accuracies in different age classes, but generally ~5.5 years. The second question is how to understand the neurobiological principles in age prediction. Although both structural and functional differences between male and female brains are increasingly reported and are manifest in the aging trajectory [5], as characterized by MRI T1 images, whether there are brain region gender- and age-effects on age prediction remains less examined. These limitations have hindered the popularization of MRI-based age prediction and the associated assessment of cognitive capabilities.

In this study, we propose an intuitive and effective age-prediction model using GM volume and the Brainnetome atlas [6] (Fig. 1). Briefly, the partial least squares (PLS) method was used to project GM volume features (classified by the Brainnetome atlas, which fully covers both cortical

Nianming Zuo and Tianyu Hu have contributed equally to this work.

Electronic supplementary material The online version of this article (https://doi.org/10.1007/s12264-020-00558-8) contains supplementary material, which is available to authorized users.

✉ Nianming Zuo
nmzuo@nlpr.ia.ac.cn

1 Brainnetome Center, Institute of Automation, Chinese Academy of Sciences (CAS), Beijing 100190, China

2 National Laboratory of Pattern Recognition, Institute of Automation, CAS, Beijing 100190, China

3 University of CAS, Beijing 100190, China

4 Chinese Institute for Brain Research, Beijing 102206, China

5 Center for Excellence in Brain Science and Intelligence Technology, Institute of Automation, CAS, Beijing 100190, China

6 Key Laboratory for NeuroInformation of the Ministry of Education, School of Life Science and Technology, University of Electronic Science and Technology of China, Chengdu 625014, China

7 Queensland Brain Institute, University of Queensland, Brisbane, QLD 4072, Australia

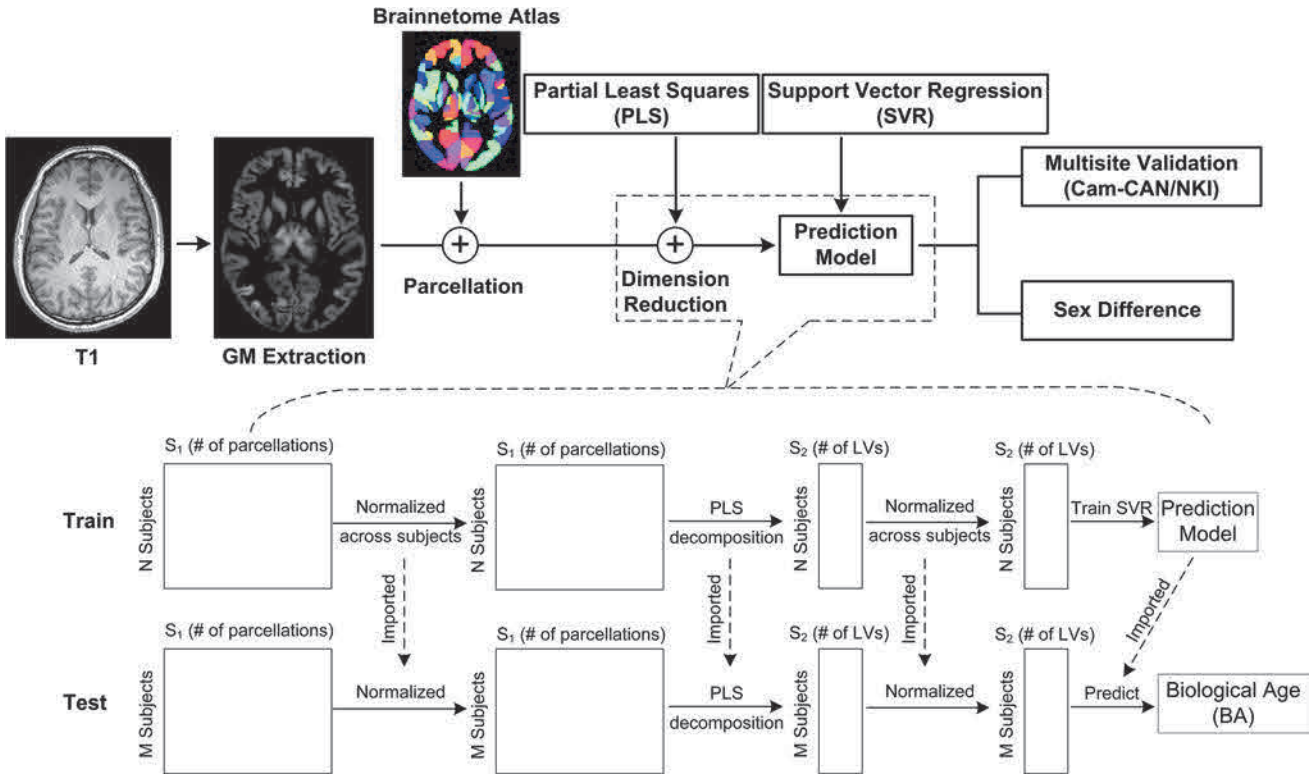

Fig. 1 Diagram showing the construction and validation of the prediction model. N and M are the number of input subjects in the training and testing processes, respectively, and S_1 and S_2 are the number of variables before and after (then selected) PLS decomposition, respectively. When the 5-fold cross-validation method was used, the training and testing processes were independently repeated.

and subcortical GM) into orthogonal space, with only the important features that explained the greatest proportion of variance in regressing observers retained [7]. Unlike traditional principal component analysis (PCA), PLS extracts the latent variables by modeling the covariance structures in both predicted and observed variable space. Thus, this supervised dimension reduction method is more efficient than PCA. The PLS algorithm is therefore suitable for exploring the relationship between functional activation and external stimulus patterns, namely, the functional activation detection in fMRI analysis, and the relationship between functional patterns and behavioral measurements [7]. Therefore, it is also reasonable to transfer to projected GM volume features. The prediction was then modeled by support vector regression (SVR) with radial basis function kernels.

The Cambridge Centre for Ageing and Neuroscience (Cam-CAN) dataset [8] was used to evaluate the proposed algorithm. Release #1 consists of 655 participants and includes T1-weighted MRI, resting-state fMRI, and diffusion MRI images. After removing the unqualified data, including degraded images and excessive head motion, 620 participants remained, with a male:female ratio of 305:315 and an age range of 18 years to 88 years. The prediction error (discrepancy between BA and CA) was estimated to determine its relationship to behavioral performance, including fluid intelligence (gF). In the Cam-CAN dataset, gF was assessed by the Cattell test, which contains four subtests of nonverbal puzzles involving series completion, classification, matrices, and conditions. Those participants scoring <12 were designated as non-engaging and were thus removed (as suggested in the Cam-CAN data package). Therefore, 603 out of the 620 participants had valid gF records, where age = 52.72 ± 18.19 years and gF score = 32.35 ± 6.59. Overview of Cam-CAN samples used in this study was shown in Fig. S1. The independent dataset, Enhanced Nathan Krow Institute-Rockland Sample (NKI) dataset was used for extended study to evaluate the prediction model.

After reviewing the influence of the numbers of latent variables on PLS decomposition, only 13 were chosen for the subsequent SVR training and prediction as there was little difference in prediction accuracy when the number of latent variables varied from 12 to 18 (Table S1). Results based on the Cam-CAN dataset showed that the MAE for age prediction was ~2.25 years through 5-fold cross-validation and the MAE was stable across 500 bootstraps (Fig. 2A, B). Validation of the prediction model based on different combinations of two independent datasets was shown in Table S2. Further validation results were shown

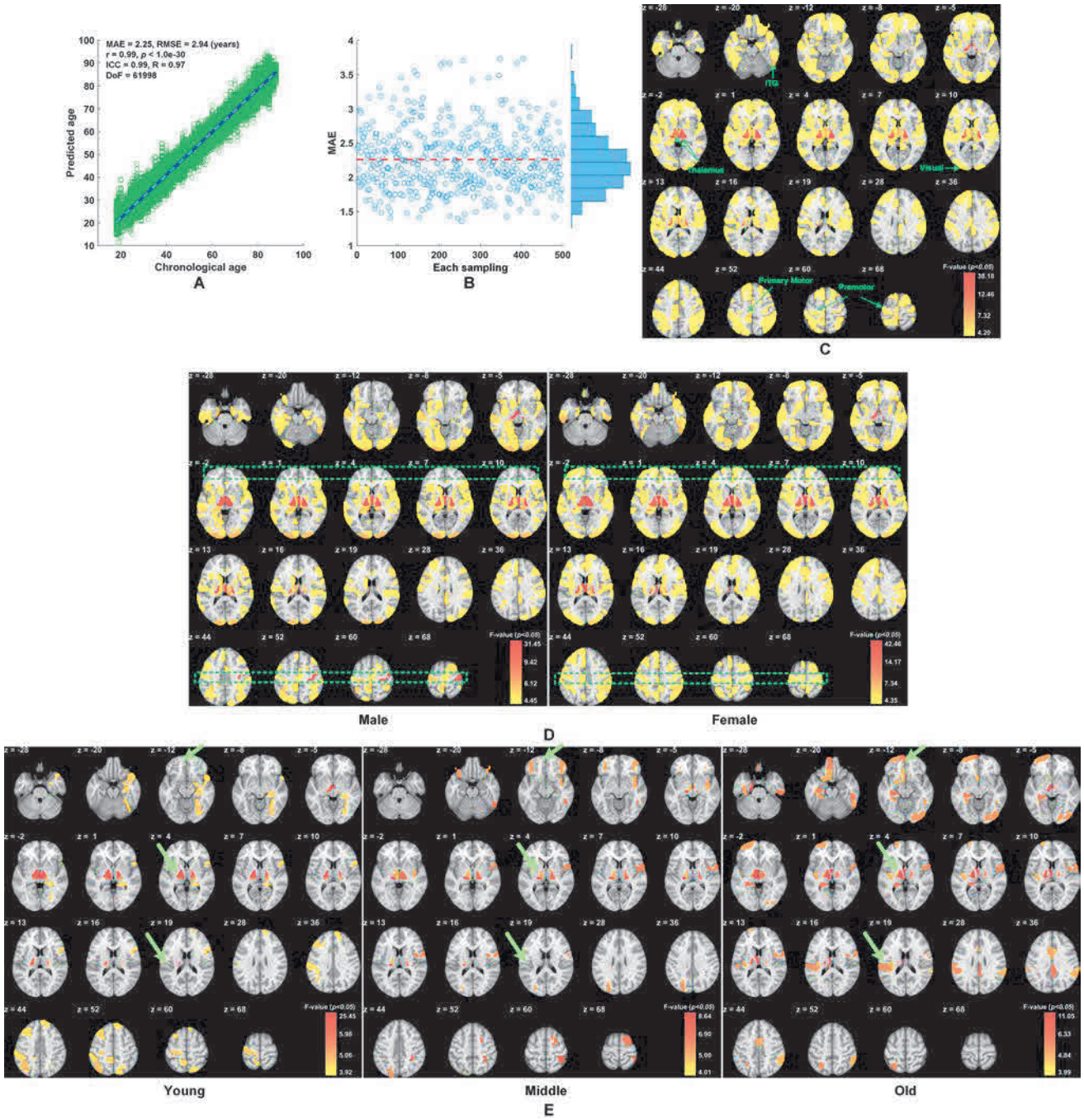

Fig. 2 **A**, **B** Mean average error (MAE) for prediction accuracy is ~2.25 years (5-fold cross-validation in the Cam-CAN dataset). **C** Regions contributing most include the posterior inferior temporal gyrus (ITG), thalamus, primary cortex (including visual and motor cortices), prefrontal cortex, lateral occipital cortex, and insular cortex (z in mm). **D** Different brain region contributions in male and female groups, particularly in prefrontal regions and motor cortex (primary and premotor cortices) (green boxes; z in mm). **E** Regional contributions in age prediction (similar to **D**) in the three subgroups, Young (163 subjects aged 17–39 years), Middle (172 subjects aged 44–61 years), and Old (175 subjects aged 69–88 years), where the green arrows in each row highlight the difference of contributions in the same anatomical regions between the three groups. MAE, mean average error; BA, biological age; CA, chronological age; ICC, intraclass correlation coefficient; RMSE, root mean squared error; DoF, degrees of freedom.

in Tables S3, S4. To evaluate the contributions from each brain region in age prediction, significance multivariate correlation (sMC) criteria were used to assess the variable importance selection in PLS [9]. Thus, the F-value for each region (246 regions in total in the Brainnetome atlas [6]) was used for selection importance. The results showed that those regions contributing most to age prediction were concentrated in the bilateral thalamus and primary cortex,

including the visual and motor cortices. The non-colored regions in Fig. 2C indicate that sMC failed to reach a significant level (by default $\alpha = 0.01$). It is well accepted that the thalamus is a pivotal hub of the brain, and connects to most parts of the cerebral cortex to form a variety of functional networks, including the thalamo-frontal, thalamo-parietal, and thalamo-limbic networks [10]. These functional networks consolidate the capabilities of the brain in attention, information processing, episodic memory, working memory, and other higher cognitive functions. Over the lifetime aging process, the thalamus and putamen are the top two subcortical structures whose variance is explained by age. Therefore, it is reasonable to conclude that the thalamus is a critical contributor in age prediction. In addition, interacting with the external environment by frequently accessing and calling, the primary cortex, including the visual and motor cortices, also intensively co-functions with the higher cortex and the thalamus, and reflects the aging process [11]. This partially addresses why the primary cortex is also an important contributor in age prediction. Other engaged regions include the frontal and parietal lobes as evidenced by Lin and colleagues [12].

Furthermore, the prediction error (CA – BA) was significantly correlated with gF: $r = -0.22$, $P < 1.0e{-}30$, DoF (degrees of freedom) = 60,483. A further question was raised regarding whether gender influenced prediction accuracy. We first checked whether the male and female samples had intrinsically different distributions, and found no significant differences in age distribution [$P = 0.59$ (t-test), $P = 0.63$ (Kolmogorov-Smirnov (KS) test), DoF = 618 for the 620 subjects and $P = 0.68$ (t-test), $P = 0.81$ (KS test), DoF = 601 for the 603 subjects]. Furthermore, we found no significant differences in age or gF distributions in the groups containing intact gF records both for mean values and distributions of male and female samples, where the distributions were tested by the two-sample KS test in MatLab using the kstest2 function. Thus, it was statistically reasonable to examine the differences in prediction errors between the male and female groups. The results demonstrated that the prediction error in the male group was significantly higher than that in the female group ($\Delta = 0.24$ years, $P = 2.2e{-}16$, DoF = 61998). Thus, males generally showed a higher estimated BA compared to their CA than that exhibited in females. Moreover, we further examined whether the brain region contributions to age-prediction showed different patterns between the male and female groups. Rather than predicting age across the entire group, we separately evaluated the regional sMC for the male and female groups and found differences in frontal and motor regions (highlighted by dashed green squares in Fig. 2D). Corresponding results of NKI were shown in Figs. S4-S6.

Intriguingly, the old group demonstrated more contributions from the frontal lobe (including frontal pole and medial frontal cortex) and left hemisphere (including the opercular cortex and thalamus) in contrast to their counterparts in the young group (Fig. 2E). The increased contributions from the frontal lobe are in agreement with the hypothesis of a posterior-anterior shift with aging [13]. Hemispheric asymmetry declines in the aging process; however, hemispheric asymmetry is a critical factor enabling modular efficiency in information processing. Our GM-based study further confirmed that hemispheric asymmetry and a left hemisphere-shift still exists in the healthy aging brain, in accordance with reports on aging [14].

We further investigated whether the gender-moderated effects on the relationship between age residuals and gF are significant. For experimental condition X, we have a dependent variable Y. In the case of significant correlations between X, Y, and an implicit factor M, the mediation analysis examines whether M indicates the underlying mechanism of the relationship between X and Y. However, the moderation analysis focuses on testing the influence of the moderator (gender in our study) on the relationship between X and Y [15]. The gender-moderated analysis (Fig. S3) revealed that gender showed a significant interaction effect on the relationship between the age residuals and intelligence ($b = -0.14$, standard error = 0.02, $t = -7.76$, $P < 2.2e{-}16$, DoF =60,483), where females showed a stronger negative correlation ($b = -0.57$, standard error = 0.01, $t = -42.7$, $P < 2.2e{-}16$, DoF = 30,319) between CA – BA and gF than males ($b = -0.43$, standard error = 0.01, $t = -35.23$, $P < 2.2e{-}16$, DoF = 30,177).

In summary, we propose an age-prediction method based on GM volumes parcellated by the Brainnetome atlas. This method is based only on GM extracted from T1-weighted MRI images, yet yields the highest accuracy reported to date for a large age-span dataset (>70 years). Furthermore, we determined that a higher estimated BA reflects a higher gF, and many regions across the brain contribute to age prediction, particularly the thalamus. There were significant gender and age differences in brain regions contributing to age prediction between males and females and between young and old. Specifically, we identified greater contributions from the prefrontal cortex and lower contributions from the primary cortex in females compared with males, and greater contributions from the frontal lobe and left hemisphere in the old group compared with the young group.

The T1-weighted image is usually the first choice for MRI scans in clinical diagnosis, so T1-based studies for clinical prediction receive more attention, and multimodal MRI only provides limited enhancement of prediction

accuracy according to a comprehensive comparative study [3]. The primary anatomical characteristics of brain tissue are extensively used, including the volumes and distinctions between GM and WM. In order to introduce an intuitive model with less of a computing burden for clinical application, we did not use the more advanced geometrical characteristics of cortex, such as cortical gyrification and complexity, and our results demonstrated better prediction accuracy than the existing reports based on single-site datasets. Although we evaluated the reproducibility of the proposed method across two datasets, practical MRI datasets usually have different features, including populations with different ages and different MRI vendors and parameters. Thus, more extensive evaluations are required to test the effectiveness of the method such as by using datasets from many MRI sites. Methodologically, the statistical test-retest strategy should be applied to evaluate the inter- and intra-class robustness. The proposed PLS+SVR prediction model structure is heuristic and can be readily extended to larger or multiple-site datasets with a low computational burden for retuning the parameters. It should be noted that the current findings are based on a cross-sectional dataset and should be further validated using multi-site and longitudinal datasets. The source code in MatLab and R (evaluating gender-moderated effects) for this study is available at https://gitee.com/nmzuo/AgePrediction.

Acknowledgments This work was supported by the National Natural Science Foundation of China (61971420), the Beijing Brain Initiative of the Beijing Municipal Science and Technology Commission (Z181100001518003), Special Projects of Brain Science of the Beijing Municipal Science and Technology Commission (Z161100000216139 and Z171100000117002), and the International Cooperation and Exchange of the National Natural Science Foundation of China (31620103905). Data were provided by the Cambridge Centre for Ageing and Neuroscience (http://www.mrc-cbu.cam.ac.uk/datasets/camcan).

Conflict of interest The authors declare that they have no conflict of interest in this work.

References

1. Zuo N, Salami A, Liu H, Yang Z, Jiang T. Functional maintenance in the multiple demand network characterizes superior fluid intelligence in aging. Neurobiol Aging 2020, 85: 145–153.
2. Cole JH, Ritchie SJ, Bastin ME, Valdes Hernandez MC, Munoz Maniega S, Royle N, *et al.* Brain age predicts mortality. Mol Psychiatry 2018, 23: 1385–1392.
3. Liem F, Varoquaux G, Kynast J, Beyer F, Kharabian Masouleh S, Huntenburg JM, *et al.* Predicting brain-age from multimodal imaging data captures cognitive impairment. Neuroimage 2017, 148: 179–188.
4. Valizadeh SA, Hanggi J, Merillat S, Jancke L. Age prediction on the basis of brain anatomical measures. Hum Brain Mapp 2017, 38: 997–1008.
5. Goyal MS, Blazey TM, Su Y, Couture LE, Durbin TJ, Bateman RJ, *et al.* Persistent metabolic youth in the aging female brain. Proc Natl Acad Sci U S A 2019, 116: 3251–3255.
6. Fan L, Li H, Zhuo J, Zhang Y, Wang J, Chen L, *et al.* The human brainnetome atlas: A new brain atlas based on connectional architecture. Cereb Cortex 2016, 26: 3508–3526.
7. Krishnan A, Williams LJ, McIntosh AR, Abdi H. Partial Least Squares (PLS) methods for neuroimaging: a tutorial and review. Neuroimage 2011, 56: 455–475.
8. Taylor JR, Williams N, Cusack R, Auer T, Shafto MA, Dixon M, *et al.* The Cambridge Centre for Ageing and Neuroscience (Cam-CAN) data repository: Structural and functional MRI, MEG, and cognitive data from a cross-sectional adult lifespan sample. Neuroimage 2017, 144: 262–269.
9. Tran TN, Afanador NL, Buydens LMC, Blanchet L. Interpretation of variable importance in Partial Least Squares with Significance Multivariate Correlation (sMC). Chemom Intell Lab Syst 2014, 138: 153–160.
10. Behrens TE, Johansen-Berg H, Woolrich MW, Smith SM, Wheeler-Kingshott CA, Boulby PA, *et al.* Non-invasive mapping of connections between human thalamus and cortex using diffusion imaging. Nat Neurosci 2003, 6: 750–757.
11. West KL, Zuppichini MD, Turner MP, Sivakolundu DK, Zhao Y, Abdelkarim D, *et al.* BOLD hemodynamic response function changes significantly with healthy aging. Neuroimage 2019, 188: 198–207.
12. Lin Y, Li M, Zhou Y, Deng W, Ma X, Wang Q, *et al.* Age-related reduction in cortical thickness in first-episode treatment-naive patients with schizophrenia. Neurosci Bull 2019, 35: 688–696.
13. Sala-Llonch R, Bartres-Faz D, Junque C. Reorganization of brain networks in aging: a review of functional connectivity studies. Front Psychol 2015, 6: 663.
14. Esteves M, Magalhaes R, Marques P, Castanho TC, Portugal-Nunes C, Soares JM, *et al.* Functional Hemispheric (A)symmetries in the aged brain-relevance for working memory. Front Aging Neurosci 2018, 10: 58.
15. Nie Y, Lau S, Liau AK. Role of academic self-efficacy in moderating the relation between task importance and test anxiety. Learn Individ Differ 2011, 21: 736–741.

Neurosci. Bull. January, 2021, 37(1):99–102
https://doi.org/10.1007/s12264-020-00566-8

www.neurosci.cn
www.springer.com/12264

LETTER TO THE EDITOR

Drosophila Ortholog of Mammalian Immediate-Early Gene *Npas4* is Specifically Responsive to Reversal Learning

Tingting Liu[1] · Linghan Wang[1] · Qian Li[1]

Received: 2 February 2020 / Accepted: 2 June 2020 / Published online: 27 August 2020

Dear Editor,

In dynamic environments, the memory system of the brain must be able to perceive and process conflicting experiences to reach an adaptive decision. In *Drosophila*, in contrast to consistent experiences, conflicting experiences trigger significantly increased Rac1 activity which mediates active forgetting [1]. The ability to cope with conflicting experiences but not simple learning experiences is impaired in mutants of multiple autism-risk genes [2]. These studies suggest that the memory system of the animal brain processes conflicting experiences through specific mechanisms. However, whether conflicting experiences activate specific early signals in the memory system is still unclear. To answer this question, suitable paradigms and possible candidates are required. In mice and *Drosophila*, reversal learning is an ideal experimental paradigm that has contributed to the understanding of both cognitive flexibility and the pathogenesis of related diseases including depression [3] and autism [2]. Immediate-early genes (IEGs) are possible candidates in the perception of different experiences and relaying signals to the memory system. First, IEGs are dominant molecules of the first wave of gene transcription induced by neuronal activity and have been suggested to be the major molecular links between external stimuli and internal neuronal modification to affect learning and memory [4, 5]. Second, IEGs respond differently to different types of stimulation [6, 7].

Drosophila is an appropriate model in which to study behavioral flexibility using reversal learning [1, 2, 8], and to test prospective assumptions based on various genetic tools [9]. Five well-known IEGs (*c-fos, Arc, Egr1, Npas4*, and *Nr4a1*), which all have orthologs in *Drosophila*, have been studied in learning and memory [5] and used to develop activity-dependent tools [10]. *Hr38* (*Nr4a1* ortholog) is reported to be responsive to many kinds of non-learning stimuli [7, 11]. As a *c-fos* ortholog, *kay* is responsive to single and repeated olfactory learning [12, 13]. For the purpose of finding potential specific early signals of conflicting experiences, we focused on testing whether the other three well-known IEGs (*Arc, Egr1*, and *Npas4*) respond specifically to reversal learning in *Drosophila*.

In one-session aversive olfactory learning [14], flies were sequentially exposed to two odors: 3-octanol (OCT) and 4-methylcyclohexanol (MCH). Only the first odor was paired with an electric shock. After such training, flies learned to avoid the electric shock-paired odor. Based on one-session learning, flies were given three types of training experience: reversal learning, 2 × learning, and 2 × backward (Fig. 1A). In reversal learning and 2 × learning, the second learning was in conflict or consistent with the previous learning. To control sensory experiences such as electric shock or odor stimuli, we used 2 × backward training [14]. In 2 × backward training, which did not induce any memory performance compared to the naïve group (Fig. S1A), the electric shock preceded the odor exposure. Since IEGs are generally activated

Tingting Liu and Linghan Wang have contributed equally to this work.

Electronic supplementary material The online version of this article (https://doi.org/10.1007/s12264-020-00566-8) contains supplementary material, which is available to authorized users.

✉ Qian Li
liqian8@tsinghua.edu.cn

[1] School of Life Sciences, Tsinghua University, Beijing 100084, China

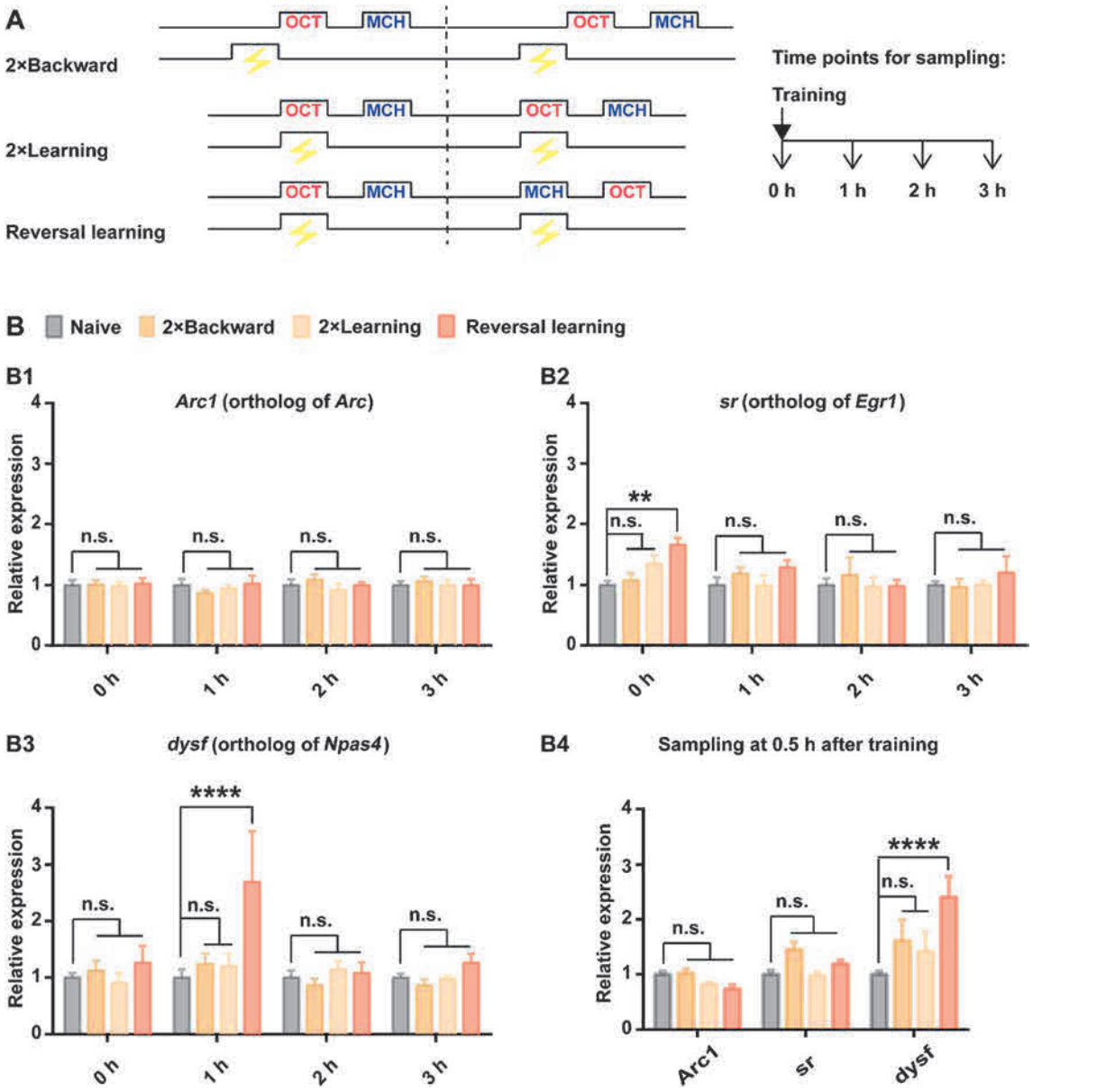

Fig. 1 Responses of *Drosophila* orthologs of three mammalian IEGs after different training experiences. **A** Left: schematics of training paradigms (OCT, 3-octanol; MCH, 4-methylcyclohexanol). Right: time points for sampling. **B** Quantitative PCR results. Experimental groups (2 × Backward, 2 × Learning, and Reversal learning) at different time points after training are compared with the corresponding naïve group. **B1** *Arc1* mRNA remains unaltered after different training processes (n = 4–5) [Interaction F(9, 63) = 0.4258, P = 0.9164; Row Factor F(3, 63) = 0.3277, P = 0.8053; Column Factor F(3, 63) = 0.2945, P = 0.8293]. **B2** *sr* mRNA is upregulated immediately after reversal learning (n = 6) [Interaction F(9, 80) = 1.176, P = 0.3215; Row Factor F(3, 80) = 2.332; P = 0.0804; Column Factor F(3, 80) = 2.794, P = 0.0456]. **B3** *dysf* mRNA increases 1 h after reversal learning (n = 6). [Interaction F(9, 80) = 1.705, P = 0.1014; Row Factor F(3, 80) = 3.323, P = 0.0238; Column Factor F(3, 80) = 4.169, P = 0.0085]. **B4** *dysf* mRNA increases at 0.5 h after reversal learning (n = 6) [Interaction F(6, 60) = 3.557, P = 0.0044; Row Factor F(2, 60) = 13.64, $P < 0.0001$; Column Factor F(3, 60) = 3.684, P = 0.0167]. Row factor represents time (**B1**–**B3**) or gene (**B4**), and column factor represents training paradigms. Data are shown as the mean ± SEM. $^{**}P < 0.01$, $^{****}P < 0.0001$. n.s., no significant difference (two-way ANOVA followed by Dunnett's multiple comparisons test).

within a few hours in animals [5] including *Drosophila* [11–13], we measured changes in the mRNA levels of the *Drosophila* orthologs of the three IEGs at 0, 1, 2,and 3 h after training in wild-type flies (*Canton-S*) and compared them with the naïve condition.

We used qPCR of fly head samples to study changes in the mRNA levels of these IEGs. The same method has been used in recent studies to assess the mRNA level of *kay* [12]. Since mushroom body (MB) neurons play a critical role in reversal learning [1, 2], it was important to test whether

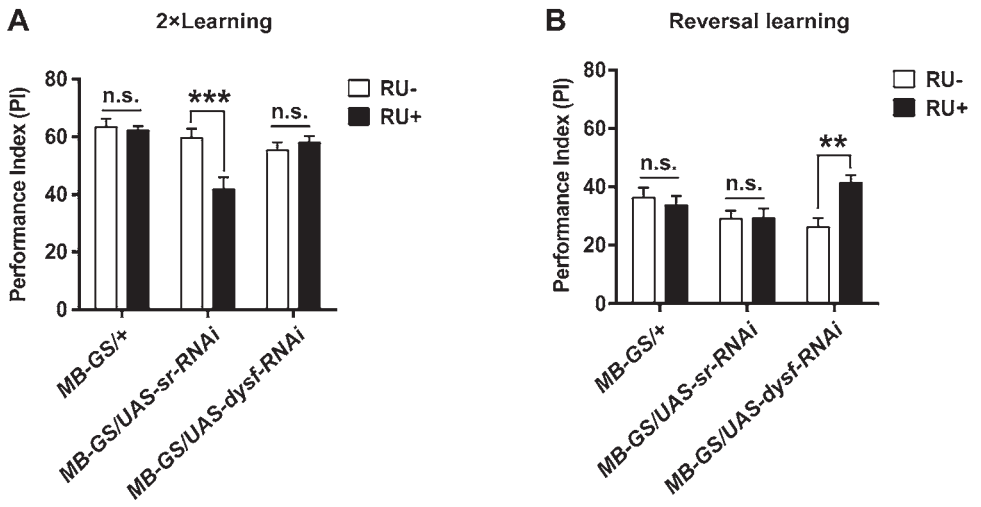

Fig. 2 Behavioral tests of the requirement for *sr* and *dysf* in aversive olfactory learning. **A** Acute knockdown of *sr* in MB neurons significantly impairs the performance of 2 × learning but not reversal learning ($n = 8$). **B** Acute knockdown of *dysf* in MB neurons does not affect 2 × learning but increases the performance of reversal learning ($n = 8$). Data are shown as the mean ± SEM. $^{**}P < 0.01$, $^{***}P < 0.001$. n.s., no significant difference (two-way ANOVA followed by Sidak's multiple comparisons test).

changes in the mRNA level of IEGs within MB neurons was detectable in whole head samples. According to a previous study [11], neural stimulation restricted to MB neurons is sufficient to induce a significant increase of *Hr38* mRNA detected by qPCR of head samples. We also confirmed this result under our experimental conditions (Fig. S1B).

We measured changes in the expression of *Arc1*, *sr*, and *dysf* at 0, 1, 2, and 3 h after training relative to naïve flies (Fig. 1B1–B3). Each experiment was repeated independently 4–6 times. No significant differences were found among all groups in the relative expression of *Arc1* (Fig. 1B1). Reversal learning experiences, but not 2 × learning or 2 × backward experiences, evoked significantly higher relative expression of *sr* at 0 h after training than in the naïve group (Fig. 1B2). No significant differences were found among all groups at other time points (1, 2, and 3 h). Compared with the naïve group, the relative expression of *dysf* was specifically increased 1h after reversal learning, but not the other training paradigms (Fig. 1B3). No significant differences were found among all groups at other time points (0, 2, and 3 h).

To further investigate the specific responses of *sr* and *dysf* to reversal learning, we performed additional experiments to measure the expression changes at 0.5 h after training relative to naïve flies (Fig. 1B4).The specific response of *dysf*, but not *sr*, to reversal learning was still evident at 0.5 h. For more stringent controls, we performed similar qPCR experiments using the MCH-OCT sequence in behavioral training (Fig. S1C). The data were consistent with those shown in Fig. 1B4.

Since *sr* and *dysf* were responsive to reversal learning at the mRNA level, we sought to test whether they also affect reversal learning at the behavioral level. We used an inducible driver of MB neurons (MB-GS) that depends on RU486 feeding [15], to acutely knock down *sr* or *dysf*. Knocking down *sr* significantly impaired the performance of 2 × learning, but not reversal learning (Fig. 2A), while knocking down *dysf* did not affect 2 × learning but increased the performance of reversal learning (Fig. 2B).

Our data support the conclusion that *dysf* is not only specifically responsive to reversal learning, but is also required to regulate reversal learning behavior, suggesting that it is an important IEG in perceiving and processing conflicting experiences in the memory system. Based on our qPCR and behavioral results, a possible explanation is that *dysf* responds to reversal learning to allow the memory system to adjust a tradeoff between old and new memories. Interestingly, a recent study reported that Fos- and Npas4-dependent ensembles drive memory expression differently: the Fos-dependent ensemble promotes memory generalization, while the Npas4-dependent ensemble promotes memory discrimination [16]. It would be of interest to test whether the Npas4-dependent ensemble also specifically responds to conflicting experiences in mice. Our findings provide interesting clues for future studies of *dysf* in *Drosophila* from two aspects. First, *dysf* may contribute to tool development in labeling neurons activated by reversal learning. Second, future studies of *dysf* may reveal novel molecular mechanisms underlying reversal learning.

In addition, *sr* emerges from the current study as an interesting IEG. It was immediately responsive to reversal learning but not 2 × learning. However, knocking down *sr* impaired 2 × learning but not reversal learning at the behavioral level. Further studies of *sr* are required to determine its role in learning and memory.

Acknowledgements We thank helpful comments on this study from Bo Lei, Yinzhong Zhou and Lingling Wang, and experimental help from Lianzhang Wang. This work was supported by grants from the National Natural Science Foundation of China (31970955 and 31700912).

Conflict of interest The authors declare that they have no conflict of interest in this work.

References

1. Shuai Y, Lu B, Hu Y, Wang L, Sun K, Zhong Y. Forgetting is regulated through rac activity in *Drosophila*. Cell 2010, 140: 579–589.
2. Dong T, He J, Wang S, Wang L, Cheng Y, Zhong Y. Inability to activate Rac1-dependent forgetting contributes to behavioral inflexibility in mutants of multiple autism-risk genes. Proc Natl Acad Sci U S A 2016, 113: 7644–7649.
3. Anacker C, Hen R. Adult hippocampal neurogenesis and cognitive flexibility - linking memory and mood. Nat Rev Neurosci 2017, 18: 335–346.
4. Yap EL, Greenberg ME. Activity-regulated transcription: bridging the gap between neural activity and behavior. Neuron 2018, 100: 330–348.
5. Sun X, Lin Y. Npas4: Linking neuronal activity to memory. Trends Neurosci 2016, 39: 264–275.
6. Bepari AK, Sano H, Tamamaki N, Nambu A, Tanaka KF, Takebayashi H. Identification of optogenetically activated striatal medium spiny neurons by Npas4 expression. PLoS One 2012, 7: e52783. https://doi.org/10.1371/journal.pone.0052783.
7. Chen X, Rahman R, Guo F, Rosbash M. Genome-wide identification of neuronal activity-regulated genes in *Drosophila*. Elife 2016, 5:e19942. https://doi.org/10.7554/elife.19942.
8. Quinn WG, Harris WA, Benzer S. Conditioned behavior in *Drosophila-Melanogaster*. Proc Natl Acad Sci U S A 1974, 71: 708–712.
9. Bier E. *Drosophila,* the golden bug, emerges as a tool for human genetics. Nat Rev Genet 2005, 6: 9–23.
10. He QY, Wang JH, Hu HL. Illuminating the activated brain: emerging activity-dependent tools to capture and control functional neural circuits. Neurosci Bull 2019, 35: 369–377.
11. Fujita N, Nagata Y, Nishiuchi T, Sato M, Iwami M, Kiya T. Visualization of neural activity in insect brains using a conserved immediate early gene, Hr38. Current Biol 2013, 23: 2063–2070.
12. Miyashita T, Kikuchi E, Horiuchi J, Saitoe M. Long-term memory engram cells are established by c-Fos/CREB transcriptional cycling. Cell Rep 2018, 25: 2716–2728.e3.
13. Awata H, Takakura M, Kimura Y, Iwata I, Masuda T, Hirano Y. The neural circuit linking mushroom body parallel circuits induces memory consolidation in *Drosophila*. Proc Natl Acad Sci U S A 2019, 116: 16080–16085.
14. Tully T, Quinn WG. Classical conditioning and retention in normal and mutant *Drosophila melanogaster*. J Compar Physiol 1985, 157: 263–277.
15. Mao ZM, Roman G, Zong L, Davis RL. Pharmacogenetic rescue in time and space of the rutabaga memory impairment by using Gene-Switch. Proc Natl Acad Sci U S A 2004, 101: 198–203.
16. Sun X, Bernstein MJ, Meng M, Rao S, Sørensen AT, Yao L, *et al.* Functionally distinct neuronal ensembles within the memory engram. Cell 2020, 181, 410–423.e417.

Neurosci. Bull. January, 2021, 37(1):103–116
https://doi.org/10.1007/s12264-020-00569-5

www.neurosci.cn
www.springer.com/12264

REVIEW

Implications of Transient Receptor Potential Cation Channels in Migraine Pathophysiology

Mamoru Shibata[1,2] · **Chunhua Tang**[1,3]

Received: 4 February 2020 / Accepted: 11 May 2020 / Published online: 1 September 2020

Abstract Migraine is a common and debilitating headache disorder. Although its pathogenesis remains elusive, abnormal trigeminal and central nervous system activity is likely to play an important role. Transient receptor potential (TRP) channels, which transduce noxious stimuli into pain signals, are expressed in trigeminal ganglion neurons and brain regions closely associated with the pathophysiology of migraine. In the trigeminal ganglion, TRP channels co-localize with calcitonin gene-related peptide, a neuropeptide crucially implicated in migraine pathophysiology. Many preclinical and clinical data support the roles of TRP channels in migraine. In particular, activation of TRP cation channel V1 has been shown to regulate calcitonin gene-related peptide release from trigeminal nerves. Intriguingly, several effective anti-migraine therapies, including botulinum neurotoxin type A, affect the functions of TRP cation channels. Here, we discuss currently available data regarding the roles of major TRP cation channels in the pathophysiology of migraine and the therapeutic applicability thereof.

Keywords Migraine · TRPV1 · TRPM8 · TRPA1 · TRPV4 · Calcitonin gene-related peptide · Trigeminal ganglion · Neurogenic inflammation

Mamoru Shibata and Chunhua Tang have contributed equally to this review.

✉ Mamoru Shibata
mshibata@a7.keio.jp

[1] Department of Neurology, Keio University School of Medicine, Tokyo 160-8582, Japan

[2] Department of Neurology, Tokyo Dental College Ichikawa General Hospital, Chiba 272-8513, Japan

[3] Department of Neurology and Center for Clinical Neuroscience, Daping Hospital, Third Military Medical University, Chongqing 400042, China

Introduction

Migraine is one of the most debilitating neurological disorders, characterized by recurrent headache attacks [1, 2]. The concept that migraine is a channelopathy has been substantiated by the fact that familial hemiplegic migraine types 1 and 3 are caused by mutations in the genes encoding the α1 subunit of the CaV2.1 P/Q-type voltage-gated Ca^{2+} channel (*CACNA1A*) [3] and the α1 subunit of the neuronal NaV1.1 voltage-gated Na^{+} channel (*SCN1A*) [4], respectively. Furthermore, genetic abnormalities of the two-pore-domain K^{+} channel, TRESK, have been shown to cause a familial form of migraine with aura. Unlike the CaV2.1 and NaV1.1 channels, the TRESK channel is strongly expressed in trigeminal ganglion (TG) neurons, pointing to the importance of peripheral trigeminal nociception in migraine pathophysiology. Transient receptor potential (TRP) channels are non-selective cation channels that transduce various noxious stimuli into pain signals [5]. They are expressed in TG neurons, and some are associated with the functions of calcitonin gene-related peptide (CGRP) [6, 7], a key target molecule of migraine therapy [8]. Considerable data support the role of TRP channels in migraine, so TRP channel modulation may be a promising therapeutic strategy for its treatment. In addition, migraine attacks are known to be provoked and worsened by environmental factors [1, 2]. TRP channels may also be involved in the trigger mechanism of attacks, because they sense changes in ambient temperature [9] and environmental pollutants [10]. Here, we discuss the roles of

TRP channels in the pathophysiology of migraine and the potential of TRP-based approaches to migraine therapy.

Migraine Pathophysiology

Migraine, a chronic neurological disorder that affects > 10% of the general population [1, 2], is clinically characterized by recurrent attacks of moderate to severe headache lasting 4–72 h without treatment. Attacks are usually accompanied by nausea, vomiting, and heightened sensitivity to light and sound. The Global Burden of Disease study has recently identified migraine as the most disabling neurological disorder and the second leading cause of years lived with disability worldwide [11]. Its pathophysiological mechanisms involve both the central and peripheral nervous systems. In 25%–30% of patients, some attacks are accompanied by an aura phase, which manifests with transient visual, sensory, and language or brainstem disturbances [12]. The aura is now believed to be caused by cortical spreading depolarization/depression (CSD), a slowly propagating wave of rapid, near-complete depolarization of brain cells that lasts for about 1 min and silences electrical activity for several minutes [13]. Moreover, many patients experience prodromes such as fatigue and changes in appetite hours before an attack. Neuroimaging data show abnormal activation of the hypothalamus during prodromes [14, 15]. On the other hand, intravenous administration of CGRP has been shown to induce attacks specifically in migraine patients [16, 17]. CGRP does not readily permeate the blood-brain barrier, thus making it likely that the neuropeptide acts at peripheral sites, such as the TG, the dura mater, and meningeal vessels in this setting. This tenet is endorsed by the fact that monoclonal antibodies targeting CGRP or its receptor, which do not cross the blood-brain barrier either, are efficacious in the prophylaxis of attacks [8]. Hence, peripheral CGRP actions clearly play a crucial role in the development of migraine attacks.

It remains elusive how migraine headaches are generated. However, it has been postulated that the release of neuropeptides such as CGRP and substance P (SP) by trigeminal nerve fibers causes neurogenic inflammation and subsequent sensitization [18]. These alterations may be responsible for the relatively long and severe headaches associated with migraine. Furthermore, animal studies have demonstrated that CSD can generate a nociceptive stimulus capable of activating the trigeminal system [19–21], which would account for the temporal relation between the aura and the headache phases. Recent studies have clarified that CSD also induces dural macrophage activation, mast cell degranulation, and dilatation of the pial and dural vessels, all of which seem to be causes of headache [22, 23].

In particular, meningeal mast cells seem to be relevant in consideration of their proximity to the meningeal nociceptors and their ability to release a plethora of pro-inflammatory and pro-algesic substances [24]. Migraine symptoms are affected by environmental factors. In some patients, attacks are triggered by changes in ambient temperature or atmospheric pressure [9]. Moreover, migraine headaches are exacerbated by light [25], sound, and chemical irritants, such as cigarette smoke [10]. These observations highlight the role of the information detected by sensory neurons in migraine pathophysiology.

Involvement of TRP Channels in Migraine

The *trp* gene was originally discovered in a *Drosophila* mutant with defective vision [26]. Subsequently, this gene was found to encode a protein that plays an important role in phototransduction. Light-activated rhodopsin induces phospholipase C to hydrolyze phosphatidylinositol 4,5-bisphosphate (PIP2) which leads to increased Ca^{2+} permeability of the TRP channel causing the depolarization of photoreceptor cells [27]. The ancestral TRP channel, which possesses six transmembrane domains, is regarded as an ion channel prototype that transduces environmental stimuli into Ca^{2+} signaling.

In 1997, Caterina *et al*. [28] isolated a cDNA clone encoding a capsaicin receptor with non-selective cation channel activity. This receptor was initially referred to as vanilloid receptor 1 (VR1) because a vanilloid moiety of capsaicin was an essential component responsible for the activation of this novel receptor. Concomitantly, it was revealed that VR1 was structurally related to the TRP channel family. Hence, VR1 was later renamed TRP cation channel V1 (TRPV1). From the functional viewpoint, the gating of TRPV1 is driven by noxious heat (> 42°C) which helps us understand why the sensation induced by capsaicin ingestion is perceived as “hot” and “burning”. With the subsequent increase in the number of mammalian TRP family members, they are now classified into six subfamilies – TRPC, TRPV, TRPM, TRPML, TRPP, and TRPA [29, 30]. Some of them were found to be activated by specific temperature ranges [31]. These thermosensitive TRP channels are expressed in primary sensory neurons, which include TG neurons, to confer the ability to detect changes in ambient temperature. Besides, most TRP channels serve in nociceptors as a transducer of noxious stimuli other than non-physiological temperature changes into pain signals [5]. TRPV1 is activated by protons [32, 33] and TRPA1 by reactive oxygen species (ROS) [34]. It should be pointed out that both of these substances have been implicated in the pathogenesis of various pain disorders including migraine [35]. Furthermore, TRP channels are known to be sensitized under pathological conditions. For example, the sensitization of TRPV1 to

heat is responsible for the thermal hyperalgesia associated with carrageenan-induced inflammation [36].

Taken together, TRP channels are involved in the detection of environmental changes and trigeminal nociception. In migraine pathophysiology, where neurogenic inflammation is considered to play an important role [37], TRP channel activity is likely to be upregulated, so blocking such sensitization would be a potential therapeutic strategy. For these reasons, the relationship between TRP channels and migraine has attracted attention [30, 38, 39]. Tremendous amounts of data on mammalian TRP channels have been accumulated since the discovery of VR1/TRPV1. In this article, we focus on the roles of TRPV1, TRPA1, TRPM8, and TRPV4 in the pathophysiology of migraine, because relatively sufficient data relevant to migraine are available for these four channels (Fig. 1).

TRPV1

TRPV1 Localization and Function in the Trigeminal System

TRPV1 is expressed mainly in small- and medium-sized TG neurons [6, 40, 41]. Approximately 10%–20% of TG neurons are reported to be positive for TRPV1 with slight species differences [6, 40–42]. Moreover, a subset of TRPV1-positive neurons is known to contain CGRP [6, 41], and TRPV1 stimulation induces CGRP release [43–45]. The coexistence of TRPV1 and CGRP has also been confirmed in dural trigeminal fibers [6, 7]. The dura mater is considered to be an important disease locus of migraine [46]. Clinical features of attacks, such as a throbbing headache exacerbated by physical activity, nausea, and photophobia, have also been reported in patients with meningitis [46]. Sumatriptan, which is widely used in acute migraine therapy, was developed with success in animal studies using plasma protein extravasation and vasodilation in the dura mater as surrogate markers [37]. Although the exact role of TRPV1 in migraine pathogenesis remains obscure, the simplistic view that the headaches are caused by nociceptive stimuli to TRPV1-expressing nociceptors is not tenable, because the TRPV1 antagonist SB-705498 was not effective as an acute therapy in a clinical study [30, 47]. In the trigeminal nervous system, the CGRP receptor components calcitonin receptor-like receptor and receptor activity-modifying protein 1 are expressed in thinly-myelinated Aδ-fibers, whereas CGRP is present in unmyelinated C-fibers [48, 49]. This implies that C-fiber-derived CGRP would

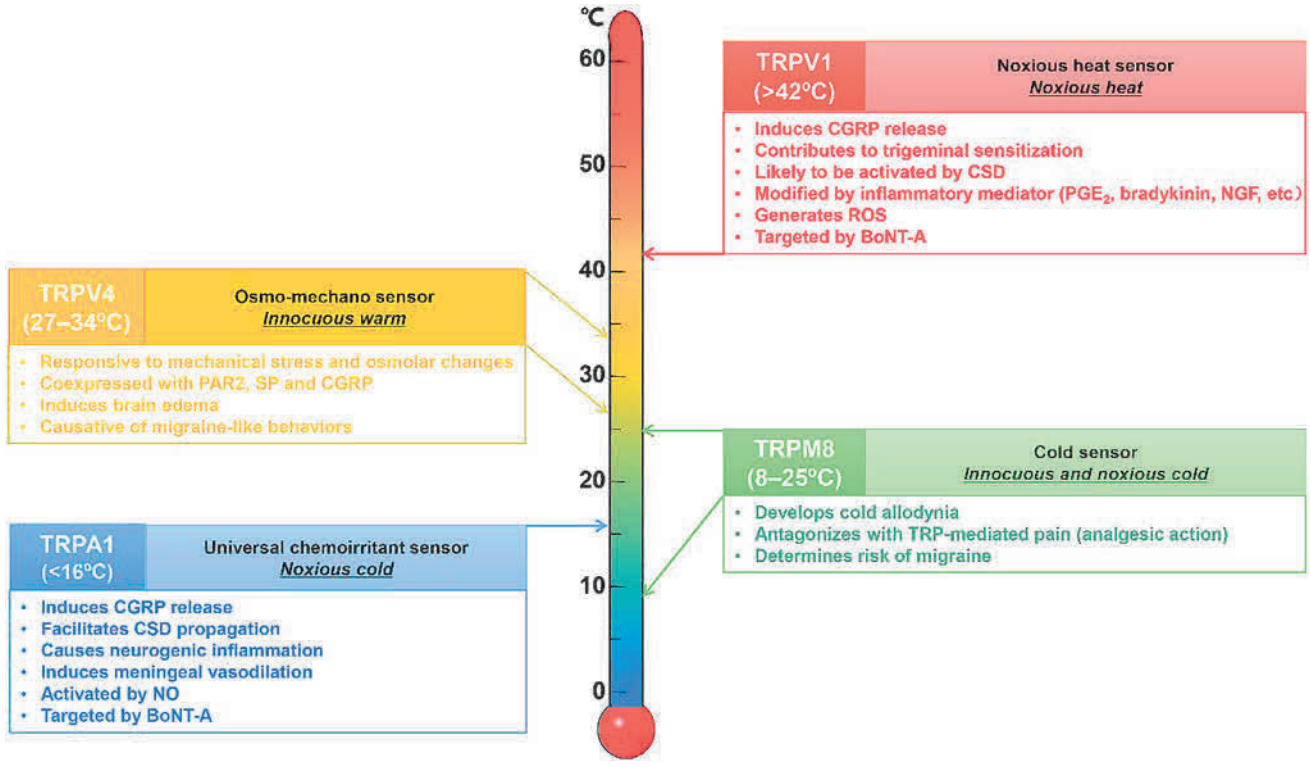

Fig. 1 Major functions of TRPV1, TRPM8, TRPA1, and TRPV4 channels relevant to migraine pathophysiology. BoNT-A, botulinum neurotoxin type A; CSD, cortical spreading depression; NGF, nerve growth factor; PGE_2, prostaglandin E2; ROS, reactive oxygen species; TRP, transient receptor potential.

act on CGRP receptors located on Aδ-fibers. CGRP itself does not directly cause migraine; rather it induces migraine attacks in a delayed manner [16, 17]. Several lines of evidence show that CGRP is involved in sensitization [50–53]. CGRP-induced sensitization is known to play a role in the potentiation of *N*-methyl-D-aspartic acid receptor functions through protein kinase A-mediated phosphorylation [54–57]. Both CGRP and glutamate are increased in the cerebrospinal fluid from patients with chronic migraine [58]. Thus, it has speculated that TRPV1 contributes to trigeminal sensitization by promoting the release of CGRP from C-fibers (Fig. 2). This paradigm would be compatible with the failure of TRPV1 blockade to abort migraine attacks because TRPV1 activation is positioned as an upstream event in the development of attacks. Consequently, TRPV1 inhibition after an attack had begun would be too late to relieve the headache.

CSD and TRPV1 Functions

CSD is known to activate the MAP kinase extracellular signal-regulated kinase (ERK) in TG neurons [21]. Since this activation is disrupted by the TRPV1 inhibitor capsazepine, TRPV1 is likely to be activated by CSD [21]. TRPV1 is known to be expressed in those central nervous system regions relevant to migraine pathophysiology, such as the hippocampus, basal ganglia, thalamus, and hypothalamus [59]. Mechanically-induced CSD is not inhibited by TRPV1 blockade with A-993610, implying that TRPV1 activity does not play a significant role in the process of eliciting CSD [60]. However, repetitive capsaicin stimulation of the trigeminal region has been shown to lower the threshold of CSD induction by suppressing GABAergic activity [61]. It is inferred that repeated trigeminal nociceptive stimulation renders the cerebral cortex susceptible to CSD induction. An important clinical implication of this finding is that clustering of migraine aura attacks may increase the likelihood of recurrence.

Therapeutic Strategies in Migraine with Regard to TRPV1 Functions

TRPV1 functions are known to be modified by inflammatory mediators. Prostaglandin E_2 sensitizes TRPV1 channels through protein kinase A-induced phosphorylation of the scaffold protein named A-kinase anchoring protein 150 [62]. Bradykinin enhances TRPV1-mediated currents in a protein kinase C-dependent manner [63]. complete Freund's adjuvant promotes the translocation of TRPV1 to the cell surface *via* cyclin-dependent kinase 5-mediated TRPV1 phosphorylation at threonine 407 [64] and increases TRPV1 channel activity *via* small ubiquitin-like modifier (SUMO)ylation at lysine 822 [65]. Although nerve growth factor (NGF) promotes neuronal growth during development, it also serves as an inflammatory mediator with pro-algesic actions [66]. Of particular relevance, NGF is increased in the plasma and cerebrospinal fluid of patients experiencing chronic daily headaches [67]. NGF increases TRPV1 expression by activating p38 MAP kinase [68], which is mediated by the ubiquitin ligase MYCBP2 [69]. Furthermore, ligation of NGF to the TrkA receptor leads to TRPV1 phosphorylation at tyrosine 200 *via* Src kinase, causing increased insertion of TRPV1 into the plasma membrane [70]. Toll-like receptors (TLRs) are involved in innate immunity [71, 72], and TLR4 coexists with TRPV1 in TG neurons [73]. Recent evidence has shown that TLR4 inhibits the endocytosis of TRPV1, thus increasing its cell-surface expression level [74]. Collectively, in migraine management, anti-inflammatory measures would be favorable for restricting TRPV1 activity.

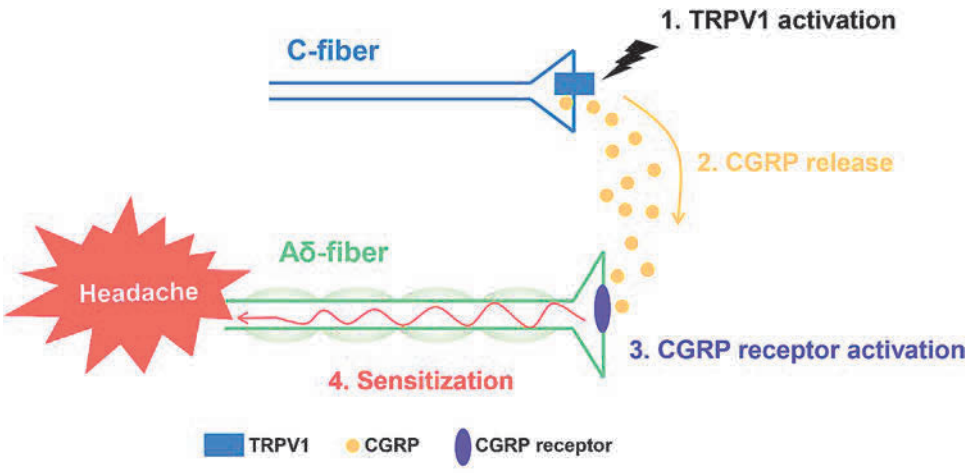

Fig. 2 Possible action of TRPV1 on CGRP release from trigeminal terminals. TRPV1 activation (1) leads to CGRP release from C-fibers (2). Subsequently, CGRP acts on the CGRP receptor expressed on the surface of Aδ-fibers (3), resulting in the development of sensitization (4). Such sensitization of the trigeminal system may be responsible for the generation of the headache. CGRP, calcitonin gene-related peptide.

Botulinum neurotoxin type A (BoNT-A) is used to treat chronic migraine. Electrophysiological analyses have revealed that BoNT-A selectively inhibits the C-fibers of meningeal nociceptors [75]. There is anatomical evidence for meningeal nociceptors that send collaterals to the scalp, which provides a rationale for the ability of subcutaneously injected BoNT-A to affect dural trigeminal functions [76–78]. Furthermore, TRPV1 and TRPA1 functions are blocked by BoNT-A [79]. In agreement with these findings, BoNT-A decreases TRPV1 expression in the TG and trigeminal nerve fibers, while P_2X_3 expression is unaffected [80]. BoNT-A-treated mice are less responsive to capsaicin [80] and in primary cultures of TG neurons, TRPV1 cell-surface expression levels are reduced by BoNT-A treatment. Site-directed mutagenesis of TRPV1 at tyrosine 200 leads to a remarkable decrease in its expression, and this effect is reversed by proteasome inhibition. The last finding raises the possibility that TRPV1 that cannot be normally inserted into the plasma membrane is degraded by the cytoplasmic proteasome system (Fig. 3). The TRPV1 antagonist SB-705498 was not only abandoned as an acute anti-migraine therapy, but hyperthermia was found to be its unfavorable side-effect [30, 47]. By contrast, BoNT-A-mediated TRPV1 inhibition has the major advantage of not causing hyperthermia.

TRPM8

TRPM8 as a Cold Sensor

TRPM8 was discovered as a non-selective cation channel responsive to cold (8°C–25°C) and menthol [81, 82]. Regarding its activation, there is an interaction between these stimuli, such that exposure to menthol elevates the threshold temperature for cold stimulation [81, 82]. Intriguingly, PIP2, which negatively regulates TRPV1 functions, conversely enhances TRPM8 activity. Hence, phospholipase C activation following TRPM8 stimulation downregulates TRPM8 functions, thus causing rapid desensitization [83–85]. Genetic ablation studies have corroborated that TRPM8 plays a crucial role in cold sensation [86, 87]. Unlike TRPV1, TRPM8 expression is restricted to primary sensory neurons in the nervous system [82]. In the TG, TRPM8 is mainly expressed in small neurons [78, 88, 89].

Functional Roles of TRPM8 in Pain Disorders and Migraine

TRPM8 seems to have dual implications for pain; it is involved in the development of cold allodynia, whereas cold stimulation in the temperature range that activates TRPM8 provides innocuous and soothing sensations. Nerve injury-associated and complete Freund's adjuvant-induced cold allodynia is attenuated in TRPM8-knockout mice [87]. In accord with this, there is a movement for therapeutic application of TRPM8 antagonists to pain disorders [90]. On the other hand, TRPM8 has been found to mediate the analgesic effects of moderate cooling against the painful stimulus induced by formalin administration [86]. From the clinical viewpoint, menthol application can relieve migraine headaches [91, 92]. It has been pointed out that menthol has differing effects on capsaicin-induced pain depending on the time between exposure to capsaicin and menthol [93]. Hence, it is inferred that TRPM8 is involved in either sensing unpleasant cold stimuli or mediating the effects of cold analgesia in a context-dependent manner. Since its discovery, TRPM8 has been found to be co-expressed with TRPV1 in a subset of TG neurons [81]. Although the significance of this coexistence remains to be fully elucidated, TG neurons co-expressing TRPM8 and TRPV1 may be involved in eliciting noxious pain [94]. The co-expression frequency of TRPV1 and TRPM8 in TG neurons is increased in inflammatory soup-induced meningeal inflammation [78]. While this may favor the occurrence of cold allodynia, the increased coexistence concomitantly provides a greater chance for the ability of TRPM8 stimulation to antagonize TRPV1 functions (Fig. 4). In support of the latter, TRPM8 activation with icilin alleviates thermal allodynia in inflammatory soup-induced meningeal inflammation [78], reminiscent of the efficacy of menthol in acute migraine attacks as noted above [91, 92].

TRPM8 Gene Polymorphism Determines the Susceptibility to Migraine Development

The relationship between TRPM8 and migraine has been attracting particular attention because genome-wide association studies have reproducibly shown that single nucleotide polymorphisms of the *TRPM8* gene (rs10166942[C/T] and rs17862920[T/C]) determine an increased risk of migraine [95–97]. *TRPM8* mRNA expression from the chromosome harboring rs10166942[C] was found to be lower than that derived from the chromosome harboring rs10166942[T] in dorsal root ganglion samples, and rs10166942[C] carriers are significantly less sensitive to cold pain than non-carriers [98]. Although the exact mechanism of this allelic expression imbalance is unclear, impaired transcription and/or transcript instability might be involved. Intriguingly, TRPM8 channels are subject to a variety of post-transcriptional modifications [99]. Epidemiologically, rs10166942[T] carriers are associated with reduced migraine risk compared to rs10166942[C] carriers. Hence, increased TRPM8 activity seems to favor the risk of

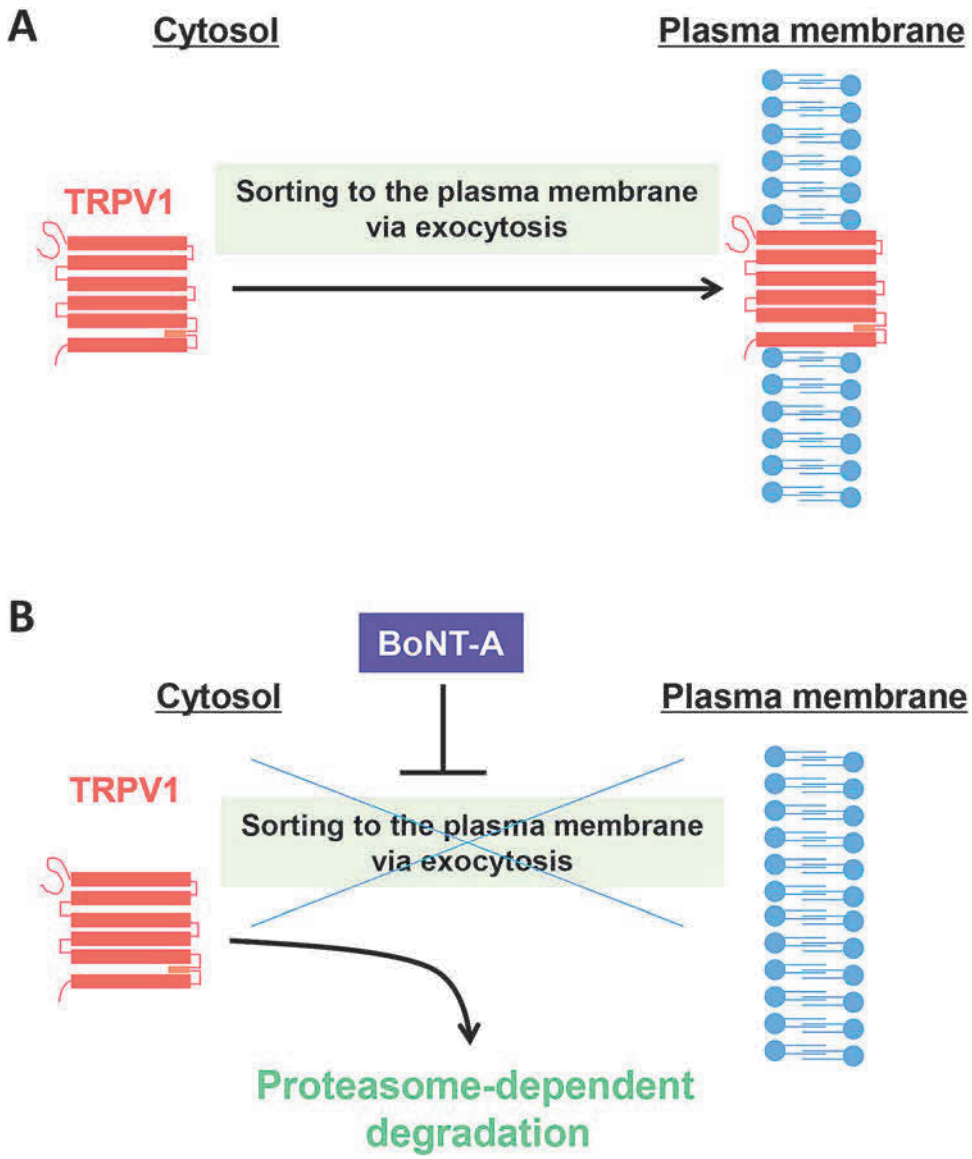

Fig. 3 Impaired sorting of TRPV1 to the plasma membrane reduces the TRPV1 expression level. **A** Normally, TRPV1 is translocated to the plasma membrane *via* exocytosis. **B** BoNT-A inhibits the exocytosis-mediated sorting of TRPV1 to the plasma membrane. TRPV1 proteins that reside in the cytoplasm are subjected to proteolysis by the proteasome system, leading to reduced expression of TRPV1. BoNT-A, botulinum neurotoxin type A.

developing migraine. This is consistent with preclinical findings in rats showing that icilin applied to the dura results in cutaneous allodynia [100]. Furthermore, migraine patients carrying rs10166942[T] are more likely to have chronic migraine and allodynic symptoms [101] indicating that TRPM8-related single nucleotide polymorphisms can affect the clinical phenotypes of migraine as well.

TRPA1

TRPA1 as a Polymodal TRP Cation Channel

TRPA1 (also known as ANKTM1), the sole member of the TRPA subfamily, was cloned from cultured human fetal lung fibroblasts [102]. TRPA1 is co-expressed with TRPV1 in a subpopulation of non-myelinated or thinly myelinated C- or Aδ-fiber neurons in the dorsal root ganglion, TG, and vagus ganglion [103]. TRPA1 expression has been identified in both peptidergic sensory neurons (enriched in CGRP, SP, and neurokinin A) and non-peptidergic, IB4-binding neurons [104]. There is direct evidence for the involvement of TRPA1 in pain disorders. A gain-of-function mutation in TRPA1 (p.Asp855Cys) has been identified as the cause of familial episodic pain syndrome characterized by recurrent episodes of debilitating upper body pain, triggered or exacerbated by fatigue, cold exposure, fasting, and weather changes [105]. TRPA1 was originally identified as a noxious cold-sensitive cation channel activated by temperatures below 16°C [106]. In addition, TRPA1 is sensitive to pungent food ingredients (e.g., allyl isothiocyanate [mustard oil], cinnamaldehyde

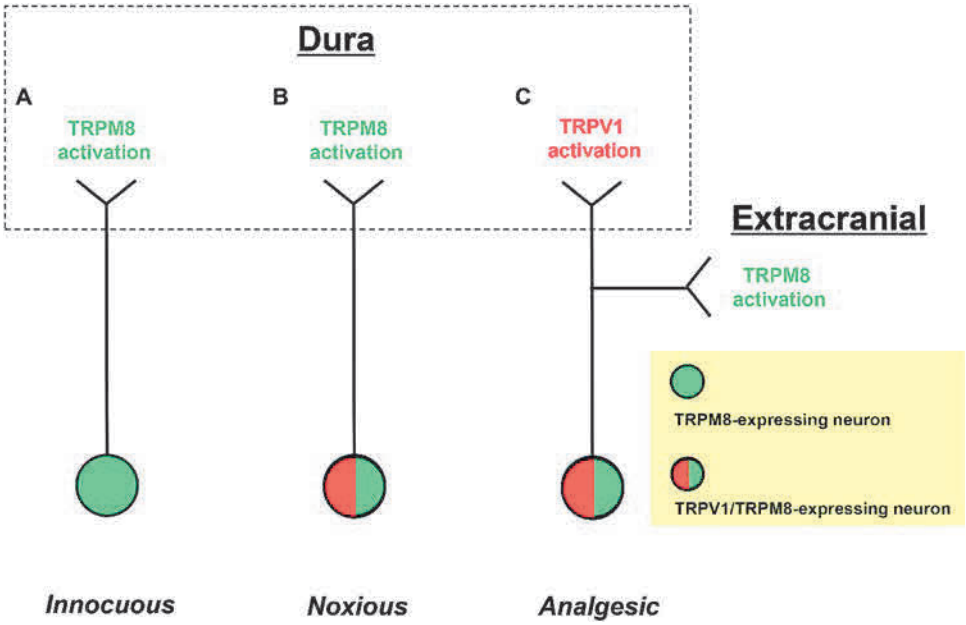

Fig. 4 Altered actions of TRPM8 in different situations. **A** TRPM8 activation in TG neurons exclusively expressing TRPM8 channels is believed to generate only innocuous sensations. **B** TRPM8 activation of TG neurons expressing both TRPV1 and TRPM8 causes noxious sensations. **C** When TRPV1/TRPM8-expressing TG neurons are subjected to TRPV1 activation in the dura, TRPM8 activation in their extracranial collateral axons can exert an analgesic effect, thus assuaging pain.

[cinnamon], allicin [garlic], and eugenol [clove bud oil compounds]), environmental irritants, and industrial pollutants, as well as endogenous substances (e.g., bradykinin, ROS, nitric oxide [NO], and lipid oxidation products) [107, 108], some of which are known to trigger migraine attacks.

Is TRPA1 a Crucial Molecule for Migraine Headache Generation?

A growing number of studies have implicated TRPA1 in the development of migraine headache [109], and this is supported by the finding from the "headache tree". It has long been known that exposure to *Umbellularia californica*, a tree native to southwestern Oregon and northern California, causes headache crises. Umbellulone, the major volatile component of its leaves, was found to increase the intracellular Ca^{2+} concentration in TRPA1-transfected HEK293 cells in a concentration-dependent manner, and umbellulone-evoked currents in mouse TG neurons were abrogated by TRPA1 knockout [110]. These findings indicate that umbellulone is a TRPA1 agonist. Furthermore, umbellulone administration evokes CGRP release from TG neurons and dural trigeminal nerves, increases meningeal blood flow [110], and facilitates CSD propagation [111]. Regarding the involvement of TRPA1 in CSD induction, a recent study using brain slices demonstrated that local ROS application (H_2O_2) promotes cortical responsiveness to CSD in a way that involves TRPA1 and CGRP [112]. Consistent with this, cortical neurons have been shown to express TRPA1 [112, 113] and CGRP [114]. However, in this paradigm, it is unclear how ROS is generated within the cerebral cortex at the initial step. Another possible scenario for the involvement of these three key players in determining CSD susceptibility might be that CSD stimulates meningeal nociceptors [20], thereby causing TRPA1/TRPV1 activation [21], CGRP release, and neurogenic inflammation in the dura mater [22, 23], thus lowering the threshold for CSD induction [61]. In this model, it is envisioned that ROS production in meningeal nociceptors is induced by CSD [115] and/or TRPV1 activation [116], where TRPV1-generated ROS might be able to activate TRPA1 in an autocrine and/or paracrine manner. The involvement of ROS-induced TRPA1 activation has also been reported in a trigeminal neuropathic pain model, where chemokine (C-C motif) ligand 2-medated mobilization of macrophages/monocytes plays a pivotal role [117]. Moreover, it has been shown that ROS production downstream of TRPA1 activation in Schwann cells may contribute to the development of neuropathic pain [118].

TRPA1 and Environmental Migraine Triggers

In addition, some substances cause headaches in susceptible individuals. Acrolein is known to be a major irritant in cigarette smoke and an established migraine trigger [10]. The intranasal application of acrolein also evokes CGRP-dependent meningeal vasodilation *via* TRPA1 activation [119]. Furthermore, acrolein exposure produces chronic migraine phenotypes, such as peri-orbital allodynia, c-Fos induction in the trigeminal nucleus caudalis, and altered behavior in rats [120]. Therapeutically, the acrolein-induced increase in meningeal blood flow is attenuated

by sumatriptan and valproic acid [120], the latter of which is known to be a prophylactic drug for migraine [121]. Hence, these anti-migraine drugs seem to exert an inhibitory action on TRPA1 itself or its downstream events.

Migraine attacks are provoked by NO donors, such as nitroglycerin and glyceryl trinitrate [122]. Glyceryl trinitrate has been reported to cause facial allodynia by inducing the TRPA1-mediated generation of reactive oxygen and carbonyl species within the TG [123]. Furthermore, endogenous NO and hydrogen sulfide contribute to CGRP release by activating TRPA1 in sensory nerves [108], which promotes nociceptive firing in the primary afferents underlying migraine pain under neuroinflammatory conditions [124].

TRPA1 as a Therapeutic Target of Migraine

Intriguingly, a number of anti-migraine drugs have been shown to desensitize or inhibit TRPA1 activity [108]. In particular, isopetasin (a major constituent of butterbur extracts) is reported to desensitize TRPA1, which may account for the anti-migraine action of butterburs [125]. Caffeine has been demonstrated to suppress human TRPA1 channels by an unknown mechanism [126]. Paracetamol (acetaminophen) has been demonstrated to exert an anti-nociceptive effect by desensitizing TRPA1 [127, 128]. Lastly, extracranial administration of BoNT-A inhibits meningeal nociceptors by reducing the expression of TRPA1 as well as TRPV1 [79]. However, it should be noted that it takes 7 days for BoNT-A to reduce the cell-surface expression of TRPV1 and TRPA1 in the dural nerve endings of meningeal nociceptors [79, 80]. Hence, the development of BoNT-like drugs with a more rapid onset of action is awaited.

TRPV4

TRPV4 is a Unique Polymodal TRP Cation Channel Discovered as an Osmotic Sensor

TRPV4 (also called VR-OAC [vanilloid receptor-related osmotically activated ion channel], VRL-2 [vanilloid receptor-like channel 2], TRPL2 [transient receptor-like channel 2], and OTRPC4 [osmosensory protein 9-like TRP channel, member 4]) was originally cloned as the vanilloid receptor-related channel activated by osmotic changes; it is strongly expressed in the kidney, liver, and heart [129, 130]. TRPV4 is a mammalian homolog of OSM-9 in *Caenorhabditis elegans* [130–133], and TRPV4 expression has been found to restore the osmotic avoidance response in OSM-9-deficient worms [134]. TRPV4 is now known to play an evolutionarily-conserved role in the transduction of osmotic and mechanical stimuli [29, 135, 136].

TRPV4 is a polymodal receptor with pleiotropic functions and widespread expression in various cell types/tissues throughout the body [103, 137]. It can be activated by various stimuli including physical factors (altered osmolarity, moderate heat [27°C–34°C] and mechanical stimuli such as membrane stretch and shear stress), chemical factors (endocannabinoids, arachidonic acid and its metabolites, and 4α-phorbol esters), and protons [103, 138–141].

Function and Localization of TRPV4 in Relation to Pain Disorders

TRPV4 is also involved in a plethora of pain conditions [29], encompassing mechanically-evoked [132, 142], inflammatory [143], neuropathic [144], visceral [145], and trigeminal pain conditions [146, 147]. Moreover, ultraviolet B-induced TRPV4 activation in the epidermis may be responsible for the development of sunburn pain [148]. A recent study has disclosed that the Piezo1–TRPV4 axis is involved in the exacerbation of pancreatitis *via* sustained elevation of intracellular Ca^{2+}, thus highlighting the role of TRPV4 in visceral pain [149]. TRPV4 activation is known to potentiate the tetrodotoxin-sensitive Na^{+} current [150] and TRPV1 function [151] in TG neurons. Thus, TRPV4 also seems to serve as a pain enhancer in TG neurons.

TRPV4 expression has been reported not only in primary sensory neurons [147, 152] but also in satellite glial cells [153]. TRPV4 expression has also been recognized in the central nervous system [154]. *TRPV4* mRNA has been found in neurons [132, 155], astrocytes [156], and microglia [157]. Astroglial TRPV4 has been shown to mediate brain edema after traumatic injury [158], a condition frequently encountered in familial hemiplegic migraine [159].

Emerging Evidence for the Importance of TRPV4 as a Novel Therapeutic Target for Migraine

Evidence for the role of TRPV4 in migraine pathophysiology is still scarce. However, its activation in response to mechanical stress and osmolarity changes fits into several aspects of migraine. For example, TRPV4 sensitization may be responsible for the worsening of migraine headaches by routine physical activity [160]. Also, trigeminal afferents are known to be sensitized by dural application of solutions with either increased or decreased osmolarity [161, 162]. In agreement with this, *in vivo* electrophysiological patch-clamp recordings demonstrated TRPV4-like currents in dural afferents in response to the application of

hypotonic solutions and the TRPV4 activator 4α-PDD [163]. Furthermore, activation of TRPV4 within the dura of freely-moving animals induces migraine-like behaviors (cephalic and extracephalic allodynia) that are inhibited by a TRPV4 antagonist [163]. Formalin injection into the whisker pad has been found to induce trigeminal nocifensive behavior by activating Ca^{2+} entry through TRPV4 [147]. Mechanistically, concomitant exposure to formalin and high humidity seems to activate the TRPV4–p38 MAP kinase pathway [164].

In rat sensory neurons, immunoreactive TRPV4 is co-expressed with protease-activated receptor 2 (PAR2), SP, and CGRP, all of which are associated with migraine pathophysiology [165]. In particular, PAR2 activation in the meninges has been found to cause migraine-like pain behaviors [166]. Since PAR2 is known to underpin sustained activation of TRPV4 [167], a vicious cycle can be formed between these two molecules. Hence, the involvement of the PAR2–TRPV4 pathway in migraine pathophysiology may warrant further investigations.

Collectively, these findings raise the possibility that TRPV4 blockade can be a promising novel therapeutic strategy against migraines. A novel small molecule dual-channel inhibitor of TRPV4 and TRPA1 has been developed for attenuation of inflammation and pain including trigeminal irritant pain [143, 168].

Concluding Remarks

We reviewed the possible roles of four thermosensitive TRP channels in the pathophysiology of migraine. It is apparent that each of these channels operates as a detector of specific noxious stimuli. As discussed in this article, numerous preclinical and clinical data are available that support their various roles in migraine. The efficacy of BoNT-A in the management of chronic migraine implies that TRPV1 and TRPA1 are *bona fide* therapeutic targets of migraine. Notwithstanding, there is no definite proof that TRP channels mediate migraine headaches because TRP channel blockade has never been successful as a migraine therapy. Considering that migraine is a paroxysmal disorder, it is necessary to develop TRP antagonists with a rapid onset of action. Concomitantly, they should not have any adverse effect on body temperature in terms of clinical application. A better understanding of the relationship between TRP channels and CGRP, as well as adequate control of inflammatory conditions, may be key to maximizing the effectiveness of TRP channel-based anti-migraine therapies. Furthermore, TRP channel overactivity can profoundly affect cellular functions, for example, *via* mitochondrial toxicity [169, 170]. Hence, proper management of TRP channel activity would be protective against neuropathic changes.

Acknowledgements This review was supported by the Japan Society for the Promotion of Science KAKENHI (26460706 and 19K07849), a Japan-China Sasakawa Medical Fellowship (2017816), and a State Scholarship Fund of the China Scholarship Council (201908500072).

Conflict of interest The authors claim that there are no conflicts of interest.

References

1. Charles A. Migraine. N Engl J Med 2017, 377: 553–561.
2. Dodick DW. Migraine. Lancet 2018, 391: 1315–1330.
3. Ophoff RA, Terwindt GM, Vergouwe MN, van Eijk R, Oefner PJ, Hoffman SM, *et al.* Familial hemiplegic migraine and episodic ataxia type-2 are caused by mutations in the Ca^{2+} channel gene CACNL1A4. Cell 1996, 87: 543–552.
4. Dichgans M, Freilinger T, Eckstein G, Babini E, Lorenz-Depiereux B, Biskup S, *et al.* Mutation in the neuronal voltage-gated sodium channel SCN1A in familial hemiplegic migraine. Lancet 2005, 366: 371–377.
5. Julius D. TRP channels and pain. Annu Rev Cell Dev Biol 2013, 29: 355–384.
6. Shimizu T, Toriumi H, Sato H, Shibata M, Nagata E, Gotoh K, *et al.* Distribution and origin of TRPV1 receptor-containing nerve fibers in the dura mater of rat. Brain Res 2007, 1173: 84–91.
7. Huang D, Li S, Dhaka A, Story GM, Cao YQ. Expression of the transient receptor potential channels TRPV1, TRPA1 and TRPM8 in mouse trigeminal primary afferent neurons innervating the dura. Mol Pain 2012, 8: 66.
8. Dodick DW. CGRP ligand and receptor monoclonal antibodies for migraine prevention: evidence review and clinical implications. Cephalalgia 2019, 39: 445–458.
9. Prince PB, Rapoport AM, Sheftell FD, Tepper SJ, Bigal ME. The effect of weather on headache. Headache 2004, 44: 596–602.
10. Kunkler PE, Zhang L, Pellman JJ, Oxford GS, Hurley JH. Sensitization of the trigeminovascular system following environmental irritant exposure. Cephalalgia 2015, 35: 1192–1201.
11. Collaborators GBDH. Global, regional, and national burden of migraine and tension-type headache, 1990–2016: a systematic analysis for the Global Burden of Disease Study 2016. Lancet Neurol 2018, 17: 954–976.
12. Goadsby PJ, Holland PR, Martins-Oliveira M, Hoffmann J, Schankin C, Akerman S. Pathophysiology of migraine: a disorder of sensory processing. Physiol Rev 2017, 97: 553–622.
13. Pietrobon D, Moskowitz MA. Chaos and commotion in the wake of cortical spreading depression and spreading depolarizations. Nat Rev Neurosci 2014, 15: 379–393.
14. Maniyar FH, Sprenger T, Monteith T, Schankin C, Goadsby PJ. Brain activations in the premonitory phase of nitroglycerin-triggered migraine attacks. Brain 2014, 137: 232–241.
15. Schulte LH, May A. The migraine generator revisited: continuous scanning of the migraine cycle over 30 days and three spontaneous attacks. Brain 2016, 139: 1987–1993.
16. Lassen LH, Haderslev PA, Jacobsen VB, Iversen HK, Sperling B, Olesen J. CGRP may play a causative role in migraine. Cephalalgia 2002, 22: 54–61.

17. Hansen JM, Hauge AW, Olesen J, Ashina M. Calcitonin gene-related peptide triggers migraine-like attacks in patients with migraine with aura. Cephalalgia 2010, 30: 1179–1186.
18. Moskowitz MA. The neurobiology of vascular head pain. Ann Neurol 1984, 16: 157–168.
19. Zhang X, Levy D, Kainz V, Noseda R, Jakubowski M, Burstein R. Activation of central trigeminovascular neurons by cortical spreading depression. Ann Neurol 2011, 69: 855–865.
20. Zhang X, Levy D, Noseda R, Kainz V, Jakubowski M, Burstein R. Activation of meningeal nociceptors by cortical spreading depression: implications for migraine with aura. J Neurosci 2010, 30: 8807–8814.
21. Iwashita T, Shimizu T, Shibata M, Toriumi H, Ebine T, Funakubo M, *et al.* Activation of extracellular signal-regulated kinase in the trigeminal ganglion following both treatment of the dura mater with capsaicin and cortical spreading depression. Neurosci Res 2013, 77: 110–119.
22. Karatas H, Erdener SE, Gursoy-Ozdemir Y, Lule S, Eren-Kocak E, Sen ZD, *et al.* Spreading depression triggers headache by activating neuronal Panx1 channels. Science 2013, 339: 1092–1095.
23. Schain AJ, Melo-Carrillo A, Stratton J, Strassman AM, Burstein R. CSD-induced arterial dilatation and plasma protein extravasation are unaffected by Fremanezumab: implications for CGRP's role in migraine with Aura. J Neurosci 2019, 39: 6001–6011.
24. Levy D, Burstein R, Strassman AM. Mast cell involvement in the pathophysiology of migraine headache: a hypothesis. Headache 2006, 46 Suppl 1: S13–S18.
25. Noseda R, Kainz V, Jakubowski M, Gooley JJ, Saper CB, Digre K, *et al.* A neural mechanism for exacerbation of headache by light. Nat Neurosci 2010, 13: 239–245.
26. Montell C, Rubin GM. Molecular characterization of the Drosophila trp locus: a putative integral membrane protein required for phototransduction. Neuron 1989, 2: 1313–1323.
27. Hardie RC, Minke B. The trp gene is essential for a light-activated Ca^{2+} channel in Drosophila photoreceptors. Neuron 1992, 8: 643–651.
28. Caterina MJ, Schumacher MA, Tominaga M, Rosen TA, Levine JD, Julius D. The capsaicin receptor: a heat-activated ion channel in the pain pathway. Nature 1997, 389: 816–824.
29. Moore C, Gupta R, Jordt SE, Chen Y, Liedtke WB. Regulation of pain and itch by TRP channels. Neurosci Bull 2018, 34: 120–142.
30. Benemei S, Dussor G. TRP channels and migraine: recent developments and new therapeutic opportunities. Pharmaceuticals (Basel) 2019, 12: 54.
31. Vay L, Gu C, McNaughton PA. The thermo-TRP ion channel family: properties and therapeutic implications. Br J Pharmacol 2012, 165: 787–801.
32. Tominaga M, Caterina MJ, Malmberg AB, Rosen TA, Gilbert H, Skinner K, *et al.* The cloned capsaicin receptor integrates multiple pain-producing stimuli. Neuron 1998, 21: 531–543.
33. Caterina MJ, Leffler A, Malmberg AB, Martin WJ, Trafton J, Petersen-Zeitz KR, *et al.* Impaired nociception and pain sensation in mice lacking the capsaicin receptor. Science 2000, 288: 306–313.
34. Bessac BF, Sivula M, von Hehn CA, Escalera J, Cohn L, Jordt SE. TRPA1 is a major oxidant sensor in murine airway sensory neurons. J Clin Invest 2008, 118: 1899–1910.
35. Salvemini D, Little JW, Doyle T, Neumann WL. Roles of reactive oxygen and nitrogen species in pain. Free Radic Biol Med 2011, 51: 951–966.
36. Davis JB, Gray J, Gunthorpe MJ, Hatcher JP, Davey PT, Overend P, *et al.* Vanilloid receptor-1 is essential for inflammatory thermal hyperalgesia. Nature 2000, 405: 183–187.
37. Williamson DJ, Hargreaves RJ. Neurogenic inflammation in the context of migraine. Microsc Res Tech 2001, 53: 167–178.
38. Dussor G, Cao YQ. TRPM8 and migraine. Headache 2016, 56: 1406–1417.
39. Meents JE, Neeb L, Reuter U. TRPV1 in migraine pathophysiology. Trends Mol Med 2010, 16: 153–159.
40. Ichikawa H, Sugimoto T. VR1-immunoreactive primary sensory neurons in the rat trigeminal ganglion. Brain Res 2001, 890: 184–188.
41. Hou M, Uddman R, Tajti J, Kanje M, Edvinsson L. Capsaicin receptor immunoreactivity in the human trigeminal ganglion. Neurosci Lett 2002, 330: 223–226.
42. Quartu M, Serra MP, Boi M, Poddighe L, Picci C, Demontis R, *et al.* TRPV1 receptor in the human trigeminal ganglion and spinal nucleus: immunohistochemical localization and comparison with the neuropeptides CGRP and SP. J Anat 2016, 229: 755–767.
43. Meng J, Ovsepian SV, Wang J, Pickering M, Sasse A, Aoki KR, *et al.* Activation of TRPV1 mediates calcitonin gene-related peptide release, which excites trigeminal sensory neurons and is attenuated by a retargeted botulinum toxin with anti-nociceptive potential. J Neurosci 2009, 29: 4981–4992.
44. Akerman S, Kaube H, Goadsby PJ. Vanilloid type 1 receptors (VR1) on trigeminal sensory nerve fibres play a minor role in neurogenic dural vasodilatation, and are involved in capsaicin-induced dural dilation. Br J Pharmacol 2003, 140: 718–724.
45. Akerman S, Kaube H, Goadsby PJ. Anandamide acts as a vasodilator of dural blood vessels *in vivo* by activating TRPV1 receptors. Br J Pharmacol 2004, 142: 1354–1360.
46. Olesen J, Burstein R, Ashina M, Tfelt-Hansen P. Origin of pain in migraine: evidence for peripheral sensitisation. Lancet Neurol 2009, 8: 679–690.
47. Gunthorpe MJ, Hannan SL, Smart D, Jerman JC, Arpino S, Smith GD, *et al.* Characterization of SB-705498, a potent and selective vanilloid receptor-1 (VR1/TRPV1) antagonist that inhibits the capsaicin-, acid-, and heat-mediated activation of the receptor. J Pharmacol Exp Ther 2007, 321: 1183–1192.
48. Eftekhari S, Salvatore CA, Calamari A, Kane SA, Tajti J, Edvinsson L. Differential distribution of calcitonin gene-related peptide and its receptor components in the human trigeminal ganglion. Neuroscience 2010, 169: 683–696.
49. Melo-Carrillo A, Noseda R, Nir RR, Schain AJ, Stratton J, Strassman AM, *et al.* Selective inhibition of trigeminovascular neurons by Fremanezumab: a humanized monoclonal anti-CGRP antibody. J Neurosci 2017, 37: 7149–7163.
50. Nakamura-Craig M, Gill BK. Effect of neurokinin A, substance P and calcitonin gene related peptide in peripheral hyperalgesia in the rat paw. Neurosci Lett 1991, 124: 49–51.
51. Sun RQ, Lawand NB, Willis WD. The role of calcitonin gene-related peptide (CGRP) in the generation and maintenance of mechanical allodynia and hyperalgesia in rats after intradermal injection of capsaicin. Pain 2003, 104: 201–208.
52. Sun RQ, Tu YJ, Lawand NB, Yan JY, Lin Q, Willis WD. Calcitonin gene-related peptide receptor activation produces PKA- and PKC-dependent mechanical hyperalgesia and central sensitization. J Neurophysiol 2004, 92: 2859–2866.
53. Natura G, von Banchet GS, Schaible HG. Calcitonin gene-related peptide enhances TTX-resistant sodium currents in cultured dorsal root ganglion neurons from adult rats. Pain 2005, 116: 194–204.
54. Han JS, Adwanikar H, Li Z, Ji G, Neugebauer V. Facilitation of synaptic transmission and pain responses by CGRP in the amygdala of normal rats. Mol Pain 2010, 6: 10.
55. Liang X, Wang S, Qin G, Xie J, Tan G, Zhou J, *et al.* Tyrosine phosphorylation of NR2B contributes to chronic migraines via

increased expression of CGRP in rats. Biomed Res Int 2017, 2017: 7203458.
56. Okutsu Y, Takahashi Y, Nagase M, Shinohara K, Ikeda R, Kato F. Potentiation of NMDA receptor-mediated synaptic transmission at the parabrachial-central amygdala synapses by CGRP in mice. Mol Pain 2017, 13: 1744806917709201.
57. Wang XY, Zhou HR, Wang S, Liu CY, Qin GC, Fu QQ, *et al.* NR2B-Tyr phosphorylation regulates synaptic plasticity in central sensitization in a chronic migraine rat model. J Headache Pain 2018, 19: 102.
58. Gallai V, Alberti A, Gallai B, Coppola F, Floridi A, Sarchielli P. Glutamate and nitric oxide pathway in chronic daily headache: evidence from cerebrospinal fluid. Cephalalgia 2003, 23: 166–174.
59. Cristino L, de Petrocellis L, Pryce G, Baker D, Guglielmotti V, Di Marzo V. Immunohistochemical localization of cannabinoid type 1 and vanilloid transient receptor potential vanilloid type 1 receptors in the mouse brain. Neuroscience 2006, 139: 1405–1415.
60. Summ O, Holland PR, Akerman S, Goadsby PJ. TRPV1 receptor blockade is ineffective in different *in vivo* models of migraine. Cephalalgia 2011, 31: 172–180.
61. Toriumi H, Shimizu T, Ebine T, Takizawa T, Kayama Y, Koh A, *et al.* Repetitive trigeminal nociceptive stimulation in rats increases their susceptibility to cortical spreading depression. Neurosci Res 2016, 106: 74–78.
62. Schnizler K, Shutov LP, Van Kanegan MJ, Merrill MA, Nichols B, McKnight GS, *et al.* Protein kinase A anchoring via AKAP150 is essential for TRPV1 modulation by forskolin and prostaglandin E2 in mouse sensory neurons. J Neurosci 2008, 28: 4904–4917.
63. Premkumar LS, Ahern GP. Induction of vanilloid receptor channel activity by protein kinase C. Nature 2000, 408: 985–990.
64. Liu J, Du J, Yang Y, Wang Y. Phosphorylation of TRPV1 by cyclin-dependent kinase 5 promotes TRPV1 surface localization, leading to inflammatory thermal hyperalgesia. Exp Neurol 2015, 273: 253–262.
65. Wang Y, Gao Y, Tian Q, Deng Q, Wang Y, Zhou T, *et al.* TRPV1 SUMOylation regulates nociceptive signaling in models of inflammatory pain. Nat Commun 2018, 9: 1529.
66. Mizumura K, Murase S. Role of nerve growth factor in pain. Handb Exp Pharmacol 2015, 227: 57–77.
67. Sarchielli P, Alberti A, Floridi A, Gallai V. Levels of nerve growth factor in cerebrospinal fluid of chronic daily headache patients. Neurology 2001, 57: 132–134.
68. Ji RR, Samad TA, Jin SX, Schmoll R, Woolf CJ. p38 MAPK activation by NGF in primary sensory neurons after inflammation increases TRPV1 levels and maintains heat hyperalgesia. Neuron 2002, 36: 57–68.
69. Holland S, Coste O, Zhang DD, Pierre SC, Geisslinger G, Scholich K. The ubiquitin ligase MYCBP2 regulates transient receptor potential vanilloid receptor 1 (TRPV1) internalization through inhibition of p38 MAPK signaling. J Biol Chem 2011, 286: 3671–3680.
70. Zhang X, Huang J, McNaughton PA. NGF rapidly increases membrane expression of TRPV1 heat-gated ion channels. EMBO J 2005, 24: 4211–4223.
71. Kawai T, Akira S. The role of pattern-recognition receptors in innate immunity: update on Toll-like receptors. Nat Immunol 2010, 11: 373–384.
72. Liu JF, Wu R, Li JX. Toll of mental disorders: TLR-mediated function of the innate immune system. Neurosci Bull 2019, 35: 771–774.
73. Wadachi R, Hargreaves KM. Trigeminal nociceptors express TLR-4 and CD14: a mechanism for pain due to infection. J Dent Res 2006, 85: 49–53.
74. Min H, Cho WH, Lee H, Choi B, Kim YJ, Lee HK, *et al.* Association of TRPV1 and TLR4 through the TIR domain potentiates TRPV1 activity by blocking activation-induced desensitization. Mol Pain 2018, 14: 1744806918812636.
75. Burstein R, Zhang X, Levy D, Aoki KR, Brin MF. Selective inhibition of meningeal nociceptors by botulinum neurotoxin type A: therapeutic implications for migraine and other pains. Cephalalgia 2014, 34: 853–869.
76. Kosaras B, Jakubowski M, Kainz V, Burstein R. Sensory innervation of the calvarial bones of the mouse. J Comp Neurol 2009, 515: 331–348.
77. Schueler M, Messlinger K, Dux M, Neuhuber WL, De Col R. Extracranial projections of meningeal afferents and their impact on meningeal nociception and headache. Pain 2013, 154: 1622–1631.
78. Kayama Y, Shibata M, Takizawa T, Ibata K, Shimizu T, Ebine T, *et al.* Functional interactions between transient receptor potential M8 and transient receptor potential V1 in the trigeminal system: Relevance to migraine pathophysiology. Cephalalgia 2018, 38: 833–845.
79. Zhang X, Strassman AM, Novack V, Brin MF, Burstein R. Extracranial injections of botulinum neurotoxin type A inhibit intracranial meningeal nociceptors' responses to stimulation of TRPV1 and TRPA1 channels: are we getting closer to solving this puzzle? Cephalalgia 2016, 36: 875–886.
80. Shimizu T, Shibata M, Toriumi H, Iwashita T, Funakubo M, Sato H, *et al.* Reduction of TRPV1 expression in the trigeminal system by botulinum neurotoxin type-A. Neurobiol Dis 2012, 48: 367–378.
81. McKemy DD, Neuhausser WM, Julius D. Identification of a cold receptor reveals a general role for TRP channels in thermosensation. Nature 2002, 416: 52–58.
82. Peier AM, Moqrich A, Hergarden AC, Reeve AJ, Andersson DA, Story GM, *et al.* A TRP channel that senses cold stimuli and menthol. Cell 2002, 108: 705–715.
83. Daniels RL, Takashima Y, McKemy DD. Activity of the neuronal cold sensor TRPM8 is regulated by phospholipase C via the phospholipid phosphoinositol 4,5-bisphosphate. J Biol Chem 2009, 284: 1570–1582.
84. Liu B, Qin F. Functional control of cold- and menthol-sensitive TRPM8 ion channels by phosphatidylinositol 4,5-bisphosphate. J Neurosci 2005, 25: 1674–1681.
85. Rohacs T, Lopes CM, Michailidis I, Logothetis DE. PI(4,5)P2 regulates the activation and desensitization of TRPM8 channels through the TRP domain. Nat Neurosci 2005, 8: 626–634.
86. Dhaka A, Murray AN, Mathur J, Earley TJ, Petrus MJ, Patapoutian A. TRPM8 is required for cold sensation in mice. Neuron 2007, 54: 371–378.
87. Colburn RW, Lubin ML, Stone DJ, Jr., Wang Y, Lawrence D, D'Andrea MR, *et al.* Attenuated cold sensitivity in TRPM8 null mice. Neuron 2007, 54: 379–386.
88. Abe J, Hosokawa H, Okazawa M, Kandachi M, Sawada Y, Yamanaka K, *et al.* TRPM8 protein localization in trigeminal ganglion and taste papillae. Brain Res Mol Brain Res 2005, 136: 91–98.
89. Kobayashi K, Fukuoka T, Obata K, Yamanaka H, Dai Y, Tokunaga A, *et al.* Distinct expression of TRPM8, TRPA1, and TRPV1 mRNAs in rat primary afferent neurons with adelta/c-fibers and colocalization with trk receptors. J Comp Neurol 2005, 493: 596–606.
90. Horne DB, Biswas K, Brown J, Bartberger MD, Clarine J, Davis CD, *et al.* Discovery of TRPM8 antagonist (S)-6-(((3-fluoro-4-(trifluoromethoxy)phenyl)(3-fluoropyridin-2-

yl)methyl)carbamoy l)nicotinic Acid (AMG 333), a clinical candidate for the treatment of migraine. J Med Chem 2018, 61: 8186–8201.
91. Gobel H, Schmidt G, Soyka D. Effect of peppermint and eucalyptus oil preparations on neurophysiological and experimental algesimetric headache parameters. Cephalalgia 1994, 14: 228–234; discussion 182.
92. Borhani Haghighi A, Motazedian S, Rezaii R, Mohammadi F, Salarian L, Pourmokhtari M, *et al.* Cutaneous application of menthol 10% solution as an abortive treatment of migraine without aura: a randomised, double-blind, placebo-controlled, crossed-over study. Int J Clin Pract 2010, 64: 451–456.
93. Green BG, McAuliffe BL. Menthol desensitization of capsaicin irritation. Evidence of a short-term anti-nociceptive effect. Physiol Behav 2000, 68: 631–639.
94. Takashima Y, Ma L, McKemy DD. The development of peripheral cold neural circuits based on TRPM8 expression. Neuroscience 2010, 169: 828–842.
95. Freilinger T, Anttila V, de Vries B, Malik R, Kallela M, Terwindt GM, *et al.* Genome-wide association analysis identifies susceptibility loci for migraine without aura. Nat Genet 2012, 44: 777–782.
96. Chasman DI, Schurks M, Anttila V, de Vries B, Schminke U, Launer LJ, *et al.* Genome-wide association study reveals three susceptibility loci for common migraine in the general population. Nat Genet 2011, 43: 695–698.
97. Anttila V, Winsvold BS, Gormley P, Kurth T, Bettella F, McMahon G, *et al.* Genome-wide meta-analysis identifies new susceptibility loci for migraine. Nat Genet 2013, 45: 912–917.
98. Gavva NR, Sandrock R, Arnold GE, Davis M, Lamas E, Lindvay C, *et al.* Reduced TRPM8 expression underpins reduced migraine risk and attenuated cold pain sensation in humans. Sci Rep 2019, 9: 19655.
99. Kayama Y, Shibata M, Takizawa T, Ibata K, Nakahara J, Shimizu T, *et al.* Signaling pathways relevant to nerve growth factor-induced upregulation of transient receptor potential M8 expression. Neuroscience 2017, 367: 178–188.
100. Burgos-Vega CC, Ahn DD, Bischoff C, Wang W, Horne D, Wang J, *et al.* Meningeal transient receptor potential channel M8 activation causes cutaneous facial and hindpaw allodynia in a preclinical rodent model of headache. Cephalalgia 2016, 36: 185–193.
101. Ling YH, Chen SP, Fann CS, Wang SJ, Wang YF. TRPM8 genetic variant is associated with chronic migraine and allodynia. J Headache Pain 2019, 20: 115.
102. Jaquemar D, Schenker T, Trueb B. An ankyrin-like protein with transmembrane domains is specifically lost after oncogenic transformation of human fibroblasts. J Biol Chem 1999, 274: 7325–7333.
103. Shibasaki K. TRPV4 activation by thermal and mechanical stimuli in disease progression. Lab Invest 2020, 100: 218–223.
104. Barabas ME, Kossyreva EA, Stucky CL. TRPA1 is functionally expressed primarily by IB4-binding, non-peptidergic mouse and rat sensory neurons. PLoS One 2012, 7: e47988.
105. Kremeyer B, Lopera F, Cox JJ, Momin A, Rugiero F, Marsh S, *et al.* A gain-of-function mutation in TRPA1 causes familial episodic pain syndrome. Neuron 2010, 66: 671–680.
106. Story GM, Peier AM, Reeve AJ, Eid SR, Mosbacher J, Hricik TR, *et al.* ANKTM1, a TRP-like channel expressed in nociceptive neurons, is activated by cold temperatures. Cell 2003, 112: 819–829.
107. Bandell M, Story GM, Hwang SW, Viswanath V, Eid SR, Petrus MJ, *et al.* Noxious cold ion channel TRPA1 is activated by pungent compounds and bradykinin. Neuron 2004, 41: 849–857.
108. Koivisto A, Jalava N, Bratty R, Pertovaara A. TRPA1 antagonists for pain relief. Pharmaceuticals (Basel) 2018, 11: 117.
109. Nassini R, Materazzi S, Benemei S, Geppetti P. The TRPA1 channel in inflammatory and neuropathic pain and migraine. Rev Physiol Biochem Pharmacol 2014, 167: 1–43.
110. Nassini R, Materazzi S, Vriens J, Prenen J, Benemei S, De Siena G, *et al.* The 'headache tree' via umbellulone and TRPA1 activates the trigeminovascular system. Brain 2012, 135: 376–390.
111. Jiang L, Wang Y, Xu Y, Ma D, Wang M. The transient receptor potential ankyrin type 1 plays a critical role in cortical spreading depression. Neuroscience 2018, 382: 23–34.
112. Jiang L, Ma D, Grubb BD, Wang M. ROS/TRPA1/CGRP signaling mediates cortical spreading depression. J Headache Pain 2019, 20: 25.
113. Kheradpezhouh E, Choy JMC, Daria VR, Arabzadeh E. TRPA1 expression and its functional activation in rodent cortex. Open Biol 2017, 7: 160314.
114. Warfvinge K, Edvinsson L. Distribution of CGRP and CGRP receptor components in the rat brain. Cephalalgia 2019, 39: 342–353.
115. Shatillo A, Koroleva K, Giniatullina R, Naumenko N, Slastnikova AA, Aliev RR, *et al.* Cortical spreading depression induces oxidative stress in the trigeminal nociceptive system. Neuroscience 2013, 253: 341–349.
116. Sato H, Shibata M, Shimizu T, Shibata S, Toriumi H, Ebine T, *et al.* Differential cellular localization of antioxidant enzymes in the trigeminal ganglion. Neuroscience 2013, 248: 345–358.
117. Trevisan G, Benemei S, Materazzi S, De Logu F, De Siena G, Fusi C, *et al.* TRPA1 mediates trigeminal neuropathic pain in mice downstream of monocytes/macrophages and oxidative stress. Brain 2016, 139: 1361–1377.
118. De Logu F, Nassini R, Materazzi S, Carvalho Goncalves M, Nosi D, Rossi Degl'Innocenti D, *et al.* Schwann cell TRPA1 mediates neuroinflammation that sustains macrophage-dependent neuropathic pain in mice. Nat Commun 2017, 8: 1887.
119. Kunkler PE, Ballard CJ, Oxford GS, Hurley JH. TRPA1 receptors mediate environmental irritant-induced meningeal vasodilatation. Pain 2011, 152: 38–44.
120. Kunkler PE, Zhang L, Johnson PL, Oxford GS, Hurley JH. Induction of chronic migraine phenotypes in a rat model after environmental irritant exposure. Pain 2018, 159: 540–549.
121. Silberstein SD. Preventive migraine treatment. Continuum (Minneap Minn) 2015, 21: 973–989.
122. Olesen J. The role of nitric oxide (NO) in migraine, tension-type headache and cluster headache. Pharmacol Ther 2008, 120: 157–171.
123. Marone IM, De Logu F, Nassini R, De Carvalho Goncalves M, Benemei S, Ferreira J, *et al.* TRPA1/NOX in the soma of trigeminal ganglion neurons mediates migraine-related pain of glyceryl trinitrate in mice. Brain 2018, 141: 2312–2328.
124. Koroleva K, Mustafina A, Yakovlev A, Hermann A, Giniatullin R, Sitdikova G. Receptor mechanisms mediating the pronociceptive action of hydrogen sulfide in rat trigeminal neurons and meningeal afferents. Front Cell Neurosci 2017, 11: 226.
125. Benemei S, De Logu F, Li Puma S, Marone IM, Coppi E, Ugolini F, *et al.* The anti-migraine component of butterbur extracts, isopetasin, desensitizes peptidergic nociceptors by acting on TRPA1 cation channel. Br J Pharmacol 2017, 174: 2897–2911.
126. Nagatomo K, Kubo Y. Caffeine activates mouse TRPA1 channels but suppresses human TRPA1 channels. Proc Natl Acad Sci U S A 2008, 105: 17373–17378.
127. Andersson DA, Gentry C, Alenmyr L, Killander D, Lewis SE, Andersson A, *et al.* TRPA1 mediates spinal antinociception induced by acetaminophen and the cannabinoid Delta(9)-tetrahydrocannabiorcol. Nat Commun 2011, 2: 551.

128. Mirrasekhian E, Nilsson JLA, Shionoya K, Blomgren A, Zygmunt PM, Engblom D, *et al.* The antipyretic effect of paracetamol occurs independent of transient receptor potential ankyrin 1-mediated hypothermia and is associated with prostaglandin inhibition in the brain. FASEB J 2018, 32: 5751–5759.
129. Liedtke W, Choe Y, Marti-Renom MA, Bell AM, Denis CS, Sali A, *et al.* Vanilloid receptor-related osmotically activated channel (VR-OAC), a candidate vertebrate osmoreceptor. Cell 2000, 103: 525–535.
130. Strotmann R, Harteneck C, Nunnenmacher K, Schultz G, Plant TD. OTRPC4, a nonselective cation channel that confers sensitivity to extracellular osmolarity. Nat Cell Biol 2000, 2: 695–702.
131. Delany NS, Hurle M, Facer P, Alnadaf T, Plumpton C, Kinghorn I, *et al.* Identification and characterization of a novel human vanilloid receptor-like protein, VRL-2. Physiol Genom 2001, 4: 165–174.
132. Liedtke W. TRPV4 plays an evolutionary conserved role in the transduction of osmotic and mechanical stimuli in live animals. J Physiol 2005, 567: 53–58.
133. Lindy AS, Parekh PK, Zhu R, Kanju P, Chintapalli SV, Tsvilovskyy V, *et al.* TRPV channel-mediated calcium transients in nociceptor neurons are dispensable for avoidance behaviour. Nat Commun 2014, 5: 4734.
134. Liedtke W, Tobin DM, Bargmann CI, Friedman JM. Mammalian TRPV4 (VR-OAC) directs behavioral responses to osmotic and mechanical stimuli in *Caenorhabditis elegans*. Proc Natl Acad Sci U S A 2003, 100 Suppl 2: 14531–14536.
135. Liedtke W. TRPV4 as osmosensor: a transgenic approach. Pflug Arch 2005, 451: 176–180.
136. Moore C, Liedtke WB. Osmomechanical-sensitive TRPV channels in mammals. Neurobiology of TRP Channels. 2nd ed. Boca Raton (FL): CRC Press/Taylor & Francis; 2017, 85–94.
137. Watanabe H, Vriens J, Prenen J, Droogmans G, Voets T, Nilius B. Anandamide and arachidonic acid use epoxyeicosatrienoic acids to activate TRPV4 channels. Nature 2003, 424: 434–438.
138. Nilius B, Vriens J, Prenen J, Droogmans G, Voets T. TRPV4 calcium entry channel: a paradigm for gating diversity. Am J Physiol Cell Physiol 2004, 286: C195–C205.
139. Vriens J, Watanabe H, Janssens A, Droogmans G, Voets T, Nilius B. Cell swelling, heat, and chemical agonists use distinct pathways for the activation of the cation channel TRPV4. Proc Natl Acad Sci U S A 2004, 101: 396–401.
140. Garcia-Elias A, Mrkonjic S, Jung C, Pardo-Pastor C, Vicente R, Valverde MA. The TRPV4 channel. Handb Exp Pharmacol 2014, 222: 293–319.
141. White JP, Cibelli M, Urban L, Nilius B, McGeown JG, Nagy I. TRPV4: molecular conductor of a diverse orchestra. Physiol Rev 2016, 96: 911–973.
142. Dias FC, Alves VS, Matias DO, Figueiredo CP, Miranda ALP, Passos GF, *et al.* The selective TRPV4 channel antagonist HC-067047 attenuates mechanical allodynia in diabetic mice. Eur J Pharmacol 2019, 856: 172408.
143. Kanju P, Chen Y, Lee W, Yeo M, Lee SH, Romac J, *et al.* Small molecule dual-inhibitors of TRPV4 and TRPA1 for attenuation of inflammation and pain. Sci Rep 2016, 6: 26894.
144. Chen Y, Yang C, Wang ZJ. Proteinase-activated receptor 2 sensitizes transient receptor potential vanilloid 1, transient receptor potential vanilloid 4, and transient receptor potential ankyrin 1 in paclitaxel-induced neuropathic pain. Neuroscience 2011, 193: 440–451.
145. Brierley SM, Page AJ, Hughes PA, Adam B, Liebregts T, Cooper NJ, *et al.* Selective role for TRPV4 ion channels in visceral sensory pathways. Gastroenterology 2008, 134: 2059–2069.
146. Chen Y, Williams SH, McNulty AL, Hong JH, Lee SH, Rothfusz NE, *et al.* Temporomandibular joint pain: a critical role for TRPV4 in the trigeminal ganglion. Pain 2013, 154: 1295–1304.
147. Chen Y, Kanju P, Fang Q, Lee SH, Parekh PK, Lee W, *et al.* TRPV4 is necessary for trigeminal irritant pain and functions as a cellular formalin receptor. Pain 2014, 155: 2662–2672.
148. Moore C, Cevikbas F, Pasolli HA, Chen Y, Kong W, Kempkes C, *et al.* UVB radiation generates sunburn pain and affects skin by activating epidermal TRPV4 ion channels and triggering endothelin-1 signaling. Proc Natl Acad Sci U S A 2013, 110: E3225–E3234.
149. Swain SM, Romac JM, Shahid RA, Pandol SJ, Liedtke W, Vigna SR, *et al.* TRPV4 channel opening mediates pressure-induced pancreatitis initiated by Piezo1 activation. J Clin Invest 2020, 130: 2527–2541.
150. Li L, Liu C, Chen L, Chen L. Hypotonicity modulates tetrodotoxin-sensitive sodium current in trigeminal ganglion neurons. Mol Pain 2011, 7: 27.
151. Liu L, Chen L, Liedtke W, Simon SA. Changes in osmolality sensitize the response to capsaicin in trigeminal sensory neurons. J Neurophysiol 2007, 97: 2001–2015.
152. Zhang Y, Wang YH, Ge HY, Arendt-Nielsen L, Wang R, Yue SW. A transient receptor potential vanilloid 4 contributes to mechanical allodynia following chronic compression of dorsal root ganglion in rats. Neurosci Lett 2008, 432: 222–227.
153. Rajasekhar P, Poole DP, Liedtke W, Bunnett NW, Veldhuis NA. P2Y1 receptor activation of the TRPV4 ion channel enhances purinergic signaling in satellite glial cells. J Biol Chem 2015, 290: 29051–29062.
154. Kanju P, Liedtke W. Pleiotropic function of TRPV4 ion channels in the central nervous system. Exp Physiol 2016, 101: 1472–1476.
155. Wang Z, Zhou L, An D, Xu W, Wu C, Sha S, *et al.* TRPV4-induced inflammatory response is involved in neuronal death in pilocarpine model of temporal lobe epilepsy in mice. Cell Death Dis 2019, 10: 386.
156. Benfenati V, Amiry-Moghaddam M, Caprini M, Mylonakou MN, Rapisarda C, Ottersen OP, *et al.* Expression and functional characterization of transient receptor potential vanilloid-related channel 4 (TRPV4) in rat cortical astrocytes. Neuroscience 2007, 148: 876–892.
157. Konno M, Shirakawa H, Iida S, Sakimoto S, Matsutani I, Miyake T, *et al.* Stimulation of transient receptor potential vanilloid 4 channel suppresses abnormal activation of microglia induced by lipopolysaccharide. Glia 2012, 60: 761–770.
158. Lu KT, Huang TC, Tsai YH, Yang YL. Transient receptor potential vanilloid type 4 channels mediate Na–K–Cl-co-transporter-induced brain edema after traumatic brain injury. J Neurochem 2017, 140: 718–727.
159. Ferrari MD, Klever RR, Terwindt GM, Ayata C, van den Maagdenberg AM. Migraine pathophysiology: lessons from mouse models and human genetics. Lancet Neurol 2015, 14: 65–80.
160. Burstein R, Cutrer MF, Yarnitsky D. The development of cutaneous allodynia during a migraine attack clinical evidence for the sequential recruitment of spinal and supraspinal nociceptive neurons in migraine. Brain 2000, 123 (Pt 8): 1703–1709.
161. Strassman AM, Raymond SA, Burstein R. Sensitization of meningeal sensory neurons and the origin of headaches. Nature 1996, 384: 560–564.
162. Levy D, Strassman AM. Mechanical response properties of A and C primary afferent neurons innervating the rat intracranial dura. J Neurophysiol 2002, 88: 3021–3031.

163. Wei X, Edelmayer RM, Yan J, Dussor G. Activation of TRPV4 on dural afferents produces headache-related behavior in a preclinical rat model. Cephalalgia 2011, 31: 1595–1600.
164. Duan J, Xie J, Deng T, Xie X, Liu H, Li B, *et al.* Exposure to both formaldehyde and high relative humidity exacerbates allergic asthma by activating the TRPV4-p38 MAPK pathway in Balb/c mice. Environ Pollut 2020, 256: 113375.
165. Grant AD, Cottrell GS, Amadesi S, Trevisani M, Nicoletti P, Materazzi S, *et al.* Protease-activated receptor 2 sensitizes the transient receptor potential vanilloid 4 ion channel to cause mechanical hyperalgesia in mice. J Physiol 2007, 578: 715–733.
166. Hassler SN, Ahmad FB, Burgos-Vega CC, Boitano S, Vagner J, Price TJ, *et al.* Protease activated receptor 2 (PAR2) activation causes migraine-like pain behaviors in mice. Cephalalgia 2019, 39: 111–122.
167. Poole DP, Amadesi S, Veldhuis NA, Abogadie FC, Lieu T, Darby W, *et al.* Protease-activated receptor 2 (PAR2) protein and transient receptor potential vanilloid 4 (TRPV4) protein coupling is required for sustained inflammatory signaling. J Biol Chem 2013, 288: 5790–5802.
168. Lawhorn BG, Brnardic EJ, Behm DJ. Recent advances in TRPV4 agonists and antagonists. Bioorg Med Chem Lett 2020, 30: 127022.
169. Dedov VN, Roufogalis BD. Mitochondrial calcium accumulation following activation of vanilloid (VR1) receptors by capsaicin in dorsal root ganglion neurons. Neuroscience 2000, 95: 183–188.
170. Szoke E, Seress L, Szolcsanyi J. Neonatal capsaicin treatment results in prolonged mitochondrial damage and delayed cell death of B cells in the rat trigeminal ganglia. Neuroscience 2002, 113: 925–937.

Neurosci. Bull. January, 2021, 37(1):117–131
https://doi.org/10.1007/s12264-020-00578-4

www.neurosci.cn
www.springer.com/12264

REVIEW

Wiring the Brain by Clustered Protocadherin Neural Codes

Qiang Wu[1] · **Zhilian Jia**[1]

Received: 27 May 2020 / Accepted: 2 August 2020 / Published online: 17 September 2020

Abstract There are more than a thousand trillion specific synaptic connections in the human brain and over a million new specific connections are formed every second during the early years of life. The assembly of these staggeringly complex neuronal circuits requires specific cell-surface molecular tags to endow each neuron with a unique identity code to discriminate self from non-self. The clustered protocadherin (*Pcdh*) genes, which encode a tremendous diversity of cell-surface assemblies, are candidates for neuronal identity tags. We describe the adaptive evolution, genomic structure, and regulation of expression of the clustered *Pcdh*s. We specifically focus on the emerging 3-D architectural and biophysical mechanisms that generate an enormous number of diverse cell-surface Pcdhs as neural codes in the brain.

Keywords Clustered protocadherins · Genome architecture · Neuronal identity · Adhesion specificity · Self-avoidance · Cell recognition

✉ Qiang Wu
qiangwu@sjtu.edu.cn

[1] Center for Comparative Biomedicine, Ministry of Education Key Lab of Systems Biomedicine, State Key Laboratory of Oncogenes and Related Genes, Joint International Research Laboratory of Metabolic and Developmental Sciences, Institute of Systems Biomedicine, Xinhua Hospital, School of Life Sciences and Biotechnology, Shanghai Jiao Tong University, Shanghai 200240, China

Introduction

The human brain contains a staggering 86 billion neurons, each with numerous branches of dendrites covering receptive fields and of axons innervating diverse regions with minimal overlap. The correct patterning of dendritic and axonal arbors is central for establishing and maintaining enormously complex networks with specific neuronal connectivity in the brain. These vast networks of synaptic connections between axons and dendrites form specific neuronal circuits to fulfill complicated cognitive functions and to determine personality traits and behavior. Aberrant assemblies of neuronal circuits underlie neuropsychiatric diseases. Neuronal circuit assemblies require each neuron to have an identity code for self-recognition and non-self discrimination. How these fascinating and diverse neuronal networks are generated is of the utmost importance. In addition, how the limited size of the human genome encodes the enormous number of neuronal cell-surface identity codes is intriguing.

Over the past few decades, great progress has been made to uncover large families of adhesion proteins that are candidates for cell-surface identity codes for neuronal circuit assembly, such as neurexins [1], olfactory receptors [2], cadherins and families of other adhesion molecules [3–6]. For example, in *Drosophila melanogaster*, 38,016 isoforms of *Dscam1* (Down syndrome cell adhesion molecule 1)—generated by alternative splicing—endow each neuron with a unique identity code to discriminate self from non-self [7–10]. In vertebrates, this is achieved through the stochastic and combinatorial expression of ~60 clustered protocadherin (*Pcdh*) genes [11–13].

Cadherins are a superfamily of Ca^{2+}-dependent cell-adhesion proteins that are required for specific cell-cell recognition in metazoans. Members of the cadherin

superfamily include classical cadherins (type I and type II), clustered Pcdhs (α, β, γ), and non-clustered Pcdhs [6]. Compared with classical cadherins with five ectodomains (ECs), Pcdhs have six or more ECs with characteristic genome organization, in which multiple ECs are encoded by single unusually large exons [14, 15], and have diverse functions such as neuronal migration and axonal development [15, 16]. Clustered *Pcdh* genes are arranged in closely-linked clusters in one chromosomal region, while non-clustered *Pcdh* genes are scattered on different chromosomes [17]. As the largest subfamily of the cadherin superfamily, clustered *Pcdh* genes are prominently expressed in the brain, and each encodes a cadherin-like protein with six characteristic EC repeats. Their variable and constant genomic architectures are remarkably similar to those of the immunoglobulin (*Ig*), T cell receptor *(Tcr)*, and UDP glucuronosyltransferase (*Ugt*) gene clusters, which generate tremendous diversity for the humoral immunity, cellular immunity, and chemical defense systems, respectively [11, 18].

In this review, we describe 3-D architectural and biophysical mechanisms for Pcdh neural codes in the brain. We first describe the 1-D genomic organization of the three *Pcdh* gene clusters and the 3-D architectural mechanisms that generate their combinatorial repertoires for single neurons. We then discuss *cis*- and *trans*-interactions between the extracellular domains of cell-surface Pcdh proteins to ensure neurons for self-recognition as well as self and non-self discrimination. These interactions transduce extracellular contact-dependent signals into the cytoplasm to induce actin dynamics and cytoskeletal remodeling through the common intracellular constant domains. It is this cytoskeletal remodeling that leads to the many functions of Pcdh such as neuronal migration, neurite morphogenesis, dendritic self-avoidance, axonal projection, spine elaboration, synaptogenesis, and neuronal connectivity. We refer interested readers to other excellent reviews discussing various aspects of the clustered *Pcdh* genes [5, 6, 19–25].

If It Looks Like a Code and Organizes Like a Code, It is a Code

Genetic studies have a long history of describing the phenomena of heredity. While individual genes determine certain phenotypes, the genome with the entire gene assembly holds the characteristics of a species and every creature has a genome that is passed on to the next generation. The genome encodes the brain, but the environment shapes and sharpens the brain: so-called neural epigenetics. The complexity of the brain determines the mind and consciousness. Both the brain and genome code and store information that is vital for the life of creatures. While the genome and genetic codes have been decoded [26, 27], the nature of the neural codes that wire the brain is still under intense investigation.

Setting the Stage for Neural Identity Codes

In the early 1940s, the Chemoaffinity Hypothesis posited that neurons express on their plasma membranes individual identification tags that specify synaptic connections [28]. Intensive efforts have since been devoted to uncovering the proposed neural codes but the exact nature of the neuronal chemoaffinity tags remains elusive [29, 30]. Among the four cell-adhesion families of cadherins, selectins, integrins, and Ig-containing proteins, cadherins are the only family that functions in direct Ca^{2+}-dependent plasma membrane-to-membrane homotypic interactions, and are thus strong candidates for the chemoaffinity tags of neural codes in the brain [3, 5, 6, 31, 32]. However, only about a dozen classical cadherin genes and a few *Pcdh* genes were cloned in the nineties [33, 34]. Using the yeast two-hybrid system, 2 full-length and 6 partial cadherin-related receptor genes were cloned from mouse brain tissues and found to be expressed at synaptic junctions in neuronal subpopulations [35]. However, where exactly these proteins are located remains to be determined.

It turned out that these genes are members of the *Pcdhα* cluster which happens to be located upstream of the two other large gene clusters of *Pcdhβ* and *Pcdhγ* [11]. In total, there are 15 *Pcdhα*, 16 *Pcdhβ*, and 22 *Pcdhγ* genes that are highly similar and organized in tandem arrays in a single locus of the human genome. These large numbers and the striking organization immediately suggest that the clustered *Pcdh* genes are the long-sought neuronal address codes for the brain [4, 36–38]. These numbers are orders of magnitude less than that of neurons in the brain; however, mathematic analyses suggest that they are enough to encode the synaptic address codes required for geometrically constrained local brain regions or nuclei [39].

Genomic Organization of Clustered *Pcdh* Genes

The mammalian clustered Pcdh proteins are encoded by three closely-linked gene clusters (*Pcdhα*, *Pcdhβ*, and *Pcdhγ*) which span nearly 1 million base pairs [11]. The genomic arrangements of the *Pcdhα* and *Pcdhγ* clusters are similar, both with tandem arrays of large variable exons followed by respective single sets of three small constant exons (Fig. 1A) [11, 14, 40]. Within the *Pcdhα* and *Pcdhγ* clusters, each variable exon carries its own promoter and can be spliced to the single set of downstream constant exons of its respective cluster. Through stochastic promoter activation and *cis*-alternative splicing, clustered *Pcdh*s can generate dozens of different isoforms [41, 42].

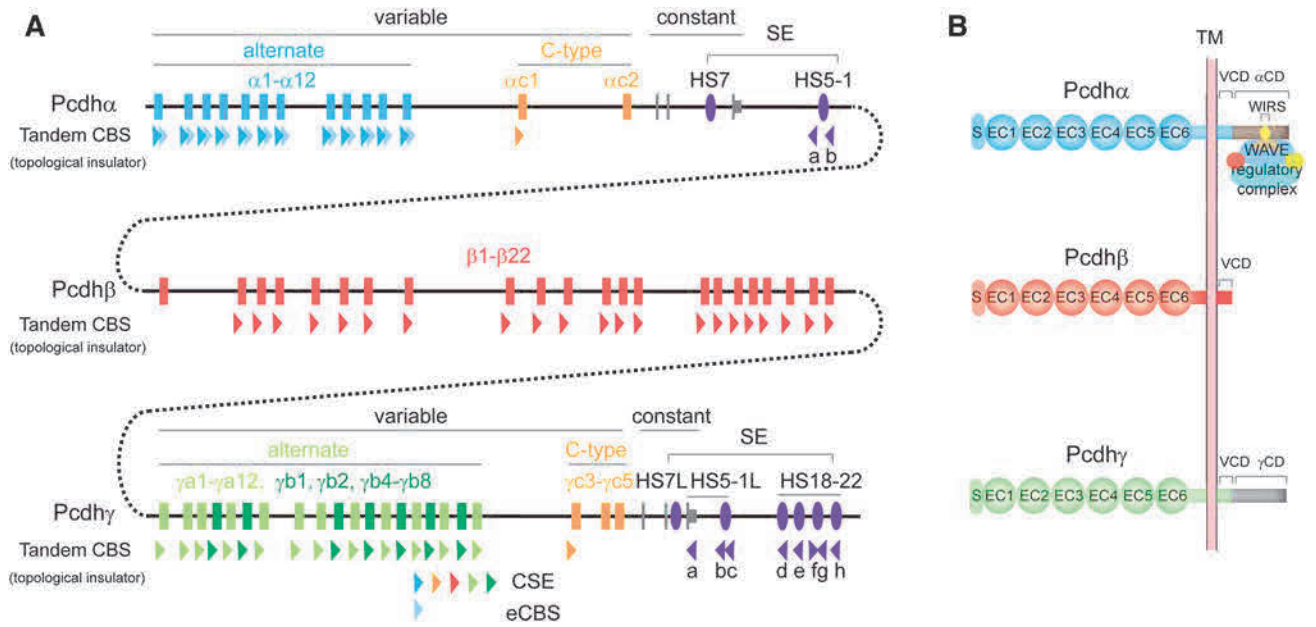

Fig. 1 Genomic organization and domain structure of clustered protocadherins. **A** Mouse clustered protocadherin genes have 58 isoforms arranged into three closely-linked clusters: *Pcdh* α, *β*, and *γ*. The *Pcdh* α and *γ* gene clusters contain more than a dozen of unusually large, highly similar, and repetitive variable exons, each of which is associated with a promoter and can be spliced to a common set of three downstream small constant exons within the respective cluster. These variable exons can be separated into alternate and C-type groups, based on the encoded protein sequence similarity. The *Pcdhβ* gene cluster lacks constant exons and only contains 22 variable exons each of which encodes a full-length protein. HS7 and HS5-1 constitute a super-enhancer (SE) for the *Pcdhα* cluster. HS7L, HS5-1L, and HS18-22 constitute a super-enhancer for the *Pcdh β* and *γ* clusters. The locations and relative orientations of tandem CTCF sites (CBS, CTCF binding site), which function as topological insulators, are marked as arrowheads under the respective promoters and enhancers. Note that each *Pcdhα* alternate promoter is flanked by two CBS elements (CSE and eCBS). HS, DNaseI hypersensitive site. **B** The domain organization of the encoded protein structure of clustered Pcdhs. Each large variable exon encodes an extracellular domain with a signal peptide, followed by 6 ectodomain (EC) repeats, a transmembrane (TM) domain, and a juxtamembrane variable cytoplasmic domain (VCD). The three small constant exons encode a common membrane-distal intracellular constant domain (CD) shared by all isoforms of the *Pcdh* α or *γ* cluster. There is a WAVE interacting receptor sequence (WIRS) motif located near the C-terminal end of the *Pcdhα* CD that recruits the WAVE-regulatory complex and links to actin cytoskeletal dynamics.

The variable exons of *Pcdhα* and *Pcdhγ* can be further divided into alternate and C-type gene groups based on their genomic location and sequence similarity (Fig. 1A). The mouse *Pcdhα* cluster contains 12 alternate genes (*α1–α12*) and two C-type genes (*αc1* and *αc2*). The mouse *Pcdhγ* cluster contains 19 alternate genes (12 A-types: *γa1–γa12*; 7 B-types: *γb1*, *γb2*, *γb4–γb8*) and three C-type genes (*γc3–γc5*). Different from *Pcdhα* and *Pcdhγ*, the mouse *Pcdhβ* cluster, however, contains 22 genes (*β1–β22*) and no C-type gene (Fig. 1A). In total, there are five C-type variable exons that are more similar to each other than to members of the alternate gene group [11, 40]. However, *Pcdhβ* contains only large variable exons and lacks constant exons (Fig. 1A). Therefore, each member of the *Pcdhβ* cluster is a single-exon gene [11, 40]. Together, these three clusters encode 58 Pcdh isoforms (14α, 22β, and 22γ) in mice and 53 Pcdh isoforms (15α, 16β, and 22γ) in humans (Fig. 1A).

In the *Pcdhα* cluster, the promoter of each alternate gene is flanked by two CTCF-binding sites (CBS or CTCF sites). In the *Pcdhβ* cluster, the promoter of each gene is associated with one CBS element except *β1* which has no CBS element (Fig. 1A). In the *Pcdhγ* cluster, the promoter of each alternate gene is associated with one CBS element. Finally, among the five C-type *Pcdh* genes, only the first C-type gene of the *Pcdhα* cluster (*αc1*) and the first C-type gene of the *Pcdhγ* cluster (*γc3*) are associated with a CBS element (Fig. 1A).

Each variable exon encodes a signal peptide, followed by an extracellular domain containing 6 ECs, a transmembrane region, and a juxtamembrane variable cytoplasmic domain (VCD). The three constant exons encode a common membrane-distal intracellular constant domain (CD) shared by all members of the *Pcdhα* or *Pcdhγ* family. Since the *Pcdhβ* cluster has only a variable region with no constant region, each *Pcdhβ* variable exon is an independent gene, which encodes a Pcdh protein with an extracellular domain of 6 ECs, a transmembrane region, and a short VCD, but lacks a common CD (Fig. 1B) [11, 14].

The *Pcdha* cluster is regulated by a super-enhancer composed of two *cis*-regulatory elements, *HS7* and *HS5-1* (HS, hypersensitive site) (Fig. 1A). Similarly, a super-

enhancer, composed of *HS7L* (HS7 like), *HS5-1L* (HS5-1 like), and *HS18-22*, was also identified downstream of the *Pcdhγ* cluster for both the *Pcdhβ* and *Pcdhγ* clusters (Fig. 1A) [43–48].

Fifteen DNaseI hypersensitive sites (*HS15-HS1*) were initially identified in the *Pcdhα* cluster, among which *HS7* and *HS5-1* have strong enhancer activity in a transgenic reporter assay [49]. In mice, genetic deletion of *HS5-1*, which is located 30 kb downstream of the last *Pcdhα* constant exon, results in a significant decrease in the expression levels of *Pcdhα1*–*α12* and *Pcdhαc1* in the brain, but does not affect the expression of *Pcdhαc2* [48, 50]. By contrast, deletion of *HS7*, which is located between the constant exons 2 and 3, results in a significant decrease of expression levels of all *Pcdhα* genes, including *Pcdhαc2* [50].

Adaptive Evolution of Clustered *Pcdh* Genes

Initial studies on *Pcdh* genes showed that the encoded extracellular domain contains a "primordial" cadherin motif, similar to cadherin motifs in the *Drosophila* Fat protein [34]. It was thought that Pcdhs may be evolutionarily more ancient than the classical cadherins [34]. In addition, the *Pcdh* genes have characteristic genomic organizations in which multiple ECs are encoded by large exons, a feature that is distinct from the genomic organizations of classical cadherins [14]. Complete sequencing of the *Drosophila* genome revealed, however, that it does not contain clustered *Pcdh* genes [51]. Thus, the "proto" affix in the "protocadherin" nomenclature is a misnomer and the clustered *Pcdh* genes are thought to have adaptively evolved later and may be related to functions of more advanced nervous systems.

Similar to the human genome, the chimpanzee, mouse, and rat genomes contain the three *Pcdh* gene clusters [40, 52, 53]. Clustered *Pcdh* genes also exist in the anole lizard, frog, coelacanth, fugu, and zebrafish [52, 54–59]. The genome of the frog *Xenopus tropicalis* contains the *Pcdh* α and *γ* clusters but lacks *Pcdhβ*; however, the *Pcdhγ* cluster has been duplicated into two clusters [59]. In addition, the fugu and zebrafish genomes lack the *Pcdhβ* cluster but contain two *Pcdh* α and *γ* clusters because of the whole-genome duplication in the ray-finned lineage [52, 54, 57].

The anole and coelacanth genomes contain the *Pcdhβ* cluster [55, 58]. This suggests that the *Pcdhβ* cluster in mammals, anole, and coelacanth probably results from the duplication of variable exons of the *Pcdhγ* cluster. The duplicated variable exons subsequently lost their ability to be spliced to the constant exon 1 of the *Pcdhγ* cluster. Another possibility is that the *Pcdhβ* cluster results from duplication of the entire *Pcdhγ* cluster. The duplicated cluster then lost its constant exons through mutation or degeneration. Further research is needed to distinguish these two scenarios. Nevertheless, the topological regulation of both *Pcdh β* and *γ* clusters by a single super-enhancer composed of tandem arrays of CTCF sites (Fig. 1A) suggests that they share a common ancestor [48], consistent with their evolutionary trees [52]. Finally, molecular and structural analyses revealed that *Pcdhβ* and *Pcdhγ* share characteristics that are distinct from *Pcdhα* [12, 60].

The cartilaginous shark genome contains a single locus composed of four closely-linked *Pcdh* clusters that are para-orthologous to the three mammalian *Pcdh* gene clusters, suggesting that the ancestral jawed vertebrates contained seven *Pcdh* gene clusters [61]. During the evolution of the genomes of cartilaginous fish and bony vertebrates, this ancestral *Pcdh* locus experienced differential losses in that the mammalian lineages lost four clusters and the shark lineage lost three clusters [61]. Interestingly, clustered *Pcdh* genes are vastly expanded in the invertebrate octopus genome and enriched in neural tissues, consistent with their roles in establishing and maintaining the large and complex octopus nervous system [62, 63].

3-D Genome Architecture of Clustered *Pcdhs*

The three *Pcdh* gene clusters are organized as a large superTAD (super topologically associating domain) which can be divided into two subTADs of α and *βγ* (Fig. 2A) [45, 64]. The *Pcdhα* subTAD is formed by long-distance chromatin interactions between tandem arrays of forward CBS elements or CTCF sites of the variable region and the two reverse CBS elements flanking HS5-1 (Fig. 2A). The *Pcdhβγ* subTAD is formed by long-distance chromatin interactions between tandem arrays of forward and reverse CBS elements within the promoter and super-enhancer regions (Fig. 2A). We outline the important role of higher-order chromatin structures in the regulation of clustered *Pcdhs* in this section.

CTCF Protein as a Key 3-D Chromatin Architect

CTCF (CCCTC-binding factor) is the best-characterized insulator-binding protein in mammals that organizes the 3-D architecture of the genome. It regulates gene expression of the clustered *Pcdh*s through mediating long-range chromatin contacts between remote enhancers and target promoters. The topological chromatin loops between enhancers and promoters are formed by cohesin-mediated active loop extrusion [48]. Cohesin, a ring-shaped complex embracing double-stranded DNA, continuously extrudes

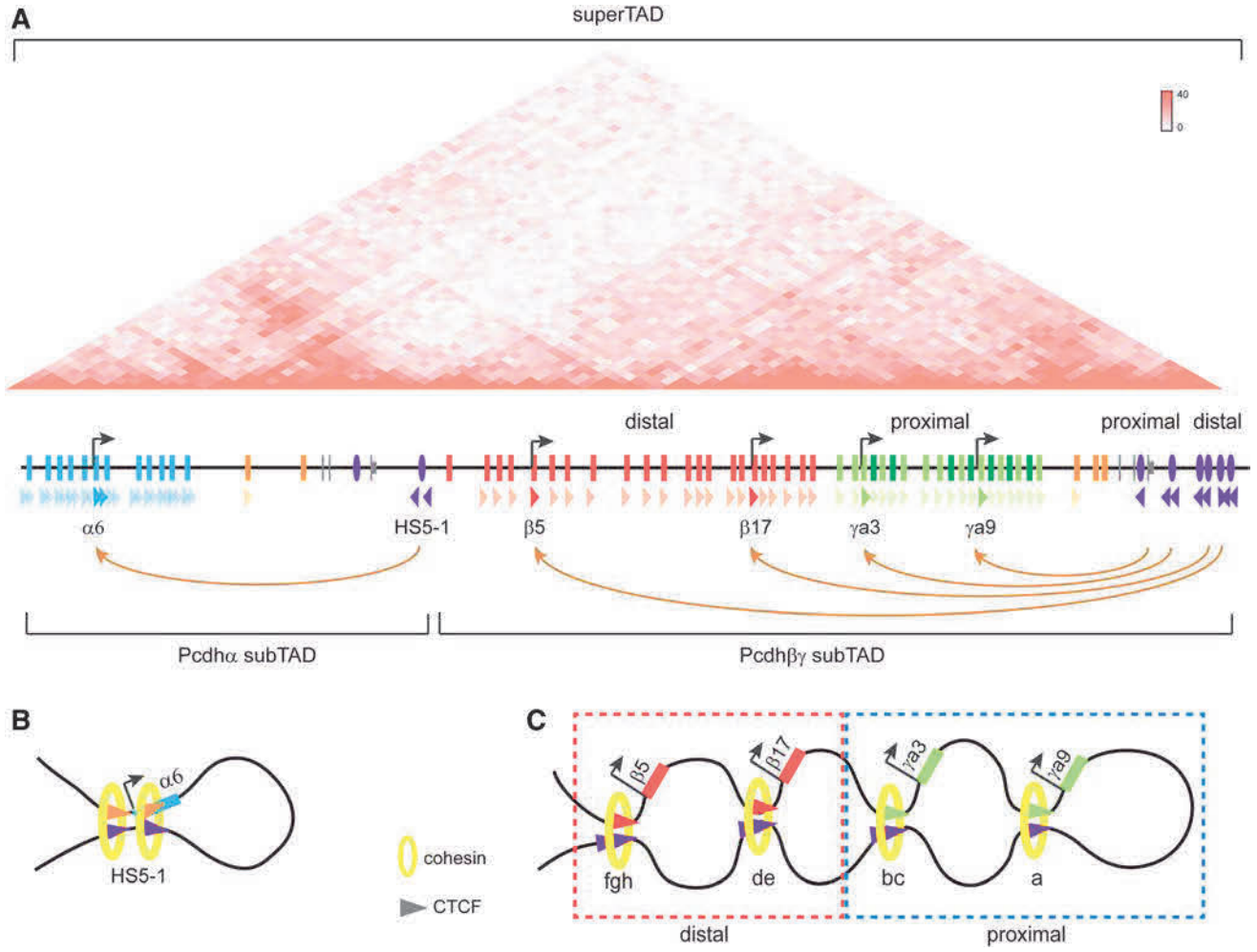

Fig. 2 Topological regulation of the clustered *Pcdh* genes in single alleles by tandem CTCF sites. **A** Hi-C map showing the three *Pcdh* clusters are organized into one superTAD composed of two subTADs. In the *Pcdhα* cluster, each promoter-associated CTCF site functions as a topological insulator for all of its upstream genes. In the *Pcdhβγ* clusters, tandem CTCF sites function as topological insulators, resulting in proximal-proximal and distal-distal CBS interactions. **B** HS5-1 forms spatial chromatin contacts with one and only one chosen alternate promoter through CTCF/cohesin-mediated "double-clamp" looping in the *Pcdhα* cluster. **C** Tandem CTCF sites function as topological insulators to balance spatial chromatin contacts and enhancer-promoter selection. The proximal CTCF sites of the super-enhancer form long-distance chromatin interactions with the *Pcdhγ* cluster while the distal CTCF sites of the super-enhancer form long-distance chromatin interactions with the *Pcdhβ* cluster, reminiscent of nested cohesin-extruded loops in the extended "Hulu model" [48].

chromatin fibers until blocked by CTCF-bound CBS elements. The cohesin loop extrusion brings the two remote DNA fragments with forward-reverse convergent CBS elements into close contact in the 3-D nuclear space [45, 65–67].

There is substantial evidence for a central role of CTCF/cohesin in clustered *Pcdh* gene regulation. First, knockdown of cohesin results in the loss of chromatin loops and downregulation of the clustered *Pcdh* genes [44, 68]. Second, knockdown of CTCF in cell lines also results in the loss of chromatin loops and a significant decrease of *Pcdh* expression levels [44, 68, 69]. Finally, conditional knockout of CTCF in neurons markedly downregulates a staggering 53 out of the total 58 clustered *Pcdh* genes in mice [70], providing strong evidence that CTCF is a master regulator for clustered *Pcdhs* [69].

Oriented CTCF Sites as Codes of Articulation Joints for Building 3-D Genome Architecture

Initial computational analyses identified a conserved sequence element (CSE), with a highly-conserved CGCT box, located at about the same distance upstream of the translational start codon of each member of the three *Pcdh* clusters (except for *αc2*, *β1*, *γc4*, and *γc5*) [40]. These CSEs were later shown to bind CTCF proteins, and thus are CBS elements (Fig. 1A) [44, 68, 69].

In the *Pcdhα* cluster, there is an additional CBS element located at ~700 bp downstream of the CSE within the coding region of each alternate variable exon (known as eCBS for exonic CBS) (Fig. 1A) [44, 68]. Thus, there are two CBS elements (CSE and eCBS) flanking each *Pcdhα* alternate promoter. However, there is only one CBS element (CSE) associated with the *αc1* promoter and no CBS element associated with the *αc2* promoter (Fig. 1A). Interestingly, the *HS5-1* enhancer is also flanked by two CBS elements, *HS5-1a* and *HS5-1b*, with an intervening distance similar to that between each promoter-flanking CBS pair of CSE and eCBS (Fig. 1A) [44, 68].

All of the CBS elements (CSE and eCBS) flanking the *Pcdhα* promoters are in the forward orientation. By contrast, the two CBS elements (*HS5-1a* and *HS5-1b*) flanking the *HS5-1* enhancer are in the reverse orientation (Fig. 1A). Namely, the CBS elements in the *Pcdhα* promoter and enhancer regions are in the opposite orientation [44]. Forward-oriented CBS elements flanking a *Pcdhα* promoter and reverse-oriented CBS elements flanking the *HS5-1* enhancer interact spatially to form a "double-clamp" transcription hub through CTCF/cohesin-mediated chromatin looping (Fig. 2B) [44, 71].

CTCF Site Orientation Determines the Directionality of Chromatin Looping

Inversion of the two enhancer CBS elements (*HS5-1a* and *HS5-1b*) in cells and mice by using the CRISPR/Cas9-mediated DNA fragment editing method provides strong evidence for the causality between CBS orientation and chromatin-looping directionality [45, 48]. Specifically, the reverse-oriented CBS elements flanking the *HS5-1* enhancer normally form long-distance chromatin interactions with the forward-oriented CBS elements associated with the upstream *Pcdhα* promoters (Fig. 2A, B) [44]. After inversion by CRISPR DNA-fragment editing [72, 73], however, they no longer form long-distance chromatin interactions with the upstream *Pcdhα* promoters. Strikingly, the inverted CBS elements form long-distance chromatin interactions with the downstream CBS elements [45]. Thus, the relative orientation determines the directionality of long-distance chromatin looping [45]. In addition, spatial chromatin contacts are preferentially formed between forward-reverse CBS elements through CTCF/cohesin-mediated loop extrusion throughout the entire genome [45, 47, 48, 65, 67, 74]. Finally, these experiments also provide strong *in vivo* evidence that enhancers do not function in an orientation-independent manner, at least those associated with CBS [45].

Tandem CTCF Sites as Genome Topological Insulators

In the *Pcdhβγ* clusters, only a single CTCF site is associated with each variable promoter (except *β1*, *γc4*, and *γc5*) (Fig. 1A) [44, 68, 70]. Similar to the *Pcdhα* cluster, all of the promoter CTCF sites are in the forward orientation in the *Pcdhβγ* clusters. By contrast, the downstream super-enhancer contains several reverse-oriented CTCF sites organized in tandem (Fig. 1A) [45, 46, 48].

Genetic deletion of *HS18-20* (part of the super-enhancer [46]) in mice results in a significant decrease of expression levels of the *Pcdhβ* genes [43]. In addition, deletion or inversion of *HS5-1bL* together with *HS18-20* in mice totally abolishes the expression of all *Pcdhβ* genes, suggesting that these regulatory elements, bypassing the *Pcdhγ* cluster, are enhancers for members of the *Pcdhβ* cluster [43, 47]. However, the expression levels of the *Pcdhγ* genes are mostly unaffected in these deletions, leaving the regulation of the *Pcdhγ* genes an unresolved question [43, 47].

The *Pcdhβγ* genes are topologically regulated by the tandem CTCF sites of the downstream super-enhancer. Specifically, chromosome conformation capture experiments have revealed that the *Pcdhγ* genes are in close spatial contact with the proximal CTCF sites of the super-enhancer (Fig. 2A, C). By contrast, the *Pcdhβ* genes are in close spatial contact with the distal CTCF sites of the super-enhancer (Fig. 2A, C) [48]. This topological regulation solves the long-standing mystery of *Pcdhγ* gene regulation.

These proximal-to-proximal and distal-to-distal topological chromatin regulations were further confirmed by a series of genetic manipulations of the CTCF sites in the super-enhancer *in vivo*. Specifically, when CTCF sites in the super-enhancer are deleted or inverted, the downstream reverse-oriented CTCF sites show increased chromatin interactions with members of the *Pcdhγ* cluster and decreased chromatin interactions with members of the *Pcdhβ* cluster [47, 48]. Thus, tandem CTCF sites function as topological insulators to mitigate the chromatin contacts with and usage of the proximal *Pcdhγ* promoters. In addition, these topological insulators, counter-intuitively, promote chromatin contacts with and the usage of the distal *Pcdhβ* promoters. In conclusion, tandem arrays of oriented CBS elements determine the allocation of spatial resources of enhancers for promoters of both distal and proximal *Pcdh* genes.

Epigenetic Regulation of Chromatin Loops

Methylation of the CpG dinucleotide within the CGCT box of the CTCF sites of *Pcdh* promoters precludes CTCF binding, suggesting epigenetic regulations of the clustered *Pcdh* genes [44]. In each cell, these CTCF sites are differentially methylated, with one and only one alternate exon being activated through long-range chromatin contacts with the *HS5-1* enhancer (Fig. 2B) [48, 75–77]. In the neuroblastoma cell line SK-N-SH, *Pcdhα* expression levels are inversely correlated with promoter methylation. Specifically, the CBS elements of expressed isoforms are unmethylated and bound by CTCF, but the CBS elements of silenced isoforms are methylated and devoid of CTCF proteins [44]. Consistently, demethylation of CBS elements activates *Pcdhα* gene expression [78]. Finally, recent structural analyses suggest that the addition of a methyl group at the 5th position of cytosine within the CpG interferes with the binding of CTCF zinc finger 3 to the CGCT box [79].

In neurons, the DNA methylation states of the *Pcdh* promoters are also inversely correlated with the transcription states of the *Pcdh* genes. For example, alternate *Pcdhα* genes, which are stochastically expressed by individual Purkinje cells, show mosaic and differential methylation patterns. In contrast, the C-type isoforms, which are constitutively expressed, are hypomethylated [75]. Thus, stochastic expression of *Pcdh* isoforms is probably determined by the DNA methylation in individual neurons.

Recent studies revealed that the eCBS element of each alternate exon is associated with an antisense promoter which transcribes a long non-coding RNA (lncRNA) [78]. Stochastic transcription of this lncRNA extends through the sense promoter, leading to DNA demethylation of the corresponding CBS element. This CBS demethylation then facilitates CTCF binding and subsequent activation of the sense promoter [78]. Interestingly, the promoter activation mediated by antisense lncRNA transcription is only found in alternate but not C-type *Pcdhα* genes. This is consistent with the fact that the C-type *Pcdhα* variable exons do not contain an eCBS element.

Other Potential Regulatory Proteins

In addition to the architectural proteins CTCF and cohesin, other potential 3-D genome architectural proteins have been shown to regulate expression of the clustered *Pcdh* genes. For example, a protein known as structural maintenance of chromosome hinge domain containing 1 (SMCHD1), which is critically involved in the pathogenesis of facioscapulohumeral muscular dystrophy, antagonizes CTCF in *Pcdh* gene regulation [80]. The SMCHD1 occupancy at *Pcdhα* promoters and enhancers coincides with CTCF sites. Loss of *Smchd1* results in increased CTCF binding to the *Pcdhα* alternate promoters and upregulation of *Pcdh α* and *β* gene expression [80]. However, the underlying mechanism by which SMCHD1 antagonizes CTCF DNA binding remains unknown.

SET domain bifurcated 1 (*Setdb1*) is required for the maintenance of the superTAD structure in *Pcdh* clusters [64]. Conditional knockout of *Setdb1* in forebrain neurons results in the loss of H3K9me3, leading to demethylation of DNA and subsequent recruitment of CTCF to *Pcdh* promoters [64]. The increased CTCF binding strengthens the chromatin interactions between *Pcdh* promoters and enhancers, but weakens the chromatin interactions between the boundaries of the superTAD. Neurons without *Setdb1* lose the stochastic constraint and express increased numbers of *Pcdh* isoforms [64].

Neuron-restrictive silencer factor (*NRSF*) regulates the neuron-restrictive expression of *Pcdhα* through binding to *HS5-1* and *Pcdhα* variable exons [50, 81]. In addition, Wiz (widely-interspaced zinc finger-containing protein) defines cell identity by functioning as a DNA loop anchor in collaboration with CTCF and cohesin [82]. Wiz has been shown to regulate *Pcdhβ* gene expression in mice [83]. Consistently, Wiz proteins are enriched at all of the *Pcdhβ* promoters (except *Pcdhβ1,* which is the only *Pcdhβ* gene with no CTCF site) and at the *HS5-1bL* site of the *Pcdhβγ* super-enhancer [83]. All in all, various transcription factors may regulate the stochastic expression of clustered *Pcdh*s by altering higher-order architectural chromatin loops between enhancers and promoters.

Mechanisms for Generating Clustered Pcdh Codes of Neuronal Identity

Combinatorial Expression of Pcdhs as Cell-Surface Identity Codes

Each cortical neuron stochastically expresses up to 2 alternate *Pcdhα* genes, 4 *Pcdhβ* genes, and 4 alternate *Pcdhγ* genes as well as all of the 5 C-type *Pcdh* genes (up to 15 in total) [48, 84]. These combinatorial expression patterns could generate the large number of address codes required for neuronal identity. For example, the 22 encoded Pcdhγ proteins have been predicted to form up to 234,256 distinct tetramers of cell-surface assemblies [85]. In conjunction with the encoded 15 Pcdhα and 22 Pcdhβ proteins, Pcdh proteins could generate the enormous diversity of cell-surface assemblies required for coding single neurons in the brain. We summarize the mechanisms of *Pcdh* promoter choice and expression regulation in this section.

Establishment and Maintenance of Clustered *Pcdh* Expression Patterns

A remarkable property of the clustered *Pcdh* genes is that their promoter choice is inherited and stably maintained by daughter cells as seen in the SK-N-SH cell line and differentiated neurons [44, 86]. This suggests that, once chosen, the expression patterns of clustered *Pcdh* genes are epigenetically inheritable. In addition, *Pcdh* promoter choice occurs early during the naive-to-primed conversion of ESCs (embryonic stem cells) [86]. The *Pcdh* promoters are modified with both active (H3K4me3) and repressive (H3K27me3) chromatin marks, so called bivalent promoters, in the primed ESCs before being activated. The chosen *Pcdh* genes are then stably inherited by differentiated neurons [86].

As the methylation states of promoters are inversely correlated with the expression levels of clustered *Pcdh* genes, a fundamental question is how single neurons achieve the stochastic activation of *Pcdh* promoters. On the one hand, stochastic activation of a *Pcdh* promoter could be achieved through demethylation of the chosen target promoter by antisense transcription of lncRNA [78]. On the other hand, this could be achieved through methylation of all of the non-chosen promoters [75]. Consistently, all of the *Pcdhα* alternate promoters are enriched with CTCF in naive ESCs, while only chosen promoters are enriched with CTCF in primed ESCs [86], suggesting hypomethylation-to-hypermethylation conversion of the non-chosen promoters during cellular differentiation. This indicates that the ground state of *Pcdh* promoters is unmethylated or hypomethylated and that the activation of specific promoters requires methylation of all of the other promoters (Fig. 3A, B).

Cell-Specific and Stochastic Expression of Clustered *Pcdh* Genes

Clustered *Pcdhs* are widely expressed in the developing and adult central nervous systems [11, 34, 35, 42, 53, 87–90]. The expression of members of the *Pcdhα* cluster is highly specific to the central nervous system. While members of the *Pcdh β* and *γ* clusters are prominently expressed in the central nervous system, they are also expressed in several other tissues such as the kidney and lung [87, 89, 91]. Detailed expression patterns of each isoform were initially analyzed by *in situ* hybridization using isoform-specific probes, which showed that they are stochastically expressed in neuronal subpopulations in various brain nuclei or regions [35, 42, 53, 89, 90, 92].

Single Purkinje neurons express alternate members of clustered *Pcdh* genes in a stochastic and monoallelic manner (Fig. 3C) [92–94]. In addition, single cortical neurons also express alternate members of the three *Pcdh* clusters in a similar manner [48, 75, 84]. In the *Pcdhα* cluster, each tandem pair of the promoter CTCF sites (CSE and eCBS) functions as an insulator for all of its upstream *Pcdhα* genes. A single chromatin loop between the *HS5-1* enhancer and a variable promoter determines the expression of the chosen *Pcdhα* gene in each allele (Fig. 2A, B) [48].

In the *Pcdhβγ* clusters, the super-enhancer is composed of four CBS-containing elements. Up to two *Pcdhβ* genes (activated by enhancers with CTCF sites "*de*" and "*fgh*") and two alternate *Pcdhγ* genes (activated by enhancers with CTCF sites "*a*" and "*bc*") could be expressed from each allele through nested chromatin loops (Fig. 2A, C) [48].

In olfactory sensory neurons (OSNs), clustered *Pcdh* genes are stochastically expressed, except for the C-types (Fig. 3D) [76]. In addition, diploid chromatin conformation capture of single OSNs has shown that there are significant cell-to-cell heterogeneities of *Pcdh* chromatin architectures and that *Pcdh* enhancers communicate with distinct *Pcdh* promoters in different cells [95]. This may reflect the stochastic *Pcdh* promoter choice. Specifically, each OSN expresses a distinct set of up to 10 alternate *Pcdh* genes, among which 5 are stochastically and monoallelically expressed from each allele (Fig. 2). In summary, these findings suggest that the clustered *Pcdh* genes are stochastically expressed in single neurons of the cerebellum, cerebrum, and olfactory epithelium in a cell-specific manner.

Cell Type-Specific Expression of Clustered *Pcdh* Genes

All of the C-type *Pcdh* genes appear to be constitutively and biallelically expressed in single neurons of the cerebellum and cerebrum in the mouse brain (Fig. 3B, C) [48, 75, 84, 92–94]. By contrast, none of the C-type *Pcdh* genes is expressed in mouse OSNs (Fig. 3D) [76]. Finally, only *Pcdhαc2* is predominantly expressed in serotonergic neurons (Fig. 3E) [96, 97]. Collectively, these studies suggest that C-type *Pcdh* genes are expressed in a cell-type-specific manner, in stark contrast to the stochastic expression of alternate *Pcdh* genes in the brain.

Molecular Logic of Neuronal Self-avoidance and Coexistence

Promiscuous *Cis*-interactions for Diverse Cell-Surface Assemblies

The Pcdhα proteins co-immunoprecipitate with Pcdhγ in cell lysates. In addition, cell-surface delivery of Pcdhα proteins (except for Pcdhαc2) requires the co-expression of Pcdhγ because Pcdhα alone cannot be sufficiently

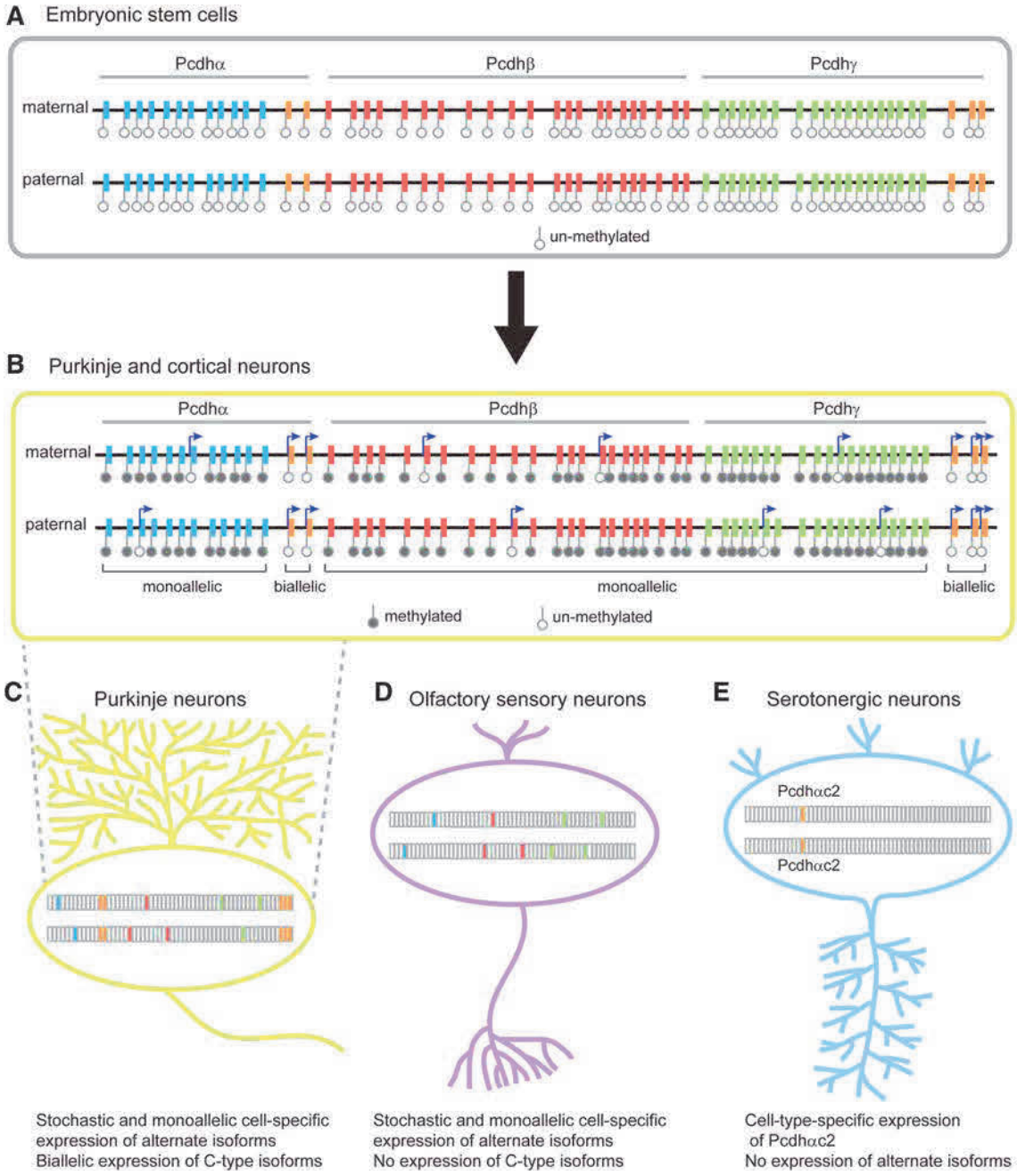

Fig. 3 Cell-specific and cell-type-specific expression of clustered *Pcdh* genes. **A** In embryonic stem cells, the ground state of clustered *Pcdh* gene promoters is unmethylated. **B** Gene regulation of the three *Pcdh* clusters by DNA methylation in mature neurons such as Purkinje and cortical cells. **C** In the Purkinje neurons of the cerebellum, alternate genes are stochastically and monoallelically expressed in a cell-specific manner, while C-type genes are constitutively and biallelically expressed presumably in every cell. **D** In olfactory sensory neurons, alternate genes are stochastically and monoallelically expressed in a cell-specific manner, while the C-type genes are not expressed. **E** In serotonergic neurons in the raphe nuclei of the midbrain, only *Pcdhαc2* is expressed in a cell-type-specific manner.

expressed at the plasma membrane [12, 98], suggesting that Pcdhα and Pcdhγ may form heterodimers. Moreover, distinct members interact with each other in membrane fractions [85, 99]. Finally, each member of Pcdhβ or Pcdhγ (except for Pcdhγc4) can form homodimers or heterodimers; however, members of Pcdhα and Pcdhγc4 cannot form homodimers. They can only form heterodimers with Pcdhβ or other Pcdhγ isoforms [12, 100].

Structural studies support the formation of *cis*-homodimers or *cis*-heterodimers between isoforms of clustered Pcdhs. The *cis*-dimerization requires both EC5 and EC6 domains [13, 60, 101]. Specifically, the Pcdh *cis*-dimer

interfaces are asymmetric, with one molecule providing the EC5 and EC6 side of the interface, and the other providing only the EC6 side (Fig. 4A) [13, 60]. Isoforms of Pcdhβ and Pcdhγ (except for Pcdhγc4) form *cis*-homodimers or *cis*-heterodimers in that each isoform can participate as either the EC5–EC6 or EC6 side of the interface [13, 60]. However, isoforms of Pcdhα and Pcdhγc4 can only form *cis*-heterodimers and cannot form *cis*-homodimers because they cannot participate as the EC6 side of the interface. Namely, they participate only as the EC5–EC6 side of the heterodimer interface. They need isoforms of either Pcdhβ or Pcdhγ (also known as carrier isoforms, except for Pcdhγc4) to provide the EC6 side of the heterodimer interface [60].

In summary, clustered Pcdh isoforms appear as a cell-surface repertoire composed of homodimers and promiscuous heterodimers of members of all three Pcdh clusters on the plasma membrane of single neurons [12, 13, 60, 85, 100].

Homophilic *Trans*-interactions for Self-recognition

Great progress has been made in deciphering the *trans*-interactions of clustered Pcdh proteins for generating cell-recognition specificity. The *trans*-interactions of the Pcdh isoforms have been tested using an efficient cell-aggregation assay by transfecting two cell populations [12, 85, 101]. Different cell populations expressing the same combinations of Pcdh isoforms display strict homophilic interactions and can form cell aggregates, but those expressing different combinations of Pcdh isoforms cannot [12].

All of the clustered Pcdh β and γ isoforms, except for Pcdhγc4, can engage in robust and highly specific *trans*-homophilic interactions in cell aggregation assays. These isoforms are delivered to cell membrane, probably because they can form *cis*-homodimers [60]. Pcdhα (except for Pcdhαc2) and Pcdhγc4, on the other hand, cannot form *cis*-homodimers and cannot be delivered to cell membrane by themselves. Therefore, they cannot induce cell aggregates [12]. Pcdhαc2, however, is unique in that it can induce cell aggregates by itself because it can form *cis*-homodimers and be delivered to cell membrane [12].

The Pcdhα proteins can form *cis*-heterodimers with isoforms of Pcdh β and γ (except for Pcdhγc4). They can be delivered to cell membrane when they are co-expressed with Pcdh β or γ isoforms. Therefore, Pcdhα (except for Pcdhαc1) does induce cell aggregates through homophilic *trans*-interactions when co-expressed with Pcdh β and γ isoforms (except for Pcdhγc4). Finally, homophilic interactions are abolished when there is a single mismatched isoform between the two transfected cell populations [12].

Structural analyses revealed that the *trans*-homophilic interactions are mediated by EC1–EC4 in an antiparallel manner. These *trans*-interactions form a zipper-like ribbon structure in apposed plasma membranes. Specifically, the EC1, EC2, EC3, and EC4 of one isoform at a cell surface interact with the EC4, EC3, EC2, and EC1 of the same isoform from the apposed cell surface, respectively [13, 101–105]. Among the six EC domains of clustered Pcdhs, EC2 and EC3 have been positively selected for diversity during evolution and are thus the most diversified ECs in amino-acid residues [52]. Consistently, they determine the stringent specificity of *trans*-homophilic interactions [12, 85, 104].

The Chain-Termination Model for Non-self Discrimination

The crystal structure of the full-length extracellular domain of Pcdhγb4 reveals a zipper-like lattice through *cis*-interactions mediated by EC5–EC6/EC6 and *trans*-interactions mediated by EC1–EC4 [13]. When tethered to liposomes, Pcdh extracellular domains spontaneously assemble into zipper-like linear arrays through *trans*-homophilic interactions between Pcdh dimers [13]. These linear assemblies extend through the contacted membranes as a chain to form a larger lattice (Fig. 4B). In this chain termination model, once a certain size threshold is reached, the assemblies trigger intracellular Pcdh signaling pathways to regulate various cellular behaviors such as repulsion. By contrast, when mismatched isoforms are incorporated, the Pcdh chain extension terminates and the lattice size cannot reach the presumed signaling threshold (Fig. 4B) [13, 101]. This isoform-mismatch chain-termination model can explain the recognition initiation process of self and non-self discrimination mediated by the extracellular domains of clustered Pcdhs.

Intracellular Signaling of Clustered Pcdhs Leads to Cytoskeletal Rearrangement and Morphological Remodeling

The intracellular domains of the Pcdhα and Pcdhγ isoforms contain a respective common membrane-distal region encoded by constant exons that is shared by all isoforms from the same cluster [11, 14]. The Pcdhα and Pcdhγ isoforms are cleaved by metalloproteinase and subsequently by γ-secretase to generate a soluble extracellular fragment and an intracellular fragment that may function locally or translocate into the cell nucleus [106–109]. This proteolytic process requires endocytosis and is regulated during animal development and neuronal differentiation [110].

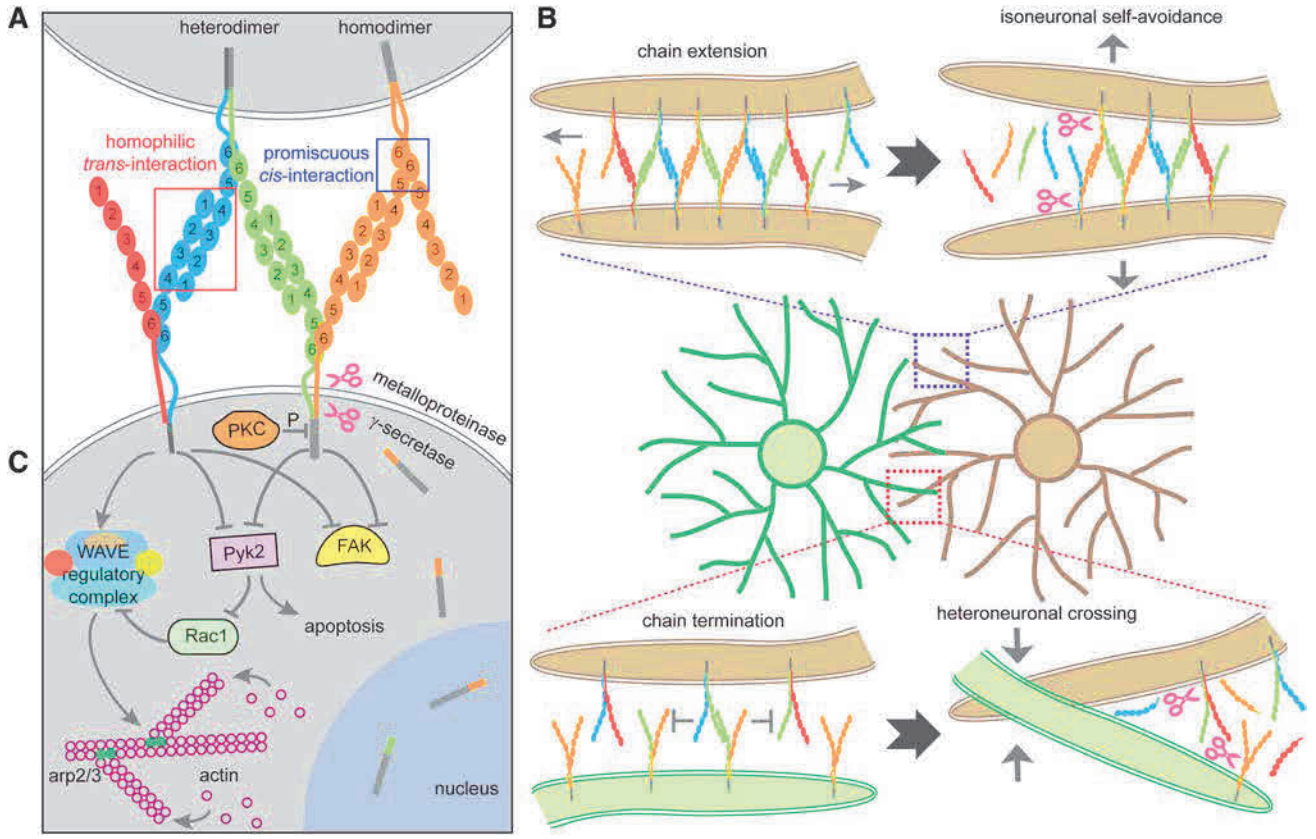

Fig. 4 The molecular basis of self-recognition for self-avoidance and non-self coexistence mediated by clustered Pcdhs. **A** Clustered Pcdh isoforms form heterodimers and homodimers in the cell membrane through promiscuous *cis*-interactions between the EC5–EC6 domains of one isoform and the EC6 domain of the other isoform to endow each cell with an identity code. Clustered Pcdh isoforms from different neurites recognize each other through strict homophilic *trans*-interactions of the EC1–EC4 domains in an anti-parallel fashion. **B** Molecular arrangements of an extended self-recognition complex between identical combinatorial profiles expressed on the same neuron, resulting in adhesion-mediated repulsion between sister neurites from single neurons (isoneuronal self-avoidance). Specifically, when the expressed isoforms are the same between two neurites (from the same cell, for example), Pcdh isoforms linearly assemble into parallel arrays through *cis*- and *trans*-interactions to form larger zipper-like lattices between membranes. These structures trigger intracellular signaling and cytoskeletal rearrangement. Subsequent Pcdh cleavage may result in neurite self-avoidance. By contrast, when the two neurites from different neurons stochastically express distinct combinations of Pcdh isoforms, their assembly is interrupted by the mismatched isoforms, as proposed by the isoform-mismatch chain-termination model. This results in heteroneuronal crossing and coexistence. **C** Intracellular signaling of the clustered Pcdhs. Pcdh isoforms are cleaved by metalloproteinase and γ-secretase into an extracellular fragment and an intracellular fragment. The latter may translocate into the nucleus to regulate gene transcription. PKC phosphorylates the intracellular domain of Pcdhγ. Isoforms of *Pcdh* α and γ clusters bind and inhibit the activities of Pyk2 and FAK through the Pcdh intracellular domain. The intracellular domain of Pcdhα isoforms recruits the WAVE complex through the WIRS motif and activates actin-filament branching. Pyk2 also inhibits Rac1 and disinhibits the WAVE complex. These intracellular signaling pathways eventually lead to cytoskeletal remodeling and sister-neurite repulsion.

The Pcdhα and Pcdhγ proteins can bind and inhibit two cell-adhesion kinases, FAK (focal adhesion kinase) and Pyk2 (proline-rich tyrosine kinase 2), through the cytoplasmic domain (Fig. 4C) [111]. In the mouse hippocampus and cortex, Pcdhα and Pcdhγ regulate dendritic arborization and spine morphogenesis through inhibiting Pyk2 and FAK activity [112–114]. Knockout or knockdown of *Pcdhα* in hippocampal neurons results in the phosphorylation and activation of Pyk2 [113]. The activation of Pyk2 inhibits Rac1, leading to defects in dendritic and spine morphogenesis. Consistently, knockdown of *Pyk2* or overexpression of *Rac1* rescues the phenotype caused by *Pcdh* α or γ knockdown [113]. *Pcdhγ* knockout induces extensive neuronal apoptosis in the spinal cord [6], which could be related to aberrantly up-regulated Pyk2 activity. Consistent with this, over expression of Pyk2 also induces apoptosis [111]. Together, these data suggest that diverse extracellular signals acting on different Pcdhα and Pcdhγ isoforms converge into the same intracellular pathways through common downstream effectors of Pyk2 and FAK (Fig. 4C).

The common intracellular domain of Pcdhα isoforms, but not Pcdhγ isoforms, contains a conserved peptide WIRS (WAVE-interacting receptor sequence) motif that

interacts with the WAVE (Wiskott-Aldrich syndrome family verprolin homologous protein) regulatory complex (WRC) to modulate cytoplasmic actin assembly (Fig. 1B) [115, 116]. Specifically, Pcdhα isoforms (except for Pcdhαc2) regulate cytoskeletal dynamics during cortical neuron migration and dendrite morphogenesis through the WAVE regulatory complex (Fig. 4C) [116]. Overexpression of Pcdhα isoforms (except for Pcdhαc2) rescues the migration defects caused by *Pcdhα* knockdown and the rescue is abolished by WIRS mutation. In addition, overexpression of WRC subunits also rescues the migration defects of *Pcdhα* knockdown [116]. Given that Pcdhα forms *cis*-heterodimers with Pcdh β or γ on the cell surface (Fig. 4A), the Pcdh β and γ isoforms may also modulate the WAVE complex through interacting with Pcdhα (Fig. 4C). Specifically, Pcdh β and γ proteins, together with Pcdhα, may regulate neuronal morphogenesis and dendrite self-avoidance through WAVE dynamics and cytoskeletal rearrangements (Fig. 4C). In summary, the establishment and maintenance of neuronal connectivity and self-avoidance likely require coordinated collaborations between members of all three *Pcdh* gene clusters.

Concluding Remarks and Future Perspectives

In the central nervous system, individual neurons stochastically express combinatorial sets of clustered Pcdhs. These Pcdh expression profiles constitute diverse cell-surface identity codes through *cis*-promiscuous pairing and discriminate self from non-self through strict *trans*-homophilic interactions. Their tremendous diversity is generated by intriguing 3-D genome architecture, stochastic promoter choice balanced by topological insulators, long-range spatial chromatin contacts between distal enhancers and target promoters, and alternative splicing.

Elucidating the regulatory mechanisms of clustered *Pcdhs* in different cell types throughout the nervous system will be of great importance in deciphering the molecular basis underlying neural-circuit coding. Several lines of investigation of the *Pcdh* clusters have provided deep insights into various aspects of gene expression mechanisms, from 1-D genomic organization to 2-D epigenetic regulation and 3-D chromatin architecture. However, many important questions remain unanswered. For example, when are Pcdh isoforms chosen to be expressed in neuronal progenitor cells during brain development? What is the mechanistic basis for the epigenetic memory of clustered *Pcdh* expression profiles? What are the mechanistic differences between the regulation of expression of alternate and C-type isoforms? How do serotonergic neurons selectively express only the *Pcdhαc2* gene in a cell-type-specific manner? Finally, how do clustered Pcdhs collaborate with other families of cell-adhesion proteins to specify synaptic connectivity? Answering these questions about neural coding mechanisms in the brain requires interdisciplinary endeavors in the future.

Acknowledgements We thank Drs J. Li and J. Shou, and other members of our laboratory for critical reading and discussion. This work was supported by Grants from the National Natural Science Foundation of China (31630039 and 31700666), the Ministry of Science and Technology of China (2017YFA0504203 and 2018YFC1004504), and the Science and Technology Commission of Shanghai Municipality (19JC1412500).

Conflict of interest The authors declare that they have no conflict of interest.

References

1. Südhof TC. Synaptic neurexin complexes: a molecular code for the logic of neural circuits. Cell 2017, 171: 745–769.
2. Buck L, Axel R. A novel multigene family may encode odorant receptors: a molecular basis for odor recognition. Cell 1991, 65: 175–187.
3. Hynes RO. Cell adhesion: old and new questions. Trends Cell Biol 1999, 9: M33–M37.
4. Shapiro L, Colman DR. The diversity of cadherins and implications for a synaptic adhesive code in the CNS. Neuron 1999, 23: 427–430.
5. Honig B, Shapiro L. Adhesion protein structure, molecular affinities, and principles of cell-cell recognition. Cell 2020, 181: 520–535.
6. Sanes JR, Zipursky SL. Synaptic specificity, recognition molecules, and assembly of neural circuits. Cell 2020, 181: 536–556.
7. Schmucker D, Clemens JC, Shu H, Worby CA, Xiao J, Muda M, *et al*. *Drosophila* Dscam is an axon guidance receptor exhibiting extraordinary molecular diversity. Cell 2000, 101: 671–684.
8. Neves G, Zucker J, Daly M, Chess A. Stochastic yet biased expression of multiple Dscam splice variants by individual cells. Nat Genet 2004, 36: 240–246.
9. Wojtowicz WM, Flanagan JJ, Millard SS, Zipursky SL, Clemens JC. Alternative splicing of *Drosophila* Dscam generates axon guidance receptors that exhibit isoform-specific homophilic binding. Cell 2004, 118: 619–633.
10. Jin Y, Li H. Revisiting Dscam diversity: lessons from clustered protocadherins. Cell Mol Life Sci 2019, 76: 667–680.
11. Wu Q, Maniatis T. A striking organization of a large family of human neural cadherin-like cell adhesion genes. Cell 1999, 97: 779–790.

12. Thu CA, Chen WV, Rubinstein R, Chevee M, Wolcott HN, Felsovalyi KO, *et al.* Single-cell identity generated by combinatorial homophilic interactions between alpha, beta, and gamma protocadherins. Cell 2014, 158: 1045–1059.
13. Brasch J, Goodman KM, Noble AJ, Rapp M, Mannepalli S, Bahna F, *et al.* Visualization of clustered protocadherin neuronal self-recognition complexes. Nature 2019, 569: 280–283.
14. Wu Q, Maniatis T. Large exons encoding multiple ectodomains are a characteristic feature of protocadherin genes. Proc Natl Acad Sci U S A 2000, 97: 3124–3129.
15. Ying G, Wu S, Hou R, Huang W, Capecchi MR, Wu Q. The protocadherin gene Celsr3 is required for interneuron migration in the mouse forebrain. Mol Cell Biol 2009, 29: 3045–3061.
16. Jia Z, Guo Y, Tang Y, Xu Q, Li B, Wu Q. Regulation of the protocadherin Celsr3 gene and its role in globus pallidus development and connectivity. Mol Cell Biol 2014, 34: 3895–3910.
17. Frank M, Kemler R. Protocadherins. Curr Opin Cell Biol 2002, 14: 557–562.
18. Zhang T, Haws P, Wu Q. Multiple variable first exons: a mechanism for cell- and tissue-specific gene regulation. Genom Res 2004, 14: 79–89.
19. Zipursky SL, Grueber WB. The molecular basis of self-avoidance. Annu Rev Neurosci 2013, 36: 547–568.
20. Hirayama T, Yagi T. Regulation of clustered protocadherin genes in individual neurons. Semin Cell Dev Biol 2017, 69: 122–130.
21. Lefebvre JL. Neuronal territory formation by the atypical cadherins and clustered protocadherins. Semin Cell Dev Biol 2017, 69: 111–121.
22. Peek SL, Mah KM, Weiner JA. Regulation of neural circuit formation by protocadherins. Cell Mol Life Sci 2017, 74: 4133–4157.
23. Rubinstein R, Goodman KM, Maniatis T, Shapiro L, Honig B. Structural origins of clustered protocadherin-mediated neuronal barcoding. Semin Cell Dev Biol 2017, 69: 140–150.
24. Mountoufaris G, Canzio D, Nwakeze CL, Chen WV, Maniatis T. Writing, reading, and translating the clustered protocadherin cell surface recognition code for neural circuit assembly. Annu Rev Cell Dev Biol 2018, 34: 471–493.
25. Canzio D, Maniatis T. The generation of a protocadherin cell-surface recognition code for neural circuit assembly. Curr Opin Neurobiol 2019, 59: 213–220.
26. Watson JD, Crick FH. Molecular structure of nucleic acids; a structure for deoxyribose nucleic acid. Nature 1953, 171: 737–738.
27. Nirenberg MW, Matthaei JH. The dependence of cell-free protein synthesis in *E. coli* upon naturally occurring or synthetic polyribonucleotides. Proc Natl Acad Sci U S A 1961, 47: 1588–1602.
28. Sperry RW. Chemoaffinity in the orderly growth of nerve fiber patterns and connections. Proc Natl Acad Sci 1963, 50: 703–710.
29. Trisler GD, Schneider MD, Nirenberg M. A topographic gradient of molecules in retina can be used to identify neuron position. Proc Natl Acad Sci U S A 1981, 78: 2145–2149.
30. Edelman GM. Cell adhesion molecules. Science 1983, 219: 450–457.
31. Takeichi M. Functional correlation between cell adhesive properties and some cell surface proteins. J Cell Biol 1977, 75: 464–474.
32. Li H, Zeng J, Huang L, Wu D, Liu L, Liu Y, *et al.* Microarray analysis of gene expression changes in Neuroplastin 65-knockout mice: implications for abnormal cognition and emotional disorders. Neurosci Bull 2018, 34: 779–788.
33. Takeichi M. Morphogenetic roles of classic cadherins. Curr Opin Cell Biol 1995, 7: 619–627.
34. Sano K, Tanihara H, Heimark RL, Obata S, Davidson M, St John T, *et al.* Protocadherins: a large family of cadherin-related molecules in central nervous system. EMBO J 1993, 12: 2249–2256.
35. Kohmura N, Senzaki K, Hamada S, Kai N, Yasuda R, Watanabe M, *et al.* Diversity revealed by a novel family of cadherins expressed in neurons at a synaptic complex. Neuron 1998, 20: 1137–1151.
36. Chun J. Developmental neurobiology: a genetic Cheshire cat? Curr Biol 1999, 9: R651–R654.
37. Mombaerts P. Digging for gold in the human genome. Nat Neurosci 1999, 2: 686–687.
38. Serafini T. Finding a partner in a crowd: neuronal diversity and synaptogenesis. Cell 1999, 98: 133–136.
39. Itzkovitz S, Baruch L, Shapiro E, Segal E. Geometric constraints on neuronal connectivity facilitate a concise synaptic adhesive code. Proc Natl Acad Sci U S A 2008, 105: 9278–9283.
40. Wu Q, Zhang T, Cheng JF, Kim Y, Grimwood J, Schmutz J, *et al.* Comparative DNA sequence analysis of mouse and human protocadherin gene clusters. Genom Res 2001, 11: 389–404.
41. Tasic B, Nabholz CE, Baldwin KK, Kim Y, Rueckert EH, Ribich SA, *et al.* Promoter choice determines splice site selection in protocadherin alpha and gamma pre-mRNA splicing. Mol Cell 2002, 10: 21–33.
42. Wang X, Su H, Bradley A. Molecular mechanisms governing Pcdh-gamma gene expression: evidence for a multiple promoter and cis-alternative splicing model. Genes Dev 2002, 16: 1890–1905.
43. Yokota S, Hirayama T, Hirano K, Kaneko R, Toyoda S, Kawamura Y, *et al.* Identification of the cluster control region for the protocadherin-beta genes located beyond the protocadherin-gamma cluster. J Biol Chem 2011, 286: 31885–31895.
44. Guo Y, Monahan K, Wu H, Gertz J, Varley KE, Li W, *et al.* CTCF/cohesin-mediated DNA looping is required for protocadherin alpha promoter choice. Proc Natl Acad Sci U S A 2012, 109: 21081–21086.
45. Guo Y, Xu Q, Canzio D, Shou J, Li J, Gorkin DU, *et al.* CRISPR inversion of CTCF sites alters genome topology and enhancer/promoter function. Cell 2015, 162: 900–910.
46. Zhai YN, Xu Q, Guo Y, Wu Q. Characterization of a cluster of CTCF-binding sites in a protocadherin regulatory region. Yi Chuan 2016, 38: 323–336.
47. Lu Y, Shou J, Jia Z, Wu Y, Li J, Guo Y, *et al.* Genetic evidence for asymmetric blocking of higher-order chromatin structure by CTCF/cohesin. Protein Cell 2019, 10: 914–920.
48. Jia Z, Li J, Ge X, Wu Y, Guo Y, Wu Q. Tandem CTCF sites function as insulators to balance spatial chromatin contacts and topological enhancer-promoter selection. Genom Biol 2020, 21: 75.
49. Ribich S, Tasic B, Maniatis T. Identification of long-range regulatory elements in the protocadherin-alpha gene cluster. Proc Natl Acad Sci U S A 2006, 103: 19719–19724.
50. Kehayova P, Monahan K, Chen W, Maniatis T. Regulatory elements required for the activation and repression of the protocadherin-alpha gene cluster. Proc Natl Acad Sci U S A 2011, 108: 17195–17200.
51. Rubin GM, Yandell MD, Wortman JR, Gabor Miklos GL, Nelson CR, Hariharan IK, *et al.* Comparative genomics of the eukaryotes. Science 2000, 287: 2204–2215.
52. Wu Q. Comparative genomics and diversifying selection of the clustered vertebrate protocadherin genes. Genetics 2005, 169: 2179–2188.

53. Zou C, Huang W, Ying G, Wu Q. Sequence analysis and expression mapping of the rat clustered protocadherin gene repertoires. Neuroscience 2007, 144: 579–603.
54. Noonan JP, Grimwood J, Schmutz J, Dickson M, Myers RM. Gene conversion and the evolution of protocadherin gene cluster diversity. Genom Res 2004, 14: 354–366.
55. Noonan JP, Grimwood J, Danke J, Schmutz J, Dickson M, Amemiya CT, *et al.* Coelacanth genome sequence reveals the evolutionary history of vertebrate genes. Genom Res 2004, 14: 2397–2405.
56. Tada MN, Senzaki K, Tai Y, Morishita H, Tanaka YZ, Murata Y, *et al.* Genomic organization and transcripts of the zebrafish Protocadherin genes. Gene 2004, 340: 197–211.
57. Yu WP, Yew K, Rajasegaran V, Venkatesh B. Sequencing and comparative analysis of fugu protocadherin clusters reveal diversity of protocadherin genes among teleosts. BMC Evol Biol 2007, 7: 49.
58. Jiang XJ, Li S, Ravi V, Venkatesh B, Yu WP. Identification and comparative analysis of the protocadherin cluster in a reptile, the green anole lizard. PLoS One 2009, 4: e7614.
59. Etlioglu HE, Sun W, Huang Z, Chen W, Schmucker D. Characterization of a single genomic locus encoding the clustered protocadherin receptor diversity in *Xenopus tropicalis*. G3 (Bethesda) 2016, 6: 2309–2318.
60. Goodman KM, Rubinstein R, Dan H, Bahna F, Mannepalli S, Ahlsen G, *et al.* Protocadherin cis-dimer architecture and recognition unit diversity. Proc Natl Acad Sci U S A 2017, 114: E9829–E9837.
61. Yu WP, Rajasegaran V, Yew K, Loh WL, Tay BH, Amemiya CT, *et al.* Elephant shark sequence reveals unique insights into the evolutionary history of vertebrate genes: a comparative analysis of the protocadherin cluster. Proc Natl Acad Sci U S A 2008, 105: 3819–3824.
62. Albertin CB, Simakov O, Mitros T, Wang ZY, Pungor JR, Edsinger-Gonzales E, *et al.* The octopus genome and the evolution of cephalopod neural and morphological novelties. Nature 2015, 524: 220–224.
63. Styfhals R, Seuntjens E, Simakov O, Sanges R, Fiorito G. In silico Identification and expression of protocadherin gene family in octopus vulgaris. Front Physiol 2018, 9: 1905.
64. Jiang Y, Loh YE, Rajarajan P, Hirayama T, Liao W, Kassim BS, *et al.* The methyltransferase SETDB1 regulates a large neuron-specific topological chromatin domain. Nat Genet 2017, 49: 1239–1250.
65. Nichols MH, Corces VG. A CTCF code for 3D genome architecture. Cell 2015, 162: 703–705.
66. Sanborn AL, Rao SS, Huang SC, Durand NC, Huntley MH, Jewett AI, *et al.* Chromatin extrusion explains key features of loop and domain formation in wild-type and engineered genomes. Proc Natl Acad Sci U S A 2015, 112: E6456–E6465.
67. Fudenberg G, Imakaev M, Lu C, Goloborodko A, Abdennur N, Mirny LA. Formation of chromosomal domains by loop extrusion. Cell Rep 2016, 15: 2038–2049.
68. Monahan K, Rudnick ND, Kehayova PD, Pauli F, Newberry KM, Myers RM, *et al.* Role of CCCTC binding factor (CTCF) and cohesin in the generation of single-cell diversity of protocadherin–alpha gene expression. Proc Natl Acad Sci U S A 2012, 109: 9125–9130.
69. Golan-Mashiach M, Grunspan M, Emmanuel R, Gibbs-Bar L, Dikstein R, Shapiro E. Identification of CTCF as a master regulator of the clustered protocadherin genes. Nucl Acids Res 2012, 40: 3378–3391.
70. Hirayama T, Tarusawa E, Yoshimura Y, Galjart N, Yagi T. CTCF is required for neural development and stochastic expression of clustered Pcdh genes in neurons. Cell Rep 2012, 2: 345–357.
71. Allahyar A, Vermeulen C, Bouwman BAM, Krijger PHL, Verstegen M, Geeven G, *et al.* Enhancer hubs and loop collisions identified from single-allele topologies. Nat Genet 2018, 50: 1151–1160.
72. Li J, Shou J, Guo Y, Tang Y, Wu Y, Jia Z, *et al.* Efficient inversions and duplications of mammalian regulatory DNA elements and gene clusters by CRISPR/Cas9. J Mol Cell Biol 2015, 7: 284–298.
73. Shou J, Li J, Liu Y, Wu Q. Precise and predictable CRISPR chromosomal rearrangements reveal principles of Cas9-mediated nucleotide insertion. Mol Cell 2018, 71: 498–509 e494.
74. Rao SS, Huntley MH, Durand NC, Stamenova EK, Bochkov ID, Robinson JT, *et al.* A 3D map of the human genome at kilobase resolution reveals principles of chromatin looping. Cell 2014, 159: 1665–1680.
75. Toyoda S, Kawaguchi M, Kobayashi T, Tarusawa E, Toyama T, Okano M, *et al.* Developmental epigenetic modification regulates stochastic expression of clustered protocadherin genes, generating single neuron diversity. Neuron 2014, 82: 94–108.
76. Mountoufaris G, Chen WV, Hirabayashi Y, O'Keeffe S, Chevee M, Nwakeze CL, *et al.* Multicluster Pcdh diversity is required for mouse olfactory neural circuit assembly. Science 2017, 356: 411–414.
77. Wada T, Wallerich S, Becskei A. Stochastic gene choice during cellular differentiation. Cell Rep 2018, 24: 3503–3512.
78. Canzio D, Nwakeze CL, Horta A, Rajkumar SM, Coffey EL, Duffy EE, *et al.* Antisense lncRNA transcription mediates DNA demethylation to drive stochastic protocadherin alpha promoter choice. Cell 2019, 177: 639–653 e615.
79. Yin M, Wang J, Wang M, Li X, Zhang M, Wu Q, *et al.* Molecular mechanism of directional CTCF recognition of a diverse range of genomic sites. Cell Res 2017, 27: 1365–1377.
80. Chen K, Hu J, Moore DL, Liu R, Kessans SA, Breslin K, *et al.* Genome-wide binding and mechanistic analyses of Smchd1-mediated epigenetic regulation. Proc Natl Acad Sci U S A 2015, 112: E3535–E3544.
81. Tan YP, Li S, Jiang XJ, Loh W, Foo YK, Loh CB, *et al.* Regulation of protocadherin gene expression by multiple neuron-restrictive silencer elements scattered in the gene cluster. Nucl Acids Res 2010, 38: 4985–4997.
82. Justice M, Carico ZM, Stefan HC, Dowen JM. A WIZ/cohesin/CTCF complex anchors DNA loops to define gene expression and cell identity. Cell Rep 2020, 31: 107503.
83. Isbel L, Prokopuk L, Wu H, Daxinger L, Oey H, Spurling A, *et al.* Wiz binds active promoters and CTCF-binding sites and is required for normal behaviour in the mouse. Elife 2016, 5: e15082.
84. Tasic B, Yao Z, Graybuck LT, Smith KA, Nguyen TN, Bertagnolli D, *et al.* Shared and distinct transcriptomic cell types across neocortical areas. Nature 2018, 563: 72–78.
85. Schreiner D, Weiner JA. Combinatorial homophilic interaction between gamma-protocadherin multimers greatly expands the molecular diversity of cell adhesion. Proc Natl Acad Sci U S A 2010, 107: 14893–14898.
86. Almenar-Queralt A, Merkurjev D, Kim HS, Navarro M, Ma Q, Chaves RS, *et al.* Chromatin establishes an immature version of neuronal protocadherin selection during the naive-to-primed conversion of pluripotent stem cells. Nat Genet 2019, 51: 1691–1701.
87. Kallenbach S, Khantane S, Carroll P, Gayet O, Alonso S, Henderson CE, *et al.* Changes in subcellular distribution of protocadherin gamma proteins accompany maturation of spinal neurons. J Neurosci Res 2003, 72: 549–556.
88. Phillips GR, Tanaka H, Frank M, Elste A, Fidler L, Benson DL, *et al.* Gamma-protocadherins are targeted to subsets of synapses

and intracellular organelles in neurons. J Neurosci 2003, 23: 5096–5104.
89. Frank M, Ebert M, Shan W, Phillips GR, Arndt K, Colman DR, *et al.* Differential expression of individual gamma-protocadherins during mouse brain development. Mol Cell Neurosci 2005, 29: 603–616.
90. Miralles CP, Taylor MJ, Bear J, Jr., Fekete CD, George S, Li Y, *et al.* Expression of protocadherin-gammaC4 protein in the rat brain. J Comput Neurol 2020, 528: 840–864.
91. Dallosso AR, Hancock AL, Szemes M, Moorwood K, Chilukamarri L, Tsai HH, *et al.* Frequent long-range epigenetic silencing of protocadherin gene clusters on chromosome 5q31 in Wilms' tumor. PLoS Genet 2009, 5: e1000745.
92. Hirano K, Kaneko R, Izawa T, Kawaguchi M, Kitsukawa T, Yagi T. Single-neuron diversity generated by Protocadherin-beta cluster in mouse central and peripheral nervous systems. Front Mol Neurosci 2012, 5: 90.
93. Esumi S, Kakazu N, Taguchi Y, Hirayama T, Sasaki A, Hirabayashi T, *et al.* Monoallelic yet combinatorial expression of variable exons of the protocadherin-alpha gene cluster in single neurons. Nat Genet 2005, 37: 171–176.
94. Kaneko R, Kato H, Kawamura Y, Esumi S, Hirayama T, Hirabayashi T, *et al.* Allelic gene regulation of Pcdh-alpha and Pcdh-gamma clusters involving both monoallelic and biallelic expression in single Purkinje cells. J Biol Chem 2006, 281: 30551–30560.
95. Tan L, Xing D, Daley N, Xie XS. Three-dimensional genome structures of single sensory neurons in mouse visual and olfactory systems. Nat Struct Mol Biol 2019, 26: 297–307.
96. Chen WV, Nwakeze CL, Denny CA, O'Keeffe S, Rieger MA, Mountoufaris G, *et al.* Pcdhalphac2 is required for axonal tiling and assembly of serotonergic circuitries in mice. Science 2017, 356: 406–411.
97. Katori S, Noguchi-Katori Y, Okayama A, Kawamura Y, Luo W, Sakimura K, *et al.* Protocadherin-alphaC2 is required for diffuse projections of serotonergic axons. Sci Rep 2017, 7: 15908.
98. Murata Y, Hamada S, Morishita H, Mutoh T, Yagi T. Interaction with protocadherin-gamma regulates the cell surface expression of protocadherin-alpha. J Biol Chem 2004, 279: 49508–49516.
99. Han MH, Lin C, Meng S, Wang X. Proteomics analysis reveals overlapping functions of clustered protocadherins. Mol Cell Proteomics 2010, 9: 71–83.
100. Goodman KM, Rubinstein R, Thu CA, Mannepalli S, Bahna F, Ahlsen G, *et al.* gamma-Protocadherin structural diversity and functional implications. Elife 2016, 5: e20930.
101. Rubinstein R, Thu CA, Goodman KM, Wolcott HN, Bahna F, Mannepalli S, *et al.* Molecular logic of neuronal self-recognition through protocadherin domain interactions. Cell 2015, 163: 629–642.
102. Nicoludis JM, Lau SY, Scharfe CP, Marks DS, Weihofen WA, Gaudet R. Structure and sequence analyses of clustered protocadherins reveal antiparallel interactions that mediate homophilic specificity. Structure 2015, 23: 2087–2098.
103. Goodman KM, Rubinstein R, Thu CA, Bahna F, Mannepalli S, Ahlsen G, *et al.* Structural basis of diverse homophilic recognition by clustered alpha- and beta-protocadherins. Neuron 2016, 90: 709–723.
104. Nicoludis JM, Vogt BE, Green AG, Scharfe CP, Marks DS, Gaudet R. Antiparallel protocadherin homodimers use distinct affinity- and specificity-mediating regions in cadherin repeats 1-4. Elife 2016, 5: e18449.
105. Nicoludis JM, Green AG, Walujkar S, May EJ, Sotomayor M, Marks DS, *et al.* Interaction specificity of clustered protocadherins inferred from sequence covariation and structural analysis. Proc Natl Acad Sci U S A 2019, 116: 17825–17830.
106. Haas IG, Frank M, Veron N, Kemler R. Presenilin-dependent processing and nuclear function of gamma-protocadherins. J Biol Chem 2005, 280: 9313–9319.
107. Hambsch B, Grinevich V, Seeburg PH, Schwarz MK. {gamma}-Protocadherins, presenilin-mediated release of C-terminal fragment promotes locus expression. J Biol Chem 2005, 280: 15888–15897.
108. Reiss K, Maretzky T, Haas IG, Schulte M, Ludwig A, Frank M, *et al.* Regulated ADAM10-dependent ectodomain shedding of gamma-protocadherin C3 modulates cell-cell adhesion. J Biol Chem 2006, 281: 21735–21744.
109. Bonn S, Seeburg PH, Schwarz MK. Combinatorial expression of alpha- and gamma-protocadherins alters their presenilin-dependent processing. Mol Cell Biol 2007, 27: 4121–4132.
110. Buchanan SM, Schalm SS, Maniatis T. Proteolytic processing of protocadherin proteins requires endocytosis. Proc Natl Acad Sci U S A 2010, 107: 17774–17779.
111. Chen J, Lu Y, Meng S, Han MH, Lin C, Wang X. alpha- and gamma-Protocadherins negatively regulate PYK2. J Biol Chem 2009, 284: 2880–2890.
112. Garrett AM, Schreiner D, Lobas MA, Weiner JA. Gamma-protocadherins control cortical dendrite arborization by regulating the activity of a FAK/PKC/MARCKS signaling pathway. Neuron 2012, 74: 269–276.
113. Suo L, Lu H, Ying G, Capecchi MR, Wu Q. Protocadherin clusters and cell adhesion kinase regulate dendrite complexity through Rho GTPase. J Mol Cell Biol 2012, 4: 362–376.
114. Keeler AB, Schreiner D, Weiner JA. Protein Kinase C Phosphorylation of a gamma-protocadherin C-terminal lipid binding domain regulates focal adhesion kinase inhibition and dendrite arborization. J Biol Chem 2015, 290: 20674–20686.
115. Chen B, Brinkmann K, Chen Z, Pak CW, Liao Y, Shi S, *et al.* The WAVE regulatory complex links diverse receptors to the actin cytoskeleton. Cell 2014, 156: 195–207.
116. Fan L, Lu Y, Shen X, Shao H, Suo L, Wu Q. Alpha protocadherins and Pyk2 kinase regulate cortical neuron migration and cytoskeletal dynamics via Rac1 GTPase and WAVE complex in mice. Elife 2018, 7: e35242.

Neurosci. Bull. January, 2021, 37(1):132–134
https://doi.org/10.1007/s12264-020-00559-7

www.neurosci.cn
www.springer.com/12264

RESEARCH HIGHLIGHT

Cortical Astrocyte-neuronal Metabolic Coupling Emerges as a Critical Modulator of Stress-induced Hopelessness

Giannina Descalzi[1]

Received: 16 May 2020 / Accepted: 5 June 2020 / Published online: 13 August 2020

Stress is a major risk factor for the development of mental illness, such as major depression disorder (MDD) [1]. Despite decades of progress, including findings that stress-induced depression corresponds with numerous morphological and functional neuronal changes within brain structures associated with cognition and mood, such as the medial prefrontal cortex (mPFC) [1–3], a thorough understanding of how stress induces the core symptoms of depression, such as hopelessness, is still lacking. In an exciting new paper in mice, Yin *et al*. show that astrocyte–neuronal metabolic coupling in the mPFC is critically involved in the stress-induced passive coping response in mice [4].

Changes in neuronal activity within the brain increase metabolic demand, and astrocytes respond to this increase by elevating lactate production and shuttling it to neurons [5]. In the brain, neurons have the highest energy needs and interact with astrocytes, which extract glucose from the blood, mobilize glycogen, and release lactate in response to neuronal activity [5]. Behavioral tests that expose mice to uncontrollable stressors, such as the forced swim test (FST), reveal that they express behavioral passivity and immobility (the passive coping response), reflecting the hallmark symptom of hopelessness in MDD patients [6]. This provides a controllable and quantifiable measure of a core symptom of MDD and allows for experimental assessment of the cellular mechanisms within the mPFC involved in this stress-induced response.

✉ Giannina Descalzi
gdescalz@uoguelph.ca

[1] Department of Biomedical Sciences, Ontario Veterinary College, University of Guelph, Guelph, ON N1G 2W1, Canada

Yin *et al*. first demonstrate that the passive coping response corresponds with increases in lactate shuttling in the mPFC by *in vivo* microdialysis of freely-moving mice in the FST. This allowed them to sample the extracellular space by collecting dialysate samples before and during 6 min of FST or control conditions. They found that FST significantly increased lactate levels in the mPFC compared to the control group and to baseline levels before FST exposure. These findings correspond well with previous reports that the aversive experience of a foot-shock increases extracellular lactate levels in the rat dorsal hippocampus [7]. In astrocytes, glucose is converted and stored as glycogen, which can be rapidly metabolized *via* glycogenolysis to produce lactate, which can be shuttled to neurons in an activity-dependent manner – termed the astrocyte-neuronal lactate shuttle [8].

The increases in extracellular lactate levels that Yin and colleagues measured in the mPFC of mice exhibiting the passive coping response suggested that astrocyte–neuronal lactate shuttling is involved in stress-induced behavioral changes. To directly test this hypothesis, Yin *et al*. performed a series of clever experiments aimed at determining the necessity for the astrocyte–neuronal lactate shuttle in FST-induced immobility time. First, taking advantage of the fact that astrocytic lactate is generated *via* glycogenolysis, they micro-injected DAB, a glycogen phosphorylase inhibitor that reduces lactate levels in the rodent brain [7], into the mPFC of mice prior to exposing them to the FST. Remarkably, 1000 μmol/L but not 300 μmol/L DAB significantly reduced the passive coping response, whereas no effects were found in locomotor activity in an open field test (OFT). Critically, the reductions in passive coping caused by DAB were eliminated if 100 mmol/L of *L*-lactate was co-administered with the DAB, highlighting that glycogenolysis is necessary, and *L*-lactate is sufficient for

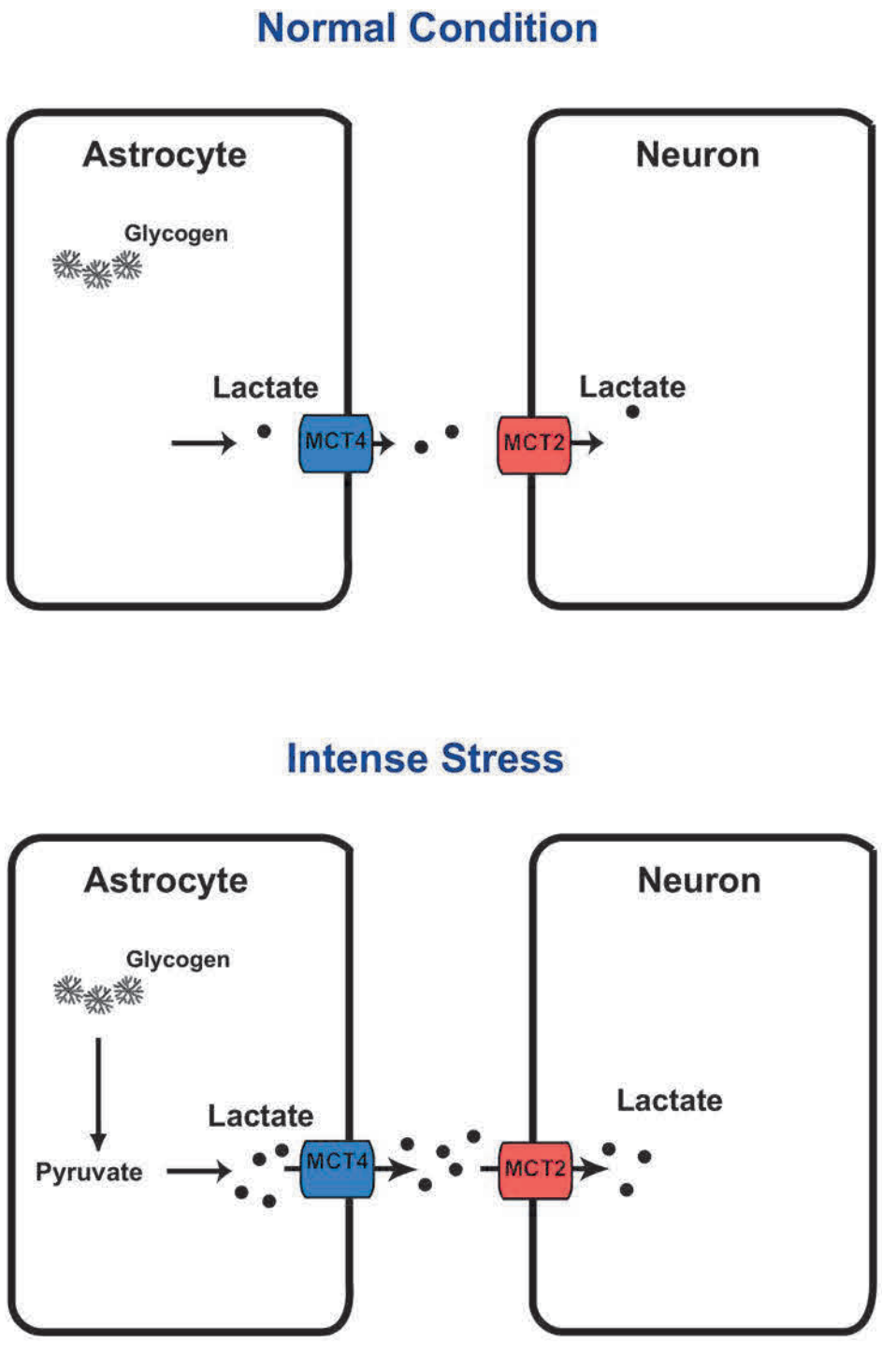

Fig. 1 Illustration of astrocyte–neuronal lactate shuttling under normal and stressed conditions

the passive coping response in mice exposed to the FST. However, whether the FST increased glycogenolysis-dependent lactate in astrocytes or neurons was still not clear. To address this question, Yin and colleagues developed three adeno-associated virus shRNA constructs targeting the expression of the monocarboxylate transporter MCT4, which bidirectionally transports monocarboxylates like lactate, and is exclusively expressed on astrocytes [9]. In this manner, the authors were able to test whether the astrocytic export of lactate is necessary for the passive coping response. Being careful to ensure they were using a valid shRNA construct, the authors confirmed that *Mct4*-shRNA significantly decreased the MCT4 mRNA and protein levels when injected into the mPFC. Remarkably, knocking down MCT4 expression in the mPFC reduced the passive coping response in the FST, but did not affect

locomotor activity in the OFT. However, as MCT4 transports lactate bidirectionally, whether the flow of lactate from astrocytes to neurons is necessary for the coping response was still unclear. What if the prevention of lactate entry into astrocytes is driving the effect? Thus, Yin *et al*. tested a separate group of mice that were also exposed to a reduction of MCT4 in the mPFC *via Mct4*-shRNA, but were also injected with lactate prior to the FST. Critically, the bilateral administration of L-lactate rescued the decreased immobility in mice treated with *Mct4*-shRNA, indicating that the passive coping response involves the flow of lactate from astrocytes to neurons. Last, to determine the cellular mechanism through which lactate could influence the passive coping response, Yin and colleagues turned to electrophysiology, to probe the effects of disrupting the export of astrocytic lactate on synaptic transmission and neuronal activity of pyramidal neurons in layer V of the mouse mPFC. They found that reducing the export of astrocytic lactate *via* Mct4-shRNA had no effect on spontaneous activity, but found that neurons from slices in which MCT4 was reduced were more excitable, generating significantly more spikes in response depolarizing current injection. Remarkably, bath application of *L*-lactate returned the spiking activity to levels comparable to those of the control group. Similar findings were obtained with DAB, whereby *L*-lactate rescued the DAB-induced increases in depolarizing current-induced neuronal spiking. Together, these findings showed that decreasing astrocyte–neuronal lactate shuttling increases the excitability of mPFC pyramidal neurons.

What could be the function of the stress-induced, lactate-dependent modulation of mPFC excitability? Extensive evidence implicates alterations within the mPFC in the pathophysiology of depression, and reports consistently indicate that stress-related disorders correspond with a loss of excitatory tone within the mPFC, and involve a reduction in top-down cortical control over subcortical limbic structures [1, 2]. Notably, chronic stress results in altered dendritic spine morphology in the mPFC of rats [3] and optogenetic stimulation of the mPFC induces resiliency to the depressive effects of chronic social defeat stress in mice [2]. Lactate is bidirectionally transported *via* monocarboxylate transporters, and is thus released from astrocytes *via* MCT1 and MCT4, and enters neurons through MCT2 [9], where it is converted to pyruvate and processed through oxidative phosphorylation in mitochondria to produce ATP [10]. Nevertheless, the functional significance and direction of lactate shuttling *in vivo* is currently under debate [5, 11], and our understanding of astrocyte–neuronal metabolic coupling in stress-induced neuronal changes remains limited. These experiments provide evidence that one functional role of astrocyte–neuronal lactate shuttling is to modulate stress-induced effects on neuronal excitability in layer V pyramidal neurons of the mPFC.

These findings emphasize that complex behavioral responses to stress engage cooperative mechanisms involving multiple cell types. Therefore, a thorough understanding of the mechanisms involved in the pathophysiology of MDD will require a comprehensive analysis of all cells within mood-related circuits, not just neurons. Despite decades of research, and multiple therapeutic strategies, our ability to effectively treat patients suffering from MDD is still woefully inadequate, with >50% of patients finding little to no efficacy from their antidepressant treatment or therapy [6]. This may be in part because current treatment options reflect our current state of understanding, which has thus far focused on neurons. This important paper identifies astrocyte–neuronal lactate shuttling as a critical mechanism for the passive-coping response (Fig. 1). Moving forward, studies will need to integrate the role of astrocyte–neuronal metabolic coupling within stress-induced circuit-wide changes.

References:

1. Krishnan V, Nestler EJ. The molecular neurobiology of depression. Nature 2008, 455: 894–902.
2. Bagot RC, Parise EM, Pena CJ, Zhang HX, Maze I, Chaudhury D, *et al.* Ventral hippocampal afferents to the nucleus accumbens regulate susceptibility to depression. Nat Commun 2015, 6: 7062.
3. Cook SC, Wellman CL. Chronic stress alters dendritic morphology in rat medial prefrontal cortex. J Neurobiol 2004, 60: 236–248.
4. Yin YN, Hu J, Wei YL, Li ZL, Luo ZC, Wang RQ, *et al*. Astrocyte-derived lactate modulates the passive coping response to behavioral challenge in male mice. Neurosci Bull 2020. https://doi.org/10.1007/s12264-020-00553-z.
5. Barros LF, Weber B. CrossTalk proposal: an important astrocyte-to-neuron lactate shuttle couples neuronal activity to glucose utilisation in the brain. J Physiol 2018, 596: 347–350.
6. Daniels S, Horman T, Lapointe T, Melanson B, Storace A, Kennedy SH, *et al.* Reverse translation of major depressive disorder symptoms: A framework for the behavioural phenotyping of putative biomarkers. J Affect Disord 2020, 263: 353–366.
7. Suzuki A, Stern Sarah A, Bozdagi O, Huntley George W, Walker Ruth H, Magistretti Pierre J, *et al.* Astrocyte-neuron lactate transport is required for long-term memory formation. Cell 2011, 144: 810–823.
8. Pellerin L, Magistretti PJ. Glutamate uptake into astrocytes stimulates aerobic glycolysis: a mechanism coupling neuronal activity to glucose utilization. Proc Natl Acad Sci U S A 1994, 91: 10625–10629.
9. Pierre K, Pellerin L. Monocarboxylate transporters in the central nervous system: distribution, regulation and function. J Neurochem 2005, 94: 1–14.
10. Gray LR, Tompkins SC, Taylor EB. Regulation of pyruvate metabolism and human disease. Cell Mol Life Sci 2014, 71: 2577–2604.
11. Diaz-Garcia CM, Mongeon R, Lahmann C, Koveal D, Zucker H, Yellen G. Neuronal stimulation triggers neuronal glycolysis and not lactate uptake. Cell Metab 2017, 26: 361–374 e364.

Neurosci. Bull. January, 2021, 37(1):135–137
https://doi.org/10.1007/s12264-020-00537-z

www.neurosci.cn
www.springer.com/12264

RESEARCH HIGHLIGHT

Adding Fuel to the Fire by Increased GABAergic Inhibition: A Seizure-Amplifying Nigra-Parafascicular Pathway

Yeping Ruan[1] · Rongrong Chen[2] · Jie Yu[2] · Chengping Wen[2] · Zhenghao Xu[2]

Received: 11 March 2020 / Accepted: 24 April 2020 / Published online: 22 June 2020

Epilepsy is a common neurological disorder characterized by recurrent seizures. Most antiepileptic drugs (AEDs) work by regulating the balance of the excitatory glutamatergic and inhibitory GABAergic transmission. However, the current AEDs cannot successfully control seizures in most (>70%) patients with temporal lobe epilepsy (TLE) [1], in whom seizures typically begin in the hippocampus. This may be caused by changes in the synaptic efficacy and remodeling of neural circuits, such as alterations in the distribution/expression of $GABA_A$ receptor subunits and mossy-fiber sprouting. Since Dr. Karen Gale and colleagues originally described the seizure-modulating effects of nigral GABAergic transmission in the early 1980s [2], the substantia nigra pars reticulata (SNpr) has been considered an important seizure-modulating area. For example, lesioning or pharmacological inhibition of the SNpr suppresses seizures in animal models; besides, the anticonvulsant effect of valproate, a first-line AED, is correlated with its inhibitory effect on SNpr neurons [3]. However, the cell types and neural circuits responsible for the control of epilepsy by the SNr are elusive. In a recent *Nature Communications* article, Chen *et al*. identified a pathway from the SNpr to the parafascicular (PF) thalamus that has seizure-amplifying effects in models of TLE (Fig. 1), and this may be targeted for the control of TLE seizures [4].

The SNpr is a GABAergic projection nucleus mainly constituted by parvalbumin-positive (PV^+) neurons. Using *in vivo* single-unit recording and fiber photometry of Ca^{2+} signals, Chen *et al*. found SNpr GABAergic or PV^+ neurons were hyperactivated during hippocampal seizures in kindling mice, consistent with the previous finding that SNpr neurons are hyperactivated in kindled rats [5]. Notably, Chen's results show two peaks of hyperactivation in SNpr GABAergic or PV^+ neurons during hippocampal seizures. The first peak is within 10 s, followed by a second peak ~25 s after the kindling stimulation. The latency of the first peak is similar to the previous therapeutic time-window of brain stimulation or optogenetic intervention (their anti-seizure effects disappear or are greatly reduced when delivered with a 10-s or longer delay) [6]. Besides, the amplitude of the second peak might be an indicator of seizure severity, as it gradually increases from focal to generalized seizures.

A key piece of evidence in Chen's work for the seizure-amplifying effect of the SNpr is that optogenetic or chemogenetic activation of SNpr GABAergic or PV^+ neurons promoted hippocampal seizures in kindling and kainic acid mouse models. Besides, inhibiting these neurons alleviated the severity of hippocampal seizures. Thus, in addition to previous evidence from pharmacological interference targeting the SNpr [2], Chen's data provide more direct evidence for the seizure-amplifying effect of the SNpr. Of note, the activation of SNpr NOS^+ GABAergic neurons, and probably the activation of overlapping SNpr PV^+ neurons, has no such seizure-amplifying effect. Thus, their results further highlight the crucial role of SNpr PV^+/NOS^- GABAergic neurons in amplifying seizures, and raise new questions on the

Yeping Ruan and Rongrong Chen contributed equally to this article.

✉ Zhenghao Xu
xuzhenghao@zcmu.edu.cn

[1] Zhejiang Chinese Medical University, Hangzhou 310053, China

[2] School of Basic Medical Science, Zhejiang Chinese Medical University, Hangzhou 310053, China

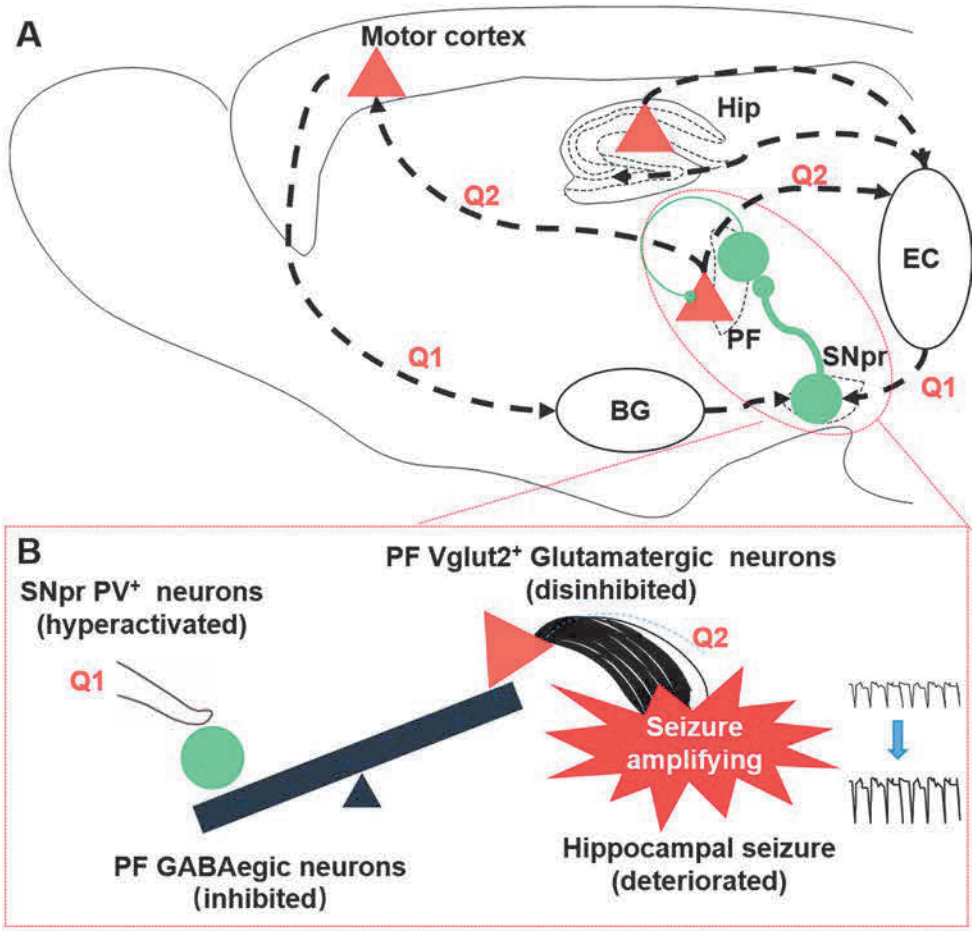

Fig. 1 Schematic of the seizure-amplifying nigral–parafascicular pathway and its associated neural circuits. **A** Schematic of the potential neuronal circuit associated with the seizure-amplifying nigra-parafascicular (PF) pathway. **B** Schematic of the seizure-amplifying nigra-PF pathway. Hyperactivation of the PV^+ SNpr neurons inhibits the GABAergic PF neurons, which subsequently disinhibits the vesicular-glutamate transporter 2 positive ($Vglut2^+$) PF neurons and reduces hippocampal seizures. Of note, there are mainly two unsolved important questions: (Q1) what are the underlying circuits for hippocampal seizure resulting in the hyperactivation of GABAergic SNpr neurons? The answer may be related to the afferent projections from the hippocampal-entorhinal loop or cortical areas; (Q2) what are the underlying circuits for the glutamatergic neurons PF with distant projection in promoting hippocampal seizures? The answer may be related to the PF–EC or PF–motor cortex pathways. EC, entorhinal cortex; Hip, hippocampus; PF, parafascicular; PV^+, parvalbumin positive; SNpr: substantia nigra pars reticulata; Vglut2, vesicular-glutamate transporter 2.

heterogeneity of GABAergic SNpr neurons and their precise modulation.

In addition, Chen *et al*. did some preclinical experiments to facilitate the translation of their work. They found the seizure-suppressing effect of the optogenetic inhibition of GABAergic SNpr neurons disappeared when the photostimulation was delivered 30 s in advance or delayed 10 s, indicating a similar therapeutic time-window as that in the entorhinal cortex [6, 7]. As described above, this phenomenon might be related to the two-peak profile of neural dynamics of GABAergic SNpr neurons during hippocampal seizures; this awaits further study. Besides, they found that mild chemogenetic modulation of PV^+ SNr neurons did not influence motor functions in the rotarod and open-field tests. Thus, Chen's additional findings support a role of the SNpr as an effective and safe target for future neuromodulatory treatment of epilepsy. However, one important issue that is not quite solved here could be the sub-areas of SNpr, particularly since the anterior and posterior parts of the SNpr play completely different roles in kindling rats [8].

The most novel part of Chen's work was the identification of the SNpr–PF pathway as the main circuit mediating the SNpr seizure-amplifying effect. Chen *et al*. provided evidence from fluorescent protein imaging showing that SNpr PV^+ neurons send dense innervation into the PF, the ventromedial thalamic nucleus (VM), and the reticularis nucleus (RT), but sparse projections into the reuniens nucleus (RE). Using optogenetics and chemogenetics, they confirmed that the SNpr–PF projection, but not

the SNpr–RT, SNpr–RE, or SNpr–VM pathway, is involved in the progression of kindling. Of note is the role of the SNpr, particularly the SNpr–VM pathway, in absence-type generalized seizures [9]. Thus, Chen's findings suggest that the SNpr may influence various seizure disorders through distinct thalamic circuits. Here, one inevitable issue, as a common issue in optogenetic experiments, is that modulation of the SNpr–PF projection may have retrograde effects on the SNpr where the neuronal somata are located, and hence may alter other non-PF seizure-modulating pathways.

Further, using *in vivo* and *in vitro* electrophysiology combined with retrograde neural circuit tracing, Chen *et al*. found that GABAergic neurons in the posterior PF receive structural and functional inhibitory connections from PV^+ SNpr neurons. Optogenetic activation of GABAergic PF neurons retarded the progression of kindling, while optogenetic inhibition promoted it. As the PF has long been known as a region composed of glutamatergic neurons [10], this may be the first study on the GABAergic PF neurons. According to their results, the GABAergic PF neurons are mainly located in the posterior PF, have fast-spiking electrophysiological features, and inhibit local $Vglut2^+$ glutamatergic PF neurons. Then they confirmed GABAergic PF neurons are the main direct mediators of the seizure-promoting GABAergic SNpr neurons, evidenced by the finding that optogenetic inhibition of $Vglut2^+$ PF neurons delayed the progression of kindling and their activation promoted it.

Taken together, Chen's work clearly demonstrated a "PV^+/NOS^- GABAergic SNpr neurons – GABAergic PF neurons – $Vglut2^+$ PF neurons" pathway that controls the seizure-amplification in TLE. Because of the region-specific limitation and the existence of inhibitory PF neurons unrelated to the SNpr, selective targeting of the SNr–PF PV projections may provide the most feasible and precise node for the treatment of epilepsy in this pathway. This complex "inhibition-disinhibition" pathway updates the current view of the epileptic network in TLE, and provides clues to explain why AEDs are ineffective and sometimes promote seizures in TLE patients. Their work also reveals the relationship between seizure-related neural dynamics and antiepileptic neuromodulation in the SNpr, which would be of particular concern for researchers on brain stimulation. Clearly, as shown in Fig. 1, two important questions remain: (1) what are the underlying circuits by which hippocampal seizures result in the hyperactivation of GABAergic SNpr neurons? The answer may be related to the afferent projections from the hippocampal-entorhinal loop or cortical areas; and (2) what are the underlying circuits by which glutamatergic PF neurons with distant projections promote hippocampal seizures? The answer may be related to the PF–EC or PF–motor cortex pathway.

Acknowledgements This highlight article was funded by the National Natural Science Foundation of China (81673623) and a project of the National Education Steering Committee for Postgraduate Students Majoring in Traditional Chinese Medicine (20190723-FJ-B23)

Conflict of interest The authors declare that there is no conflict of interest.

References

1. Hu Z, Wang X, Zhong K. Subicular pyramidal neurons: A key to unlock the "black box" of drug resistance in temporal lobe epilepsy. Neurosci Bull 2019, 35: 1123–1125.
2. Iadarola MJ, Gale K. Substantia nigra: site of anticonvulsant activity mediated by gamma-aminobutyric acid. Science 1982, 218: 1237–1240.
3. Tollner K, Wolf S, Loscher W, Gernert M. The anticonvulsant response to valproate in kindled rats is correlated with its effect on neuronal firing in the substantia nigra pars reticulata: a new mechanism of pharmacoresistance. J Neurosci 2011, 31: 16423–16434.
4. Chen B, Xu C, Wang Y, Lin W, Wang Y, Chen L, *et al.* A disinhibitory nigra-parafascicular pathway amplifies seizure in temporal lobe epilepsy. Nat Commun 2020, 11: 923.
5. Gernert M, Fedrowitz M, Wlaz P, Loscher W. Subregional changes in discharge rate, pattern, and drug sensitivity of putative GABAergic nigral neurons in the kindling model of epilepsy. Eur J Neurosci 2004, 20: 2377–2386.
6. Xu ZH, Wu DC, Fang Q, Zhong K, Wang S, Sun HL, *et al.* Therapeutic time window of low-frequency stimulation at entorhinal cortex for amygdaloid-kindling seizures in rats. Epilepsia 2010, 51: 1861–1864.
7. Xu Z, Wang Y, Chen B, Xu C, Wu X, Wang Y, *et al.* Entorhinal principal neurons mediate brain-stimulation treatments for epilepsy. EBioMedicine 2016, 14: 148–160.
8. Gernert M, Loscher W. Lack of robust anticonvulsant effects of muscimol microinfusions in the anterior substantia nigra of kindled rats. Eur J Pharmacol 2001, 432: 35–41.
9. Paz JT, Chavez M, Saillet S, Deniau JM, Charpier S. Activity of ventral medial thalamic neurons during absence seizures and modulation of cortical paroxysms by the nigrothalamic pathway. J Neurosci 2007, 27: 929–941.
10. Mandelbaum G, Taranda J, Haynes TM, Hochbaum DR, Huang KW, Hyun M, *et al.* Distinct cortical-thalamic-striatal circuits through the parafascicular nucleus. Neuron 2019, 102: 636–652 e637.

Brief Instructions to Authors

Neuroscience Bulletin (NB) aims to publish research advances in the field of neuroscience and promote exchange of scientific ideas within the community. The journal publishes original papers of various topics on neuroscience and focuses on potential disease implications on the nervous system. NB welcomes research contributions on molecular, cellular, or developmental neuroscience using multidisciplinary approaches and functional strategies.

Manuscript Submission

Manuscripts should be submitted through our online submission system, ScholarOne Manuscripts, at http://mc03.manuscriptcentral.com/nsb or http://www.neurosci.cn.

Manuscript file types that we accept for online submission include Word and WordPerfect. For Figure submission, we accept JPEG, TIFF, or AI files. Required items differ for each article type and are specified during the submission process.

The submitted manuscript should be accompanied with a signed "*Neuroscience Bulletin* copyright transfer statement and submission form".

Manuscript Preparation

Original Article: An original article contains original research materials and presents compelling data on conceptual advances in any area of neuroscience. The total character count of all sections of the main text (including references and figure legends but excluding supplemental data) should not exceed 80,000, including spaces. Up to 8 figures and/or tables are allowed for the entire manuscript. The minimum requirement of a submitted research article is 40,000 characters in total (or 5000 words excluding the references) and at least 6 display items (figures and tables). The submitted manuscript should be a substantial novel research study in all aspects of neuroscience organizing a complete story with complex mechanisms elucidated using multiple techniques or approaches. NB also welcomes clinical research investigating the pathogenesis or diagnostic markers of a disease. Please note that for clinical trials, an Informed Consent should be provided as supplemental material and stated in the main text. NB no long accepts clinical research that lack insightful mechanistic implications. References are limited to 100.

Review: Authoritative reviews contribute greatly to our journal and we are interested in comprehensive articles well-written to describe recent development in any field of neuroscience for a general audience. Authors are expected to cover controversies in the field and propose their own viewpoints in an unbiased and justifiable way. In particular, the scope of the review should not be dominated by the authors' own work. Review is usually 5,000 to 8,000 words in length (including an abstract of no more than 150 words, excluding the references and title) and 3-6 schematic illustrations are strongly encouraged. Reviews are often contributed by leaders in the field and solicited by the editors. The authors are encouraged to submit a letter of inquiry before the submission.

Insight: For Insight, the article should contain discussion on recent primary research literature similarly as Review. Yet, Insight is shorter in length (no more than 2,000 words, excluding the reference and title) and focuses on a narrower scope. It is possible that in Insight authors advocate a position over a controversial issue or a speculative hypothesis. One schematic illustration is allowed to make the Insight more comprehensive. References are limited to 20.

Method: NB welcomes Method article on novel experimental techniques in any field of basic neuroscience. The Method can be written in the Research Article format yet the content should follow the criteria described below. The description of the method must be accompanied by its validation, its application to an important biological question, and results illustrating its performance in comparison to available approaches. The manuscript will be judged on its novelty, general interest, through assessments of methodological performance and comprehensive technical descriptions that facilitate immediate application. The detailed step-by-step procedure must be described in the form of flow charts for readers to comprehend easily. Additional annotation for key procedures and special treatments will be encouraged. In addition, please note that NB no longer accepts Method on neurosurgery pathway, surgical techniques, or any other clinical related technical studies.

Letter to the Editor: The Letter to the Editor reports a short but exciting finding in a particular field of neuroscience with high quality and of broad interest. The letter should be brief yet concise, and no specific subsections are required. No Materials and Methods section is needed, but any technical information which the authors think is important should be submitted as supplementary materials. The total words count should not exceed 2500 (exclude references and title) and the display items should be limited to 2. References are limited to 15. No abstract and subsections are needed.

Research Highlight: The Research Highlight describes recent research advances by articles published in NB or other journals. It highlights the main results of the research, emphasizes the significance and provides further discussion on the topic. The main text of a Research Highlight is up to 1,500 words (excluding references and title) with no more than 10 references and one or two figures. Research Highlights are usually by editor invitation, but submitted manuscript with high quality will also be considered. No abstract and subsections are needed.

Submitted manuscripts should be divided into the following sections:

(1) Title Page; (2) Abstract; (3) Introduction; (4) Materials and Methods; (5) Results; (6) Discussion; (7) Acknowledgements; (8) References; (9) Figures, legends, and tables; (10) Supplementary information.

Manuscript Revision

Upon peer-reviews, the authors may be asked to revise the manuscript. If the authors have substantial reasons to believe that their manuscript was treated unfairly, they may appeal for reconsideration. Revision should be completed within four (minor revision) or eight weeks (major revision). The authors should provide a cover letter and a point-to-point response for addressing the reviewers' comments. The editor will notify the corresponding author upon the acceptance of the manuscript. Accepted papers will be processed to advanced online publication as soon as possible.

Proofs

A PDF proof will be sent to the authors for them to correct last minute errors on the manuscript.

Page Charges

Page charges for the printed form are as follows: 500 CNY (80 USD) for each text page, 800 CNY (120 USD) for each page containing black-and-white figures, 1500 CNY (250 USD) for each page containing color figures. The corresponding author will receive an invoice on all the publication-related charges once the manuscript is accepted for publication and enters the editing process.

Make checks or money orders payable to:

Center for Excellence in Brain Science and Intelligence Technology, Chinese Academy of Sciences
(中国科学院脑科学与智能技术卓越创新中心)

The bank account number is 4585 4835 7666,
Shanghai Jianguo West Road Subbranch, Bank of China
(中国银行上海市建国西路支行).

Address of Editorial Office of Neuroscience Bulletin:

319 YueYang Road, Room 612, Building 8, Shanghai 200031, China.

Phone: +86-21-64232273; 64170853; 64032696;

E-mail: nsb@ion.ac.cn
http://www.neurosci.cn

(Updated January 2021)

Neuroscience Bulletin Copyright Transfer Statement and Submission Form

We submit this type of article (√): • Original Article • Review • Research Highlight • Insight • Letter to the Editor • Method

Title of article:

Words: Figures: (Color figures:); Tables:

A signature below certifies compliance with the following statements

Copyright Transfer Statement: The copyright to this article is transferred to *Neuroscience Bulletin*, Center for Excellence in Brain Science and Intelligence Technology, CAS and Springer Nature (respective to owner if other than Center for Excellence in Brain Science and Intelligence Technology, CAS and Springer Nature and for U.S. government employees: to the extent transferable) effective if and when the article is accepted for publication. The author warrants that his/her contribution is original and that he/she has full power to make this grant. The author signs for and accepts responsibility for releasing this material on behalf of any and all co-authors. The copyright transfer covers the exclusive right and license to reproduce, publish, distribute and archive the article in all forms and media of expression now known or developed in the future, including reprints, translations, photographic reproductions, microform, electronic form (offline, online) or any other reproductions of similar nature. An author may self-archive an author-created version of his/her article on his/her own website. He/she may also deposit this version on his/her institution's and funder's (funder designated) repository at the funder's request or as a result of a legal obligation, including his/her final version, provided it is not made publicly available until after 12 months of official publication. He/she may not use the publisher's PDF version which is posted on www.springerlink.com for the purpose of self-archiving or deposit. Furthermore, the author may only post his/her version provided acknowledgement is given to the original source of publication and a link is inserted to the published article on Springer's website. The link must be accompanied by the following text: "The original publication is available at www.springerlink.com". The author is requested to use the appropriate DOI for the article. Articles disseminated *via* www.springerlink.com are indexed, abstracted and referenced by many abstracting and information services, bibliographic networks, subscription agencies, library networks, and consortia.

After submission of this agreement signed by the corresponding author, changes of authorship or in the order of the authors listed will not be accepted by *Neuroscience Bulletin*, Center for Excellence in Brain Science and Intelligence Technology, CAS and Springer Nature.

Authorship responsibilities

I/We confirm that:

(1) The work described has not been published before in any language or in any journal or media; that it is not under consideration for publication elsewhere; that its publication has been approved by all co-authors, if any, as well as (tacitly or explicitly) by the responsible authorities at the institution where the work was carried out.
(2) We also give an assurance that the material will not be submitted for publication elsewhere until a decision has been made as to its acceptability for *Neuroscience Bulletin* in 2 months, then declare this statement becomes null and void.
(3) I am/We are responsible for obtaining permission for the use of any material in the manuscript that may be under copyright to my/our employer(s) or other party(ies).
(4) I have read the complete manuscript and accept responsibility for the content and completeness.
(5) I have made a significant contribution to this work and am familiar with the contents.

Author (1) signed:	Date:	Author (2) signed:	Date:
Author (3) signed:	Date:	Author (4) signed:	Date:
Author (5) signed:	Date:	Author (6) signed:	Date:
Author (7) signed:	Date:	Author (8) signed:	Date:
Author (9) signed:	Date:	Author (10) signed:	Date:

Corresponding author signed: Date:

Corresponding author address:

Tel: E-mail:

Neuroscience Bulletin

Neuroscience Bulletin

Copyright Information

For Authors

As soon as an article is accepted for publication, authors will be requested to assign copyright of the article (or to grant exclusive publication and dissemination rights) to the publisher (respective the owner if other than Springer Nature). This will ensure the widest possible protection and dissemination of information under copyright laws.

More information about copyright regulations for this journal is available at www.springer.com/12264

For Readers

While the advice and information in this journal is believed to be true and accurate at the date of its publication, neither the authors, the editors, nor the publisher can accept any legal responsibility for any errors or omissions that may have been made. The publisher makes no warranty, express or implied, with respect to the material contained herein.

All articles published in this journal are protected by copyright, which covers the exclusive rights to reproduce and distribute the article (e.g., as offprints), as well as all translation rights. No material published in this journal may be reproduced photographically or stored on microfilm, in electronic data bases, on video disks, etc., without first obtaining written permission from the publisher (respective the copyright owner if other than Springer Nature). The use of general descriptive names, trade names, trademarks, etc., in this publication, even if not specifically identified, does not imply that these names are not protected by the relevant laws and regulations.

Springer Nature has partnered with Copyright Clearance Center's RightsLink service to offer a variety of options for reusing Springer Nature content. For permission to reuse our content please locate the material that you wish to use on link.springer.com or on springerimages.com and click on the permissions link or go to copyright.com and enter the title of the publication that you wish to use. For assistance in placing a permission request, Copyright Clearance Center can be contacted directly via phone: +1-855-239-3415, fax: +1-978-646-8600, or e-mail: info@copyright.com

Journal Website

www.springer.com/12264
For the actual version of record please always check the online version of the publication.

Subscription Information

Volume 37 (12 issues) will be published in 2021.

ISSN: 1673-7067 print
ISSN: 1995-8218 electronic

For information on subscription rates please contact Springer Nature Customer Service Center: customerservice@springernature.com

The Americas (North, South, Central America and the Caribbean)
Springer Nature Journal Fulfillment,
Harborside Plaza II,
200 Hudson Street, Jersey City,
NJ 07302, USA
Tel. 800-SPRINGER (777-4643);
212-460-1500 (outside North America)

Outside the Americas
Springer Nature Customer Service Center GmbH, Tiergartenstr. 15,
69121 Heidelberg, Germany
Tel.: +49-6221-345-4303

Advertisements

E-mail contact: advertising@springer.com or anzeigen@springer.com (Germany)

Disclaimer

Springer Nature publishes advertisements in this journal in reliance upon the responsibility of the advertiser to comply with all legal requirements relating to the marketing and sale of products or services advertised. Springer Nature and the editors are not responsible for claims made in the advertisements published in the journal. The appearance of advertisements in Springer Nature publications does not constitute endorsement, implied or intended, of the product advertised or the claims made for it by the advertiser.

Office of Publication

Springer Nature Singapore Pte Ltd.
152 Beach Road, #21-01/04
Gateway East, Singapore 189721,
Singapore

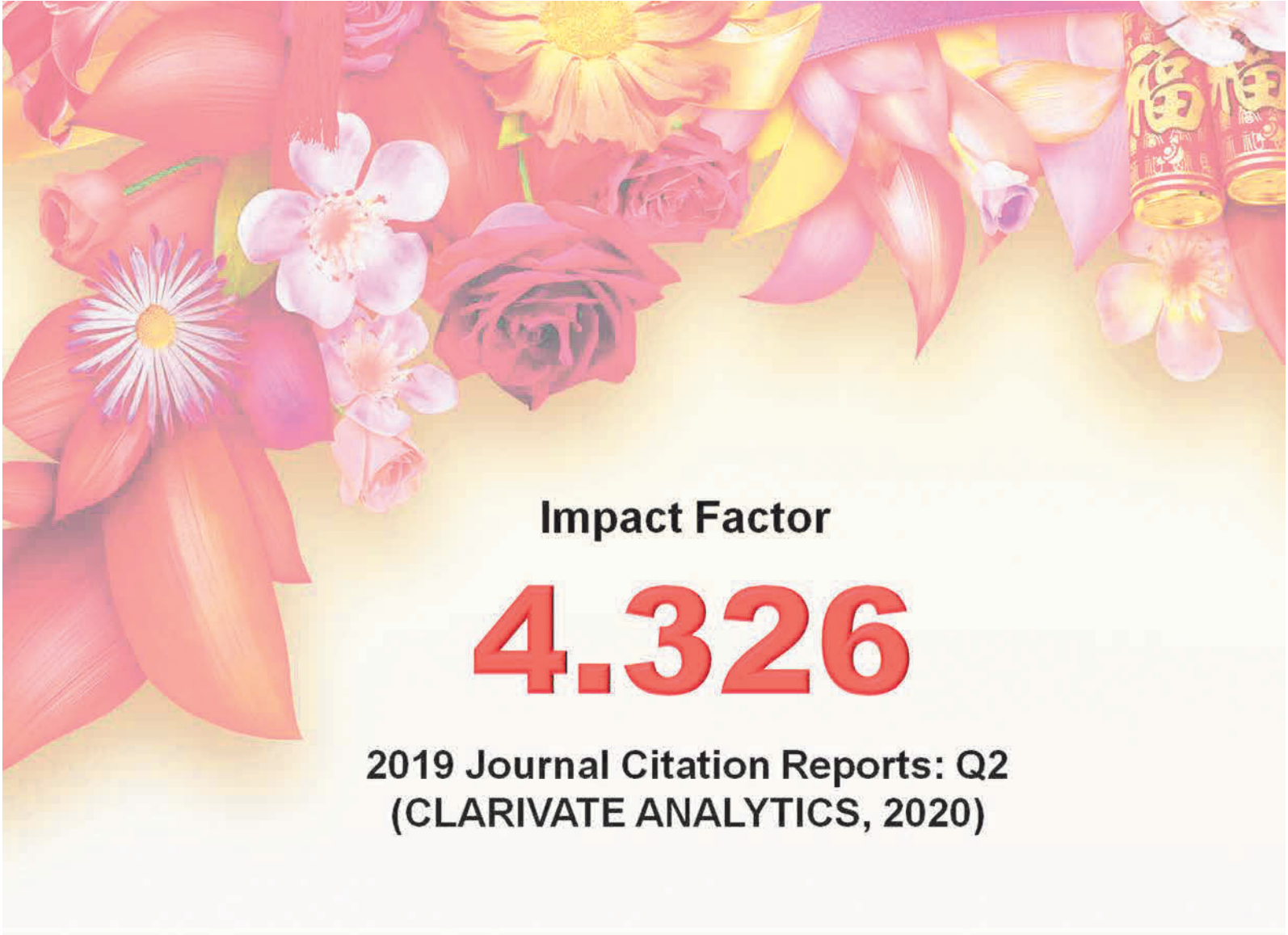

Impact Factor

4.326

2019 Journal Citation Reports: Q2
(CLARIVATE ANALYTICS, 2020)

NEUROSCIENCE BULLETIN 神经科学通报 (Monthly)

Vol. 37 No. 1 January 15, 2021

Sponsored by: Center for Excellence in Brain Science and Intelligence Technology, Chinese Academy of Sciences
Chinese Neuroscience Society

Editors-in-Chief: Shunmin Duan, Ru-Rong Ji

Edited by: Editorial Board of *Neuroscience Bulletin*
319 Yueyang Road, Building 8, Room 612, Shanghai 200031, China
Phone: +86-21-64032273; 64170853; 64032696;
E-mail: nsb@ion.ac.cn; www.neurosci.cn

Editors: Bin Wei, Fei Dong

Published by: Center for Excellence in Brain Science and Intelligence Technology, Chinese Academy of Sciences

Printed by: Shanghai Shengtong Times Printing Co.,Ltd (A6, No. 2888, Caolang Highway, Jinshan District, Shanghai)

Overseas Distributed by: Springer Nature

Home Distributed by: Local Post Offices

ISSN 1673-7067
CN 31-1975/R

Post Office Code Number: 4-608
Permit of Ad. Number: 3100420130051
Price: ¥ 100.00

ISSN 1673-7067

9 771673 706216

OLYMPUS

转盘共聚焦超分辨显微镜

SpinSR10

IXplore

兼顾分辨率和速度的
转盘共聚焦活细胞超分辨系统 SpinSR10

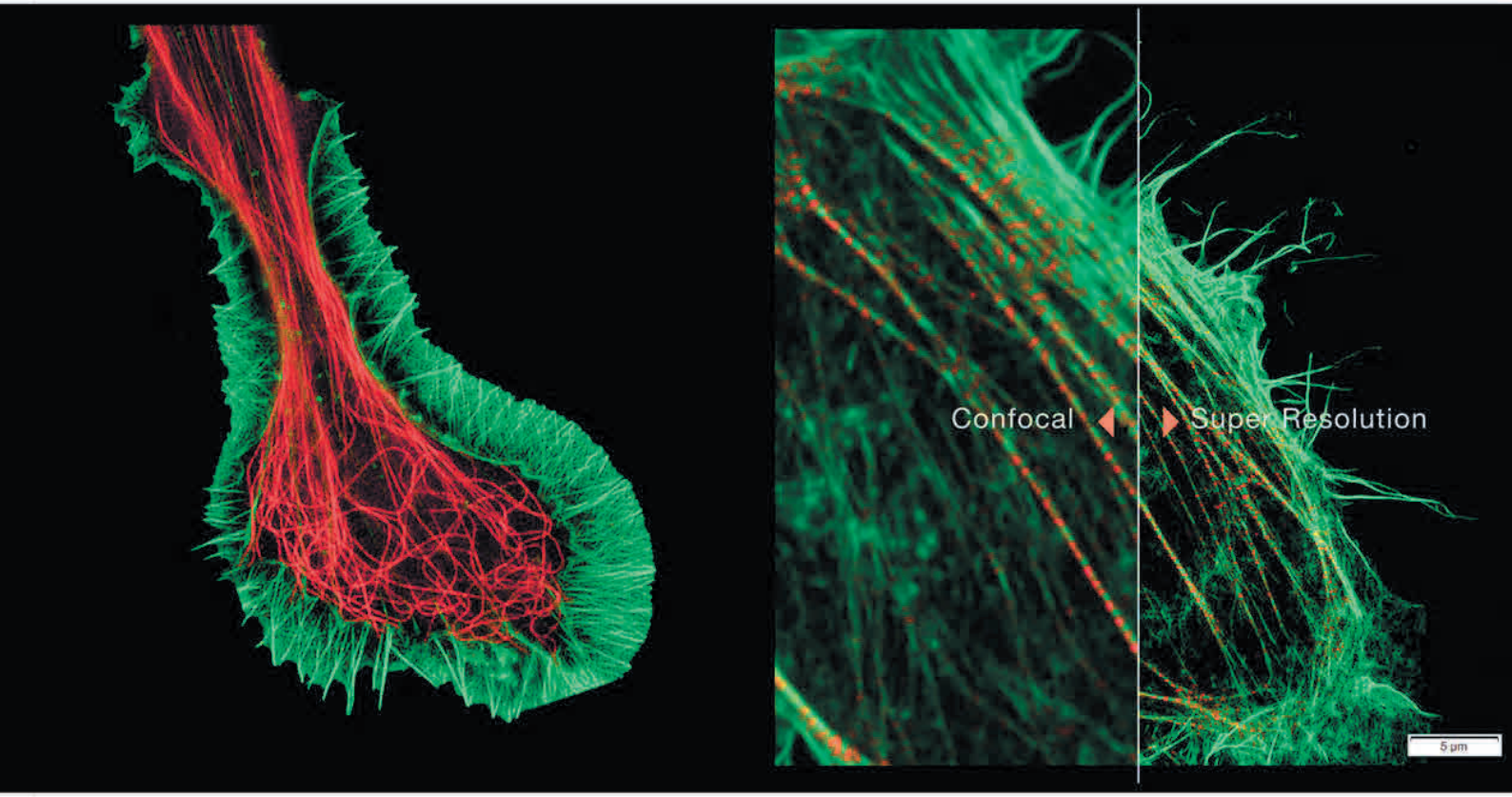

- 分辨率高达110 nm的实时超分辨率成像
- 专有反卷积算法进一步提升图像质量
- 宽视野成像，速度高达 200fps
- 特色硅油物镜可以实现活细胞深层成像
- 宽场、共聚焦、超分辨率模式自由切换
- 功能强大的智能cellSens软件平台

奥林巴斯（北京）销售服务有限公司

北京朝阳区酒仙桥路10号恒通商务园B12C座2F （北京） 010-59756006
上海市徐汇区淮海中路1010号嘉华中心11楼 （上海） 021-51582084
广州市环市东路403号广州电子大厦16楼 （广州） 020-61227171

陕西省西安市新城区尚德路85号太平洋保险大厦8F （西安） 029-87206108
湖北省武汉市江岸区中山大道1628号武汉天地企业中心5号7楼701单元 （武汉） 027-82718838
四川省成都市人民南路四段三号来福士广场T1-11楼 （成都） 028-86703700
辽宁省沈阳市沈河区友好街10号新地中心1号楼3501室 （沈阳） 024-23342084

http://www.olympus-lifescience.com.cn/zh/